A Thesis Submitted for the Degree of PhD at the University of Warwick

Permanent WRAP URL:

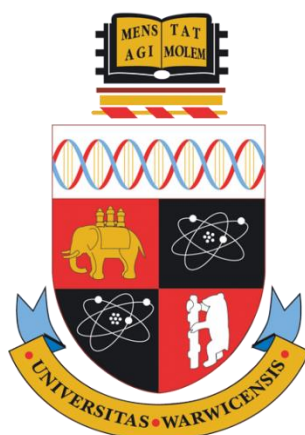http://wrap.warwick.ac.uk/101542/

Copyright and reuse:

warwick.ac.uk/lib-publications

Crystallisation at Functionalised Interfaces

By

Emma Rosanna Ravenhill

A thesis submitted for the degree of Doctor of Philosophy

Department of Chemistry

September 2017

WARWICK

THE UNIVERSITY OF WARWICK

To my loving family, for always believing in me.

'Experiment is the only means of knowledge at our disposal. Everything else is poetry, imagination.'

-   Max Planck

Table of Contents

List of Figures

List of Tables

List of Abbreviations

Abbreviation	Definition
1L	Top Land
2D	Two-Dimensional
2G	Second Ring Groove
2L	Second Land
3D	Three-Dimensional
ACC	Amorphous Calcium Carbonate
AFM	Atomic Force Microscopy
AOT	Dioctyl Sodium Sulfosuccinate
BCF	Burton-Cabrera-Frank
C	Crown
CE	Counter Electrode
CFM	Chemical Force Microscopy
CNT	Classical Nucleation Theory
CV	Cyclic Voltammetry
DCE	Dichloroethane
DDT	Dodecanethiol
DOS	Density of States
EDX	Energy-Dispersive X-Ray Analysis
GC/MS	Gas Chromotography/Mass Spectrometry
HDD	Heavy Duty Diesel
HER	Hydrogen Evolution Reaction
HOPG	Highly Oriented Pyrolytic Graphite
ICDD	International Centre for Diffraction Data
IR	Infrared Spectroscopy
JKR	Johnson-Kendall-Roberts
KSV	Kossel-Stranski-Volmer Theory

m-CNB	*meta*-chloronitrobenzene
MD	Molecular Dynamics
MUA	11-mercaptoundecanoic acid
MUD	11-mercapto-1-undecanol
OCP	Open Circuit Potential
OER	Oxygen Evolution Reaction
OM	Optical Microscopy
PZC	Potential of Zero Charge
QRCE	Quasi-Reference Counter Electrode
RE	Reference Electrode
SAM	Self-Assembled Monolayer
SE2	Secondary Electron
SCE	Saturated Calomel Electrode
SEM	Scanning Electron Microscopy
SICM	Scanning Ion Conductance Microscopy
STM	Scanning Tunneling Microscopy
TBN	Total Base Number
TEM	Transmission Electron Microscopy
TGA	Thermogravimetric Analysis
TRG	Top Ring Groove
VSFS	Vibrational Sum Frequency Spectroscopy
WE	Working Electrode
XPS	X-Ray Photoelectron Spectroscopy
XRD	X-Ray Diffraction
ZDDP	Zincdialkyldithiophosphate

List of Symbols

Symbol	Quantity
J	Nucleation rate
J_0	Intrinsic kinetic parameter for nucleation rate
k	Spring constant
k_B	Boltzmann constant
k_{sp}	Solubility constant
R	Reaction rate
r^*	Critical nucleus radius
S	Saturation level
V	Molecular volume
Z	Formula units (per unit cell)
γ_{cl}	Crystal-liquid interfacial energy
γ_{cs}	Crystal-surface interfacial energy
γ_{sl}	Surface-liquid interfacial energy
ΔG	Gibbs free energy
ΔG^*	Critical nucleus free energy
ΔG_s	Change in surface free energy
ΔG_v	Change in volume free energy
$\Delta \mu$	Chemical potential

Acknowledgements

First and foremost, my greatest thanks go to Prof. Patrick Unwin for his endless energy, ideas and passion, from which I have learnt so much. Thank you for being so supportive and understanding, allowing me the independence to find my own way. Dr. Paul Kirkman, thank you for all the time and effort you have put in over the last four years, for all the coffee breaks and for your unbelievable pickiness, which has no doubt improved my papers, presentations and thesis tremendously. Special thanks are also owed to my industrial supervisors, Dr. Steve Cook, Joanne Jones, and Dr. Mike Sutton.

I am forever indebted and incredibly grateful to Prof. Christopher Poole and all of his team at UHCW. I will never have the words to thank you for everything you have given me. Thank you for filling the hardest times with laughs and jokes, and providing me with the energy I needed, both physically and mentally, to complete my PhD.

Thank you to the '*Crystal Crew*': Maria, Faduma and Harriet, for all our conference adventures, your academic support, and for being caring friends throughout. Special thanks go to Dr. David Walker for all his time invested teaching me XRD. Prof. Aleix Garcia Güell, thank you for all you have taught me. Your help with Illustrator, my many random questions, and all your general advice is greatly appreciated.

Special thanks go to my housemates, Ross, Sam and Connah. I couldn't have found three nicer people to have lived with throughout my PhD. Thank you for all the memories, for putting up with my chaotic lifestyle, and for all your emotional support. Sam, I couldn't have got through these last few tough years without you. You have been the most compassionate friend I could have wished for and without you I would be lost.

Last but not least, I am extremely thankful to my wonderful parents, especially for all your time spent proof reading and for all the trips between Birmingham and Coventry, making these crazy times as 'normal' as possible for me. Mum, thank you for always being there day and night, no matter what the hour. I know you are never far away. Dad, I will be forever grateful for the hundreds of appointments you attended, as well as for your terrible 'Dad jokes', making my thesis writing (slightly) more bearable. To my little sister Natbat, thank you for playing the role of big sister, visiting me when I've needed cheering up, and for always being you, no matter what. Without the support of all my family, this thesis wouldn't exist.

Declaration

This thesis is submitted to the University of Warwick in support of my application for the degree of Doctor of Philosophy. It has been composed by myself and has not been submitted in any previous application for any degree.

The work presented (including data generated and data analysis) is entirely my own, except in the cases outlined below, and parts of this thesis have been published or submitted for publication as detailed below.

Chapter 1:

Ravenhill, E. R.; Unwin, P. R., Crystallisation at Functionalised Interfaces, *review submitted to J. Colloid Interface Sci.*

Chapter 3:

Ravenhill, E. R.; Kirkman, P. M.; Unwin, P. R., Microscopic Studies of Calcium Sulfate Crystallization and Transformation at Aqueous-Organic Interfaces, *Cryst. Growth. Des.* **2016**, *16*, 5887-5895.

Chapter 4:

Ravenhill, E. R.; Kirkman, P. M.; Unwin, P. R., The use of Atomic Force Microscopy for Investigating Surface Forces at Calcium Sulfate Anhydrite Crystals in Organic Solvents, *article finalised and under review with Lubrizol.*

Chen, C.-H.; Ravenhill, E. R.; Momotenko, D.; Kim, Y.-R.; Lai, S. C. S.; Unwin, P. R., Impact of Surface Chemistry on Nanoparticle-Electrode Interactions in the Electrochemical Detection of Nanoparticle Collisions, *Langmuir* **2015**, *31*, 11932-11942. Some sections of this paper also feature in the PhD thesis of the first author, who performed the CFM experiments conducted in aqueous solvents.

Chapter 5:

Ravenhill, E. R.; Adobes-Vidal, M.; Unwin, P. R., Calcium Carbonate Crystallisation at Charged Graphite Surfaces, *Chem. Commun* **2017**, *53,* 12552-12555.

Abstract

Within this thesis, a broad range of microscopic and spectroscopic methods are employed to investigate crystallisation processes initiated at novel functionalised interfaces. This approach combines in situ optical microscopy (OM) with several surface sensitive techniques, including atomic force microscopy (AFM), scanning electron microscopy (SEM) and interferometry, with further structural analysis provided via Raman spectroscopy and X-ray diffraction (XRD). This method allows the key mechanistic phenomena to be elucidated to a high level of detail for crystal growth processes with extreme industrial and biological importance.

The main focus of the thesis is around a specific industrial problem, concerning the detrimental growth of inorganic crystalline materials within internal combustion engines. Firstly, the deposit structure is revealed by implementing analytical techniques such as SEM, Raman spectroscopy and XRD to characterise real engine deposits. This in depth analysis demonstrates the high abundance of the calcium sulfate polymorphs bassanite ($CaSO_4 \cdot 0.5H_2O$) and anhydrite ($CaSO_4$) within the deposit, providing initial insights into this unfavourable growth process.

These deposit growth mechanisms are further studied via in situ OM, monitoring calcium sulfate crystallisation at aqueous-organic liquid-liquid interfaces to mimic real life conditions within the engine environment. As well as providing a wealth of knowledge on the deposit formation process, this approach highlights the unique properties liquid-liquid interfaces offer for crystal growth, revealing via Raman spectroscopy and XRD analysis their applicability for synthesising typically unstable materials under low energy, ambient conditions.

This industrial problem is further investigated by studying the surface reactivity of the growing calcium sulfate mineral faces via AFM force spectroscopy. This allows interaction forces between the deposit surface and different additive chemistries to be quantitatively determined in an oil-based environment, opening up methods for preventing deposition on engine surfaces. Unexpected, low adhesion values are obtained between polar additive head groups and the polar crystal deposit surface, a consequence of electrostatic repulsion. Thus, this work reveals key aspects related to the structure of charge in organic environments, an area still under much debate.

The last chapter of this thesis switches focus to one of the key minerals responsible for engine deposit growth, calcium carbonate. Charged graphite interfaces are implemented to study their effects on the oriented nucleation and polymorphism of this crystal system, in the absence of defects and chemical functionalities. This highlights the significant role electrostatics play in nucleating high energy crystal planes and polymorphs, which is of huge importance for biomineralisation, and scale-prone, charged industrial surfaces. Overall, this thesis elucidates the unexplored properties of two highly relevant functionalised crystal growth interfaces, demonstrating their importance for preventing deposit growth, as well as their diverse application for the synthesis of high energy crystalline materials.

Chapter 1: Introduction

Why Study Crystallisation?

Crystallisation is the term used to describe the growth of a solid material consisting of repeating growth units (i.e. atoms, ions or molecules), displaying a high level of structural order.[1] The resulting structure is defined as a 'crystal', and the structural pattern as a 'lattice'.[1] Although the majority of solids display some degree of ordering, the term 'crystal' is reserved for solids with growth units in rigid, characteristic locations, resulting in an external morphology portraying flat crystal faces, defined by edges.[1] In fact, most solid materials, including most metals, are polycrystalline, comprising many individual crystalline building blocks of differing size and orientation, with the overall structure displaying no long-range order.[2] Solids which cannot be classed as crystalline or polycrystalline are termed amorphous solids, such as glasses, waxes and many polymers.[1,2]

The importance of crystallisation spans a diverse range of fields, from biomineralisation[3-6] to geochemistry[7-9] and the pharmaceutical industry,[10,-12] with almost every area of the chemical industry depending on the use of crystallisation techniques at some stage, for example, for production, purification or material recovery.[1] The stringent control nature exerts over crystal nucleation and growth during biomineralisation results in the formation of materials with extreme strength, with applications in bone reconstruction.[13] Understanding the crystallisation phenomena occuring in geological systems provides insight into key environmental processes including CO_2 sequestration[8,14] and oil recovery.[15-17] Within the pharmaceutical industry, control over crystallisation ensures only the pharmaceutically active forms of drugs are synthesised, and may even result in the discovery of new crystal structures and thus medicines.[10] In this thesis, biomimetic and industrial applications of inorganic crystal growth are investigated, highlighting the importance of controlling the crystallisation process on the polymorphic outcomes.

1.1. Crystal Nucleation and Growth Theory

1.1.1. Supersaturation

The growth and dissolution of a crystalline solid from an aqueous solution of ions A and B can be defined by Equation 1:

$$x A^{y+}{}_{(aq)} + y B^{x-}{}_{(aq)} \rightleftharpoons A_x B_{y\,(s)} \tag{1.1}$$
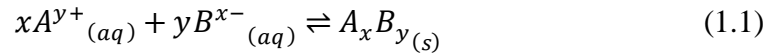
where $y+$ and $x-$ are the charges of ions A and B, respectively. The forward reaction represents nucleation and growth, and the backward reaction, dissolution. When the rates of these are equal, there is no net change in the system, and an equilibrium state is reached at which neither growth nor dissolution occurs overall.[18] This is represented by the equilibrium concentration curve (solid line) in Figure 1.1, shown for a system where solubility increases with temperature. This is the case for most substances,[19] however, for the calcium carbonate system, this relationship is reversed, with solubility decreasing with an increase in temperature.[20]
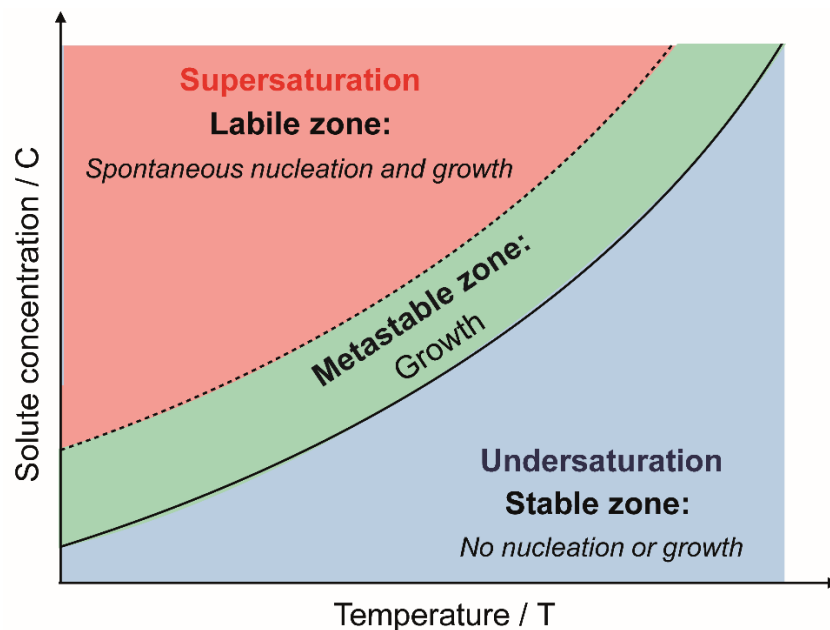
Figure 1.1. Solubility curve, highlighting regions where the solution is undersaturated (blue) and supersaturated (red). The thick and dotted lines represent the equilibrium concentration curve and saturation curve, respectively. The region between the two (green) is the metastable region.

The saturation level of the system is defined by:

$$S = \frac{(\alpha_{A^{y+}})^x \, (\alpha_{B^{x-}})^y}{K_{sp}} \qquad (1.2)$$

where $\alpha_{A^{y+}}$ and $\alpha_{B^{x-}}$ are the activities of ions A and B, respectively, and K_{sp} is the solubility constant. At equilibrium, the solution is saturated ($S = 1$). If the product of the activities of the solute ions is greater than the solubility product, the solution is supersaturated, *i.e.* $S > 1$ and nucleation and growth occur.[21] Conversely, if $S < 1$, the solution is undersaturated and crystal dissolution ensues.[21] The larger the deviation of S from 1, the higher the levels of supersaturation and undersaturation, and therefore, the greater the driving force for growth or dissolution.[18] At low supersaturations and thus low driving forces, a metastable region is established as shown in Figure 1.1, where existing crystals are able to grow, but nucleation of new crystalline material is rare.[21]

Supersaturation may be achieved by combining solutions of highly soluble species to precipitate less soluble species, as demonstrated by Equation 1.1. Other ways of reaching supersaturation include changing either the temperature[18] or pH[22,23] to decrease the solute solubility, or using methods which serve to gradually increase the solute concentration over time, such as solvent evaporation[18] and the Kitano method used for calcium carbonate growth.[24]

1.1.2. Crystal Nucleation

Nucleation events at the very start of the crystal growth process play a key role in determining the structure of the resulting crystals. The nucleation stage is defined as the rearrangement and aggregation of ions, atoms or molecules of the reactant phase into clusters of the product phase that are stable enough to grow on a macroscopic scale.[25] This process is classed as primary nucleation, and can either occur via homogeneous or heterogeneous routes.[1]

1.1.2.1. Homogeneous Nucleation

The spontaneous formation of nuclei from supersaturated solutions in the absence of a surface is known as homogeneous nucleation.[21] However, for this to occur, there must be a decrease in the free energy of the system.[26] The change in free energy during the nucleation process (ΔG) is a balance between the decrease in free energy due to the aggregation of ions (the change in energy per unit volume of nucleus generated, $-\Delta G_v$),

and the energy increase due to the formation of a new solid surface with the solution (the change in energy per unit area of solid-liquid interface generated, $+\Delta G_s$):[27]

$$\Delta G = -\Delta G_v + \Delta G_s \tag{1.3}$$

Assuming the nucleus formed is spherical, of radius, r, and making use of the Gibbs-Thomson relation:[26]

$$\Delta G = -\frac{4\,\pi r^3}{3v}\,k_B T\,\ln S + 4\pi r^2 \gamma_{cl} \tag{1.4}$$

where v is the molecular volume, k_B is the Boltzmann constant and γ_{cl} is the interfacial energy between the solid crystal phase and the surrounding liquid phase. The forms of ΔG_s, ΔG_v and ΔG as a function of r are shown schematically in Figure 1.2.
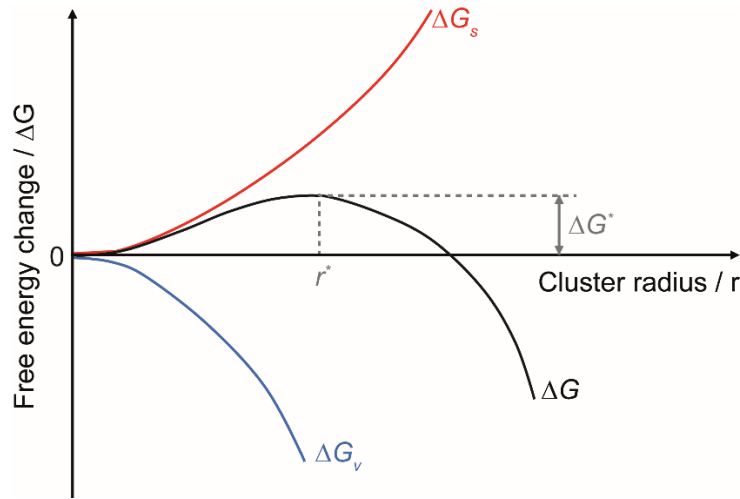
Figure 1.2. Change in free energy of a system as a function of the cluster radius during homogeneous nucleation (ΔG-black line), as the sum of the change in surface energy (ΔG_s-red line) and the change in volume energy (ΔG_v-blue line).

It can be seen that the energy required for nucleation increases with r, until a maximum energy value (ΔG^*) is reached, which represents the energetic barrier needed to achieve nucleation.[21] The corresponding critical nucleus radius required for this process, (r^*), is readily obtained:[26]

$$\frac{d(\Delta G)}{dr} = 0 = -\left(\frac{4\pi r^2}{v}\right)k_B T\,\ln S + 8\pi r \gamma_{cl} \tag{1.5}$$

$$r^* = \frac{2\gamma_{cl}\,v}{k_B T\,\ln S} \tag{1.6}$$

At this size, the nucleus is able to grow to a macroscopic size.[28] Inserting the expression for r^* (Equation 1.6) into Equation 1.4 gives the energetic barrier for nucleation:[26]

$$\Delta G^* = \frac{16\pi \gamma_{cl}^3 v^2}{3(k_B T \ln S)^2} \tag{1.7}$$

Therefore, to decrease the free energy of the system, clusters with a radius smaller than r^* dissolve, while those that have a radius larger than r^* continue to grow.[26,29]

As the driving force increases with increasing supersaturation, an increase in supersaturation will lead to a decrease in the critical nucleus radius and the energy barrier for nucleation (Equations 1.6 and 1.7), as shown by Figure 1.3.
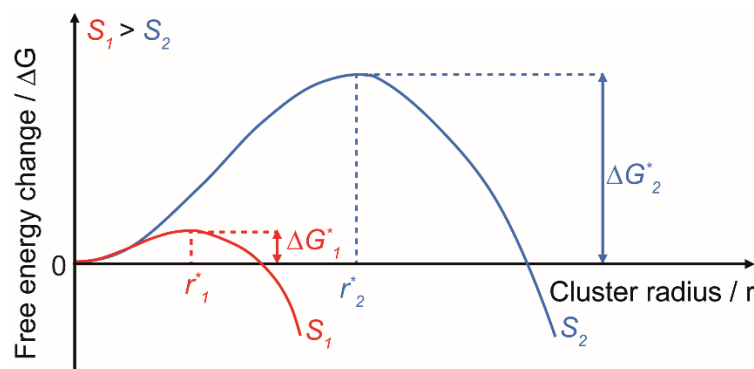
Figure 1.3. Change in free energy during nucleation (ΔG) on nucleus radius (r) for two different supersaturations. The red line represents a system with a higher supersaturation than the blue line.

Homogeneous nucleation usually only takes place at very high supersaturation ($S \gg 1$), and is unlikely to occur close to equilibrium conditions ($S = 1$), where there is an extremely high energetic barrier.[30] The critical energy required for nucleation also explains why at lower supersaturations, the previously described metastable region is established, where only existing crystals grow and spontaneous, homogenous nucleation rarely occurs[19] (see Figure 1.1). Consequently, in most real systems, heterogeneous nucleation is preferred, as this is much less energetically demanding,[18] as discussed in section 1.1.2.4.

1.1.2.2. Classical Nucleation Theory

The rate of nucleation, defined by classical nucleation theory (CNT), is the number of nuclei formed per unit volume per unit time, and is described by an Arrhenius-type Equation:[26]

$$J = J_0 \; e^{\frac{-\Delta G^*}{k_B T}} \tag{1.8}$$

where the pre-exponential factor, J_0, is an intrinsic kinetic parameter, the magnitude of which depends on the rate of the attachment of atoms (ions) or molecules to the nucleus surface,[30] k_B is the Boltzmann constant and T is the temperature. When ΔG^* is large (i.e. > 0), the rate of nucleation will be very slow, and the probability of nucleation occurring is unlikely, but when ΔG^* is small (i.e. < 0), the rate and probability of nucleation are both high.

Substitution of Equation 1.7 in Equation 1.8 gives:

$$J = J_0 \; e^{\frac{-16 \pi \gamma_{cl}{}^3 v^2}{3 (\ln S)^2 k_B{}^3 T^3}} \tag{1.9}$$

From this, it can be seen that the nucleation rate increases with increasing supersaturation, and decreasing solid-liquid interfacial energy, γ_{cl}.

1.1.2.3. Non-Classical Nucleation Theory

In contrast to the classical view of nucleation described above, where unstable clusters grow via monomer-by-monomer addition of elementary species (atoms, ions or molecules) until they reach the critical nucleus radius and become stable,[28] several studies[31-41] show evidence for nucleation via the aggregation of 'precursor clusters' or 'growth units', consisting of ion complexes or multi-ion clusters, which then aggregate to form amorphous phases, feeding the growth of mineral phases via amorphous to crystalline transitions.[42] This aspect to crystallisation has been reviewed recently in some detail.[29,43] Although these multistep nucleation pathways are still to be understood in detail, it is thought that these particles lower the free energy of the system,[31,37,44] with aggregation avoiding the high free energy barriers required of CNT,[44] such that nucleation may even occur in undersaturated solutions.[31,37] These precursor clusters have been extensively reported for the calcium carbonate[31,37-39,45-55] and calcium phosphate[32,35,36,40] crystal systems, which revealed (via techniques such as cryo-

TEM,[32,33,35,36] and in-situ TEM[34]), the presence of initial amorphous structures,[31-33,35,45-55] transforming over time into ordered crystalline forms,[32,33,35,36,45-55] often via metastable phases.[32,34]

Polymorph stabilities are dependent on crystal size, especially in the nanoscale regime, where crystal surface energies become increasingly dominant.[41,56-60] Thus, for an initial growing nucleus, where the surface area/volume ratio is orders of magnitude higher than for microcrystals, surface energy effects, often overlooked in classical thermodynamic polymorph studies, have a significant impact on the polymorph stability.[41] As a result, the most thermodynamically stable polymorphs at the microscale may not necessarily have the most stable surface structures, and therefore, at the nanoscale, become metastable, as highlighted in Figure 1.4. Consequently, an inversion in the stability of the different crystal phases has been reported with decreasing particle size.[41,57,61] As the attachment energies and surface stabilities (and thus resulting polymorph free energies and stabilities) of nanoscale crystals are highly dependent on the solvent environment, control over polymorphism at the nanoscale has been achieved by not only controlling particle size, but also through careful choice of the nature and concentration of the crystallising solvent.[41] A more in depth discussion on controlling polymorphism is provided in section 1.1.3.3.
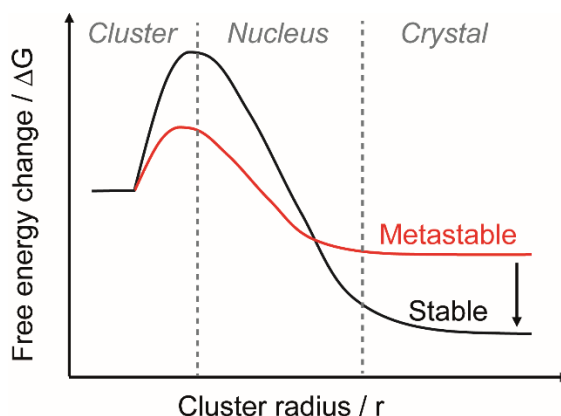
Figure 1.4. Free energy (ΔG) as a function of cluster radius (r) for two crystal polymorphs: a metastable polymorph (red line) and a stable polymorph (black line).

1.1.2.4. Heterogeneous Nucleation

In contrast to homogeneous nucleation, heterogeneous nucleation is considered to occur via aggregation at a 'heterogeneous nucleation site'.[18] In practical systems, this may be

an uneven or scratched surface of the reaction vessel, or dispersed particles in the solution (i.e. impurities, dust, etc.)[18, 26] When a nucleus sits at a solid surface (Figure 1.5), the surface area of the nucleus in contact with the surrounding solution is reduced, as with the system described by:[26]

$$\gamma_{sl} = \gamma_{cs} + \gamma_{cl} \cos\theta \qquad (1.10)$$

where γ_{sl}, γ_{cs} and γ_{cl} are the interfacial energies between the crystal (c), surrounding liquid (l) and solid surface (s).
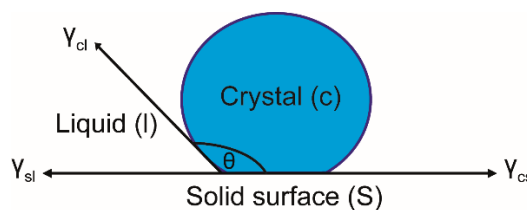
Figure 1.5. Surface energies between the crystal phase (c), surrounding liquid (l) and solid surface (s), where θ is the angle formed between the crystal phase and the solid surface.

The smaller the contact angle between the solid surface and the crystal, the smaller the crystal surface area exposed to the solution, leading to a decrease in the contribution of γ_{cl}. As the energy barrier for nucleation is proportional to $\gamma_{cl}{}^3$ (see Equation 1.7), this dramatically reduces the energy demand, and leads to a decrease in the critical nucleus radius (see Equation 1.6) and the supersaturations needed to realise crystallisation practically, manifested as an increase in the nucleation rate (see Equation 1.9).[21] Thus, the nucleation rate is faster at surfaces where the nucleus forms a smaller contact angle, such as pits or cracks on the reaction vessel (as mentioned above), chemically functionalised interfaces (*vide infra*) or surfaces which curve towards the liquid.[26]

The lower superaturations achievable by heterogeneous nucleation are highly favourable for the formation of uniform crystals, in contrast to high supersaturations, where the high rates at which atoms and molecules are incorporated into the crystal lattice tends to result in crystals that are often non-uniform in size, morphology and orientation, and dendritic growth.[18]

If a carefully designed surface or interface is used, epitaxial growth may occur with considerable control,[8] with the greatest reduction in surface free energy occurring when the structures of the substrate and precipitating phase are well matched,[21] for example, as is the case for templated crystal growth.[62-67] This is much more favourable than both homogeneous and heterogeneous nucleation, as it occurs at low supersaturations within the metastable zone.[21] In this regime, the structure of the surface or interface at which crystal nucleation occurs has a huge impact on the structure of the crystals obtained.

1.1.3. Crystal Growth

Once the critical nucleus radius has been reached, nucleation is complete, and ions, atoms or molecules become incorporated into the crystal surface, resulting in their growth to a visible size[26] (or, in the case of multistep pathways, highlighted in section 1.1.2.3, via attachment of more complex species, such as multi-ion complexes,[32] clusters,[37] and amorphous[40] or crystalline[68] nanoparticles). At the simplest level, crystal growth can be split into four different stages: (i) transport of atoms, ions, molecules or growth units from the solution to the crystal surface, (ii) the adsorption of these to the crystal surface, (iii) their diffusion along the surface and (iv) their attachment at 'positions of low energy', incorporating them into the crystal lattice (plus loss of any remaining solvent).[69] Thus, growth is either transport or surface controlled, depending on whether step (i) or steps (ii-iv) are the slowest.[70] For transport (diffusion)-controlled growth, step (i) is the slowest, whereas for a surface controlled reaction, steps (ii-iv) are the slowest.[21] In many instances, growth is in a mixed kinetic regime and the analysis of growth kinetics requires very well-defined mass transport rates and detailed analysis of interfacial fluxes.[71-73] There are several classical mechanisms that have been proposed for crystal growth, which are briefly summarised below. The mechanism operating depends on factors such as the temperature, driving force and roughness of the different crystal faces.

1.1.3.1. Key Growth Models

Based on experiments conducted by Volmer,[74] which proposed that growth units diffuse across the crystal surface before becoming incorporated into the crystal lattice, a nucleation/growth theory was established by Kossel,[75] Stranski[76] and Volmer,[74]

known as the KSV theory. This portrays the crystal structure as small cube growth units, termed a 'Kossel crystal', with flat terraces, steps, and kinks, as shown in Figure 1.6.
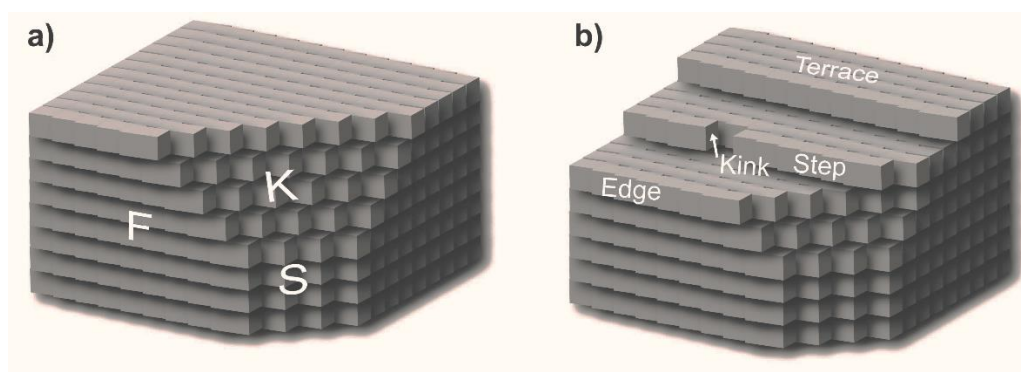
Figure 1.6. (a) Kossel crystal, showing a smooth, atomically flat face (F face), an incomplete kink face (K face), and faces consisting entirely of steps (S face). (b) Schematic showing the position of terraces, edges, steps and kinks within a crystal structure.

This theory considers that the cubic growth units are incorporated into the crystal structure at the most energetically favourable positions, i.e., where the maximum binding energy occurs between the growth unit and the crystal surface. At kink sites, the growth units are able to interact with the surface at three faces of the growth unit, and this is thus the most energetically favourable site for incorporation, followed by steps, which have two interaction areas, and finally flat terraces, which have only one. Therefore, growth occurs preferentially at kink sites, followed by steps and terraces. In fact, growth units which impinge on a terrace are likely to diffuse across the surface, and either become incorporated at lower energy step or kink sites, or leave the surface and return to the liquid phase. In contrast, growth units which impinge at kink sites will be directly incorporated into the crystal structure, due to the much lower attachment energy here. In the absence of impurities, growth would therefore proceed in a 'layer-by-layer' fashion via this adhesive-type mechanism, with the growth units attaching to kink sites and steps and the layers spreading outwards until they reach the edge of the face, forming a completed, smooth terrace.[18,21,26] Once the step of a plane has advanced to the edge of the crystal face, a growth unit must nucleate on the flat terrace for growth to continue. When this 'island' has been formed, growth then continues as before, via the attachment of units to the low energy steps and kinks

produced by this new island, spreading in two dimensions. This is therefore referred to as two-dimensional (2D) nucleation,[26] and is shown schematically in Figure 1.7.
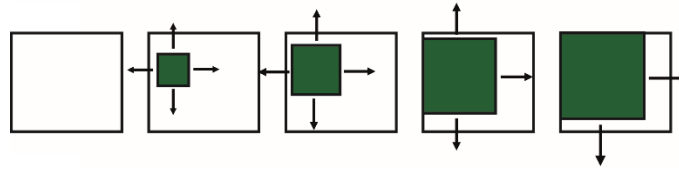
Figure 1.7. Schematic representing 2D nucleation.

A high driving force is required for 2D nucleation, so this mechanism tends to only occur at high supersaturation.[21] However, crystal growth is often witnessed at supersaturations as low as 1%.[18] This is because the above mechanism assumes perfect crystal forms, whereas real crystals contain defects.

To account for the growth of crystals at lower supersaturations, an alternative model was suggested by Frank in 1949.[77] This advocated that the presence of defects, particularly screw dislocations allow growth to occur at lower supersaturations, removing the need for surface nucleation. Along with Burton and Cabrera in 1951,[78] a model (known as BCF theory) was proposed to explain how screw dislocations are able to continuously generate steps, avoiding the need for surface nucleation and thus providing a much lower energy site for attachment than 2D nucleation. Growth at screw dislocations results in the formation of a spiral around the dislocation centre, as a result of the dislocation rotating around the screw axis, with the inner parts of the step moving at a faster rate than the outer parts, in a radial direction.[18,21] The resulting spiral pattern is demonstrated in Figure 1.8.
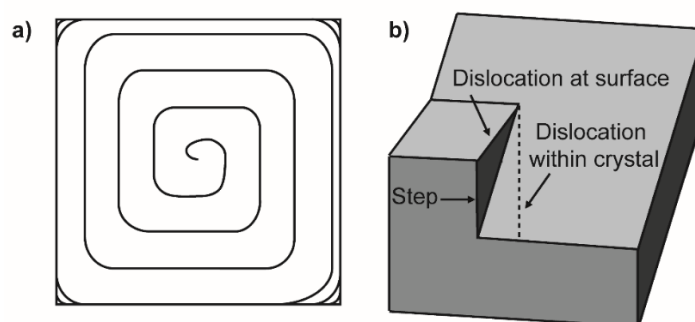
Figure 1.8. (a) Spiral morphology obtained via growth at a screw dislocation. (b) Schematic representing the screw dislocation from which this spiral morphology forms.

These dislocations, or defects may occur due to the presence of impurities in the crystal, or due to rapid crystal growth. In general, this mechanism tends to occur mainly on smooth surfaces, as roughened surfaces do not require screw dislocations for growth, where adhesive-type growth is able to occur.[18]

1.1.3.2. Relevance of Key Growth Models Today

A recent review by Woodruff evaluates the key theoretical concepts realised from BCF theory in the 1950s,[78] and how these have been developed due to significant research conducted since this time, with advances in both computational and experimental methods yielding much more detailed, precise information on crystal growth processes.[79] In summary, several aspects of BCF theory are commonly observed, such as single layer spiral growth occurring at surfaces due to the presence of screw dislocations, although these mechanisms are not necessarily always consistent with BCF theory,[80] particularly for complex crystals. For example, for chiral L-cysteine crystals, single dislocations can form closed loops rather than the spiral morphology predicted by BCF theory.[78] It has also been recently shown that when considering crystals of higher complexity than simple Kossel crystals, different kink structures at the crystal steps are not equivalent, which has a significant impact on the growth kinetics of the crystal.[81]

Although the main ideas behind classical nucleation and growth models are still highly relevant, the behaviour of more complex systems can be much better understood due to the development of higher resolution microscopy techniques, such as atomic force microscopy (AFM),[82-84] which has been used in situ to reveal the kinetics and mechanisms of growth processes, highlighting the occurrence of surface morphologies predicted by early theoretical models and any deviations therefrom.[71,85,86]

As mentioned above, the development of *in-situ*[34] and cryo-TEM[32,33,35,36,87] have revealed the importance of non-classical crystallisation pathways, modifying our view of the early stages of growth processes. Combined with advances in computational modelling[88-90] nucleation/growth models and experiments are increasingly being linked to provide a more holistic understanding. Functionalised interfaces have been employed to study mono-classical two-step nucleation mechanisms, by tailoring the structure of the templating heterogeneous surface to stabilise the prenucleation clusters of interest,[33,91-93] followed by TEM analysis.[33,91] This has been achieved using stearic acid

monolayers,[33] self-assembled monolayers (SAMs),[92,94] carbon nanohorns with amine groups,[91] and nanopores.[93] In addition, we now know more about the structure of the crystal-solution interface, due to the development of techniques such as X-ray diffraction,[95] as well as a range of multi-technique approaches.[83,87,96] As discussed in section 1.2.2, we also have a much clearer picture of the structure of the liquid-liquid interface. This has enabled the more rational use of these interfaces and has fuelled developments that make use of functionalised interfaces to control crystal growth.

The three main growth mechanisms discussed above are summarised in Figure 1.9.
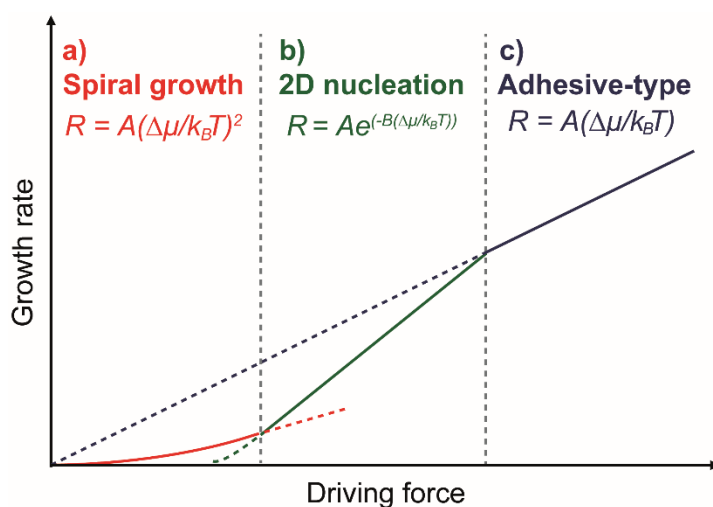
Figure 1.9. Growth rate vs. driving force for (a) spiral growth, (b) 2D nucleation and (c) adhesive-type growth. Moving from left to right, R corresponds to the growth rates of spiral growth, 2D nucleation and adhesive-type growth, respectively. $\Delta\mu$ corresponds to the difference in chemical potential between the solution phase and solid phase, and A and B are constants.

When growth conditions become constant, crystals take their final form (the equilibrium form), where the crystal has the minimum total surface energy at a specific volume. Crystals typically grow as polyhedra, with different exposed crystal planes, each of which have a different roughness,[12] and may therefore grow via different mechanisms. Increasing the driving force leads to an increase in the surface roughness. Thus, at lower supersaturations, the roughness of the interface is low and dislocations are required for growth, resulting in spiral growth, (section (a) in Figure 1.9) with layers forming at screw dislocations in the centre of the face moving outwards. This results in

the formation of relatively flat faces and a stable polyhedral morphology. As the supersaturation is increased, the critical value for 2D nucleation to occur is passed, and this becomes a viable option (section (b) in Figure 1.9). At higher supersaturations, the surface is much rougher and adhesive-type growth occurs, where the attachment energies become equal in all crystallographic directions, resulting in the formation of non-crystallographic, rounded faces and thus spherulitic, fractal and dendritic growth.[21]

1.1.3.3. Factors Affecting Polymorphism

Many important crystal systems are able to crystallise as more than one crystal structure, consisting of the same growth units (or atoms). These structures, known as polymorphs, have different thermodynamic stabilities, due to differences in their bulk structure (i.e. different intermolecular interactions, conformers, crystal symmetry), as well as their surface structure (i.e. different crystallography, different interactions with the solvent environment and the presence of different impurities), which may be significant or subtle.[41] The most thermodynamically stable form (the polymorph with the lowest lattice free energy at a given temperature and pressure)[41] is usually the final bulk phase formed. However, several studies have highlighted the formation of metastable phases prior to this stable phase,[32,34] as described in section 1.1.2.3. This process, of evolving crystal morphology, follows Ostwald's rule of stages,[97] as shown in Figure 1.10. If the system remains under conditions which favour the formation of a metastable phase over the stable phase, it is the metastable phase that will develop. However, if the conditions change to allow a transition from the metastable to the stable phase, the transformation to the stable phase will occur via a solution or solid-mediated process.[97] This has been demonstrated via in situ TEM for the calcium carbonate crystal system,[34,87] with amorphous calcium carbonate (ACC) phases transforming into the metastable vaterite phase, followed by a transition to a second metastable polymorph, aragonite, and finally formation of the thermodynamically stable calcite polymorph, via dissolution-precipitation pathways.[31,34,87,98]

The formation of metastable polymorphs has been frequently reported in highly supersaturated solutions,[87,99,100] as the solution is then supersaturated with respect to all possible polymorphs. As the interfacial energies of the metastable phases are likely to be lower than those of the stable phases, the former grow at a faster rate than the latter.[44] Thus, when the supersaturation is high, kinetic pathways dominate and metastable

phases are produced (see Figure 1.10). However, if the supersaturation of the solution decreases below that of the metastable solubility products, the metastable phases dissolve and recrystallise as the stable phases.[44] Therefore, at lower supersaturations, the first phase visualised is usually the most stable phase, with the system being controlled by thermodynamics rather than kinetics (see Figure 1.10).
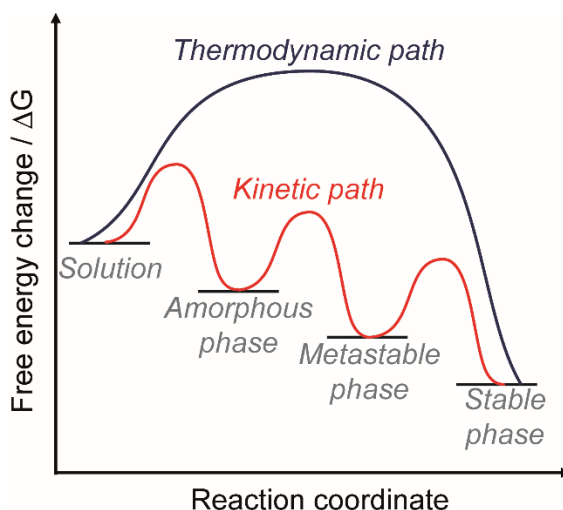
Figure 1.10. Thermodynamic vs. kinetic pathways during crystallisation.

1.1.3.4. Factors Affecting Crystal Frequency and Size

The frequency and size of crystals is highly dependent on the growth solution supersaturation.[101] At low supersaturations, there is a higher energy barrier for nucleation, as described in section 1.1.2.1 (Equation 1.7). Thus, growth is favoured over nucleation, and fewer, larger crystals are obtained.[101] However, at high supersaturations, the energy barrier for nucleation is much lower, resulting in rapid formation of many small crystals,[101] favouring nucleation over growth.

Ostwald ripening also has a large effect on the frequency and size of the crystals obtained. This process describes the dissolution of smaller crystals (with higher surface area/volume ratios and thus higher free energies), resulting in further growth of the larger crystals. However, this only occurs for crystals of the same polymorph.[102] Thus, over time, the average size of the crystals increases, while the number of crystals decreases. This reduces the overall energy of the system, making it more thermodynamically stable.

Thus, it follows that a wide range of experimental parameters, including the supersaturation, temperature, size of the growth environment, solvent and underlying templating surface can be manipulated to control the thermodynamics and kinetics of crystal growth, so as to obtain crystals of the desired size, morphology and polymorph. Efforts made in this field by implementing functionalised interfaces and liquid-liquid interfaces will now be discussed.

1.2. Crystallisation at Functionalised Interfaces

1.2.1. Templated Crystal Growth

There are several detailed reviews focussed on crystallisation at functionalised interfaces, based on biomimetic approaches.[3-5,103-105] Typical examples of these interfaces include SAMs,[62-67] Langmuir monolayers at the air-water interface,[106-110] soluble[111-113] and insoluble[6,114,115] growth additives, and the use of confined environments.[27,56,116] These biomimetic interfaces have been employed to further understand and achieve the high level of control exerted over crystal growth in nature (termed 'biomineralisation'). Unique, complex crystal structures and morphologies are achieved as a result of templated growth on specifically designed organic frameworks and matrices, consisting of complex molecules such as polypeptides, polysaccharides and proteolipid membranes.[105] These direct the assembly and orientation of the crystal growth units through pre-organisation and molecular recognition, rigorously controlling the shape, size, texture and polymorph of the resulting crystals.[4] Extremely well-ordered crystal structures are obtained, with much more desirable structural properties and different structures and morphologies, as compared to their synthetic equivalents.[3-6]

The calcium carbonate system is heavily studied for understanding these biomimetic mechanisms, as this is one of the most highly abundant biominerals. Biomineralisation processes often involve the transformation of ACC to single crystal $CaCO_3$ structures with complex morphologies,[45,55,117] via non-classical crystallisation pathways, as described in section 1.1.2.3. Calcium carbonate has a variety of purposes in several organisms, demonstrating rich polymorphism.[3,4] For example, single crystals of the most thermodynamically stable calcium carbonate polymorph, calcite, are found in sea urchin spines, mollusc-shells, sponges and corals, where their high strength properties offer protection, thus differing significantly to brittle, synthetic calcite.[5,118]

Most studies in this area attempt to mimic the key mechanisms of biomineralisation, by incorporating specific structural features into crystal growth experiments.[3] These principles are applied to obtain new, highly controlled crystal growth pathways to synthesise specialised materials with desirable properties.[4,5] The main methods used thus far are briefly described below.

1.2.1.1. Self-Assembled Monolayers

Self-assembled monolayers (SAMs) of long-chain alkanethiols have been frequently investigated as model templating surfaces[62-67,117,119,120] (for more details on the formation of SAMs see section 1.5.2.3). This provides specifically designed templates, exposing functional groups of interest to the growth solution, at which the organisation and orientation of crystal nuclei can be monitored, and the effects on the resulting crystal growth process studied.

The head group exposed promotes a particular interfacial interaction with the growing crystal surface, which can result in preferred crystallographic orientations at the SAM, and thus the selective growth of crystals with different orientations, morphologies and polymorphs.[3-5,103-105,117,120] However, a strict match of the crystallographic structures of the nuclei and underlying substrates is not necessarily required for these processes, with some lattice mismatch between the two often seen.[4,105] Therefore, these growth mechanisms are not purely controlled by epitaxial relationships, (see section 1.1.2.4.), but through a combination of electrostatic, geometric and stereochemical effects,[4,105,121,122] as demonstrated by the key examples provided below for the calcium carbonate system below.

The growth of calcite has been investigated at SAMs with different head groups on Au and Ag surfaces, resulting in crystals of particular orientation with respect to the surfaces, due to the templated nucleation of specific crystallographic planes (see Figure 1.11). Early studies demonstrated that at Au surfaces, exposing COO^-, OH and SO_3^- groups to the crystal growth solution caused calcite crystals to preferentially nucleate from the (015), (104) and (1 0 12) planes, respectively.[62,63] Very little vaterite (a metastable calcium carbonate polymorph) was grown. In contrast, for the bare metal surfaces, a significant amount of vaterite (as well as calcite) nucleated.[62] This example illustrates how selective polymorph crystallisation can be achieved through the use of functionalised interfaces. It has been suggested that certain negatively charged head

groups act as 'surrogate oxyanions' for specific growing calcite nucleating planes, thereby promoting their growth.[66]
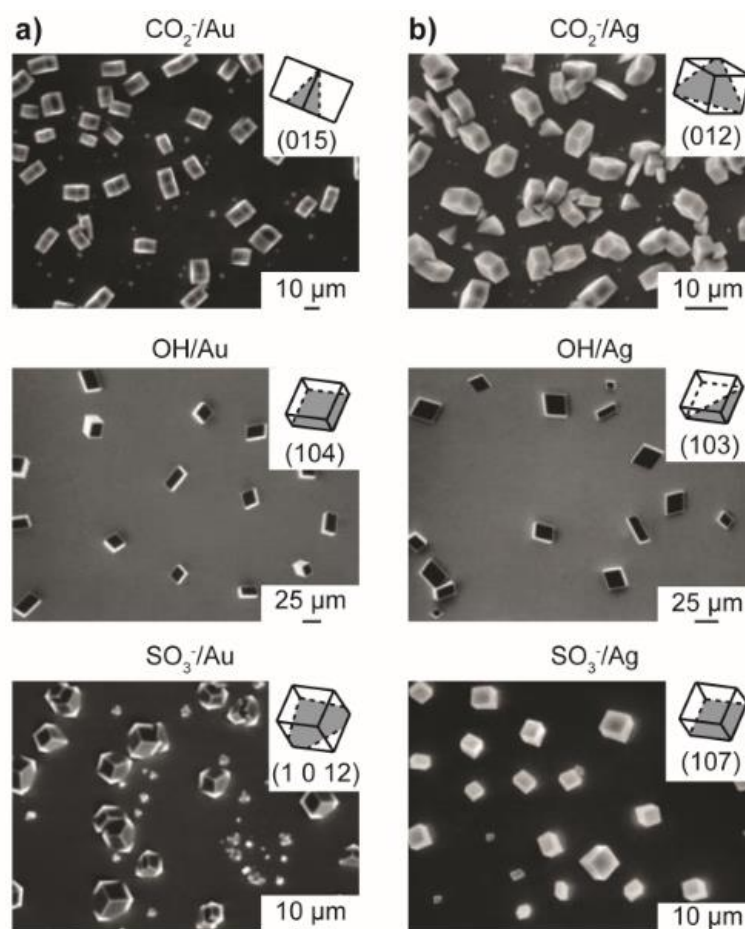
Figure 1.11. Oriented $CaCO_3$ growth at SAMs with three different head groups formed on (a) Au and (b) Ag surfaces. Reprinted (adapted) with permission from ref. 62. Copyright 1999 American Chemical Society.

In addition, changing the underlying metal surface from Au to Ag gave different calcite orientations for the same SAM head groups. For example, SAMs formed at an Ag surface with exposed COO^- groups resulted in preferential nucleation of the (012) face, rather than the (015) face at Au SAMs[62] (see Figure 1.11). This is due to the different orientations of the SAMs at the Au and Ag surfaces, changing the angle of the COO^- head group normal to the substrate surface. As the COO^- SAM head group orientations were found to very closely match the orientations of the carbonate groups in the nucleating calcite planes,[119] the result was the preferential nucleation from a particular crystallographic plane of calcite.

The presence of ions between the SAM and the nucleating plane also has a large impact on the resulting crystal growth kinetics,[67] sizes and morphologies,[66] as well as the orientation as described above. For example, incorporating bicarbonate ions into the plane of the SAM, and thus terminating the SAMs with these ions compressed the monolayer molecules, compensating for lattice and charge mismatches between the SAM and specific calcite crystal faces, thereby enhancing the nucleation of calcite from certain crystal faces which may usually have poor lattice matches with the SAM.[67] This demonstrates that there is a strong correlation between the external shape of the crystal produced and the lattice mismatch between the templating surface and the nucleating plane. The nucleation rate was also enhanced, by reducing the interfacial energy of the growing calcite face and the SAM.[67]

More recently, the early stages of calcium carbonate growth have been studied at mercaptophenol SAMs,[117] revealing changes in the order and bonding of the SAM on Au (111) surfaces during crystallisation. Initial ACC formation resulted in structural disorder in the monolayer, However, despite this disorder, preferential nucleation of the calcite (104) face occurred, with over 70 % of the crystals nucleating from this plane. This suggests that rigid order is not required for preferential nucleation.[117]

The above studies all highlight the sensitivity of the templating process to the combination of electrostatic, geometric and stereochemical interactions occurring between the SAM head groups and the growing crystal faces.

1.2.1.2. Langmuir Monolayers at the Air-Water Interface

Langmuir monolayers have been used in a very similar way to SAMs to investigate the relationship between the templating surface and the crystal face that is nucleated. However, due to differences in the packing of molecules in Langmuir monolayers compared to SAMs on solid surfaces, due to the tilt of molecules in SAMs, even when the same functional groups are exposed to the solution, different preferred crystallographic orientations may result.[4] For example, in contrast to the preferential nucleation of calcite from the (015) and (012) faces, described above for SAMs with exposed carboxylate groups,[62,63] for Langmuir monolayers with exposed carboxylate groups, preferential nucleation of the $(1\bar{1}0)$ face was found. This was again a consequence of the interactions between the carbonate ions of nucleating calcite plane and the terminal groups of the Langmuir monolayer.[107] However, switching to

monolayers of self-assembled molecular ribbons with COOH end groups was found to favour nucleation from the (012) calcite plane, as seen for COOH-terminated SAMs on Ag.[62] This was attributed to the increased space around the carboxylic acid groups in the molecular ribbons compared to the compressed Langmuir monolayers, so they were able to tilt more (similarly to the increased tilt obtained at SAMs on Ag), so as to match the alignment of the carbonates in the polar (012) face.[110]

For compressed Langmuir monolayers of n-eicosylsulfate molecules, (001) planes nucleated preferentially,[107] which matched the behaviour at SO_3^--terminated SAMs at Pd surfaces,[63] but differed from the nucleation planes at Au and Ag metal surfaces.[62,63] For the Langmuir monolayers, this was attributed to the tridentate arrangement of the oxygen atoms in the SO_3^- group favouring nucleation of the (001) face, where the carbonate ions are parallel to the plane.[107,110] Finally, molecular ribbons with hydroxyl groups showed preferential (104) nucleation,[110] as seen at OH SAMs on Au.[62,63] These results are similar to experiments in the absence of monolayers, suggesting that the OH group does not have a significant template effect.[107]

As well as controlling orientation, Langmuir monolayers have been shown to exert control over polymorphism in the $CaCO_3$ system. Hydrogen-bonded 5-hexadecyloxyisophthalic acid Langmuir monolayers resulted in the selective nucleation of the metastable polymorph, aragonite. Aragonite preferentially nucleated with the [010] axis perpendicular to the monolayer surface, due to a match between the periodicities of the carboxylic acid groups of the monolayer and the Ca-Ca distances in the overlaying aragonite structure.[106] A similar effect was observed with the addition of Mg^{2+} ions to Langmuir monolayers of eicosanoic acid, eicosyl sulfate and eicosyl phosphonate. In the absence of the Mg^{2+} ions, calcite precipitation occurred, but in their presence, a switch to aragonite precipitation was seen.[107] This shows some similarity to the mechanism of controlled calcite and aragonite nucleation on β-pleated polypeptide sheet matrices in biomineralisation.[123,124] These studies further highlight the importance of the end group orientations, as well as their chemical structures, for controlling the templating process.

The importance of electrostatics in the templating process has been highlighted by the growth of $CaCO_3$ a range of macrocylic, amphiphillic calixarene and resorcarene Langmuir monolayers, oriented with carboxylic acid functionalities at the air-water

interface.[125-128] This study demonstrated that differences in the average surface charge densities of the carboxylate residues resulted in a difference in both crystal orientation and polymorph, with uniformly oriented single calcite crystals nucleated via their (012) crystal faces at the interface for monolayers of tetracarboxy-calix[4]arenes,[127] octacarboxy-calix[8]arenes,[125,126] and tetracarboxy-resorc[4]arenes,[128] which all have an average charge density of 1.90-2.44 COO^- nm^{-2}. However, for monolayers of octacarboxy-resorc[4]arenes, which display a higher average charge density of 4.71-4.75 COO^- nm^{-2}, crystallisation of acicular aragonite crystals occured,[127] similar to the growth of aragonite at 5-hexadecyloxyisophthalic acid monolayers with a surface charge density of 4.65 COO^- nm^{-2}.[106] Therefore, despite structural differences, monolayers with similar surface charges resulted in similar controlled oriented nucleation and polymorph selection, suggesting that templated $CaCO_3$ nucleation depends strongly on non-specific interfacial electrostatics, as well as geometric and stereochemical phenomena. As the monolayers portrayed a liquid-expanded state, with mobile monolayer molecules, this suggests that epitaxial relationships are not always required for oriented $CaCO_3$ nucleation.

1.2.1.3. Soluble Crystal Growth Additives

The templating action of SAMs and Langmuir monolayers show some similarities to the action of soluble growth additives, which bind to specific crystal faces via electrostatic, geometric and stereochemical interactions.[4,105,121,122] However, as soluble additives are not tethered to a surface, rather than controlling the orientation of the nucleating crystal phase, these tend to have more of an impact on the resulting crystal morphology as the crystal grows. Soluble additives may be charged organic molecules, polymers or surfactants, similar in structure to the molecules which aid morphology selection in biomineralisation.[129-132]

Similarly to SAMs and Langmuir monolayers, when the functional groups of an additive match with specific crystal faces, additives tend to adsorb.[133] For example, proteins rich in the amino acids aspartic acid and glutamic acid are commonly involved in biomineralisation processes,[134-136] as they enable the electrostatic binding of Ca^{2+} ions due to the presence of repeating negative charges within their structure, controlling the resulting crystal morphology.[137-139] Consequently, simpler, but similar-structured

negatively charged small molecules and polymers have been investigated as potential soluble additives for controlling $CaCO_3$ crystallisation.[140-149]

As discussed above, due to their similarity to biomacromolecules, most soluble additives investigated for $CaCO_3$ growth contain negatively charged functional groups. Although the majority of cationic small molecules are relatively ineffective in controlling $CaCO_3$ crystallisation, there are some exceptions. For example, additives such as poly(allylamine hydrochloride) (PAH) significantly impact the structure and morphology of calcite, resulting in the growth of single crystal fibres with lengths a couple of hundreds of microns.[136] However, this occurs as a result of phase separation, due to the interaction of the positively charged amine groups with anionic carbonate ions, rather than due to specific interactions with the growing crystal. This demonstrates that positively charged additives can affect $CaCO_3$ crystallisation in a similar way to negatively charged additives, although higher concentrations of PAH were required relative to poly(aspartate) and poly(aspartic acid) to achieve a similar effect.[136]

Polymorphism can also be controlled to some extent by growth additives. For example, polymers such as poly(sodium 4-styrene sulfonate-*co-N*-isopropylacrylamide) can be used to selectively produce calcite, vaterite and aragonite by varying the concentrations of polymer and Ca^{2+} ions in the system, thus varying the supersaturation and driving force for crystallisation.[113] Changing the driving force determines whether the experiment is under thermodynamic control (leading to the thermodynamically stable polymorph, calcite forming) or kinetic control (resulting in metastable vaterite forming), as explained in section 1.1.3.3. The polymer acts to stabilise the surface of metastable, vaterite crystals, preventing their recrystallisation and transformation to the more stable polymorph, calcite.[113] The flexibility of this soluble additive approach provides different templating opportunities than those offered by SAMs and Langmuir monolayers.

1.2.1.4. Insoluble Crystal Growth Additives

In addition to soluble growth additives, there is often an underlying insoluble organic matrix in biomineralisation, responsible for the ordered growth of the inorganic phase.[150] Several experiments have been conducted to determine the role of this insoluble growth layer, and it has been found that there are mutual synergistic interactions of both soluble 'control' macromolecules and the underlying insoluble

matrix during biomineralisation processes.[135] For example, the precipitation of $CaCO_3$ has been studied in the presence of mimics of the insoluble organic matrix present in the mollusc nacreous layer, containing layers of β-chitin and silk fibroin.[135,151,152] Incorporating soluble macromolecules extracted from the calcite and aragonite forming layers of this structure resulted in the formation of calcite and aragonite, respectively,[135] mimicking the abruptly changing layers of calcite and aragonite present in the mollusc shell. A similar experiment was conducted using calcite seeds rather than an insoluble inorganic matrix, again resulting in the selective synthesis of aragonite and calcite.[118] This demonstrates the full control achievable over polymorphism from bio-inspired processes.

Polymers entrapped on surfaces have also been investigated as model surfaces for biomimetic processes. Poly(acrylic acid) coated chitosan films were found to promote the heterogeneous nucleation of $CaCO_3$ over the whole film, suppressing homogeneous nucleation in the solution,[114] with poly(aspartate) on glass substrates resulting in similar thin $CaCO_3$ films, consisting of calcite and vaterite crystals, as shown in Figure 1.12.[153] These films resemble the structure of the growing surface of nacre. Again, this was considered to be due to the carboxylic groups of the polymer strongly binding to Ca^{2+} ions, increasing their local concentration, thus resulting in thin films growing as a consequence of inhibition of growth vertically due to the presence of the adsorbed acid polymers.[154,155]
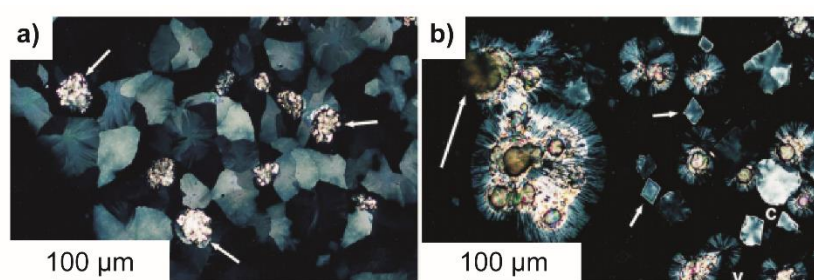
Figure 1.12. Highly birefringent $CaCO_3$ films formed on glass coverslips in the presence of polyaspartate, under polarised optical microscopy. (a) Interconnected rhombohedral calcite crystal aggregates. (b) Polycrystalline vaterite and faceted tablet calcite single crystal films formed in the presence of poly(α,β-D,L-aspartate), resulting in thicker and less connected films. Reprinted from ref. 153. Copyright 1998, with permission from Elsevier.

Monomers have been exposed to calcite crystals grown in biomineralisation, followed by addition of a cross-linker, creating synthetic polymers with morphologies corresponding to specific calcite faces. Removing the calcite crystal was found to leave behind a polymer matrix with the imprint of the crystal.[156] A fascinating example of this is the formation of single calcite crystals of the same complex, sponge-like morphology as sea urchin skeletal plates, as shown in Figure 1.13. This was achieved by taking the porous sea urchin skeleton, filling it with monomer and curing it to form a polymer with the complementary structure. The calcite skeleton was then dissolved, and $CaCO_3$ was precipitated in the presence of this polymer, forming a single calcite crystal with closely similar morphology to the sea urchin skeletal plate. This unusual structure shows non-crystallographic curved faces, as well as the more classic planar faces expected for crystalline materials,[6,157] demonstrating the diversity of morphologies available from biomimetic studies.
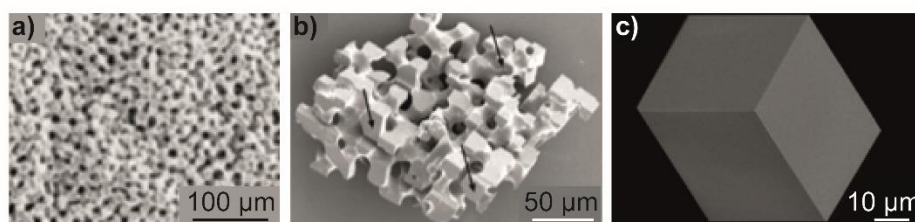
Figure 1.13. Different calcite structures. (a) Cross section through a sea urchin skeletal plate, showing a sponge-like structure. (b) A single calcite crystal precipitated in a polymer replica of the sea urchin plate. (c) Synthetic calcite grown in the absence of additives. Figures 1.13a and b reprinted from ref. 6 by permission of John Wiley & Sons, Inc. Copyright 2002 WILEY-VCH Verlag GmbH & Co. KGaA, Weinheim.

1.2.1.5. Growth in Confined Environments

Finally, there are several reviews on the use of confined crystal growth environments,[27,56,116] with several recent studies highlighting the role of confinement in the ACC crystallisation process.[158-163] Restricting the size of the crystal growth environment not only offers control over the resulting crystal size and morphology, but can also have a huge effect on polymorphic stabilities, as discussed in sections 1.1.2.3 and 1.1.3.3. An important way to achieve a confined environment is through the use of nano- and microemulsions, providing essentially defect-free liquid-liquid interfaces for

studying crystal growth.[164] Several examples of how liquid-liquid interfaces can be used in this way are discussed in the next section.

Micro-[165-167] and nanopipettes[168] have also been implemented to confine the dimensions of the growth environment. For example, nanopipettes have been used to electrochemically control the dissolution and crystallisation of calcium carbonate, highlighting the initial formation of ACC prior to transformation to the stable calcite polymorph,[168] an important precursor in the formation of $CaCO_3$, as discussed above. This study also highlighted how nanopipettes could be used to rapidly screen the effects of additives on the nucleation and growth kinetics.

1.2.2. Growth at Aqueous-Organic Interfaces

There is currently considerable interest in studying crystallisation processes at liquid-liquid interfaces. These interfaces offer unique properties, and can provide simpler synthetic routes at lower temperatures compared to bulk liquid and air-water interfaces, while also resulting in the discovery of new crystal structures and morphologies. To fully understand the power and adaptability of the liquid-liquid interface for crystallisation, it is important to understand interfacial structural properties, and how these may impact the crystallisation process. This aspect is discussed in the following section.

1.2.2.1. Structure and Properties of the Liquid-Liquid Interface

In contrast to the interfaces discussed in section 1.2.1, liquid-liquid interfaces are flexible, and dynamic. The structure of an aqueous-organic interface is highly dependent on the properties of the organic solvent used, determining the miscibility of the two phases, which impacts intermolecular interactions between the phases. Most obviously, such interactions are manifested in the thickness (or sharpness) of the liquid-liquid interface. However, determining the microscopic structure of the liquid-liquid interface is non-trivial. Techniques such as X-ray reflectivity,[169,170] neutron reflectivity[171] and molecular dynamics (MD) simulations[172] have been used to investigate liquid-liquid interfacial widths. A detailed review summarises the use of X-ray and neutron scattering for studying the interfacial widths of water-oil interfaces, and the ordering of surfactants adsorbed at these interfaces.[173] Statistical thermodynamic-based methods show that the width of the interfacial region increases with an increase in the mutual solubility of the two liquid phases, and decreases with

an increase in the size of the solvent molecules.[174] However, for essentially immiscible liquids, the interfaces are relatively sharp and smooth, with synchrotron X-ray reflectivity measurements and predictions from capillary wave theory giving interfacial widths of 3-5 Å for water-hexane and water-dodecane interfaces.[169] For slightly more polar organic phases, such as 1,2-dichloroethane, neutron reflectivity measurements demonstrated the aqueous-organic interface was relatively smooth, with a root mean square roughness of less than 10 Å.[171] This was in agreement with MD simulations and capillary wave theory, showing no substantial region of strong mixing between the two, and little change in the molecular structure and dynamics of the individual liquids at the interface.[172]

For further structural information on liquid-liquid interfaces, vibrational sum frequency spectroscopy (VSFS)[175-180] has been used, again coupled with MD simulations,[180-182] This provides information on the thickness of the interface, by analysing the water O-H stretching modes, and thus the degree with which the water molecules interact with each other, as well as with the organic solvent at the interface.[181,182] An increased interaction between the water and organic molecules was found with an increase in the polarity of the oil phase, with water molecules having a higher ability to penetrate the organic phase and vice versa.[175,180,181] Therefore, the use of more polar (but bulk-immiscible) organic solvents results in a thicker, broader liquid-liquid interface. However, overall, immiscible organic-aqueous liquid-liquid interfaces are relatively sharp, with both organic solvent and water molecules being highly oriented, although even for extremely non-polar organic solvents, there is still some degree of mixing of the water and organic molecules, with the extent being ultimately dependent on the organic solvent polarity and polarisability.[183]

In a recent review,[184] we have summarised the electrostatic properties of the liquid-liquid interface, and the impact this has on the adsorption of surfactants and thus resulting crystal growth and templating strategies achievable here. Briefly, electrostatic interactions at the liquid-liquid interface, which will interfere with the local concentration of ions involved in the crystal growth process differ considerably from those at the air-water interface and within the bulk aqueous phase.[185-188] X-ray reflectivity measurements and MD simulations show that the diffuse double layer models such as the Gouy-Chapman theory break down at liquid-liquid interfaces, as

demonstrated for the behaviour of tetrabutylammonium salts at the nitrobenzene-water interface.[164,189] Depending on details of the system, electron transfer at this interface is thought to lie somewhere between homogeneous electron transfer in solution, and heterogeneous electron transfer at an electrode-electrolyte interface,[164,190-192] and one might expect a similar situation to prevail for the crystallisation of solids from ions.

Due to the lower surface tension of organic-water interfaces compared to the air-water interface, surfactant adsorption and self-assembly at the liquid-liquid interface is much more complex than at the air-water interface, and is highly dependent on the characteristics of both the adsorbing species and the specific interface being studied. This results in differences in the way amphiphiles order and organise, and thus the templating effects of these adsorbed molecules on the resulting crystal growth. Similar techniques to those used for studying the structure of the liquid-liquid interface have been implemented to study surfactant ordering at these interfaces (*i.e.* X-ray reflectivity[193-196] and VSFS[183,197-201]). Generally, amphiphilic monolayers at the oil-water interface are more loosely packed and disordered than at water-vapour interfaces,[193,195,202,203] a consequence of the solubility of the hydrophobic surfactant tails in the organic phase, reducing attractive van der Waals interactions between the chains, and thus increasing their disorder and fluidity in comparison to assembly at the air-water interface.[198,199] Thus, there are different organisational structures of the templating molecules at liquid-liquid interfaces, in comparison to air-water interfaces. Combined with differences in electrostatics at the liquid-liquid interface, different epitaxial relationships are established with the growing crystal face.

1.2.2.2. Types of Liquid-Liquid Interface
1.2.2.2.1. Planar Liquid-Liquid Interfaces

Despite the decreased order of amphiphilic monolayers at the oil-water interface,[193,195,202,203] surfactants are still able to self-assemble to a sufficiently high enough degree to template the crystallisation process. At planar water-chloroform interfaces, it has been found that changing the charge of the surfactant head group induces a change in $SrCO_3$ crystal morphology, due to a change in the order of solute ion binding[186] (see Figure 1.14a). Similar effects were seen for the $BaSO_4$ system (see Figure 1.14b).[185] In both of these cases, the morphology obtained without a surfactant differed to that in the presence of a surfactant.[185,186]
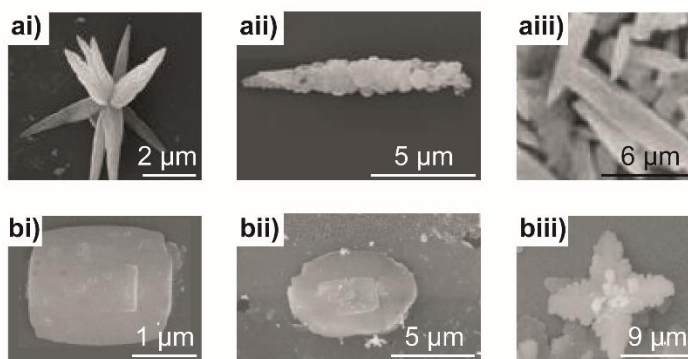
Figure 1.14. (a) SEM micrographs at different magnifications recorded from $SrCO_3$ crystals grown at water-chloroform interfaces in the presence of (i) stearic acid, (ii) octadecylamine and (iii) without ionisable surfactant. Reprinted (adapted) from ref. 186 with permission of Springer. Copyright Indian Academy of Sciences 2003. (b) SEM micrographs of $BaSO_4$ crystal growth at water-chloroform interfaces in the presence of (i) stearic acid, (ii) octadecylamine and (iii) without ionisable surfactant. Reproduced (adapted) from ref. 185 with permission of The Royal Society of Chemistry.

As well as controlling morphology, amphiphillic molecules adsorbed at planar liquid-liquid interfaces have been found to induce nucleation of specific crystal planes, in a similar way to SAMs and Langmuir monolayers at the air-water interface, as described in sections 1.2.1.1 and 1.2.1.2, respectively. For example, alcohol-based surfactant molecules adsorbed at the water-meta-chloronitrobenzene (*m*-CNB) interface induced preferential nucleation of the (020) *m*-CNB plane upon cooling.[204,205] However, in the absence of a surfactant, these crystals did not possess any specific ordering.

1.2.2.2.2. Dynamic Liquid-Liquid Interfaces

Dynamic droplet interfaces, such as the expanding interface provided by a Hele-Shaw cell have also been employed for studying crystal growth, offering unique properties unattainable at static liquid-liquid interfaces.[206-208] By injecting a liquid phase with a lower viscosity into a liquid phase of higher viscosity, viscous fringes are created at the interface of the two immiscible liquids (see Figure 1.15a).[206]

Decreasing the rate at which the interface was replenished stabilised the interface for a sufficiently long enough time to promote dissolution of metastable polymorphs, such as aragonite and the recrystallisation of stable calcite crystals, following Ostwald's

rule of stages (see section 1.1.3.3). In contrast, when the interface was quickly replenished, growth of the metastable aragonite polymorph was favoured, as the interface was not stable for a long enough amount of time for the recrystallisation process to occur.[207] Changing the viscosity of the organic solvent by varying the paraffin/chloroform ratio resulted in differences in fringe morphologies (see Figure 1.15a), with the creation of more complex, branched patterns as the viscosity of organic phase increased, as shown in Figure 1.15b.[206]
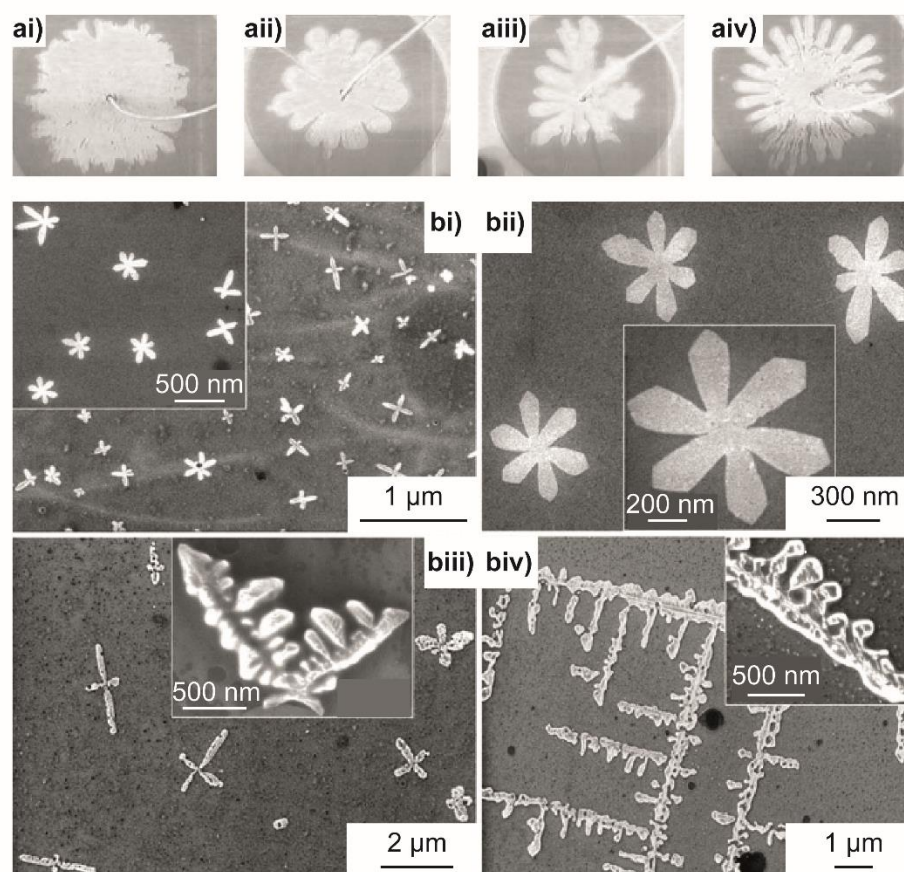
Figure 1.15. (a) Viscous fringes generated when an aqueous phase containing $CaCl_2$ and Na_2CO_3 was injected into an AOT-chloroform/paraffin organic phase. The viscosity of the organic phase was increased from (ai) to (aiv). (bi-bii) Morphologies of the $CaCO_3$ crystals obtained from the liquid-liquid interface shown in (ai). (biii-biv) Morphologies of the $CaCO_3$ crystals obtained from the liquid-liquid interface shown in (aii). Reproduced (adapted) from ref. 206 with permission of The Royal Society of Chemistry.

The surfactant head group was also found to have a significant impact on the crystal growth processes, with rhombohedral calcite crystals growing in the presence of stearic acid, but a combination of calcite and aragonite growing in the presence of AOT. This was assigned to differences in packing of the stearic acid and dioctyl sulfosuccinate (AOT) surfactants at the expanding liquid-liquid interface,[207] with the bulky AOT surfactants packing into rectangular structures, establishing an epitaxial relationship with the aragonite polymorph.

The above studies all highlight the power of introducing dynamic effects to liquid-liquid interfaces, enabling the controlled formation of a range of complex, novel crystal morphologies, as well as metastable polymorphs that are not seen at air-water interfaces, or within bulk aqueous phases.

1.2.2.2.3. Confined Liquid-Liquid Interfaces

Both aqueous[165-167] and oil droplets,[11,209] as well as oil-in-water (o-in-w)[204,205,210] and water-in-oil (w-in-o)[211,212] emulsions have been investigated as liquid-liquid interfaces, again in the presence of templating surfactant molecules, as described for the interfaces discussed above. The overall morphology and size of the crystals obtained is highly dependent on the shape of the liquid-liquid interface, with the presence of surfactants which stabilise droplets and emulsions confining growth to this area.[11,165-167,209,211,212]

As previously explained in sections 1.1.2.3 and 1.1.3.3, restricting the size of the crystal growth environment not only offers control over the resulting crystal morphology, but also has a huge effect on polymorphic stabilities.[41,56-60,210-212] For example, supersaturated glycine droplets in dodecane resulted in the crystallisation of all three glycine polymorphs, depending on the surfactant used and thus the emulsion size.[211,212] This has also been seen for other organic crystals, with the crystallisation of *n*-alkane emulsion droplets in an aqueous phase resulting in the formation of metastable polymorphs, due to templating mechanisms occurring in the presence of certain additive molecules. In the absence of these templating molecules and in the bulk solvent, only the stable polymorph was obtained.[210]

1.3. The Calcium Sulfate Crystal System

1.3.1. Crystal Growth Applications

The calcium sulfate crystal system is of extreme importance in both geological and industrial settings. This is one of the most abundant minerals in nature,[9,213,214] forming in evaporitic deposits and low hydrothermal settings.[7,8] Calcium sulfate also plays a vital role in several industrial processes, such as oil recovery from carbonate reservoirs[15-17] and CO_2 sequestration,[8,14] and is a highly valuable building material,[9] with applications in plasters and binders.[9,215] However, in certain industrial settings, similarly to calcium carbonate, calcium sulfate growth is unwelcome, being present in scale on pipes and reaction vessel surfaces.[214,216] Additionally, calcium sulfate is one of the main inorganic components of deposits formed at the surface of pistons in both gasoline and diesel internal combustion engines.[217-220] Theoretical aspects of calcium sulfate crystallisation are discussed in the following section, to better understand the mechanisms of growth of this mineral system in these key geological and industrial processes.

1.3.2. Theoretical Context

Three intriguing crystal structures exist for the calcium sulfate crystal system, each with differing degrees of hydration.[221-223] Hydrates are crystalline solids containing molecular water within the crystal structure, and are named based on the number of water molecules per parent molecule (e.g. hemihydrate, dihydrate).[221] The most thermodynamically stable phase of calcium sulfate at room temperature is the dihydrate, gypsum ($CaSO_4 \cdot 2H_2O$).[8,9,214,224-228] Both the hemihydrate, bassanite ($CaSO_4 \cdot 0.5H_2O$) and the anhydrous form, anhydrite ($CaSO_4$) are relatively thermodynamically unstable and kinetically unfavorable under ambient conditions.[9] The stabilities of these three different hydrates are shown in Figure 1.16.
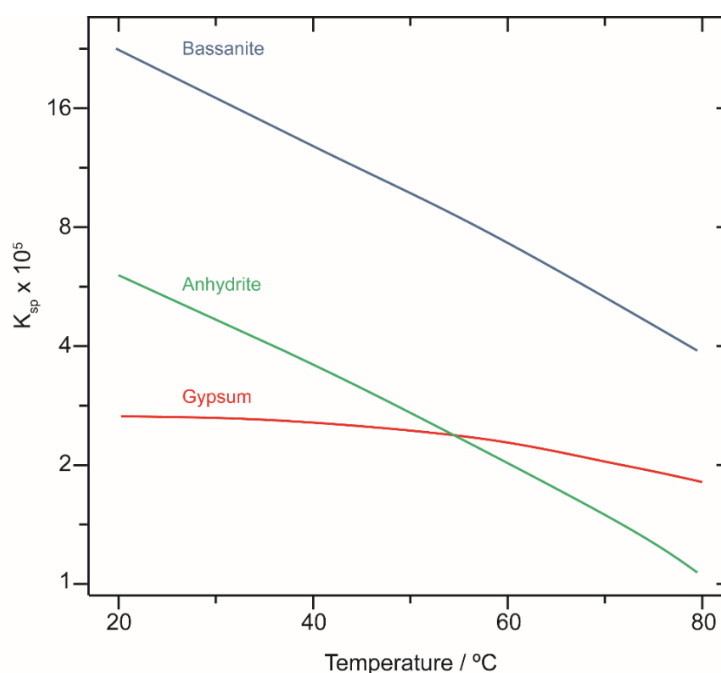
Figure 1.16. Solubility product (K_{sp}) vs. temperature for gypsum, bassanite and anhydrite in water.

Although gypsum is the most thermodynamically stable hydrate at room temperature, anhydrite is more stable at elevated temperatures.[8] [9,214,227-231] However, there is much debate as to the gypsum-anhydrite transition temperature. Previous reported values under atmospheric conditions generally fall within the broad range of 42-60 °C,[9,232] although in practice, it is extremely difficult to synthesise anhydrite at temperatures lower than 70 °C.[214,231,233] Anhydrite has a much higher surface free energy than gypsum (0.090 J m^{-2} and 0.040 J m^{-2} for anhydrite and gypsum, respectively, at 80 °C in solutions containing 0.8 M NaCl and 0.1 M H$_2$SO$_4$),[231] and given the third power dependence of nucleation rate on surface free energy (see Equation 1.9), anhydrite grows at an extremely slow rate compared to gypsum.[28, 233, 234] Anhydrite growth is thus rarely realised even at temperatures where it is the most thermodynamically stable form of calcium sulfate, which is why it is difficult to assign a precise value to this transition temperature.

The formation of anhydrite is also achievable via gypsum dehydration. However, there is much debate as to whether this occurs via direct gypsum dehydration,[214,230,232] or through a stepwise dehydration mechanism, via the formation of bassanite,[235-237] and whether intermediate hydrates (CaSO$_4$·nH$_2$O, (0.5 < n < 0.8) are involved in the latter

process.[238,239] The dehydration of gypsum to bassanite requires high temperatures, as this process is not spontaneous at 97 °C from pure calcium sulfate solutions.[233] Once bassanite is formed, further dehydration results in the formation of anhydrite, the stability of which depends on the temperature.[215,233,235,237,238] Soluble anhydrite, (γ-$CaSO_4$), is a low-temperature dehydration product (T < 110 °C) which has a very similar, 'tunneled' crystal structure to bassanite, consisting of unpopulated vacancies, or water channels[240] (see Figure 1.17). These become repopulated upon cooling, and thus soluble anhydrite readily converts back to bassanite under ambient conditions.[215] However, at temperatures greater than 110 °C, a high amount of structural rearrangement occurs,[235] resulting in the conversion of soluble anhydrite to insoluble anhydrite (β-$CaSO_4$),[237] which has a close packed array structure with no channels, and thus cannot rehydrate.[238] This process reaches completion at around 380 °C.[241] Thus, the formation of stable, pure anhydrite is non-trivial.
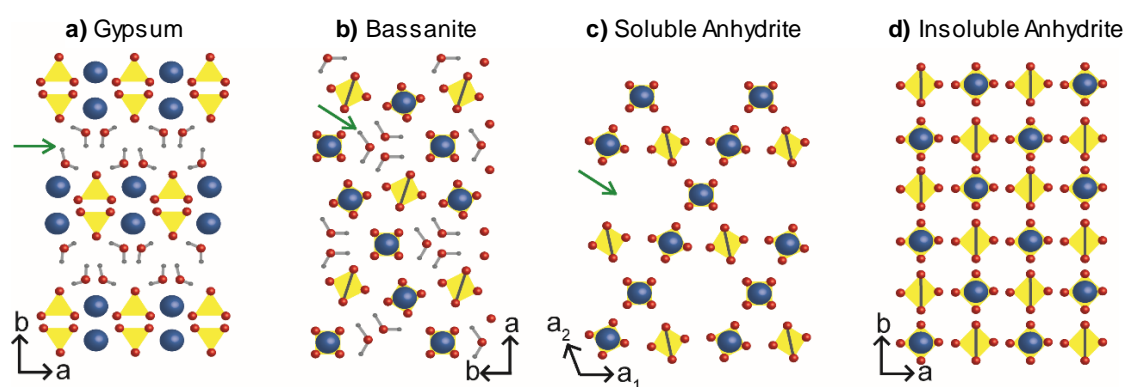
Figure 1.17. Crystal structures of (a) gypsum, (b) bassanite, (c) soluble anhydrite and (d) insoluble anhydrite. The blue atoms are Ca^{2+} ions, the tetrahedral are SO_4^{2-} ions and the arrows mark the positions of the water channels in each.

1.4. The Calcium Carbonate Crystal System

1.4.1. Crystal Growth Applications

As calcium carbonate is one of the most highly abundant biominerals,[3-5,118] a vast amount of work has been conducted to control the nucleation and growth of specific morphologies and polymorphs of this crystal system, to further understand these biomimetic processes,[3-5,103-105] as discussed in section 1.2.1. Because of this, calcium carbonate has been explored for bone reconstruction.[13] Calcium carbonate is also of great geological importance, present as limestone, and has applications within the

pharmaceutical industry in antacid tablets.[242] However, there are several examples where crystallisation of this mineral is unfavourable, being one of the key components of scale formation in a range of industrial settings.[243-245] Here, calcium carbonate growth is costly, forming on the walls on pipelines in both aqueous[243,244] and organic[245] environments, resulting in corrosion, restricted pipeline flow and decreased oil and gas production.[245] Thus, understanding the mechanisms of growth of the different calcium carbonate polymorphs is of both fundamental and industrial importance. Key theoretical concepts for this crystal system are discussed below.

1.4.2. Theoretical Context

Calcium carbonate exists as three anhydrous crystalline polymorphs: calcite, vaterite and aragonite.[246,247] Under ambient conditions, calcite is the most thermodynamically stable, followed by aragonite, and vaterite.[13,246,247] In nature, all three polymorphs can occur simultaneously, although aragonite and calcite are much more abundant, due to the rapid, irreversible conversion of vaterite to the other two polymorphs in aqueous solutions.[13] This is a consequence of the higher solubility of vaterite, which, over, time, dissolves and recrystallises as the more stable aragonite and calcite polymorphs via a dissolution-repreciptation mechanism,[248] following Ostwald's rule of stages[97] (see section 1.1.3.3).

The resulting calcium carbonate polymorph formed is also highly dependent on whether crystallisation occurs via a thermodynamic pathway at low driving forces, or a kinetic pathway at high driving forces, as explained in section 1.1.3.3. Thus, in aqueous solutions, at lower temperatures and supersaturations, the thermodynamically stable calcite polymorph precipitates, whereas aragonite often dominates at higher temperatures.[249] Vaterite is usually found at higher levels of supersaturation,[249] and at high pHs,[22,23] where crystallisation occurs via a kinetic pathway.

Differentiating between these three calcium carbonate polymorphs is often possible via imaging techniques, as they each have markedly different crystal structures and thus resulting morphologies. Calcite has a rhombohedral crystal structure, and is most commonly found with a cube-shaped morphology[249] (see Figure 1.18a), whereas aragonite has an orthorhombic crystal structure, and usually occurs as needles.[249] However, under certain conditions, aragonite possesses a flake-like, 'cauliflower-like'[250] or sheaf-of-wheat structure[34] (see Figure 1.18b). Vaterite has a hexagonal

crystal structure, and is usually found with a spherulitic, flower-like morphology[251] (see Figure 1.18c).
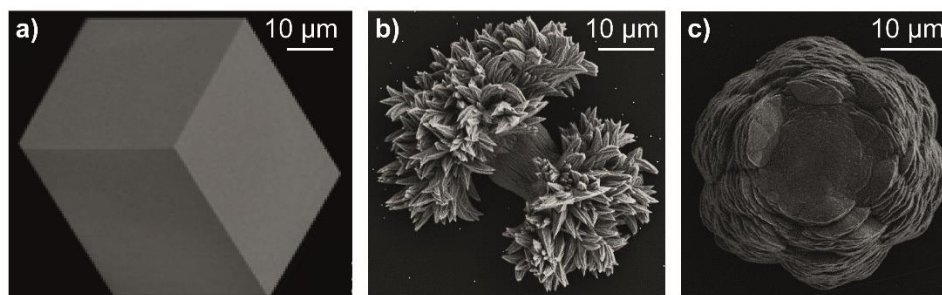
Figure 1.18. SEM micrographs showing the varied morphologies of the calcium carbonate polymorphs (a) calcite, (b) aragonite and (c) vaterite.

As well as these anhydrous, crystalline polymorphs, ACC occurs, which is hydrated,[44] and plays a key role in the nucleation mechanism,[31,34,87,98] as described in section 1.1.3.3. The structure of ACC is under high debate, and it has been suggested that this occurs as a range of hydrous and anhydrous structures,[34] often resembling the structure of the crystalline forms of calcium carbonate, with vaterite-like motifs found in ACC precipitated from alkaline solutions, and calcite-like motifs occurring in less alkaline solutions.[98] Thus, the resulting calcium carbonate polymorph formed is thought to depend on the structure of this precursor ACC phase,[98] as well as the factors discussed above, highlighting the complexity of controlling calcium carbonate polymorphism.

1.5. Analytical Characterisation Techniques

1.5.1. Techniques used for Crystal Growth Studies

In this thesis, a range of microscopic and spectroscopic techniques are used to investigate the mechanisms of inorganic crystal growth at applied functionalised interfaces. The studies described herein rely heavily on techniques ubiquitously used for studying crystallisation, and are thus only briefly discussed within the context of this thesis.

1.5.1.1. Microscopy Techniques

In situ optical microscopy (OM) is employed throughout to produce high magnification time-lapse images of crystal growth processes occurring at both liquid-liquid (aqueous-organic) interfaces and charged surfaces. By acquiring these images over the course of

the growth experiment, information is yielded on the dynamic processes occurring at each growth interface, from which crystal growth mechanisms can be deduced.

For further morphology analysis, interferometry and scanning electron microscopy (SEM) are employed. Interferometry measurements elucidate the crystal surface structure, providing quantitative measurements of the surface roughness and highlighting the presence of specific surface features formed as a consequence of the crystal growth mechanisms. SEM is used for further high resolution structural analysis of the resulting crystal morphologies, and coupling this technique with energy-dispersive X-ray analysis (SEM-EDX) allows determination of the main elements present in the resulting crystal structures, and their relative weight percentages.

1.5.1.2. Analytical Characterisation Techniques

For a more detailed structural analysis, Raman Spectroscopy is employed as quick spectroscopic technique for determining the crystal polymorphs formed. This is possible as the position of the Raman shifts are dependent on the degree of hydration of the crystal structures, as well as the symmetry of the ions in the crystal and thus their crystallographic environments,[252] as described in detail in Chapter 2 for the calcium sulfate crystal system. XRD is used as a complementary technique for determining the crystal polymorph, providing additional information on the crystal system, space group and unit cell parameters.

1.5.2. Techniques used for Determining Interaction Forces

1.5.2.1. Atomic Force Microscopy

The reactivity of the crystal faces grown and their interactions with a range of different head group chemistries are analysed using a technique known as chemical force microscopy (CFM).[253,254] This is derived from atomic force microscopy (AFM), a scanning probe microscopy technique invented by Binnig in the 1980s for high resolution topographical imaging on the nanometre or Angström scale.[255,256] Prior to this, scanning tunnelling microscopy (STM),[257,258] was used for this purpose, however this was limited to imaging conducting or semi-conducting samples. The development of AFM allowed both conducting and insulating samples to be imaged with high precision, and has since been used to determine the topography of a wide range of insulating crystal surfaces.[71,85,86,259]

For topographical imaging, the following setup is used. An AFM probe, which comprises a flexible cantilever with an extremely sharp tip (radius ~ a few nm), is positioned above the sample surface by a three-dimensional (3D) piezoelectric scanner. These probes are often made of silicon or silicon nitride, with a characteristic spring constant, k, and resonant frequency. Depending on the AFM instrumentation, either the probe or sample surface are scanned in a raster pattern in the XY plane in a very precise manner by a 3D piezoelectric scanner. Simultaneously, the topographical surface features are tracked by movement in the Z direction. As the probe-sample distance approaches a few nanometres, the cantilever is deflected, due to attractive and repulsive interactions between the two. This deflection is detected by means of a laser beam, which is focussed onto the rear of the cantilever, and reflected onto a position-sensitive photodiode detector, as shown in Figure 1.19. Depending on the imaging mode used, either the cantilever deflection, oscillation amplitude or phase is used as a feedback setpoint parameter, which is maintained at a constant value by changing the Z-position of the scanner, and thus the probe-sample distance. By plotting the Z-position of the scanner against the XY probe position, a 3D image of the surface topographical features is obtained. These images may be recorded in air, vacuum or liquid by utilising a small flow cell.
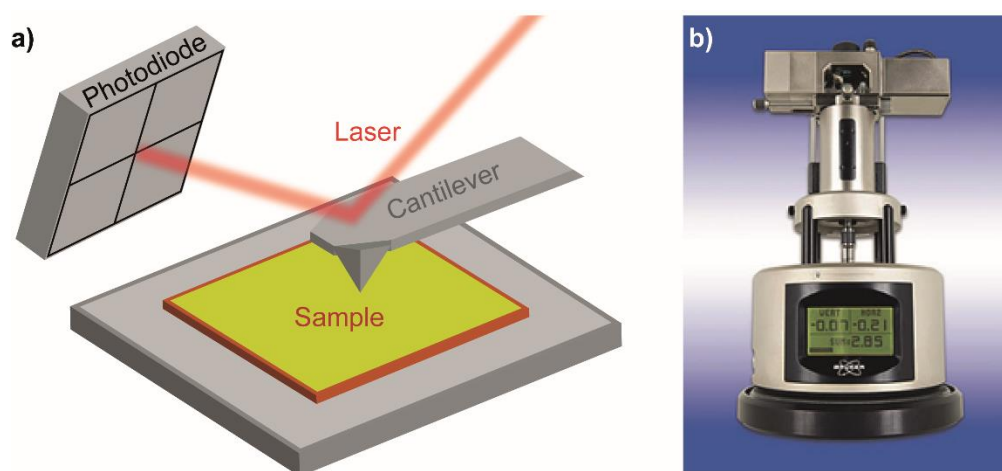
Figure 1.19. (a) Schematic showing the key components of an AFM. (b) Bruker Multimode AFM used for force measurements.[260]

1.5.2.2. Force Spectroscopy

The high sensitivity of the cantilever to probe-sample interaction forces can be exploited to quantitatively measure a wide range of adhesive and repulsive interactions

between different chemical functionalities with an extreme amount of accuracy.[256,261-264] Using this technique, it is possible to detect interaction forces as low as piconewtons.[265] This is achieved by obtaining force curves, as shown in Figure 1.20. Force curves are acquired by changing the probe-sample distance (i.e. moving in the Z direction) at fixed XY positions. Thus, a force curve can be thought of as a single pixel in an AFM 3D image. This produces both 'approach' and 'retract' curves, with the cantilever deflection recorded as a function of the Z direction (see Figure 1.20). During the approach curve, when the probe and sample are far away from each other, they do not interact and the cantilever is undeflected. However, as the probe-sample distance is decreased and one approaches the other, a small attractive force may be felt between the two, due to van der Waals forces. This causes the cantilever to slightly bend, and snap into the surface. The cantilever then deflects as the probe-sample distance is further decreased, due to repulsive interactions. In the retract curve, as the probe and sample are separated (and thus the probe-sample distance is increased), the cantilever deflection and hence the probe-sample force are progressively reduced, until a value of zero force is reached. If attractive forces exist between the probe and sample, as the probe is pulled away, it remains in contact with the surface, despite the cantilever bending inwards. At a certain Z-displacement, the probe suddenly detaches, breaking the adhesion forces between the probe and sample. The adhesion force can therefore be determined from this pull-off force, as shown in Figure 1.20. As the probe is now free from the surface, the cantilever remains once again undeflected.[264-266]
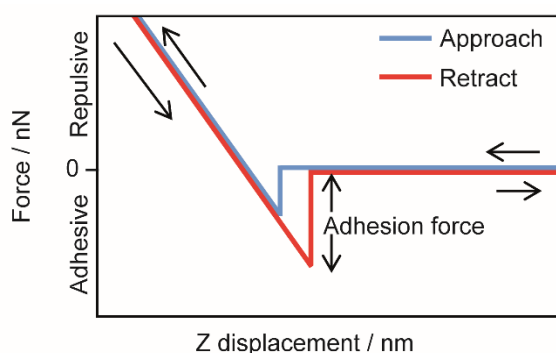
Figure 1.20. A typical force vs. Z displacement curve obtained upon approaching (blue line) and retracting (red line) the AFM probe towards and away from the sample surface.

1.5.2.3. Chemical Force Microscopy

This technique can be adapted to characterise a range of probe-surface interaction forces by chemically modifying the AFM probe and/or sample surface. This is known as chemical force microscopy (CFM).[253,254] CFM has been used in many different fields for determining both long and short range adhesive and repulsive interaction forces between a wide range of different chemical structures.[261,263,265,267] However, as standard AFM tips are extremely sharp, chemically functionalising these will only expose a small number of molecules to the surface. Therefore, Ducker and Butt improved the sensitivity of this technique by adding micron-sized glass spheres to the end of the AFM tip, increasing the surface area and therefore the number of molecules exposed to the sample surface.[261,263] If the size of the ball attached is known, this approach can be used to obtain quantitative force measurements.[264]

These colloidal spheres can then be chemically modified to expose specific chemical functional groups to the surface of interest. This is most commonly achieved through the formation of SAMs, to expose hydrophilic or hydrophobic groups to the probe surface, as previously described by Lieber et al.[253,254] AFM probes are coated with an evaporated thin metal adhesion layer (usually Ti, Cr, Ni: ~1-5 nm) to which a layer of noble metal (usually Au, Ag or Pd: ~10-200 nm) is added. These are then immersed in 1 mM solutions of alkanethiols in ethanol. Due to the strong Au-S bond formed between the gold surface and thiol molecule and the presence of stabilising van der Waals forces (between neighbouring CH_2 groups of the alkanethiol hydrophobic chains), alkanethiols self-assemble on the gold layer into highly organised, closely packed SAMs with a high degree of structural order[267-269] (see Figure 1.21). However, the organisation process of SAM stacking is very slow, so samples usually need to be soaked in thiol solutions for at least 12 hr.[268] By varying the head group of the alkanethiol, different SAMs can be formed, thus exposing different chemistries at the surface of the probe.[268,269]
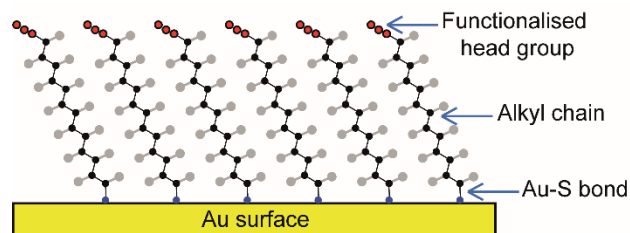
Figure 1.21. Schematic to represent the self-assembly of alkanethiols on a gold surface.

This technique has been used to quantify interaction forces between a range of inorganic mineral surfaces and chemical functionalities of both fundamental and industrial interest.[270-274] CFM measurements may also be carried out in liquids by incorporating an AFM flow cell into the experimental setup.[275]

1.6. Aims of this Thesis

In this thesis, the crystallisation of two fundamentally and industrially important inorganic crystal systems, calcium sulfate and calcium carbonate, are studied at applied interfaces, via a range of microscopic and spectroscopic techniques. Chapters 2-4 are focussed around a specific industrial problem resulting from the crystallisation of dehydrated calcium sulfate polymorphs within internal combustion engines. The study of morphological evolution and polymorphism within this unique oil-based environment is non-trivial, with behaviours deviating significantly from those established for growth in typical aqueous solvents. In Chapter 5, we lift the constraints inherent in studying an industrial system, and investigate the role of charge in determining the resulting morphologies and polymorphs obtained for one of the main deposit-causing components of the previous chapters, calcium carbonate, in considerable detail.

Chapters 2-4 have a strong industry focus, with the key aims being to elucidate the mechanisms through which calcium sulfate deposits crystallise on the surfaces of pistons within diesel internal combustion engines, and to determine ways in which this process can be prevented. An in depth, structural analysis of the inorganic components occurring in real engine deposits obtained from piston surfaces is provided in Chapter 2, to a level of detail not previously studied. The structure and morphology of the calcium sulfate polymorphs present are determined through the use of several structural and analytical techniques, including thermogravimetric analysis (TGA), SEM-EDX,

Raman spectroscopy and XRD. This detailed compositional analysis allows further investigation of the mechanism of deposit formation, as discussed in Chapter 3, and thus the development of methods to prevent this process occurring, as described in Chapter 4.

Further mechanistic details for the formation of calcium sulfate in the internal combustion engine are probed in Chapter 3. To obtain information relevant to the industrial scenario, crystal growth studies are constrained to an environment that mimics that within the engine, resulting in the use of crystal growth interfaces much more challenging and less explored than typical bulk aqueous solvents. Thus, aqueous-organic liquid-liquid interfaces are employed, incorporating aqueous sulfuric acid droplets and real industrial oil-soluble calcium carbonate detergent particles responsible for deposit formation in the engine. These studies demonstrate the effects that oil-based solvents have on polymorph stabilities, and highlight how novel liquid-liquid interfaces can be implemented in crystal growth to achieve crystal morphologies and polymorphs conventionally considered unstable in aqueous environments, as summarised in section 1.2.2 of this introduction.

Chapter 4 aims to investigate a possible strategy for preventing the formation of this calcium sulfate deposit on the piston surface. This is typically achieved by incorporating dispersant chemistries into the lubricating oil circulating around the piston surface, which must be designed with functional head groups that have a high affinity for the inorganic deposit structure. If this is achieved, deposits can be dispersed within the lubricating oil, preventing their formation on engine surfaces, where they have detrimental effects. To study these dispersant-deposit interactions and thus develop effective dispersant engine oil additives, CFM is employed, as explained in section 1.6.1, providing quantitative adhesion force values for the different dispersant-deposit interaction forces in an oil-based environment. Such studies are novel to the dispersant chemistries used in industry, and thus have yet to be investigated, with very few previous studies investigating adhesive and repulsive forces in general within an oil-based environment. As well as providing a wealth of knowledge on the efficiency of the different dispersant chemistries, these studies highlight the important role that solvent plays in determining repulsive and adhesive interactions, whilst providing

insight into the structure of charge in organic environments, an area still under much debate.

Finally, in Chapter 5, nucleation and growth phenomena are studied from a much more fundamental viewpoint for the calcium carbonate system, which forms the core of the detergent molecules responsible for deposit formation at the piston surface. As summarised in section 1.2.1, this mineral system is of extreme importance in biomineralisation, and thus several studies have investigated its growth via biomimetic templating strategies. However, very little is known on the role of surface charge in the oriented nucleation and controlled polymorphism observed in nature, which is also of industrial importance due to the formation of calcium carbonate scale on surfaces which are likely to exhibit a charge. To simplify these studies, we investigate calcium carbonate crystallisation in an aqueous solvent, employing charged Highly Oriented Pyrolytic Graphite (HOPG) surfaces, allowing the effects of charge to be analysed in the absence of surface defects and chemically functionalised head groups, both of which are inherent of the main biomimetic methods discussed in section 1.2.1. This chapter deconvolutes the role of charge in these biomimetic processes, providing further insight into their mechanistic details.

Each chapter is a distinct and self-contained study, and therefore the experimental details of the thesis are embedded within each chapter separately, rather than contained in a separate experimental chapter. All of the above studies demonstrate the vast range of conditions that can be controlled and manipulated to control polymorphism for inorganic crystal systems, and the impacts these effects have on either promoting or preventing crystallisation processes from occurring within a wide range of industrial, geological and biological settings.

1.7. Bibliography

(1)   Mullin, J. W. *Crystallization*; Eds.; Butterworth Heinemann: Oxford, 2001.

(2)   Alavudeen, A.; Venkateshwaran, N.; Winowlin Jappes, J. T. *A Textbook of Engineering Materials and Metallurgy*; Eds.; Firewall Media: New Delhi, 2006.

(3)   Meldrum, F. C.; Cölfen, H. *Chem. Rev.* **2008**, *108*, 4332-4432.

(4)   Sommerdijk, N. A. J. M.; de With, G. *Chem. Rev.* **2008**, *108*, 4499-4550.

(5)   Nudelman, F.; Sommerdijk, N. A. J. M. *Angew. Chem. Int. Ed.* **2012**, *51*, 6582-6596.

(6)   Park, R. J.; Meldrum, F. C. *Adv. Mater.* **2002**, *14*, 1167-1169.

(7)   Blount, C. W.; Dickson, F. W. *Geochim. et Cosmochim. Acta* **1969**, *33*, 227-245.

(8)   Ruiz-Agudo, E.; Putnis, C. V.; Hövelmann, J.; Álvarez-Lloret, P.; Ibáñez-Velasco, A.; Putnis, A. *Geochim. et Cosmochim. Acta.* **2015**, *156*, 75-93.

(9)   Freyer, D.; Voigt, W. *Monatsh. Chem.* **2003**, *134*, 693-719.

(10)   Baláž, P.; Achimovičová, M.; Baláž, M.; Billik, P.; Cherkezova-Zheleva, Z.; Criado, J. M.; Delogu, F.; Dutková, E.; Gaffet, E.; Gotor, F. J.; Kumar, R.; Mitov, I.; Rojac, T.; Senna, M.; Streletskiikl, A.; Wieczorek-Ciurowa, K. *Chem. Soc. Rev.* **2013**, *42,* 7571-7637.

(11)   Teychené, S.; Nicre, N.; Biscans, B. *Chem. Eng. Res. Des.* **2010**, *88*, 1631-1638.

(12)   Adobes-Vidal, M.; Maddar, F. M.; Momotenko, D.; Hughes, L. P; Wren, S. A. C.; Poloni, L. N.; Ward, M. D.; Unwin, P. R. *Cryst. Growth Des.* **2016**, *16*, 4421-4429.

(13)   Lucas, A.; Gaude, J.; Carel, C.; Michel, J. F.; Cathelineau, G. *Int. J. Inorg. Mater.* **2001**, *8*, 87-94.

(14)   Hangx, S. J. T.; Spiers, C. J.; Peach, C. J. *Energy Procedia* **2011**, *4*, 5358-5363.

(15)   Austad, T.; Shariatpanahi, S. F.; Strand, S.; Aksulu, H.; Puntervold, T. *Energy Fuels* **2015**, *29*, 6903-6911.

(16)   Sharma, H.; Dufour, S.; Pinnawala Arachchilage, G. W. P.; Weerasooriya, U.; Pope, G. A.; Mohanty, K. *Fuel* **2015**, *140*, 407-420.

(17)   ShamsiJazeyi, H.; Verduzco, R.; Hirasaki, G. J. *Colloids Surf., A*, **2014** *453*, 168-175.

(18)   Sunagawa, I., *Crystals: Growth, Morphology and Perfection*; Eds.; Cambridge University Press: Cambridge, 2005.

(19)   Schwartz, A. M.; Myerson, A. S., Solutions and Solution Properties. In *Handbook of Industrial Crystallisation*; Myerson, A. S., Eds.; Butterworth-Heinemann: Boston, USA, 2002; pp. 1-131.

(20)   Coto, B.; Martos, C.; Peña, J. L.; Rodríguez, R. Pastor, G. *Fluid Phase Equilib.* **2012**, *324*, 1-7.

(21)   Cubillas, P.; Anderson, M. W., Synthesis Mechanism: Crystal Growth and Nucleation. In *Zeolites and Catalysis, Synthesis, Reactions and Applications*; Čejka, J.; Corma, A.; Zones, S., Eds.; Wiley-VCH Verlag GmbH & Co. KGaA: Weinheim, Germany, 2010; pp. 1-55.

(22)   Plummer, L. N.; Wigley, T. M. L.; Parkhurst, D. L. *Am. J. Sci.* **1978**, *278*, 179-216.

(23)   Spanos, N.; Koutsoukos, P. G. *J. Phys. Chem. B* **1998**, *102*, 6679-6684.

(24)   Dobson, P. S., Bindley, L. A., Macpherson, J. V., Unwin, P. R. *Langmuir* **2005**, *21*, 1255-1260.

(25)   Lasaga, A. C., *Kinetic Theory in the Earth Sciences*; Eds.; Princeton University Press: Princeton, 1998.

(26)   Sangwal, K., *Etching of Crystals: Theory, Experiment and Application*; Eds.; North-Holland Physics Publishing: The Netherlands, 1987.

(27)   Hamilton, B. D.; Ha, J.-M.; Hillmyer, M. A.; Ward, M. D. *Acc. Chem. Res.* **2012**, *45*, 414-423.

(28)   Kashchiev, D., *Nucleation: Basic Theory with Applications*; Eds.; Butterworth-Heinemann: Oxford, 1999.

(29)   Karthika, S.; Radhakrishnan, T. K.; Kalaichelvi, P. *Cryst. Growth Des.* **2016**, *16*, 6663-6681.

(30)   Sangwal, K., *Additives and Crystallization Processes: From Fundamentals to Applications*; Eds.; John Wiley & Sons: Chichester, 2007.

(31)   Gebauer, D.; Völkel, A.; Cölfen, H. *Science* **2008**, *322*, 1819-1822.

(32)   Habraken, W.; Tao, J. H.; Brylka, L. J.; Friedrich, H.; Bertinetti, L.; Schenk, A. S.; Verch, A.; Dmitrovic, V.; Bomans, P. H. H.; Frederik, P. M.; Laven, J.; Van Der Schoot, P.; Aichmayer, B.; De With, G.; De Yoreo, J. J.; Sommerdijk, N. A. J. M. *Nat. Commun.* **2013**, *4*, 1507/1-1507/12.

(33)   Pouget, E. M.; Bomans, P. H. H.; Goos, J.; Frederik, P. M.; De With, G.; Sommerdijk, N. *Science* **2009**, *323*, 1455-1458.

(34)   Nielsen, M. H.; Aloni, S.; De Yoreo, J. J. *Science* **2014**, *345*, 1158-1162.

(35) Nudelman, F.; Pieterse, K.; George, A.; Bomans, P. H. H.; Friedrich, H.; Brylka, L. J.; Hilbers, P. A. J.; De With, G.; Sommerdijk, N. *Nat. Mater.* **2010,** *9*, 1004-1009.

(36) Dey, A.; Bomans, P. H. H.; Muller, F. A.; Will, J.; Frederik, P. M.; De With, G.; Sommerdijk, N. *Nat. Mater.* **2010**, *9*, 1010-1014.

(37) Demichelis, R.; Raiteri, P.; Gale, J. D.; Quigley, D.; Gebauer, D. *Nat. Commun.* **2011**, *2*, 590/1-590/8.

(38) Nassif, N.; Pinna, N.; Gehrke, N.; Antonietti, M.; Jäger, C.; Cölfen, H. *Proc. Natl. Acad. Sci. U.S.A.* **2005**, *102*, 12653.

(39) Beniash, E.; Aizenberg, J.; Addadi, L.; Weiner, S. *Proc. R. Soc. B-Biol. Sci.* **1997**, *264*, 461-465.

(40) Beniash, E.; Metzler, R. A.; Lam, R. S. K.; Gilbert, P. U. P. A. *J. Struct. Biol.* **2009**, *166*, 133-143.

(41) Belenguer, A. M.; Lampronti, G. I.; Cruz-Cabeza, A. J.; Hunter, C. A.; Sanders, J. K. M. *Chem. Sci.* **2016**, *7*, 6617-6627.

(42) Unwin, P. R. *Faraday Discuss.* **2007**, *136*, 409-416.

(43) De Yoreo, J. J.; Gilbert. P. U. P. A.; Sommerdijk, N. A. J. M.; Penn, L.; Whitelam, S.; Joester, D.; Zhang, H.; Rimer, J. D.; Navrotsky, A.; Banfield, J. F.; Wallace, A. F.; Michel, M.; Meldrum, F. C.; Cölfen, H.; Dove, P. M. *Science* **2011**, *349,* aaa6760.

(44) Van Driessche, A. E. S.; Kellermeier, M.; Benning, L. G.; Gebauer, D., *New Perspectives on Mineral Nucleation and Growth: From Solution Precursors to Solid Materials*; Eds.; Springer International Publishing: Switzerland, 2017.

(45) Gal, A.; Weiner, S.; Addadi, L. *CrystEngComm* **2015**, *17*, 2606-2615.

(46) Gebauer, D. *Chem. Soc. Rev*. **2014**, *437*, 2348-2371.

(47) Ihli, J.; Wong, W. C.; Noel, E. H.; Kim, Y.-Y.; Kulak, A. N.; Christenson, H. K.; Duer, M. J.; Meldrum, F. C. *Nat. Commun.* **2014**, *5*, 3189/1-3189/10.

(48) Schmidt, M. P.; Ilott, A. J.; Phillips, B. L.; Reeder, R. J. *Cryst. Growth. Des.* **2014**, *14*, 938-951.

(49) Goodwin, A. L.; Michel, F. M.; Phillips, B. L.; Keen, D. A.; Dove, M. T.; Reeder, R. *Chem. Mater.* **2010**, *22*, 3197-3205.

(50) Wallace, A. F.; Hedges, L. O.; Fernandez-Martinez, A.; Raiteri, P.; Gale, J. D.; Waychunas, G. A.; Whitelam, S.; Banfield, J. F.; De Yoreo, J. J. *Science* **2013**, *341*, 885-889.

(51) Neumann, M.; Epple, M. *Eur. J. Inorg. Chem.* **2007**, 1953-1957.

(52) Zou, Z.; Bertinetti, L.; Politi, Y.; Jensen, A. C. S.; Weiner, W.; Addadi, L.; Fratzl, P.; Habraken, W. J. E. M. *Chem. Mater.* **2015**, *27*, 4237-4246.

(53) Farhadi-Khouzani, M.; Chevrier, D. M.; Zhang, P.; Hedin, N.; Gebauer, D. *Angew. Chem. Int. Ed.* **2016**, *55*, 8117-8120.

(54) Lam, R. S. K.; Charnock, J. M.; Lennie, A.; Meldrum, F. C. *CrystEngComm* **2007**, *9*, 1226-1236.

(55) Addadi, L.; Raz, R.; Weiner, S. *Adv. Mater.* **2003**, *15*, 959-970.

(56) Jiang, Q.; Ward, M. D. *Chem. Soc. Rev.* **2014**, *43*, 2066-2079.

(57) Navrotsky, A *Proc Natl Acad Sci USA* **2004**, *101*, 12096-12101.

(58) Navrotsky, A.; Mazeina, L.; Majzlan, J. *Science* **2008**, *319*, 1635-1638.

(59) Navrotsky, A. *ChemPhysChem* **2011**, *12,* 2207-2215.

(60) Davey, R. J. *Faraday Discuss.* **1993**, *95*, 160-162.

(61) Gribb, A. A.; Banfield, J. F. *Am. Mineral* **1997**, *82*, 717-728.

(62) Aizenberg, J.; Black, A. J.; Whitesides, G. M. *J. Am. Chem. Soc.* **1999,** *121*, 4500-4509.

(63) Aizenberg, J.; Black, A. J.; Whitesides, G. M. *Nature* **1999**, *398,* 495-498.

(64) Adams, D. M.; Brus, L.; Chidsey, C. E. D.; Creager, S.; Creutz, C.; Kagan, C. R.; Kamat, P. V.; Lieberman, M.; Lindsay, S.; Marcus, R. A.; Metzger, R. M.; Michel-Beyerle, M. E.; Miller, J. R.; Newton, M. D.; Rolison, D. R.; Sankey, O.; Schanze, K. S.; Yardley, J.; Zhu X. *J. Phys. Chem. B* **2003,** *107*, 6668-6697.

(65) Travaille, A. M.; Donners, J. J. J. M.; Geritsen, J. W.; Sommerdijk, N. A. J. M.; Nolte, R. J. M.; van Kempen, H. *Adv. Mater.* **2002,** *14*, 492-495.

(66) Han, Y.-J.; Aizenberg, J. *J. Am. Chem. Soc.* **2003**, *125*, 4032-4033.

(67) Duffy, D. M.; Markus Travaille, A.; van Kempen, H.; Harding, J. H. *J. Phys. Chem. B* **2005**, *109*, 5713-5718.

(68) Duffy, D. M.; Markus Travaille, A.; van Kempen, H.; Harding, J. H. *Science* **2012**, *336*, 1014-1018.

(69) Nielsen, A. E. *J. Cryst. Growth* **1984**, *67*, 289-310.

(70) Nielsen, A. E.; Toft. J. M. *J. Cryst. Growth* **1984**, *67*, 278-288.

(71) Unwin, P. R.; Macpherson, J. V. *Chem. Soc. Rev.* **1995**, *24*, 109-119.

(72) Peruffo, M.; Mbogoro, M. M.; Adobes-Vidal, M.; Unwin, P. R. *J. Phys. Chem. C* **2016**, *120*, 12100-12112.

(73) Adobes-Vidal, M.; Shtukenberg. A. G.; Ward, M. D.; Unwin, P. R. *Cryst. Growth Des.* **2017**, *17*, 1766-1774.

(74) Volmer, M. *Z. Phys. Chem.* **1922**, *102*, 267-275.

(75) Kossel, W. *Nachtur. Ges. Gottingen*, **1927**, *2,* 135-145.

(76) Stranski, I. N. *Z. Phys. Chem.* **1928**, *136*, 259-278.

(77) Frank, F. C. *Discuss. Faraday Soc.* **1949**, *5*, 48-54.

(78) Burton, W. K.; Cabrera, N.; Frank, F. C. *Proc. R. Soc. London A* **1951**, *243*, 299-358.

(79) Woodruff, D. P. *Phil. Trans. R. Soc. A* **2015**, *373*, 20140230/1- 20140230/11.

(80) Shtukenberg, A. G.; Zhu, Z.; An, Z.; Bhandari, M.; Song, P.; Kahr, B.; Ward, M. D. *Proc. Natl. Acad. Sci. U.S.A.* **2013**, *110*, 17195-17198.

(81) Chernov, A. A. *J. Cryst. Growth* **2004**, *264*, 499-518.

(82) Hillner, P. E.; Manne, S.; Hansma, P. K.; Gratz, A. J. *Faraday Discuss.* **1993**, *95*, 191.

(83) Anderson, M. W.; Agger, J. R.; Meza, L. I.; Chong, C.B.; Cundy, C. S. *Faraday Discuss.* **2007**, *136*, 143-156.

(84) Hobbs, J. K.; Vasilev, C.; Humphris, A. D. *Polymer* **2005**, *46*, 10226-10236.

(85) Teng, H. H.; Dove, P. M.; Orme, C. A.; De Yoreo, J. J. *Science* **1998**, *282*, 724-727.

(86) Macpherson, J. V.; Unwin, P .R.; Hillier, A. C.; Bard, A. J. *J. Am. Chem. Soc.* **1996**, *118*, 6445-6452.

(87) Rieger, J.; Frechen, T.; Cox, G.; Heckmann, W.; Schmidt, C.; Thieme, J. *Faraday Discuss.* **2007**, *136*, 265-277.

(88) Moon, C.; Hawtin, R. W.; Rodger, P. M. *Faraday Discuss.* **2007**, 136, 367-382.

(89) Parker, S. C.; Kelsey, E. T.; Uliver, P. M.; Titiloye, J. O. *Faraday Discuss.* **1993**, *95*, 75-84.

(90) Xiao, R.-F.; Alexander, J. I. D.; Rosenberger, F. *Faraday Discuss.* **1993**, *95*, 85-95.

(91) Harano, K.; Homma, T.; Niimi, Y.; Koshino, M.; Suenaga, K.; Leibler, L.; Nakamura, E. *Nat. Mater.* **2012**, *11*, 877-881.

(92) Kulkarni, S. A.; Weber, C. C.; Myerson, A. S.; ter Horst, J. H. *Langmuir* **2014**, *30,* 12368−12375.

(93) Diao, Y.; Harada, T.; Myerson, A. S.; Hatton, T. A.; Trout, B. L. *Nat. Mater.* **2011**, *10*, 867-871.

(94)   Cui, Y.; Stojakovic, J.; Kijima, H.; Myerson, A. S. *Cryst. Growth Des.* **2016**, *16,* 6131-6138.

(95)   Robinson, K. M.; O'Grady, W. E. *Faraday Discuss.* **1993**, *95,* 55-64.

(96)   Hughes, C. E.; Harris, K. D. M.; Griffiths, P. C.; Hamad, S.; Catlow, C. R. A. *Faraday Discuss.* **2007**, *136*, 71-89.

(97)   Ostwald, W. *Z. Phys. Chem.* **1897**, *22*, 289-330.

(98)   Gebauer, D.; Gunawidjaja, P. N.; Ko, J. Y. P.; Bacsik, Z.; Aziz, B.; Liu, L.; Hu, Y.; Bergström, L.; Tai, C.-W.; Sham, T.-K.; Edén, M.; Hedin, N. *Angew. Chem. Int. Ed.* **2010**, *49*, 8889-8891.

(99)   Lee, S.; Wi, H. S.; Jo, W.; Cho, Y. C.; Lee, H. H.; Jeong, S.-Y.; Kim, Y.-K.; Lee, G. W. *Proc. Natl. Acad. Sci. U.S.A.* **2016**, *113*, 13618-13623.

(100)   Shahidzadeh, N.; Schut, M. F. L.; Desarnaud, J.; Prat, M.; Bonn, D. *Sci. Rep.* **2015** *5*, 10335/1-10335/9.

(101)   Storey, R. A.; Ymén, I., *Solid State Characterization of Pharmaceuticals*; Eds.; John Wiley & Sons: Chichester, 2011.

(102)   Ostwald, W. *Lehrbuch der Allegmeinen Chemie*; Band Bd. 1; Leipzig, 1896.

(103)   Mann, S. *Angew. Chem. Int. Ed.* **2000**, *39*, 3392-3406.

(104)   Whitesides, G. M. *Interface Focus* **2015**, *5*, 1-9.

(105)   Heywood, B. R.; Mann, S. *Adv. Mater.* **1994**, *6*, 9-20.

(106)   Litvin, A. L.; Valiyaveettil, S.; Kaplan, D. L.; Mann, S. *Adv. Mater.* **1997**, *9*, 124-127.

(107)   Heywood, B. R.; Mann, S. *Chem. Mater.* **1994**, *6*, 311-318.

(108)   Heywood, B. R.; Mann, S. *J. Am. Chem. Soc.* **1992**, *114*, 4681-4686.

(109)   Heywood, B. R.; Mann, S. *Langmuir* **1992**, *8*, 1492-1498.

(110)   Champ, S.; Dickinson, J. A.; Fallon, P. S.; Heywood, B. R.; Mascal, M. *Angew. Chem. Int. Ed.* **2000**, *39*, 2716-2719.

(111)   Mann, S.; Didymus, J. M.; Sanderson, N. P.; Heywood, B. R.; Samper, E. J. A. *J. Chem. Soc., Faraday Trans.* **1990**, *86*, 1873-1880.

(112)   Orme, C. A.; Noy, A.; Wierzbicki, A.; McBride, M. T.; Grantham, M.; Teng, H. H.; Dove, P. M.; DeYoreo, J. J. *Nature* **2001**, *411*, 775-779.

(113)   Xu, A.-W.; Dong, W.-F.; Antonietti, M.; Cölfen, H. *Adv. Funct. Mater.* **2008**, *18*, 1307-1313.

(114)   Zhang, S.; Gonsalves, K. E.. *Langmuir* **1998**, *14*, 6761-6766.

(115)   Falini, G.; Fermani, S.; Gazzano, M.; Ripamonti, A. *Chem. Eur. J.* **1998**, *4*, 1048-1052.

(116)   Pileni, M.-P. *Nat. Mater.* **2003**, *2*, 145-150.

(117)   J. Am. Chem. Soc. 2007, 129, 10370-10381

(118)   Belcher, A. M.; Wu, X. H.; Christensen, R. J.; Hansma, P. K.; Stucky, G. D.; Morse, D. E.. *Nature* **1996**, *381*, 56-58.

(119)   Laibinis, P. E.; Whitesides, G. M.; Allara, D. L.; Tao, Y. T.; Parikh, A. N.; Nuzzo, R. G. *J. Am. Chem. Soc.* **1991**, *113*, 7152-7167.

(120)   J. Am. Chem. Soc. 2003, 125, 11571-11577

(121)   Heywood, B. R.; Rajam, S.; Mann, S. *J. Chem. Soc. Faraday Trans.* **1991**, *87*, 735-743.

(122)   Rajam, S.; Heywood, B. R.; Walker, J. B. A.; Mann, S.; Davey, R. J.; Birchall, J. D. *J. Chem. Soc. Faraday Trans.* **1991**, *87*, 727-734.

(123)   Mann, S., *Biomineralization: Principles and Concepts in Bioinorganic Materials Chemistry*; Eds.; Oxford University Press: New York, 2001.

(124)   Weiner, S.; Traub, W. *FEBS Lett.* **1980**, *111*, 311-316.

(125)   Volkmer, D.; Fricke, M.; Vollhardt, D.; Siegel, S. *J. Chem. Soc. Dalton. Trans.* **2002**, *0*, 4547-4554.

(126)   Volkmer, D.; Fricke, M. *Z. Anorg. Allg. Chem.* **2003**, *629*, 2381-2390.

(127)   Volkmer, D.; Fricke, M.; Agenab, C.; Mattay, J. *J. Mater. Chem.* **2004**, *14*, 2249-2259.

(128)   Volkmer, D.; Fricke, M.; Agena, C.; Mattay, J. *CrystEngComm* **2002**, *4*, 288-295.

(129)   Ihli, J.; Kim, Y.-Y.; Noel, E. H.; Meldrum, F. C. *Adv. Funct. Mater.* **2013**, *23*, 1575-1585.

(130)   Kababya, S.; Gal, A.; Kahil, K.; Weiner, S.; Addadi, L.; Schmidt, A. *J. Am. Chem. Soc.* **2015**, *137*, 990-998.

(131)   Schenk, A. S.; Cantaert, B.; Kim, Y.-Y.; Li, Y.; Read, E. S.; Semsarilar, M.; Armes, S. P.; Meldrum, F. C. *Chem. Mater*, **2014**, *26*, 2703-2711.

(132)   Wang, Y. W.; Kim, Y. Y.; Stephens, C. J.; Meldrum, F. C.; Christenson, H. K. *Cryst. Growth Des.* **2012**, *12*, 1212-1217.

(133)   Addadi, L.; Weiner, S. *Proc. Natl. Acad. Sci. U.S.A.* **1985**, *82*, 4110-4114.

(134)   Weiner, S.; Addadi, L. *J. Mater. Chem.* **1997**, *7*, 689-702.

(135)   Gotliv, B.-A.; Addadi, L.; Weiner, S. *ChemBioChem* **2003**, *4*, 522-529.

(136) Cantaert, B.; Verch, A.; Kim, Y.-Y.; Ludwig, H.; Paunov, V. N.; Kröger, R.; Meldrum, F. C. *Chem. Mater.* **2013**, *25*, 4994-5003.

(137) Weiner, S.; Hood, L. *Science* **1975**, *190*, 987-989.

(138) Addadi, L.; Moradian, J.; Shay, E.; Maroudas, N. G.; Weiner, S. *Proc. Natl. Acad. Sci. U.S.A.* **1987**, *84*, 2732-2736.

(139) Didymus, J. M.; Oliver, P.; Mann, S. *J. Chem. Soc., Faraday Trans.* **1993**, *89*, 2891-2900.

(140) Naka, K.; Chujo, Y. *Chem. Mater.* **2001**, *13*, 3245-3259.

(141) Mukkamala, S. B.; Powell, A. K. *Chem. Commun.* **2004**, 918-919.

(142) Volkmer, D.; Fricke, M.; Huber, T.; Sewald, N. *Chem. Commun.* **2004**, *0*, 1872-1873.

(143) Wang, T. X.; Colfen, H.; Antonietti, M. *J. Am. Chem. Soc.* **2005**, *127*, 3246-3247.

(144) Elhadj, S.; Salter, E. A.; Wierzbicki, A.; De Yoreo, J. J.; Han, N.; Dove, P. M. *Cryst. Growth. Des* **2006**, *6*, 197-201.

(145) Sugawara, A.; Ishii, T.; Kato, T. *Angew. Chem. Int. Ed.* **2003**, *42*, 5299-5303.

(146) Dmitrovic, V.; Habraken, G. J. M.; Hendrix, M.; Habraken, W.; Heise, A.; de With, G.; Sommerdijk, N. *Polymers* **2012**, *4*, 1195-1210.

(147) Kim, Y. Y.; Kulak, A. N.; Li, Y. T.; Batten, T.; Kuball, M.; Armes, S. P.; Meldrum, F. C. *J. Mater. Chem.* **2009**, *19*, 387-298.

(148) Schenk, A. S.; Zope, H.; Kim, Y. Y.; Kros, A.; Sommerdijk, N.; Meldrum, F. C. *Faraday Discuss.* **2012**, *159*, 327-244.

(149) Moore, L.; Hopwood, J. D.; Davey, R. J. *J. Cryst. Growth* **2004**, *261*, 93-98.

(150) Gower, L. B. *Chem. Rev.* **2008**, *108*, 4551-4627.

(151) Falini, G.; Albeck, S.; Weiner, S.; Addadi, L. *Science* **1996**, *271*, 67-69.

(152) Levi, Y.; Albeck, S.; Brack, A.; Weiner, S.; Addadi, L. *Chem. Eur. J.* **1998**, *4*, 389-396.

(153) Gower, L. A.; Tirrell, D. A, *J. Cryst. Growth* **1998**, *191*, 153-160.

(154) Kato, T.; Amamiya, T. *Chem. Lett.* **1999**, 199.

(155) Kato, T.; Suzuki, T.; Irie, T. *Chem. Lett.* **2000**, 186.

(156) D'Souza, S. M.; Alexander, C.; Carr, S. W.; Waller, A. M.; Whitcombe, M. J.; Vulfson, E. N. *Nature* **1999**, *398*, 312-316.

(157) Yue, W. B.; Kulak, A. N.; Meldrum, F. C. *J. Mater. Chem.* **2006**, *16*, 408-416.

(158) Loste, E.; Park, R. J.; Warren, J.; Meldrum, F. C. *Adv. Funct. Mater.* **2004**, *14*, 1211-1220.

(159) Kim, Y.-Y.; Hetherington, N. B. J.; Noel, E. H.; Kroeger, R.; Charnock, J. M.; Christenson, H. K.; Meldrum, F. C. *Angew. Chem. Int. Ed.* **2011**, *50*, 12572-12577.

(160) Stephens, C. J.; Ladden, S. F.; Meldrum, F. C.; Christenson, H. K. *Adv. Funct. Mater.* **2010**, *20*, 2108-2115.

(161) Stephens, C. J.; Kim, Y.-Y.; Evans, S. D.; Meldrum, F. C.; Christenson, H. K. *J. Am. Chem. Soc.* **2011**, *133*, 5210-5213.

(162) Tester, C. C.; Whittaker, M. L.; Joester, D. *Chem. Commun.* **2014**, *50*, 5619-5622.

(163) Tester, C. C.; Brock, R. E.; Wu, C.-H.; Krejci, M. R.; Weigand, S.; Joester, D. *CrystEngComm* **2011**, *13*, 3975-3978.

(164) Dryfe, R. A. W. *Phys. Chem. Chem. Phys.* **2006**, *8*, 1869-1883.

(165) Lee, S.; Sanstead, P. J.; Wiener, J. M.; Bebawee, R.; Hilario, A. G. *Langmuir* **2010**, *26*, 9556-9564.

(166) Sanstead, P. J.; Florio, N.; Giusto, K.; Morris, C.; Lee, S. *J. Colloid Interface Sci.* **2012** *376*, 152-159.

(167) Allain, K.; Bebawee, R.; Lee, S. *Cryst. Growth Des.* **2009**, *9*, 3183-3190.

(168) Perry, D.; Parker, A. S.; Page, S.; Unwin, P. R. *ChemElectroChem* **2016**, *3*, 2212-2220.

(169) Mitrinovic, D. M.; Tikhonov, A. M.; Li, M.; Huang, Z. Q.; Schlossman, M. L. *Phys. Rev. Lett.* **2000**, *85*, 582-585.

(170) Mitrinovic, D. M.; Zhang, Z. J.; Williams, S. M.; Huang, Z. Q.; Schlossman, M. L. *J. Phys. Chem. B* **1999**, *103*, 1779-1782.

(171) Strutwolf, J.; Barker, A. L.; Gonsalves, M.; Caruana, D. J.; Unwin, P. R.; Williams, D. E.; Webster, J. R. P. *J. Electroanal. Chem.* **2000**, *483*, 163-173.

(172) Benjamin, I. *J. Chem. Phys.* **1992**, *97*, 1432-1445.

(173) Schlossman, M. L. *Curr. Opin. Coll. Int. Sci.* **2002**, *7*, 235-243.

(174) Vincze, A.; Horvai, G.; Leermakers, F. A. M. *Anal. Sci.* **1998**, *14*, 137-140.

(175) Scatena, L. F.; Richmond, G. L. *J. Phys. Chem. B* **2001**, *105*, 11240-11250.

(176) Richmond, G. L. *Annu. Rev. Phys. Chem.* **2001**, *52*, 357-389.

(177) Gragson, D. E.; Richmond, G. L. *J. Phys. Chem. B* **1998**, *102*, 3847-3861.

(178) McFearin, C. L.; Richmond, G. L. *J. Mol. Liq.* **2007**, *136*, 221-226.

(179) Walker, D. S.; Brown, M. G.; McFearin, C. L.; Richmond, G. L. *J. Phys. Chem. B* **2004**, *108*, 2111-2114.

(180) Brown, M. G.; Walker, D. S.; Raymond, E. A.; Richmond, G. L. *J. Phys. Chem. B* **2003**, *107*, 237-244.

(181) Walker, D. S.; Richmond, G. L. *J. Am. Chem. Soc.* **2007**, *129*, 9446-9451.

(182) Walker, D. S.; Moore, F. G.; Richmond, G. L. *J. Phys. Chem. C* **2007**, *111*, 6103-6112.

(183) McFearin, C. L.; Beaman, D. K.; Moore, F. G.; Richmond, G. L. *J. Phys. Chem. C* **2009**, *113*, 1171-1188.

(184) Ravenhill, E. R.; Unwin, P. R., s*ubmitted*.

(185) Rautaray, D.; Kumar, A.; Reddy, S.; Sainkar, S. R.; Pawaskar, N. R.; Sastry, M. *CrystEngComm* **2001**, *45*, 1-4.

(186) Reddy, S.; Rautaray, D.; Sainkar, S. R.; Sastry, M. *Bull. Mater. Sci.* **2003**, *26*, 283-288.

(187) Luo, G. M.; Malkova, S.; Yoon, J.; Schultz, D. G.; Lin, B. H.; Meron, M.; Benjamin, I.; Vanysek, P.; Schlossman, M. L. *Science* **2006**, *311*, 216-218.

(188) Luo, G. M.; Malkova, S.; Yoon, J.; Schultz, D. G.; Lin, B. H.; Meron, M.; Benjamin, I.; Vanysek, P.; Schlossman, M. L. *J. Electroanal. Chem.* **2006**, *593*, 142-158.

(189) Samec, Z.; Mareček, V.; Homolka, D. *Faraday Disc. Chem. Soc.* **1984**, *77*, 197-208.

(190) Peljo, P.; Smirnov, E.; Girault, H. H. *J. Electroanal. Chem.* **2016**, *779*, 187-198.

(191) Girault, H. H., Charge Transfer across Liquid-Liquid Interfaces. In *Modern Aspects of Electrochemistry*; Bockris, J. O. M.; Conway, B. E.; White, R. E., Eds.; Springer: Boston, US, 1993, pp. 1-62.

(192) Li, F.; Unwin, P. R. *J. Phys. Chem. C* **2015**, *119*, 4031-4043.

(193) Zhang, Z.; Mitrinovic, D. M.; Williams, S, M.; Huang, Z.; Schlossman, M. L. *J. Chem. Phys.* **1999**, *110*, 7421.

(194) Tikhonov, A. M.; Li, M.; Schlossman, M. L. *J Phys Chem.* **2001**, *105*, 8065-8068.

(195) Tikhonov, A. M.; Li, M.; Schlossman, M. L. X-Ray Scattering from *n*-alcohol Monolayers at the Water-Hexane Interface; BNL National Synchrotron Light Source Activity Report, 2001, pp. 2/143-1/146.

(196) Pingali, S. V.; Takiue, T.; Luo, G.; Tikhonov, A. M.; Ikeda, N.; Aratono, M.; Schlossman, M. L. *J. Phys. Chem. B* **2005**, *109*, 1210-1225.

(197) Conboy, J. C.; Messmer, M. C.; Richmond, G. L. *Langmuir* **1998**, *14*, 6722-6727.

(198) Walker, R. A.; Gruetzmacher, J. A.; Richmond, G. L. *J. Am. Chem. Soc.* **1998**, *120*, 6991-7003.

(199) Walker, R. A.; Conboy, J. C.; Richmond, G. L. *Langmuir* **1997**, *13*, 3070-3073.

(200) Watry, M. R.; Richmond, G. L. *J. Am. Chem. Soc.* **2000**, *122*, 875-883.

(201) Conboy, J. C.; Messmer, M. C.; Richmond, G. L. *J. Phys. Chem. B* **1997**, *101*, 6724-6733.

(202) Tikhonov, A. M.; Schlossman, M. L. *J. Phys. Chem. B* **2003**, *107*, 3344-3347.

(203) Tikhonov, A. M.; Pingali, S. V.; Schlossman, M. L. *J. Chem. Phys.* **2004**, *120*, 11822-11838.

(204) Davey, R. J.; Hilton, A. M.; Garside, J. *Chem. Eng. Res. Des.* **1997**, *75*, 245-251.

(205) Davey, R. J.; Hilton, A. M.; Garside, J.; de la Fuente, M.; Edmonson, M.; Rainsford, P. *J. Chem. Soc. Faraday Trans.* **1996**, *92*, 1927-1933.

(206) Rautaray, D.; Kavathekar, R.; Sastry, M. *Faraday Discuss.* **2005**, *129*, 205-217.

(207) Rautaray, D.; Banpurkar, A.; Sainkar, R.; Limaye, A. V.; Pavaskar, N. R.; Ogale, S. B.; Sastry, M. *Adv. Mater.* **2003**, *15*, 1273-1278.

(208) Rautaray, D.; Banpurkar, A.; Sainkar, R.; Limaye, A. V.; Ogale, S. B.; Sastry, M. *Cryst. Growth Des.* **2003**, *3*, 449-452.

(209) Teychené, S.; Biscans, B. *Cryst. Growth Des.* **2011**, *11*, 4810-4818.

(210) Ueno, S.; Hamada, Y.; Sato, K. *Cryst. Growth Des.* **2003**, *3*, 935-939.

(211) Yano, J.; Füredi-Milhofer, H.; Wachtel, E.; Garti, N. *Langmuir* **2000**, *16*, 9996-10004.

(212) Allen, K.; Davey, R. J.; Ferrari, E.; Towler, C.; Tiddy, G. J. *Cryst. Growth Des.* **2002**, *2*, 523-527.

(213) Ruiz-Agudo, E.; Putnis, C. V.; Putnis, A. *Chem. Geol.* **2014**, *383*, 132-146.

(214) Azimi, G; Papangelakis, V. G. *Hydrometallurgy* **2011**, *108*, 122-129.

(215) Carbone, M.; Ballirano, P.; Caminiti, R. *Eur. J. Mineral.* **2008**, *20*, 621-627.

(216) Dutrizac, J. E.; Kuiper, A. *Hydrometallurgy* **2006**, *82*, 13-31.

(217) Smith, G. C.; Hopwood, A. B.; Titchener, K. J. *Surf. Interface Anal.* **2002**, *33*, 259-268.

(218) Diaby, M.; Kinani S.; Genty, C.; Bouchonnet, S.; Sablier, M.; Le Négrate, A.; El Fassi, M. *Anal. Chem.* **2009**, *81*, 9764-9770.

(219) Diaby, M.; Singhal, P.; Ousmane, M.; Sablier, M.; Le Négrate, A.; El Fassi, M.; Zymla, V. *Fuel* **2013**, *107*, 90-101.

(220) Papke, B. L. *Lub. Eng.* **1991**, *48*, 209-218.

(221) Herbstein, F. H. *Cryst. Growth. Des.* **2004**, *4*, 1419-1429.

(222) Bernstein, J. *Cryst. Growth. Des.* **2011**, *11*, 632-650.

(223) Seddon, K. R. *Cryst. Growth Des.* **2004**, *4*, 1087.

(224) Tritschler, U.; Kellermeier, M.; Debus, C.; Kempter, A.; Cölfen, H. *CrystEngComm* **2015**, *17*, 3772-3776.

(225) Cody, R. D. F.; Hull, A. B., *Method of growth of primary anhydrite crystals under moderate conditions*. U.S. Patent 4,337,238, June 29, 1982.

(226) Wang, Y.-W.; Kim, Y.-Y.; Christenson, H. K.; Meldrum, F. C. *Chem. Commun.* **2012**, *48*, 504-506.

(227) Furby, E.; Glueckauf, E.; McDonald, L. A. *Desalination* **1968**, *4*, 264-276.

(228) Otálora, F.; García-Ruiz, J. *Chem. Soc. Rev.* **2014**, *43*, 2013-2026.

(229) Serafeimidis, K.; Anagnostou, G. *Rock. Mech. Rock. Eng.* **2015**, *48*, 15-31.

(230) Fu, H.; Guan, B.; Jiang, G.; Yates, M. Z.; Wu, Z. *Cryst. Growth Des.* **2012**, *12*, 1388-1394.

(231) Ossorio, M.; Van Driessche, A. E. S.; Pérez, P.; García-Ruiz, J. M. *Chem. Geol.* **2014**, *386*, 16-21.

(232) Hardie, L. A. *Am. Mineral.* **1967**, *52*, 171-200.

(233) Ostroff, A. G. *Geochim. Cosmochim. Acta* **1964**, *28*, 1363-1372.

(234) De Yoreo, J. J.; Velikov, P. G., *Principles of crystal nucleation and growth*. In *Reviews in Minerology and Geochemistry* in *Biomineralisation*; Dove, P. M., De Yoreo, J. J., Weiner, S., Eds.; Mineralogical Society of America: Virginia, 2003; Vol. 54, pp 57-93.

(235) Abriel, W.; Reisdorf, K. *J. Solid State Chem.* **1990**, *85*, 23-30.

(236) Hudson-Lamb, D. L.; Strydom, C. A.; Potgieter, J. H. *Thermochim. Acta* **1996**, *282/283*, 483-492.

(237) Prassad, P. S. R.; Pradhan, A.; Gowd, T. N. *Curr. Sci.* **2001**, *80*, 1203-1207.

(238) Bezou, C.; Nonat, A.; Mutin, J.-C. *J. Solid State Chem.* **1995**, *117*, 165-176.

(239) Abriel, W. W. *Acta Crystallogr.* **1983**, *39*, 956-958.

(240) Christensen, A. N.; Olesen, M.; Cerenius, Y.; Jensen, T. R. *Chem. Mater.* **2008**, *20*, 2124-2132.

(241) Ballirano, P. *Phys. Chem. Miner.* **2009**, *36*, 319-327.

(242) Ni, M.; Ratner, B. D. *Surf. Interface Anal.* **2008**, *40*, 1356-1361.

(243) MacAdam, J.; Parsons, S. A. *Rev. Environ. Sci. Bio.*, 2004, **3**, 159-169.

(244) Karabelas, A. J. *Int. J. Therm. Sci.* **2002**, *41*, 682-692.

(245) Olajire, A. A. *J. Pet. Sci. Eng.* **2015**, *135*, 723-737.

(246) Sekkal, W.; Zaoui, A. *Sci. Rep.* **2013**, *3*, 1587/1-1587/10.

(247) Wolf, G.; Königsberger, E.; Schmidt, H. G.; Königsberger, L.-C.; Gamsjäger, H. *J. Therm. Anal. Calorim.* 2000, *60*, 463-472.

(248) Andreassen, J. P. *J. Cryst. Growth* **2005**, *274*, 256-264.

(249) Flaten, E. M.; Seiersten, M.; Andreassen, J.-P. *J. Cryst. Growth* **2009**, *311*, 3533-3538.

(250) Chakrabarty, D.; Mahapatra, S. *J. Mater. Chem.* **1999**, *9*, 2953-2957.

(251) Andreassen, J. P.; Hounslow, M. J. *AIChE J.* **2004**, *50*, 2772-2782.

(252) Vandenabeele, P., *Practical Raman Spectroscopy- An Introduction*; Eds.; John Wiley and Sons Ltd.: Chichester, 2013.

(253) Frisbie, D.; Rozsnyai, L. F.; Noy, A.; Wrighton, M. S.; Lieber, C. M.. *Science* **1994**, *265*, 2071-2074.

(254) Noy, A.; Frisbie, C. D.; Rozsnyai, L. F.; Wrighton, M. S.; Lieber, C. M. *J. Am. Chem. Soc.* **1995**, *117*, 7943-7951.

(255) Martin, Y.; Williams, C. C.; Wickramasinghe, H. K. *J. Appl. Phys.* **1987**, *61*, 4723-4729.

(256) Binnig, G.; Quate, C. F. *Phys. Rev. Lett.* **1986**, *56*, 930-934.

(257) Binnig, G.; Rohrer, H.; Gerber, C.; Weibel, E. *Phys. Rev. Lett.* **1982**, *49*, 57-60.

(258) Binnig, G.; Rohrer, H.; Gerber, C.; Weibel, E. *Appl. Phys. Lett.* **1982**, *40*, 178-180.

(259) Ward, M. D. *Chem. Rev.* **2001**, *101*, 1697-1726.

(260) A. Alavudeen, N. Venkateshwaran and J.T.W. Jappes, *A Textbook of Engineering Materials and Metallurgy*, Laxmi Publications Pvt Limited, 2006.

(261) Ducker, W.A.; Senden, T. J.; Pashley, R. M. *Nature* **1991**, *353*, 239-241.

(262) Hoh, J. H.; Revelt J.-P.; Hansma P. K. *Nanotechnology* **1991**, *2*, 119-122.

(263) Butt, H.-J. *Biophys. J.* **1991**, *60*, 1438-1444.

(264) Butt, H.-J.; Cappella, B.; Kappl, M. *Surf. Sci. Rep.* **2005**, *59*, 1-152.

(265) Prater, C. B.; Maivald, P. G.; Kjoller, K. J.; Heaton, M. G., Probing Nano-Scale Forces with the Atomic Force Microscope; Digital Instruments, 1995.

(266) Veeco Instruments Inc., A Practical Guide to SPM: 2005, pp. 1-29.

(267) Bain, C. D.; Whitesides, G. M. *Science* **1988**, *240*, 62-63.

(268) Love, J. C.; Estroff, L. A.; Kriebel, J. K.; Nuzzo, R. G.; Whitesides, G. M. *Chem. Rev.* **2005**, *105*, 1103-1170.

(269) Vericat, C.; Vela, M. E.; Benitez, G.; Carro, P.; Salvarezza, R. C. *Chem. Soc. Rev.* **2010**, *39*, 1805-1834.

(270) Finot, E.; Lesniewska, E.; Mutin, J.-C.; Goudonnet, J.-P. *J. Chem. Phys.* **1999**, *111*, 6590-6598.

(271) Finot, E.; Lesniewska, E.; Mutin, J.-C.; Goudonnet, J.-P. *Langmuir* **2000**, *16*, 4237-4244.

(272) Fa, K.; Jiang, T.; Nalaskowski, J.; Miller, J. D. *Langmuir* **2003**, *19*, 10523-10530.

(273) Fa, K.; Nguyen, A. V.; Miller, J. D. *Int. J. Miner. Process.* **2006**, *81*, 166-177.

(274) Ferrari, L.; Kaufmann, J.; Winnefeld, F.; Plank, J. *J. Colloid Interface Sci.* **2010**, *347*, 15-24.

(275) Butt, H.-J.; Jaschke, M.; Ducker, W. *Bioelectrochem. Bioenerg.* **1995**, *38*, 191-201.

Chapter 2: Microscopic and Spectroscopic Characterisation of Inorganic Piston Deposit Composition

Abstract

Very little is currently known about the structure and morphology of the inorganic components of piston deposits. This is partially because their formation is often overlooked by simple laboratory bench tests, which are used to screen lubricating oils prior to expensive engine testing. Determining this is of significant industrial importance, as deposits formed towards the top of piston surfaces in internal combustion engines can contain up to 50 % inorganics, and lead to a reduction in engine power, high piston wear and ultimately, engine failure. Once their structures are known, dispersant chemistries can be tuned to suspend these inorganic structures within the lubricating oil. Thus, in this chapter, the main inorganic components present in deposits formed in bench tests and on different areas of pistons from engine tests are determined using a range of microscopic and spectroscopic techniques. Scanning electron microscopy is used to elucidate the powdery, amorphous morphology of this material, and by coupling this with energy dispersive X-ray analysis, the most abundant inorganic elements are confirmed to be calcium and sulfur. Further analysis via Raman spectroscopy and X-ray diffraction highlights the presence of the calcium sulfate polymorphs, anhydrite ($CaSO_4$) and bassanite ($CaSO_4 \cdot 0.5H_2O$), which are likely to be formed via the neutralisation of sulfuric and sulfurous acids by overbased calcium carbonate detergents added to formulations. These studies allow the development of a model inorganic deposit surface for studying binding interactions with a range of different dispersant chemistries, to prevent deposition at the piston surface.

2.1. Introduction

The formation of deposits at the piston surface is a significant problem in both gasoline and diesel internal combustion engines, due to the harsh conditions present within this enivronment (see Figure 2.1). The pistons are positioned in a highly oxidising environment, a consequence of NOx gasses passing from the combustion chamber, contaminating the lubricating oil.[1-4] Thus, a high amount of deposition occurs in this area, particularly within the ring-belt zone, as shown in Figure 2.1, where surface temperatures between 250 and 350 °C are experienced.[1,3,4]
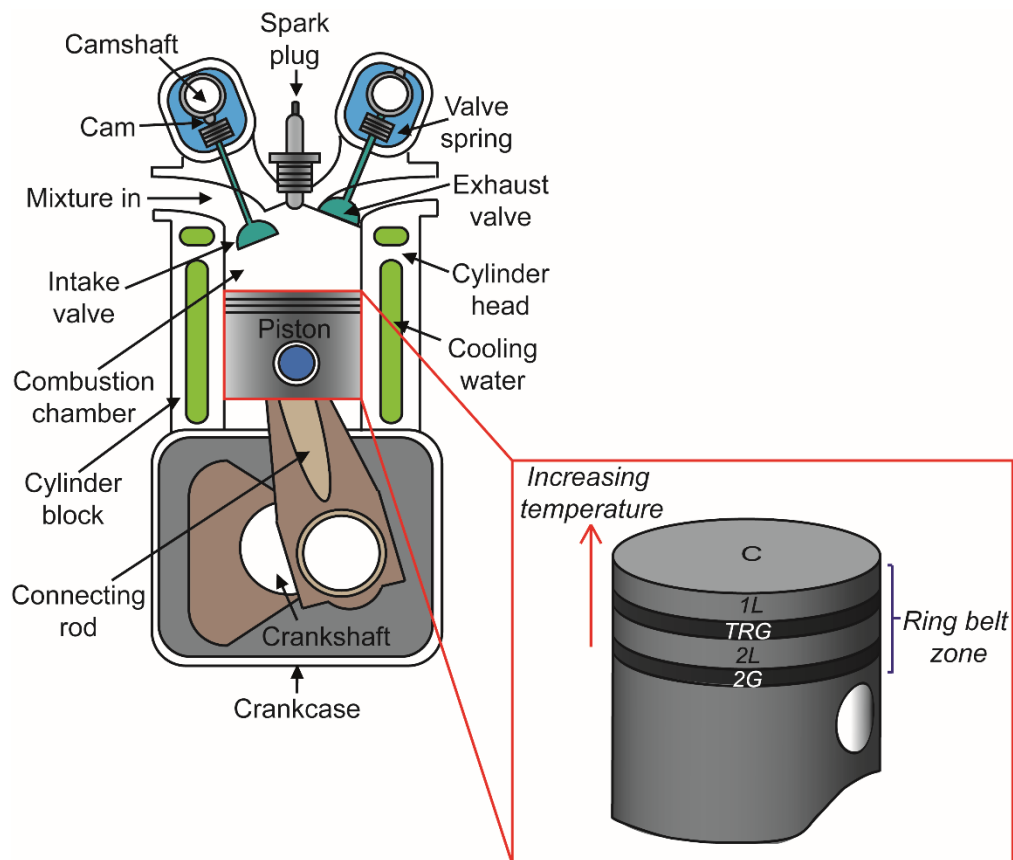
Figure 2.1. Schematic showing the position of a piston within an internal combustion engine. Inset: areas of the piston where deposition is severe, where C corresponds to the piston crown, 1L to the first land, TRG to the top ring groove, 2L to the second land and 2G to the second ring groove.

The problems caused by these deposits depend on the area of the piston where they are located. For example, deposits formed on the piston lands (1L and 2L in Figure 2.1) remove the honing pattern present on the cylinder walls, which provides gaps for the lubricating oil to fill. Therefore, removing this reduces lubrication, leading to

scuffing and wear of the piston and cylinder walls. Alternatively, deposit accumulation within the ring grooves causes the piston rings to stick, ride, flutter and fret, ultimately resulting in their breakage. As a consequence, the air-tight seal provided by these is lost, allowing the air-fuel mixture from the combustion chamber to leak into the piston cylinder, contaminating the engine oil, This is known as blow-by, and results in reduced control over oil consumption, a reduction in engine power and high piston wear.[5,6] In general, the formation of deposits has a negative impact on fuel economy and CO_2 emissions, increasing the viscosity of the oil, thus decreasing its efficiency.[7] However, if the additive chemistry of the lubricating oil is well-designed, deposit formation can be prevented and lower additive concentrations can be used, gaining efficiency through the development of thinner fluids.[7]

It is therefore vital to reduce the tendency for deposits to form on the piston metal surfaces and agglomerate within the oil. This is primarily achieved by the presence of a lubricating oil, which provides a cooling effect around the ring belt zone, whilst reducing wear between contacting metal surfaces of the engine.[5,6] The lubricating oil contains a range of additives (~ 12 wt. %), dissolved in a hydrocarbon base oil (~ 78 wt. %).[7] In addition, long-chain polymeric viscosity modifiers (~ 10 wt. %) are added, to reduce the change in viscosity of the oil with temperature.[7] A range of additives are incorporated into the lubricating oil, such as corrosion inhibitors, anti-wear additives, anti-foams, anti-oxidants and detergents.[7] However, the most abundant additives by weight are dispersants (~ 7 wt. %).[7] These prevent deposition at the piston surface by suspending deposits throughout the lubricating oil, and are known to significantly reduce both carboxylate and sulfate salt deposition.[8] A schematic of the dispersant structure is shown in Figure 2.2. Typical dispersants have a structure comprising an oil-soluble, poly(isobutylene) tail to keep the deposits dispersed and solubilised within the lubricating oil, which is bonded to a succinic anhydride linker group, attached to a polar head group to bind to the deposit functionalities. Lubrizol synthesise dispersants with a variety of different head group chemistries, which have different dispersing efficiencies for different deposit structures.
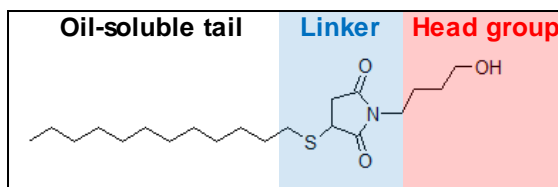
Figure 2.2. Structure of a typical dispersant molecule, showing the oil-soluble tail, linker group and polar head group.

In this way, deposition on the engine surfaces and deposit agglomeration within the lubricating oil are both prevented. However, to successfully design dispersant head groups that bind to the deposit, it is vital to determine the structure of the deposit. This is not trivial, as many variables (i.e. engine design and operating conditions)[1,3,5,6,9,10] affect deposit structure, and thus, the current literature on deposit characterisation is very scattered, with results obtained for a wide range of different engine tests, lubricating oils and operating conditions. Nonetheless, there is a common consensus that deposition is initiated by the formation of a thin non-polar oil film over the piston, which wets the surface.[1-3,9,11-13] This thermally and oxidatively degrades, due to the high oil temperatures (250-300 °C), forming a lacquer, which acts as a binder for further deposition. The products formed as a consequence of this oxidative degradation increase the polarity of the oil film, resulting in the incorporation of inorganic components.[1,11,12] This forms part of the permanent deposit, along with organic polymerisation products.[1,3] Initial deposit accumulation within the ring belt zone insulates the piston surface, preventing the lubricating oil from circulating around this region, thus causing an increase in the local temperature, leading to further deposit accumulation and rapid growth.[13]

Thus, deposits are highly carbonaceous in nature,[4] a consequence of the degradation of the hydrocarbon base oil,[4] which comprises approximately 78 % of the lubricant oil.[7] Thus, the main part of the deposit is organic in nature, and the majority of studies have focussed on characterising this.[4,12] For example, gas chromatography/mass spectrometry (GC/MS) has been used to analyse volatile organics within deposits,[4,10,12] and infrared (IR) spectroscopy has been used to determine the structure of organic oxidation products,[5,9,12,14] revealing high levels of carbonyl functionalities (i.e. aldehydes, ketones, carboxylic acids),[5,9,12,14] due to the oxidising conditions under which deposits form.

However, the presence of additives within the lubricating oil, such as the zincdialkyldithiophosphate (ZDDP) anti-wear additive, and calcium sulfonate and phenate detergent additives[7,9] result in a significant amount of inorganic residue. Fewer studies have focussed on the structure of this, and therefore, far less is currently known about how to disperse these functionalities within the lubricating oil. This is partly because standard laboratory bench tests used to screen oils for piston cleanliness are often incapable of replicating the inorganic content formed in engine tests, as demonstrated in section 2.3.1.1. However, bench tests are often used in industry to screen the performance of lubricating oils prior to expensive engine tests. It is therefore vital that representative tests are developed that allow the severity of inorganic deposit formation to be determined before oils are subjected to engine tests, and thus there is a huge need to further understand the structure and formation of these inorganic components.

Figure 2.3 shows a schematic representing the current view of piston deposit structure.[9] So far, IR spectroscopy has been implemented to detect the presence of inorganic sulfates and phosphates,[3,5,9] although Raman spectroscopy may prove a more useful tool for in depth inorganic structural analysis, as different counter-ions and the presence of crystal water in sulfates and phosphates can shift peaks by several hundreds of wavenumbers.[15] However, Raman spectroscopy has only been used for analysing graphitic nanocrystals in deposits.[13] For further analysis of the specific crystalline inorganic materials present, X-ray diffraction (XRD) has been used,[9,16] confirming the presence of well-defined calcium sulfate crystals near the piston surface[5,9] (see Figure 2.3), thought to be present as a mixture of the two polymorphs bassanite ($CaSO_4 \cdot 0.5H_2O$) and anhydrite ($CaSO_4$).[9] The low water content of this material is likely to be a consequence of the high temperatures experienced at the piston surface and high engine oil temperatures (250-350 and 200-300 °C, respectively).[1] However, the elemental ratio of calcium to sulfur is often higher than 1:1, suggesting calcium is also present as other inorganic structures.[5] This may be in the form of calcium carbonate, due to direct degradation of the overbased calcium carbonate detergent cores, as it has been suggested that unassigned XRD peaks from deposit analysis correspond to vaterite, a crystalline polymorph of $CaCO_3$.[9] Other inorganic structures detected include calcium and zinc phosphates (due to the thermal and oxidative degradation of ZDDP and detergents), as well as zinc sulfates, which are usually present

at lower concentrations than calcium sulfate.[9] Aluminium phosphates and oxides have also been detected near the piston surface (see Figure 2.3),[9] as well as metallic elements such as aluminium, iron, silicon and copper, due to wear of the piston alloy metals and other parts of the engine.
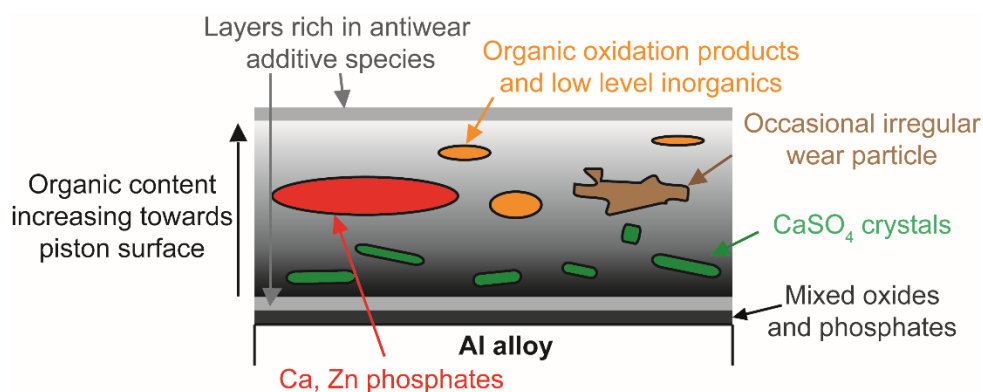
Figure 2.3. Schematic showing the key components present in a piston deposit. Adapted from ref. 9 by permission of John Wiley & Sons, Inc. Copyright 2002 John Wiley & Sons, Ltd.

One of the most significant conditions that affects deposit structure is the piston surface temperature,[3,5,6,12] which decreases on moving down the piston. As a result, a higher amount of inorganic content is generally found in deposits at the top land (1L) and top ring groove (TRG) of the piston than at the second land (2L) and second ring groove (2G), with the opposite trend seen for the organic content[5,9] (see Figure 2.1). To determine the relative percentages of organics and inorganics within deposits, thermogravimetric analysis (TGA) is frequently used.[5,6] This is because different components of the deposit degrade at different temperatures. For example, weight losses at temperatures under 200 °C in an inert, (typically N_2) environment correspond to degradation of volatile organics (i.e. solvents, light base oils and water), whereas polymeric organics degrade between 200-800 °C. Non-volatile, soot-based components are degraded in oxidising environments at temperatures greater than 500 °C, and any deposit remaining at temperatures greater than 800 °C corresponds to inorganic structures.

Finally, to determine the morphology of deposits, techniques such as scanning electron microscopy (SEM)[5,12] and transmission electron microscopy (TEM)[9] have been implemented, in combination with energy-dispersive X-ray analysis (EDX)[5,9,14]

for elemental analysis. Elemental compositions have also been determined using X-ray photoelectron spectroscopy (XPS) to profile the change in deposit composition with depth.[9] SEM and TEM analysis show piston deposits have non-uniform structures, consisting of a non-homogeneous mixture of inorganic sulfates, additive elements, soot, wear debris and oxidised lubricant binder.[5,9,12] However, the most abundant inorganic component in many deposits is thought to be calcium sulfate (see Figure 2.3).[3,9]

To determine the structure and formation of piston deposits formed in heavy duty diesel (HDD) engine tests in the presence of Lubrizol's lubricating oils, a wide range of microscopic and spectroscopic techniques were employed to study the structure and morphology of the inorganic deposits, including TGA, SEM-EDX, Raman spectroscopy and XRD. This is the first time piston deposits have been studied to this level of detail in a systematic way, providing structural information for the development of a model inorganic deposit surface and thus the application of spectroscopic techniques to measure interaction forces between this and different dispersant chemistries (see Chapter 4). By providing a better understanding of how to effectively disperse these inorganic components within the lubricating oil, these studies have a crucial impact on lubricant development, enabling additives to be better designed for their purpose, thus increasing their efficiency and reducing their concentrations within the oil. This will allow for the development of thinner fluid and therefore increased fuel economy and reduced CO_2 emissions.

2.2. Experimental

2.2.1. Preparation of Bench Test Deposit Samples

Panel Coker tests (FTM 791A-3462)[17] were conducted at Lubrizol. This test is used to determine the stability of lubricants in hot temperature environments by splashing lubricant droplets onto a hot metal panel, tilted at an angle of 25 °C. By measuring the weight of the panel before and after, the severity of lacquer and deposit formation can be determined.[17] The following test conditions were used: panel temperature: 325 °C, sump temperature: 92 °C, bake cycle: 45 s, splash cycle: 15 s, air flow rate: 350 mL min^{-1}, spindle speed: 1000 rpm, test piece: aluminium, test time: 4 hr (+ 12 min of cooling). At the end of the test, deposits were carefully scraped from the aluminium surface and analysed using thermogravimetric analysis (TGA).

2.2.2. Preparation of Engine Test Deposit Samples

Deposits were scraped off four pistons (provided by Lubrizol) from an OM501LA HDD engine test. These were obtained from the crown (C), top land (1L), top ring groove (TRG), second land (2L) and second ring groove (2G), as shown in Figure 2.1, or a combination of all these areas. Deposits from all of these areas were analysed using TGA, and deposits from only the TRG were analysed using SEM, Raman spectroscopy and XRD, in order to specifically focus on the inorganic components, present in large amounts at the TRG.

2.2.3. Thermogravimetric Analysis

2.2.3.1. Comparing Bench Test and Engine Test Deposits

TGA analysis was conducted on deposits analysed in section 2.3.1.1 using a Q500 TGA Instrument at Lubrizol. Deposits were scraped from Panel Coker test samples and the surface of pistons from an OM501LA HDD engine test. Both tests were conducted using the same lubricating oil. Deposits were heated at a rate of 10 °C min^{-1}, from 20-650 °C under an inert N_2 atmosphere and from 650-1000 °C under O_2. Weight losses were recorded as a function of temperature.

2.2.3.2. Analysing Deposits from Different Piston Areas

TGA analysis was conducted on deposits analysed in section 2.3.1.2 using a Mettler Toledo DSC1-Star instrument. Deposits were obtained from an OM501LA HDD engine test conducted using a different lubricating oil to deposits analysed in section 2.3.1.1. Deposits were placed in aluminium crucibles and heated at a rate of 1 °C min^{-1}, from 20-650 °C under an inert N_2 atmosphere and from 650-1000 °C under air. Weight losses were recorded as a function of temperature.

2.2.4. Scanning Electron Microscopy-Energy-Dispersive X-ray Analysis

A Zeiss Supra 55-VP field emission scanning electron microscope with EDAX Genesis energy-dispersive X-ray analysis was used to characterise deposits from the TRG, using secondary electron (SE2) mode and an acceleration voltage of 20 kV.

2.2.5. Raman Spectroscopy

Raman spectroscopy was used to determine the main inorganic components present in the TRG deposit, both before and after heating the deposit to 1000 °C using TGA analysis (as described in section 2.2.3.2). Spectra were obtained using a Renishaw

micro-Raman inVia spectrometer. Regions of interest were selected using an optical microscope with a 50× objective lens. The 442 nm line of a HeCd laser was used at 100 % power, with an acquisition time of 10 s for each spectrum. Spectral calibration was performed using the 520.7 nm peak of a silicon standard.

2.2.6. X-ray Diffraction

Powder X-ray diffraction (XRD) was conducted on the TRG deposit using a PANalytical X'Pert Pro X-Ray MPD powder diffractometer equipped with a curved Ge Johnasson monochromator, giving focussed Cu $K_{\alpha 1}$ radiation (1.540598 Å), with a Pixcel detector. Scans were obtained ranging from 5 to 60° in 2θ. Crystalline structures were identified using reference patterns from the HighScore Plus software (PANalytical B. V.) and the latest ICDD powder diffraction database.

2.3. Results and Discussion

2.3.1. Relative Percentages of Organic and Inorganic Content

2.3.1.1. Comparing Bench Test and Engine Test Deposits

Initially, deposits formed in a typical bench test, the Panel Coker test, and deposits obtained from the top ring groove (TRG) of pistons from a heavy duty diesel (HDD) engine test (OM501LA) were compared (see Figure 2.1). For both tests, the same lubricating oil was screened. These were analysed using thermogravimetric analysis (TGA), by heating each deposit from 20-650 °C under an inert, N_2 atmosphere, and then under O_2 from 650-1000 °C. The weight losses for each are shown in Figure 2.4 and Table 2.1. Below 200 °C, similar weight losses were obtained, corresponding to the degradation of light volatiles, such as solvents and light base oils, and water, however, between 200-800 °C, a much higher percentage weight loss occurred for the bench test deposit than the engine test deposit. This corresponds to the degradation of long chain polymers and organic matter, thus highlighting the much higher relative amounts of organic deposit formed in the bench test compared to the engine test. However, the remaining sample mass after this point was approximately three times higher for the engine test deposit than the bench test deposit. This represents the remaining inorganic residue, demonstrating that deposits from engine tests contain much higher amounts of inorganic material than those from simpler bench tests, which are incapable of fully replicating the harsh conditions within the engine environment. Thus, these results highlight a key compositional difference between deposits formed

in standard laboratory bench tests and engine tests. This demonstrates the vital need to determine the structure and formation of these inorganic species, to develop laboratory bench tests that are capable of screening the severity of inorganic deposit formation prior to testing lubricant formulations in expensive engine tests. Then, dispersant chemistries which interact with the inorganic components of piston deposits can be designed and developed, and their efficiency tested.
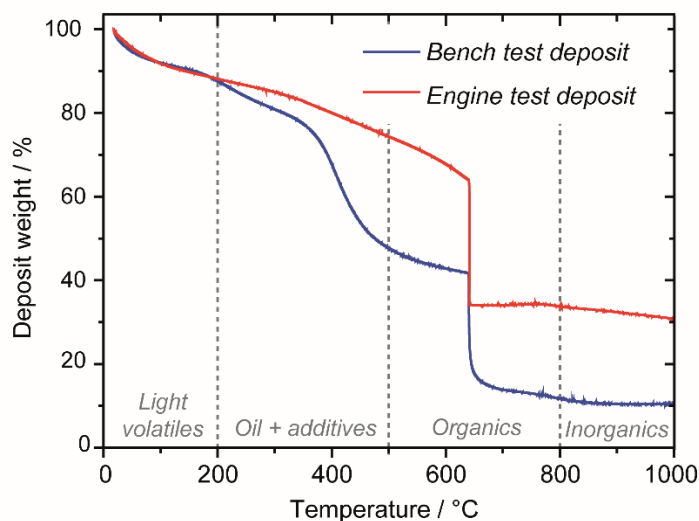
Figure 2.4. Temperature vs. remaining weight for deposits obtained from the Panel Coker bench test (blue) and the OM501LA HDD engine test (red).

Table 2.1. TGA weight loss percentages obtained for the deposits shown in Figure 2.4, and their corresponding structures. *Weight loss between 800-1000 °C plus the remaining residue at the end of the test.*

Temperature / °C	Structure	Weight loss / wt. %	
		Bench test deposit	Engine test deposit
20-200	Light volatiles	12.4	11.6
200-500	Polymeric organics	39.9	15.2
500-800	Soot-based components	35.9	39.7
800-1000	Inorganic residue	11.8*	33.5*

2.3.1.2. Analysing Deposits from Different Piston Areas

The relative percentages of organic and inorganic content in deposits formed at different areas on the surface of pistons from the same engine test subjected to a different lubricating oil were also analysed using TGA. Areas containing a higher amount of inorganic content were then further tested to determine the structures of these inorganic components. Deposits were tested from the crown (C), top land (1L), top ring groove (TRG), second land (2L) and second ring groove (2G), as shown in Figure 2.1, using the method described in section 2.2.3.2. The weight losses for each deposit are shown in Figures 2.5 and 2.6. Each deposit contained a low percentage (< 10 %) of light volatiles (i.e. light base oils, solvent and water). Between 10 and 25 % of each deposit was formed due to the thermal and oxidative degradation of polymeric organics. The majority of the crown land deposit (C) was soot-based in content (60 %), as a result of its close proximity to the combustion chamber. Therefore, this deposit is the least suitable to use for analysis of the inorganic structures present in piston deposits. Deposits from higher up the piston contained a higher percentage of inorganics than deposits from lower down the piston, with the TRG containing more inorganics than the 2G, and the 1L containing more than the 2L, as expected due to the increase in temperature on moving up the piston.[5,9] Although the highest percentage of inorganics was found in the 1L area, further analysis was conducted on deposits from the TRG, due to ~ 10 times more sample being obtained from this area (805 mg, compared to 82 mg from the 1L area), thus providing a higher amount of inorganic material for analysis.
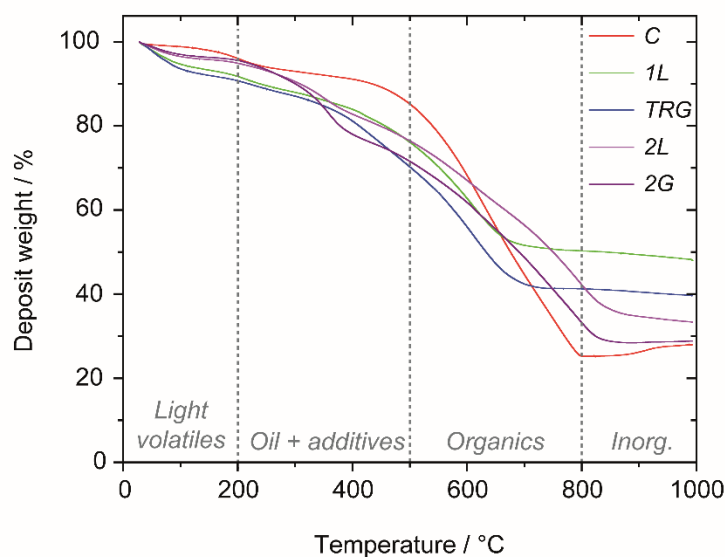
Figure 2.5. Temperature vs. remaining weight for deposits obtained from the crown (C), top land (1L), top ring groove (TRG), second land (2L) and second ring groove (2G) of a piston from an OM501LA HDD engine test.
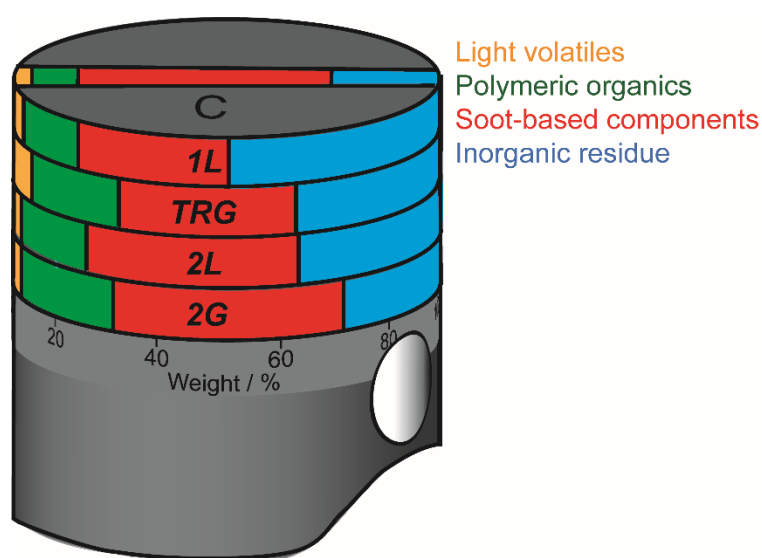
Figure 2.6. Schematic representing the relative TGA weight loss percentages obtained for deposits from different areas of the piston (as shown graphically in Figure 2.5), highlighting their corresponding structures *(areas shown in blue correspond to the weight loss between 800-1000 °C, plus the remaining residue at the end of the test).*

2.3.2. Deposit Morphology

Scanning electron microscopy (SEM) was used to determine the morphology of the deposit from the TRG. This was also coupled with energy-dispersive X-ray analysis

(EDX) to deduce the percentages of the main inorganic elements within the deposit. This was found to be a powdery material with a non-uniform morphology, consisting of small micron-sized crystallites as shown in Figure 2.7. The elemental compositions of each crystallite were fairly consistent (see Figure 2.8), with a mixture of organic and inorganic elements detected in each, present in similar ratios. Thus, individual crystallites containing a specific inorganic component were not detected, suggesting the deposit is rather amorphous in structure. As expected, the most abundant elements were carbon and oxygen, due to the thermal and oxidative degradation of the base oil and the presence of high amounts of aromatic, carbonaceous soot. The most abundant inorganic element detected was calcium, correlating with previous studies which suggest calcium sulfate constitutes the majority of the inorganic deposit.[3,9] This also accounts for the sulfur detected, however, the higher percentages of calcium compared to sulfur confirms the presence of other calcium-containing inorganic components within the deposit, as previously suggested.[5] Additionally, sulfur may be present within the TRG deposit due to the degradation of sulfur-containing detergents, (such as calcium sulfonates), anti-oxidants and corrosion inhibitors, and low levels of sulfur in the fuel. Zinc and phosphorus were also detected, but in lower amounts than calcium and sulfur, suggesting the zinc phosphate films described in the literature are present, due to the degradation of the anti-wear additive zincdialkyldithiophosphate (ZDDP).[9] Additionally, trace amounts of iron were found, either due to wear of the steel piston insert during the engine test, or unavoidably scraping some of this surface off when obtaining the deposit samples.
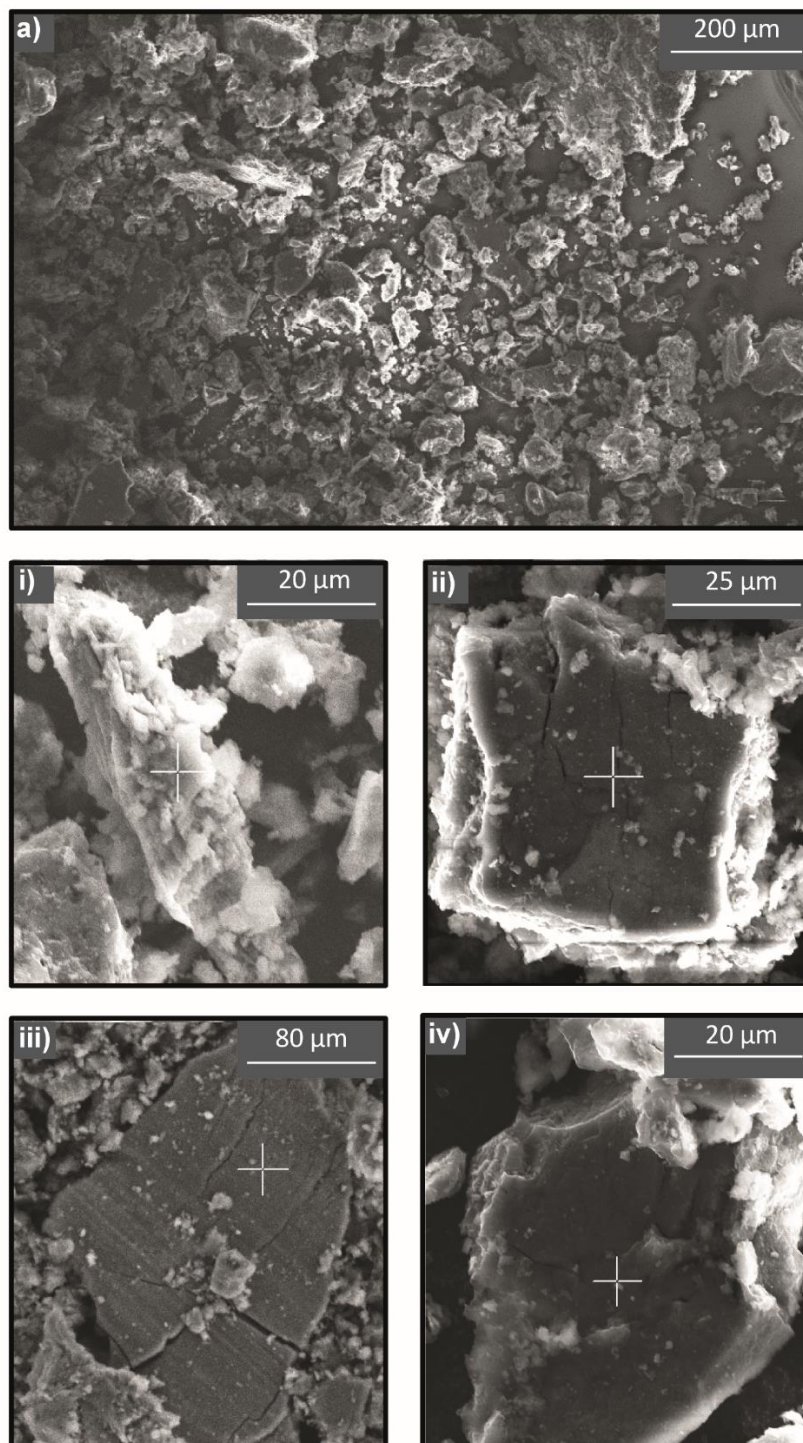
Figure 2.7. SEM images of deposit obtained from the TRG. (a) Image of a large area of the deposit, showing the powdery, non-uniform morphology. EDX analysis was performed over the whole area shown. (i-iv) Images of individual crystallites found within the area shown in (a). The crosses mark the areas where EDX analysis was performed.
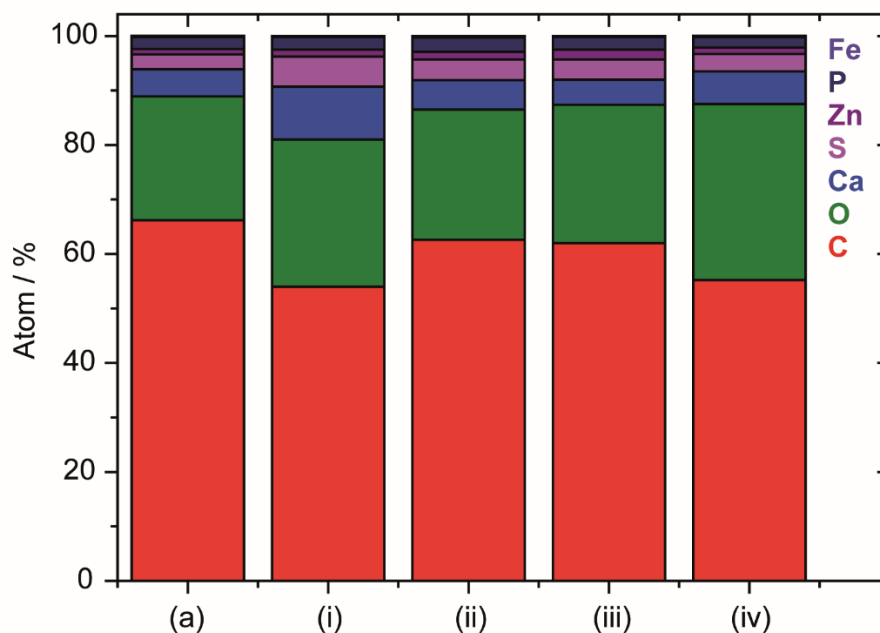
Figure 2.8. Atom percentages obtained using SEM-EDX for elements within the large deposit area and crystallites shown in Figure 2.7.

2.3.3. Determination of Inorganic Structures

2.3.3.1. Raman Spectroscopy Analysis

Raman spectroscopy was used for a more in depth analysis, to determine the inorganic structures of the elements detected above. Raman peaks arise when there is a change in polarisability of the bond, so although this technique is not sensitive to ionic bonds, the covalent bonds present in inorganic structures result in different Raman spectra. This technique is particularly useful for differentiating inorganic structures, as the presence of different counter ions and amounts of water affect the force constants of the covalent bonds and therefore their vibrational energies and peak positions.[15] For example, a decrease in the degree of hydration of the calcium sulfate polymorphs results in an increase in their S-O bond strengths. This results in an increased bond stretching force constant, shifting the ν_1 SO_4 peak to higher wavenumbers.[18,19] Additionally, both the fully hydrated, gypsum ($CaSO_4 \cdot 2H_2O$) and hemihydrate, bassanite ($CaSO_4 \cdot 0.5H_2O$) polymorphs have two ν_4 SO_4 shifts, whereas the fully dehydrated polymorph, anhydrite ($CaSO_4$) has three. This is a consequence of the higher asymmetry of the SO_4^{2-} ions in anhydrite, due to the presence of a higher number of crystallographic environments, causing these peaks to split.[18,20] Additionally, stretches due to the presence of water molecules can be used to differentiate between these three polymorphs. Two different

water peaks occur for gypsum and bassanite, the ν_1 H_2O stretch, (which corresponds to hydrogen bonding between SO_4^{2-} ions and H_2O molecules) and the ν_3 H_2O stretch, (which corresponds to H_2O molecules directly bonded to Ca^{2+} ions). As the former involves hydrogen bonding, the O-H bond strength is weakened, and therefore the ν_1 H_2O stretches appear at lower wavenumbers.[18] Similarly to the ν_1 SO_4 peaks, these water peaks appear at lower wavenumbers for gypsum compared to bassanite. For the fully dehydrated anhydrite polymorph, neither of these peaks are present due to the lack of water in this structure.

Figure 2.9 shows a representative spectrum obtained for the TRG deposit without any additional sample preparation. This resulted in very broad peaks, making it difficult to assign these to specific inorganic structures. This is a result of the high amount of amorphous carbonaceous material present within the deposit, demonstrated by the two peaks centred around 1350 and 1600 cm^{-1}, which are likely to correspond to the D and G peaks of carbon, respectively (usually centred at 1350 and 1580 cm^{-1}).[21] However, due the broadness introduced by the amorphous nature of this carbon, a lot of structural information is lost from this complex region.[22] These carbon peaks are usually dominated by sp^2 carbon sites due to visible excitation resonating within these π states.[21] The ordered G peak occurs due to the stretch vibration modes of sp^2 atoms in both aromatic rings and chains,[21] such as the C=C sp^2 stretch vibration modes of olefinic or conjugated carbon chains at 1620 cm^{-1}.[22] Additionally, peaks centred around 1580 cm^{-1} may correspond to sp^2 stretch vibrations in aromatic rings, olefinic or conjugated chains.[22] The disordered D peak occurs due to the breathing modes of sp^2 atoms in single and fused aromatic rings.[23-25] This is often increased in intensity compared to the G peak when there is a high amount of sp^3 carbon, for example, for olefinic chains connected by sp^3 bonded carbon, or a low amount of aromatic species.[22] In the spectrum shown in Figure 2.9, the peak centred around 1600 cm^{-1} appears much stronger than that at 1350 cm^{-1}, suggesting there is a high amount of sp^2 carbon in the deposit, most likely due to the presence of graphitic structures. However, as these peaks are so broad, it is hard to assign these to specific carbonaceous structures. The remaining peaks centred around 420, 570, 950, 1000 and 1100 cm^{-1} are likely to correspond to a range of different calcium and zinc sulfates, phosphates and/or carbonates. Due to the high background and thus lack of distinguishable peaks after 2000 cm^{-1}, spectra were not obtained beyond this wavenumber.
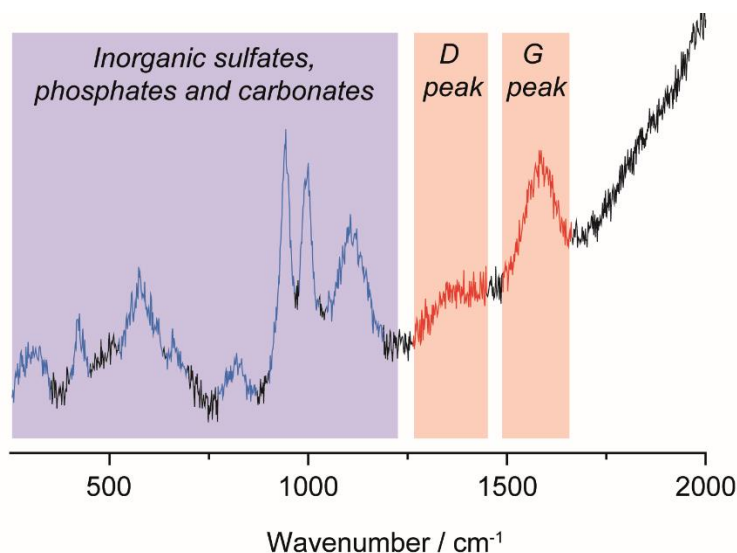
Figure 2.9. Representative Raman spectrum obtained for the TRG deposit, prior to any sample preparation.

To obtain a much clearer spectrum, the carbonaceous material was removed from the deposit by heating the sample to 1000 °C using TGA (see section 2.2.3.2 for the method used). The remaining inorganic residue gave much sharper Raman peaks, as shown in Figure 2.10. In addition, the broad peaks previously seen centred at 1350 and 1600 cm^{-1} were no longer present, confirming the carbonaceous material was removed, leaving behind only the inorganic residue. Table 2.2 provides the suggested inorganic structures assigned to each peak. The majority of the peaks correspond to calcium sulfate, confirming conclusions from previous studies which suggest this is the main inorganic compound present in these piston deposits.[3,9] The polymorphs detected were the fully dehydrated polymorph, anhydrite ($CaSO_4$) and the hemihydrate, bassanite ($CaSO_4 \cdot 0.5H_2O$). However, the presence of these dehydrated structures may be a consequence of the high temperatures used to prepare this sample, removing water molecules from the crystal structures, which was further investigated as explained in the following section. Additional peaks were assigned to zinc sulfates and phosphates, supporting the detection of sulfates and phosphates from previous IR studies,[3,5] as well as previous suggestions of zinc and phosphorus-containing ZDDP films.[9] Due to the broadness of the peak at ~ 1100 cm^{-1}, this could not be assigned to a specific inorganic structure, but is again likely to be either a sulfate, phosphate or carbonate.
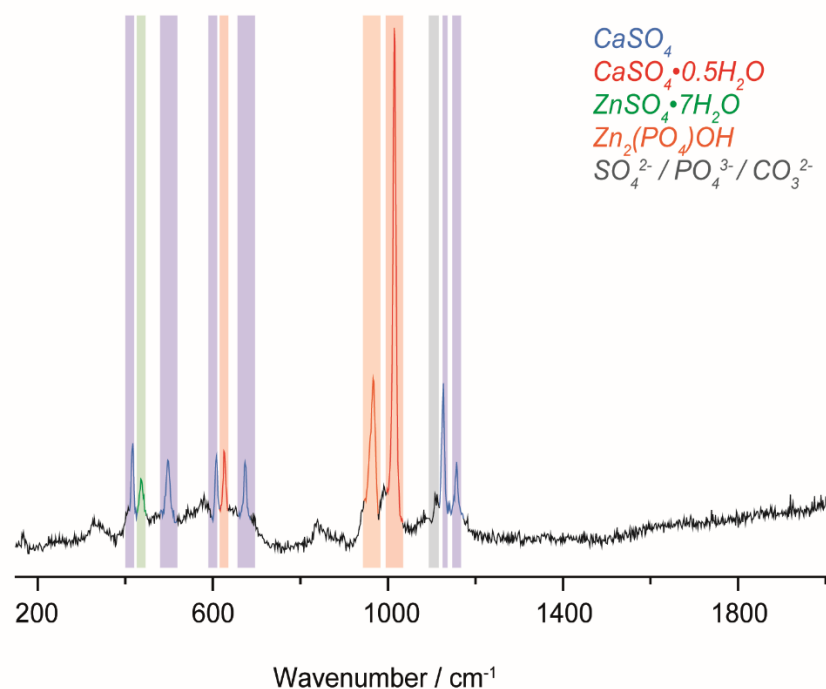
Figure 2.10. Representative Raman spectrum obtained for the TRG deposit after heating to 1000 °C using TGA.

Table 2.2. Assigned Raman peaks for the spectrum shown in Figure 2.10.

Peak / cm^{-1}	Structure	Mode	Reference value / cm^{-1}
417	CaSO$_4$	ν_2 *SO$_4$*	416[18]
437	ZnSO$_4$·7H$_2$O	ν_2 *SO$_4$*	441[26]
497	CaSO$_4$	ν_2 *SO$_4$*	499[18]
608	CaSO$_4$	ν_4 *SO$_4$*	609-612[18]
628	CaSO$_4$·0.5H$_2$O	ν_4 *SO$_4$*	628-629[18]
674	CaSO$_4$	ν_4 *SO$_4$*	675-676[18]
967	Zn$_2$(PO$_4$)OH	ν_1 *PO$_4$*	965[18]
1110 (br.)	CO$_3$$^{2-}$	ν_1 *CO$_3$*	1020-1110[15]
	PO$_4$$^{3-}$	ν_3 *PO$_4$*	1000-1180[15]
	SO$_4$$^{2-}$	ν_3 *SO$_4$*	1054-1198[26]
1015	CaSO$_4$·0.5H$_2$O	ν_1 *SO$_4$*	1015[18]
1126	CaSO$_4$	ν_3 *SO$_4$*	1128[18]
	CaSO$_4$·0.5H$_2$O	ν_3 *SO$_4$*	1128[18]
1157	CaSO$_4$	ν_3 *SO$_4$*	1159[18]

Although heating the deposit resulted in clearer, sharper peaks, it is important to be aware that this may change the structure of the inorganic components (i.e. through dehydration). Therefore, to investigate whether the fully dehydrated and hemihydrate calcium sulfate polymorphs correspond to the polymorphs actually present in the TRG deposit, X-ray diffraction analysis was conducted on the deposit prior to heating the sample.

2.3.3.2. X-ray Diffraction Analysis

X-ray diffraction was used to detect the presence of any crystalline material within the deposit sample. The resulting pattern obtained for the TRG deposit prior to sample preparation is shown in Figure 2.11. The peaks can be assigned to a mixture of the calcium sulfate polymorphs anhydrite ($CaSO_4$) and bassanite ($CaSO_4 \cdot 0.5H_2O$), thus confirming the conclusions reached from Raman analysis, proving these crystal structures occur within the TRG deposit, and not as a result of the heating method used to prepare the sample for Raman analysis. This also agrees with previous inorganic piston deposit analysis.[9] The lack of any other inorganic structures detected from the XRD analysis may be a consequence of their low concentrations or amorphous structures, which will not be seen using this technique.
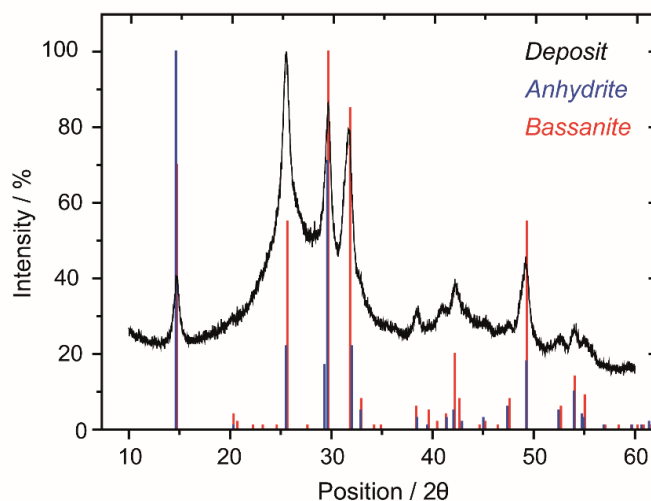
Figure 2.11. Representative X-ray diffraction pattern obtained for the TRG deposit prior to any sample preparation. For comparison, reference patterns for anhydrite (blue) and bassanite (red) are provided.

2.3.4. Mechanism of Inorganic Deposit Formation

2.3.4.1. Mechanism for the Formation of Calcium Sulfate

The above analysis suggests that the most abundant inorganic structures found in these piston deposits are the fully dehydrated and hemihydrate calcium sulfate polymorphs. This material will therefore be investigated for use as a model deposit surface for determining how to disperse inorganic piston deposits within the lubricating oil in Chapters 3 and 4. The mechanism of formation of this is likely to be due to the action of the overbased calcium carbonate detergents added to the lubricating oil. These additives are incorporated into formulations in order to neutralise sulfuric and sulfurous acids present from the combustion of fuel and lubricant oil sulfur, as shown schematically in Figure 2.12. The overbased calcium carbonate cores of these detergents (solubilised in the oil phase by long chain alkyl sulfonates) react with acid droplets emulsified in the oil by free surfactant from the detergent and other additives. However, as a consequence of this process, calcium sulfate deposits as a neutralisation product, forming the main part of the inorganic deposit on piston surfaces.[3,9] Preventing this is particularly important as it not only comprises the majority of the inorganic deposit, as confirmed in this chapter, but also acts as a binding layer, especially at the piston crown land, causing tight adhesion of carbonaceous deposits within this area.[5]
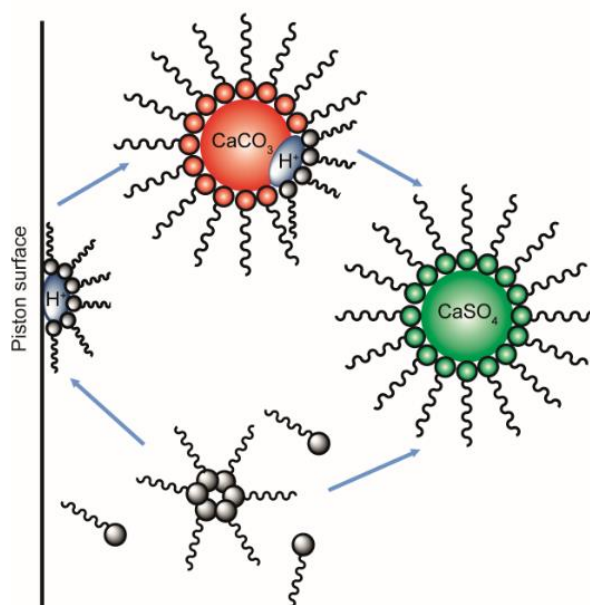
Figure 2.12. Proposed mechanism for calcium sulfate formation (green) in the engine, due to the neutralisation reaction of overbased calcium carbonate detergent particles (red) with emulsified sulfuric and sulfurous acid droplets (blue) in the oil and fuel.

2.3.4.2. Formation of the Calcium Sulfate Hydrates Anhydrite and Bassanite

The calcium sulfate material was found to be crystalline in nature, as shown by X-ray diffraction, consisting of the fully dehydrated and hemihydrated polymorphs, anhydrite and bassanite, respectively. Under ambient conditions in aqueous solvents, these two polymorphs of calcium sulfate are unstable, with the most stable being the fully hydrated form, gypsum ($CaSO_4 \cdot 2H_2O$).[27,28] The low amounts of water found in these structures is likely to be a consequence of the high temperatures experienced at the piston surface, as well as the presence of an organic solvent environment, as limiting the water content of the solvent is known to favour anhydrite precipitation.[29] The presence of both anhydrite and bassanite is likely to be due to a conversion process between the two. This is because temperatures greater than 360 °C are required to form insoluble anhydrite (γ-$CaSO_4$), which cannot rehydrate back to bassanite.[30] However, at temperatures lower than this, soluble anhydrite is formed (γ-$CaSO_4$), which has a very similar crystal structure to bassanite, and therefore still has vacancies or 'water channels' within its structure. Upon cooling, these channels will become repopulated with water, thus converting back to the hemihydrate. As the piston surface and surrounding oil experience temperatures slightly lower than 360 °C (approximately 250-350 and 250-300 °C, respectively), the latter case is likely to occur, which may explain why a mixture of anhydrite and bassanite are found in piston deposits formed here. However, to further understand how some of this anhydrite is able to remain stable under these conditions, and thus the key processes of inorganic piston deposit formation, the growth of this material is studied in further detail in Chapter 3.

2.4. Conclusions

The main inorganic components present in deposits obtained from the TRG of pistons from a Lubrizol HDD engine test have been studied in a great level of detail for the first time, using a range of microscopic and spectroscopic techniques. The most abundant inorganic structures detected were the fully dehydrated calcium sulfate polymorph, anhydrite ($CaSO_4$), and the hemihydrate, bassanite ($CaSO_4 \cdot 0.5H_2O$). This analysis agrees with the few previous studies conducted on inorganic piston deposit characterisation.[3,9] Calcium sulfate is thought to form as a consequence of the neutralisation of sulfuric and sufurous acids from the fuel and oil by overbased calcium carbonate detergents, resulting in the formation of crystalline polymorphs with low water contents, due to the high temperatures and organic solvent environment present within the engine. However, further studies will be conducted to determine the mechanism of formation of this inorganic deposit, as described in Chapter 3.

Additionally, these studies highlight the significantly higher inorganic contents present in piston deposits from engine tests compared to deposits formed in simple laboratory bench tests, demonstrating that the latter do not effectively model the severity of real-life piston deposit formation. An alternative method is therefore required for screening the ability of lubricating oil formulations to improve piston cleanliness. Thus, based on these results, a dehydrated calcium sulfate model inorganic deposit surface will be designed to elucidate the efficiencies of different dispersant head group functionalities for suspending this inorganic content within the lubricating oil, as shown in Figure 2.12, to prevent its formation on the piston surface. Results from these binding studies are provided in Chapter 4. These findings allow dispersant chemistries to be designed with higher efficiencies, thus decreasing their concentrations in the engine oil, leading to an increase in fuel economy and decreased CO_2 emissions.

2.5. Bibliography

(1)   Chen, C.-I.; Hsu, S. M. *Tribol. Lett.* **2003**, *14*, 83-90.

(2)   Lee, P. M.; Priest, M.; Stark, M. S.; Wilkinson, J. J.; Lindsay Smith, J. R.; Taylor, R. I.; Chung, S. *P I Mech. Eng. J-J Eng.* **2006**, *220*, 171-180.

(3)   Papke, B. L.; Dahlstrom, P. L.; Kreuz, K. L.; *Lub. Eng.* **1989**, *45*, 575-585.

(4)   Diaby, M.; Singhal, P.; Ousmane, M.; Sablier, M.; Le Négrate, A.; El Fassi, M.; Zymla, V. *Fuel* **2013**, *107*, 90-101.

(5)   Covitch, M. J.; Richardson, J. P.; Graf, R.T. *Lub. Sci.* **1990**, *2*, 231-251.

(6)   Shu, G.; Dong, L.; Liang, X. *Int. J. Engine Res.* **2012***, 13*, 357-369.

(7)   Additive Technical Committee, *Lubricant Additives: Use and benefits*, Document 118, 2016, 1-63.

(8)   Papke, B. L. *Lub. Eng.* **1991**, *48*, 209-218.

(9)   Smith, G. C.; Hopwood, A. B.; Titchener, K. J. *Surf. Interface Anal.* **2002**, *33*, 259-268.

(10)   Diaby, M.; Kinani, S.; Genty, C.; Bouchonnet, S.; Sablier, M.; Le Négrate, A.; El Fassi, M. *Anal. Chem.* **2009**, *81*, 9764-9770.

(11)   Papke, B. L.; Charles, C. B. *Development of a laboratory test to simulate piston deposit formation in the ASTM Sequence IIIG Engine Test*, Shell Global Solutions (US) Inc., 2012.

(12)   Diaby, M.; Sablier, M.; Le Négrate, A.; El Fassi, M.; Bocquet, J. *Carbon* **2009**, *47*, 355-366.

(13)   Zerda, T. W.; Yuan, X.; Moore, S. M.; Leon, C. A. *Carbon* **1999**, *37*, 1999-2009.

(14)   Guan Y. C.; Ng, G. K. L.; Zheng, H. Y.; Hong, M. H.; Hong, X.; Zhang, Z. *Appl. Surf. Sci.* **2013**, *270*, 526-530.

(15)   Vandenabeele, P., *Practical Raman Spectroscopy - An Introduction;* Eds.; John Wiley and Sons Ltd.: Chichester, 2013.

(16)   Tarkowski, P.; Sarzyński, J.; Budzyński, P.; Paluch, R.; Wiertel, M. *Fuel* **2001**, *80*, 1399-1403.

(17)   Boullion, V., *Overview of oxidation laboratory tests on industrial lubricants*, Lubmat '16, Les Isnes, Namur, Belgium, 2016.

(18)   Liu, Y.; Wang. A.; Freeman, J. J., *Raman, MIR, and NIR spectroscopic study of calcium sulfates: gypsum, bassanite, and anhydrite,* 40th Lunar and Planetary

Science Conference, Houston, Texas, 2009.

(19) Ruiz-Agudo, E.; Putnis, C. V.; Hövelmann, J.; Álvarez-Lloret, P.; Ibáñez-Velasco, A.; Putnis, A. *Geochim. Cosmochim. Acta* **2015**, *156*, 75-93.

(20) Buzgar, N.; Buzatu, A.; Sanislav, I. V. *An. Stiint. U. Al. I-Mat* **2009**, *55*, 5-23.

(21) Ferrari, A. C. *Solid State Commun.* **2007**, *143*, 47-57.

(22) Schwan, J.; Ulrich, S.; Batori, V.; Ehrhardt, H.; Silva, S. R. P. *J. Appl. Phys.* **1996**, *80*, 440-447.

(23) Ferrari, A. C.; Robertson, J. *Phys. Rev. B* **2000**, *61*, 14095-14107.

(24) O'Connell, M. J.; Bachilo, S. M.; Huffman, C. B.; Moore, V. C.; Strano, M. S.; Haroz, E. H.; Rialon, K. L.; Boul, P. J.; Noon, W. H.; Kittrell, C.; Ma, J.; Hauge, R. H.; Weisman, R. E.; Smalley, R. E. *Science* **2002**, *297*, 593-596.

(25) Tuinstra, F.; Koening, J. L. *J. Phys. Chem.* **1970**, *53*, 1126-1130.

(26) Jentzsch, P. V.; Kampe, P. V.; Ciobotă, V.; Rösch, P.; Popp, J. *Spectrochim. Acta A* **2013**, *115*, 697-708.

(27) Wang, Y. W.; Kim, Y. Y.; Christenson, H. K.; Meldrum, F. C. *Chem. Commun.* **2012**, *48*, 504-506.

(28) Abriel, W.; Reisdorf, K. *J. Solid State Chem.* **1990**, *85*, 23-30.

(29) Tritschler, U.; Van Driessche, A. E. S.; Kempter, A.; Kellermeier, M.; Cölfen, H. *Angew. Chem. Int. Ed.* **2015**, *54*, 4083-4086.

(30) Bezou, C.; Nonat, A.; Mutin, J. C.; Christensen, A. N.; Lehmann, M. S. *J. Solid State Chem.* **1995**, *117*, 165-176.

Chapter 3: Calcium Sulfate Crystallisation and Transformation at Industrially Relevant Aqueous-Organic Interfaces

Abstract

The calcium sulfate crystal system is of considerable industrial importance, as demonstrated by the piston deposit analysis conducted in Chapter 2. This crystal system is also fundamentally interesting, consisting of the three hydrates, gypsum ($CaSO_4 \cdot 2H_2O$), bassanite ($CaSO_4 \cdot 0.5H_2O$) and anhydrite ($CaSO_4$). The latter is one of the main components of inorganic piston deposits, however, its synthesis via conventional aqueous methods requires elevated temperatures and therefore high energy costs. Thus, to determine the mechanism of deposit formation, we investigate calcium sulfate crystal growth across non-miscible aqueous-organic (water-hexane and water-dodecane) interfaces, mimicking the environment present within the engine. This process is visualised via in situ optical microscopy, which produces high magnification videos of the crystal growth process. The use of interferometry, Raman spectroscopy and X-ray diffraction allows the full range of calcium sulfate morphologies and hydrates to be analysed subsequently in considerable detail. In the case of dodecane, gypsum is the final product, which is not found in the deposit, but the use of hexane in an open (evaporating) system results in the formation of anhydrite crystals via gypsum, at room temperature. A dissolution-precipitation mechanism between neighboring microcrystals is responsible for this transformation. This work provides insights into the mechanism of inorganic deposit formation, as well as opening up a simple, new crystal synthesis route for controlling and directing crystallisation and transformation.

3.1. Introduction

As demonstrated in Chapter 2, the calcium sulfate crystal system plays a significant role in the formation of inorganic piston deposit material. Additionally, control over polymorphism is currently a key motivation in crystal research, whereby conditions are sought to selectively synthesise specific crystalline materials. The discovery of simple, low-energy pathways for the growth of highly desirable and unstable polymorphs with vital industrial and biological applications is particularly important.[1-10] Numerous examples of this high level control over polymorphism have been established for both organic[1-3] and inorganic[4-8] crystal systems. In particular, the calcium carbonate crystal system has been extensively studied.[4-7,9,10] Crystal growth additives such as natural protein-mimics[4,10] and polymers[5-7] are commonly used to achieve the growth of the metastable polymorphs of $CaCO_3$, vaterite and aragonite, at much lower temperatures than otherwise possible. Control of polymorphism for this crystal system is investigated in Chapter 5.

Recent work demonstrates that full control is also achievable for calcium sulfate,[8, 11] a system that has been explored to a much lesser extent. The calcium sulfate system consists of three intriguing crystal structures, with different degrees of hydration,[12-14] as explained in section 1.3.2. These are the most thermodynamically stable phase of calcium sulfate, gypsum ($CaSO_4 \cdot 2H_2O$), the hemihydrate, bassanite ($CaSO_4 \cdot 0.5H_2O$) and the anhydrous form, anhydrite ($CaSO_4$), the latter two of which are relatively thermodynamically unstable and kinetically unfavourable under ambient conditions. However, understanding and controlling the growth of these two unstable hydrates under ambient conditions is of great interest, as they each have important industrial applications (see section 1.3.1). Bassanite (more commonly known as plaster of Paris), is a highly valuable building material, whereas anhydrite has applications as a binder in cements and adhesives.[15]

As explained in section 1.3.2, anhydrite becomes the most thermodynamically stable hydrate at elevated temperatures.[15-22] However, as anhydrite has a much higher surface free energy than gypsum,[22] it grows at an extremely slow rate in comparison to gypsum.[23-25] Thus, anhydrite growth is rarely seen even at temperatures where it is the most thermodynamically stable form of calcium sulfate[16,22,23] (i.e. at 54.5 °C),[19] which is why it is difficult to assign a precise value to this transition temperature. Several

methods have been investigated to reduce the gypsum-anhydrite transition temperature. Decreasing the water activity of the crystal growth solution has been shown to be effective, and this can be achieved by employing salts such as sodium chloride.[15,16,22,23,26] Crystal growth inhibitors have also been shown to favor the formation of anhydrite.[27] Finally, anhydrite seeding is often employed to bias growth towards the metastable hydrates.[16,26] However, for all of these methods, anhydrite growth has still not been accomplished at ambient temperatures, and even at the elevated temperatures employed, it often took days or even weeks for conversion to be realised.

Although there has been little success in establishing moderate conditions for the synthesis of dehydrated calcium sulfate hydrates in aqueous systems, recent work reveals that, through the use of organic solvents, it is possible to precipitate phase-pure bassanite and anhydrite nanoparticles at room temperature, as a consequence of greatly decreasing and controlling the water content of the solvent.[8,11] More broadly, there are several examples where organic solvents have been exploited to study both the mechanisms and kinetics of crystallisation, as well as crystal morphology.[28,29]

In this chapter, a two-phase, non-miscible, liquid-liquid (water-hexane or water-dodecane) system was employed to study calcium sulfate crystallisation, mimicking the environment present during piston deposit formation. The aqueous phase provided a source of SO_4^{2-} in the form of sulfuric acid, representing the sulfuric acids present in the fuel and lubricating oil, and the organic phase contained a Ca^{2+} source in the form of overbased calcium carbonate detergent particles, one of the main additives in engine oil formulations responsible for inorganic deposit formation.[30] Comparison of dodecane and highly volatile hexane as organic solvents in an open system permitted investigation of the effect of solvent evaporation on calcium sulfate crystallisation and transformation. In situ optical microscopy analysis of the aqueous-organic interfacial region during the crystal growth process allowed elucidation of the crystal morphologies and hydrates formed, providing new perspectives on the mechanisms of inorganic deposit formation, as well as the formation of anhydrite, which does not readily grow at room temperature. Our studies reinforce other work that show oil-water interfaces may be used to effectively promote the growth of crystals.[31-34] To the best of our knowledge, this is the first time the gypsum-anhydrite phase transformation has

been observed and microscopically analysed at room temperature, and opens up new ideas and methodology for the formation of unstable hydrates under low-energy conditions.

3.2. Experimental

3.2.1. Crystal Growth Experiments

All aqueous solutions contained 0.5 M H_2SO_4 (Fischer Scientific, $\geq$ 95%) as a sulfate source and were prepared using ultrapure water (Milli-Q Reagent, Millipore) with a typical resistivity of 18.2 MΩ cm at 25 °C. Two organic solvents (VWR) were studied separately: *n*-hexane and *n*-dodecane, which have fast and negligible evaporation rates, respectively. In these, 2 wt. % of an oil-soluble overbased detergent (donated by Lubrizol) was dissolved. This contained a 10 nm 400 total base number (TBN) amorphous calcium carbonate core (0.35 M), surrounded by long-chain alkyl-sulfonate groups, ensuring the calcium source was fully dispersed within the organic phase.

Calcium sulfate crystallisation and transformation was investigated by monitoring crystal growth across an aqueous-organic interface, assembled on 47 mm diameter circular glass slides (Thermo Scientific) that were cleaned thoroughly with ultrapure water, ethanol (VWR, $\geq$ 99.9%), and blown dry using nitrogen gas (BOC). These were fitted into Petri dishes (Willco Wells) equipped with a perspex rim and lid. In each experiment, 2 mL of the organic phase was added and a small aqueous droplet (either 1 or 20 µL) was pipetted underneath, directly onto the glass slide at the centre of the Petri dish.

3.2.2. Analysis of Crystal Morphologies

A Leica DM4000 M optical microscope was used to monitor crystal growth in situ. A range of magnifications were used, depending on the sample area analysed. Crystal growth of the entire interface of a 1 µL droplet was imaged using a 2.5× objective lens, whereas greater magnifications and larger droplets (20 µL) were used to image crystal growth at higher resolution, at a section of the aqueous-organic interface (20×) and within the bulk oil (100×). A series of time-lapse images were taken throughout the crystal growth experiment to provide information on the dynamic processes occurring in each of these areas. At the end of the experiment, interferometry was used to analyse the topography of selected crystals using a Contour GT-I 3D Optical Microscope.

Images were obtained using a 50× objective lens and processed using SPIP (6.0.14, Image Metrology) software.

3.2.3. Analysis of Crystal Hydrates

Crystals selected for interferometry were further analysed using Raman spectroscopy to determine the hydrate. Spectra were obtained using a Renishaw micro-Raman inVia spectrometer. Regions of interest were selected using an optical microscope with a 50× objective lens. The 633 nm line of a HeNe laser was used at 100 % power, with an acquisition time of 30 s for each spectrum. Due to the small laser spot size (515 nm radius), it was possible to resolve and obtain spectra for individual crystals. Spectral calibration was performed using the 520.7 nm peak of a silicon standard, and reference spectra were obtained for natural gypsum (St. Gobain Gyproc), bassanite (formed by heating natural gypsum, cleaved along the [010] plane, dehydrated at 200 °C using a Mettler Toledo DSC1-Star instrument under an inert N_2 atmosphere) and natural anhydrite (UKGE Limited).

Powder X-ray diffraction (XRD) provided further information on the crystals present in each sample. A PANalytical X'Pert Pro X-Ray MPD powder diffractometer equipped with a curved Ge Johnasson monochromator was used, giving focused Cu $K_{\alpha 1}$ radiation (1.540598 Å), with a Pixcel detector. Scans were obtained ranging from 5-60° in 2θ. Crystalline structures were identified using reference patterns from the HighScore Plus software (PANalytical B. V.) and the latest ICDD powder diffraction database.

3.2.4. Karl Fischer Water Content Tests

The water contents of pure hexane and dodecane solvents, as well as bulk solutions of hexane and dodecane containing 0.35 M $CaCO_3$ overbased detergent particles were determined by Karl Fischer volumetric titration. These were conducted at Lubrizol using a Mettler DL 35 titrimeter fitted with a DM 143-SC electrode. Sample masses were determined using a Precisa EP220A balance and Aqualine Titrant 5 (Fischer) was used as a titrant. A reference standard of Analar Distilled Water (ReAgent) was used. All samples tested contained less than 0.5 wt. % water, which corresponds to an internal repeatability value quoted for this setup of ± 0.02 wt. %.

3.2.5. Solvent Evaporation Rates

The evaporation rates of hexane and dodecane were measured by filling the same Petri dishes used for crystal growth experiments with 2 mL of solvent and recording the weight of solvent remaining at minute intervals over a 1 hr period. This procedure was carried out twice for each solvent, and results were averaged to give the percentage solvent weight remaining as a function of time.

3.3. Results and Discussion

3.3.1. Crystal Growth Characteristics in the Aqueous-Dodecane System

The experimental setup used to microscopically monitor crystal growth is shown in Figure 3.1. Images were acquired from above the sample, providing a view of the whole circumference of the aqueous-organic interface when small aqueous droplets (1 μL volume) and low magnifications (2.5$\times$) were used.
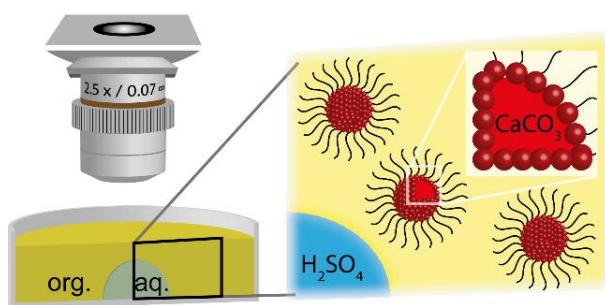
Figure 3.1. Schematic of experimental setup, representing an aqueous H_2SO_4 droplet surrounded by overbased calcium carbonate detergent particles in oil.

Initially, dodecane was employed as the bulk organic phase, which does not evaporate appreciably over the time scale of these studies (see Figure 3.2). As outlined in the experimental section, this solution contained 0.35 M amorphous calcium carbonate (ACC) from the core of overbased calcium carbonate detergent particles, and a droplet containing 0.5 M H_2SO_4.
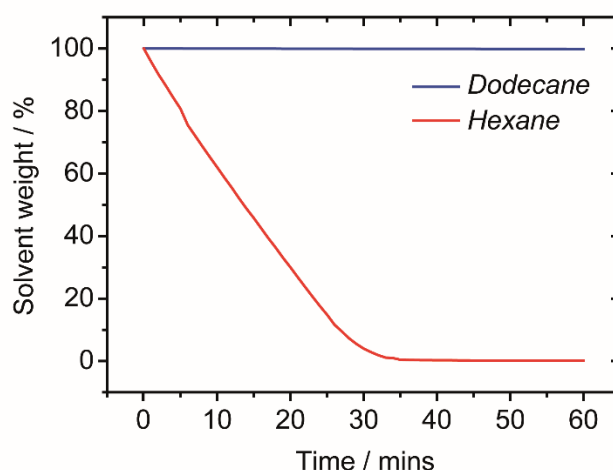
Figure 3.2. Evaporation rates of dodecane and hexane from Petri dishes identical to those used for all crystal growth experiments. Solvent weight recorded every minute for two different samples for each solvent, and results averaged to obtain % solvent weight each minute. These results were obtained under ambient conditions, as for crystal growth experiments.

Due to the immiscibility of aqueous solutions with dodecane, a well-defined interface was established (see Figure 3.3a). Figure 3.3b shows a snapshot of the resulting crystal growth (after 6 hr) for the whole interface (for a full video of this process, see 'video_dodecane_overall.avi' attached with this thesis). The first crystals were detected after approximately three hours, nucleating at the aqueous-organic interface and initially, spreading mainly into the aqueous droplet. This modification evidently led to a decrease of surface tension, with the interface expanding outward and crystal growth progressing in the oil phase. To determine the morphology of these crystals, a higher magnification (20×) was employed to fully resolve crystal growth directly at the interface. This highlighted the presence of needle-shaped crystals (see Figure 3.3.c and 'video_dodecane_interface.avi' attached with this thesis). A representative crystal was imaged at 100× magnification and analysed using interferometry. Figures 3.3d and 3.3e demonstrate that the crystal had a very smooth, featureless surface (on this scale), which was true for all other crystals analysed throughout the sample, as shown in Figure 3.4.
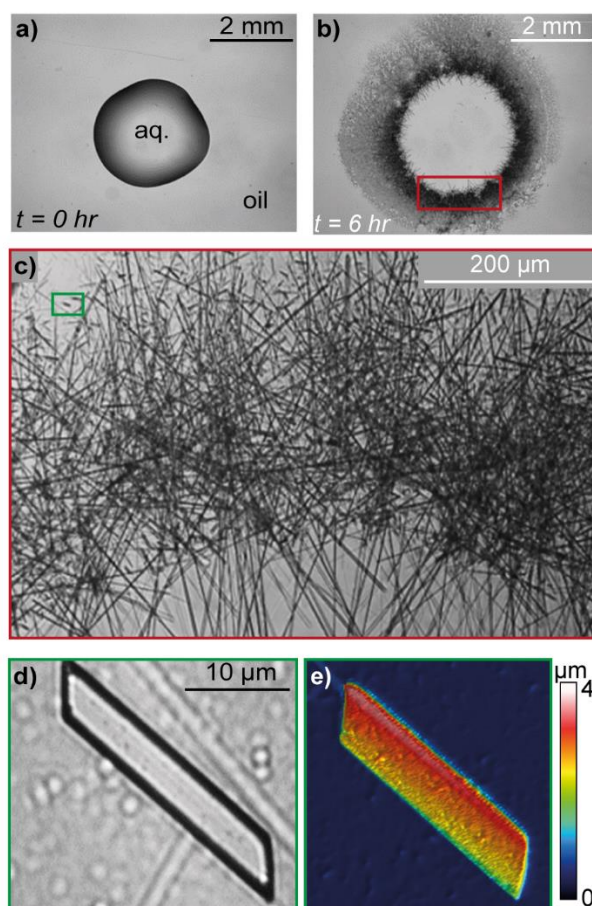
Figure 3.3. Results obtained for a configuration comprising 0.35 M $CaCO_3$ in 2 mL dodecane and a droplet containing 0.5 M H_2SO_4. (a) Optical image of a 1 μL droplet in dodecane, (b) optical image of overall crystal growth for a 1 μL droplet, (c) optical image of crystal growth at the interface of a 20 μL droplet, (d) optical image of a typical needle crystal formed during the experiment and (e) interferometry image of the same crystal.
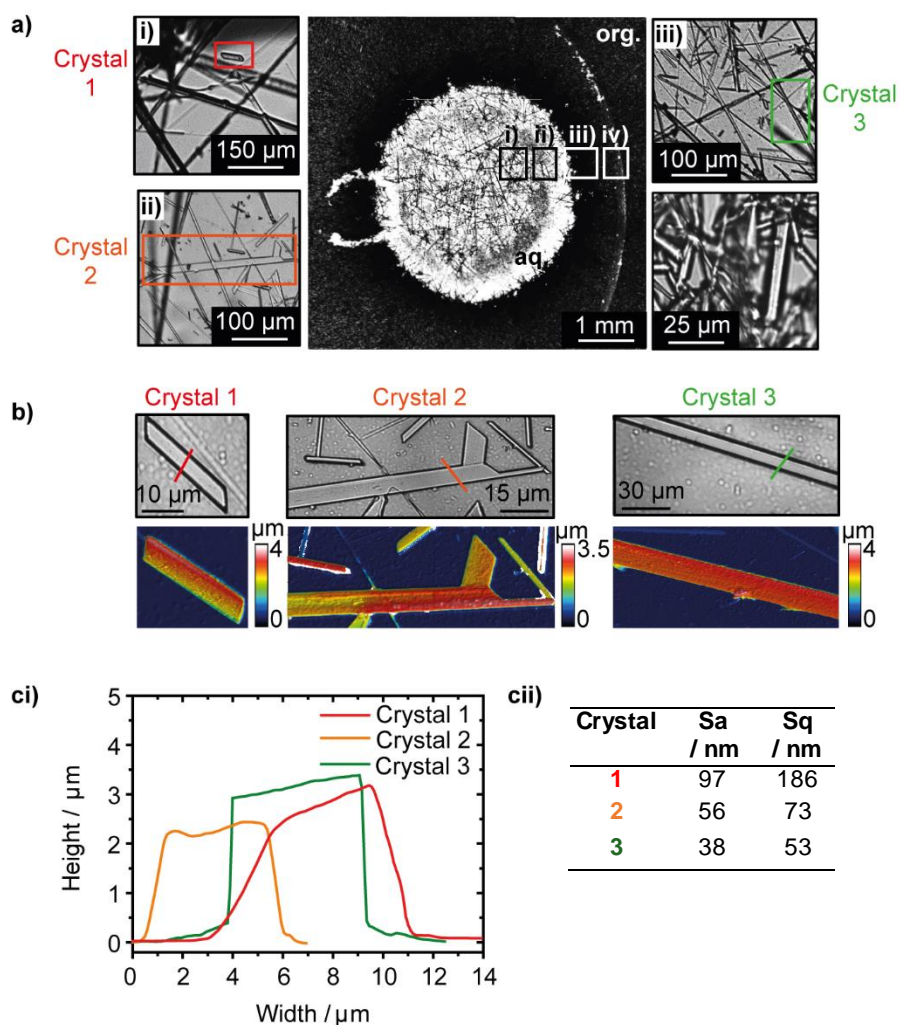
Figure 3.4. (a) Optical images showing a range of crystal morphologies formed from a system comprising 0.35 M CaCO$_3$ overbased detergent in 2 mL dodecane and 20 µL of 0.5 M H$_2$SO$_4$. (b) Optical and interferometry images of the crystals selected in (a). (ci) Height and (cii) roughness data for each crystal, where Sa is the average roughness and Sq is the root mean square roughness over the whole crystal surface. Profile lines selected for height data are marked on the optical images in (b).

The hydrated phase of these needle-shaped crystals was determined using Raman spectroscopy. Due to the small spot size of the laser (515 nm radius; calculated from the laser wavelength and the numerical aperture of the lens),[35] it was possible to obtain Raman spectra corresponding only to the crystal of interest. Figure 3.5a shows that the crystals analysed gave a strong peak centered at 1008 cm^{-1}, which corresponds to the ν_1 SO$_4$ shift for gypsum (CaSO$_4$·2H$_2$O), previously reported at 1008-1010 cm^{-1}.[17,36-38] Due to the higher degree of hydration in the crystal structure, this peak occurs at lower

wavenumbers than for bassanite ($CaSO_4 \cdot 0.5H_2O$), present at 1015-1016 cm^{-1},[17,37,38] and anhydrite ($CaSO_4$), at 1017-1018 cm^{-1}.[17,36-38] This is therefore a definitive way of deducing the calcium sulfate phase grown. To further confirm this finding, Figure 3.5b shows that all crystals analysed had a peak at 3404 cm^{-1}, corresponding to the ν_1 H_2O shift of gypsum (previously reported at 3404-3407 cm^{-1}).[17,38] Again, this is proof that these crystals are the dihydrate phase, as the ν_1 H_2O peak occurs at higher wavenumbers for bassanite, at 3556 cm^1,[17] and is absent for anhydrite. The absence of the ν_3 H_2O gypsum peak (at 3494-3500 cm^{-1})[17,38] in both the reference and sample spectra is most likely due to variations in crystal orientation, or may also indicate the presence of impurities and irregularities within the crystal structure.[38]
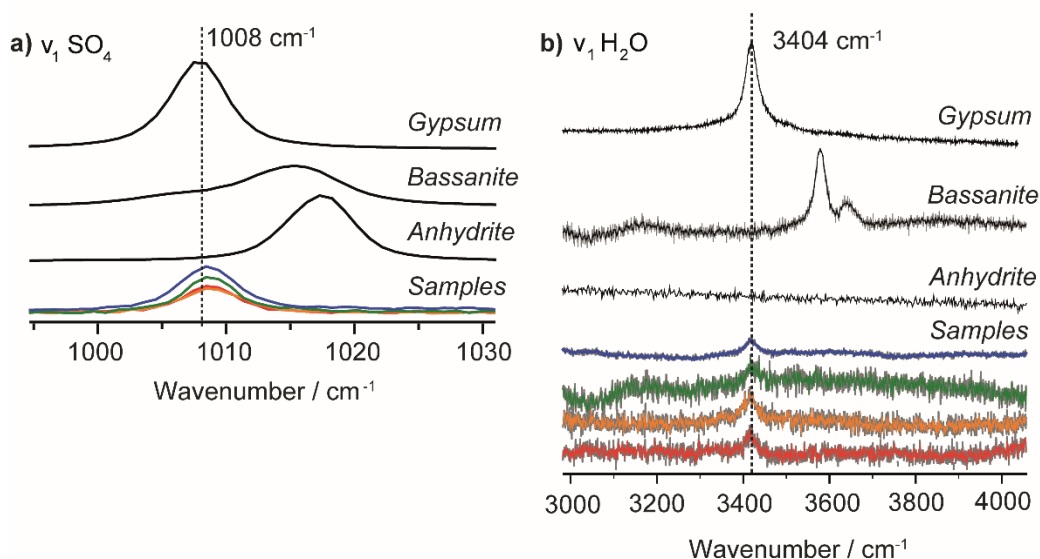
Figure 3.5. Raman reference spectra for gypsum, bassanite and anhydrite, together with spectra (bottom in each case) obtained for a range of samples grown in dodecane.

3.3.2. Mechanism of the ACC-Gypsum Transition

It is clear from these results that the initial ACC core of the overbased detergent in the oil phase reacts with SO_4^{2-} ions from the aqueous droplet to form the dihydrate phase of calcium sulfate, gypsum. It has been shown previously that when overbased calcium carbonate detergent particles are exposed to water, a thin film with a thickness of one or two water molecules forms between the ACC core and the stabilising sulfonate head groups.[39] Thus, for the system employed in our work, it is plausible that the presence of the H_2SO_4 droplet results in the formation of an aqueous SO_4^{2-} layer, in direct contact with the ACC core. To test this idea, Karl Fischer measurements were conducted for

pure hexane and dodecane solvents, as well as bulk solutions of hexane and dodecane containing 0.35 M $CaCO_3$ overbased detergent particles (the same concentrations and volumes as those used in crystal growth experiments). Table 3.1 shows that addition of the overbased detergent particles resulted in a similar increase in the water content of both solvents, implying that these particles already contain a small amount of water.

Table 3.1. Karl Fischer water content values obtained for hexane and dodecane, in the presence and absence of 0.35 M $CaCO_3$ overbased detergent particles (error = ± 0.02 wt. %).

	Water content values / wt. %			
	Hexane		Dodecane	
	Test 1	Test 2	Test 1	Test 2
Solvent only	0.00	0.00	0.00	0.00
$CaCO_3$ particles	0.13	0.13	0.10	0.14

Although the sampling of these solvents was in bulk solution, we expect these results to be representative of the immiscible two-phase system used. Previous analysis of similar interfaces shows the bulk phase has a similar water content to the organic solvent close to the interface. For example, molecular dynamics calculations of the water-1,2-dichloroethane (DCE) interface show this is molecularly sharp, with no substantial region of strong mixing.[40] Neutron reflectivity measurements support this.[41] Synchrotron X-ray reflectivity measurements and predictions from capillary-wave theory give interfacial widths of the water-hexane and water-dodecane interfaces in the range of 3-5 Å.[42] This suggests that the interfaces employed in our crystal growth experiments will be very smooth.

Interestingly, the pseudomorphic replacement of calcite by an epitaxial layer of $CaSO_4$ (either gypsum, bassanite or anhydrite depending on the temperature of the reaction) has recently been reported.[17] This was achieved by part-dissolving millimetre-sized calcite pieces in H_2SO_4. At room temperature, gypsum was the precipitating phase, due to a closer match between the gypsum and calcite structures, compared to the other calcium sulfate hydrates. However, the formation of the gypsum layer passivated the calcite piece, and only a thin surface layer of gypsum was formed.[17] It is likely that an analogous mineral replacement reaction takes place in our system, but the process goes to completion because the parent phase in our system is in the form of

nanoparticles, and a large percentage of the $CaCO_3$ is present at the nanoparticle surface and is thus highly accessible to the surrounding SO_4^{2-}-containing fluid. The hydrated $CaSO_4$ produced is the precursor to the gypsum that grows as needles in the aqueous phase and, ultimately, within the oil phase, due to stabilisation of the nanoparticles by the hydrophobic alkyl sulfonate surfactant.

3.3.3. Crystal Growth Characteristics in the Aqueous-Hexane System

Hexane is much more volatile than dodecane, and therefore evaporates if the system is left open to the atmosphere. This serves to gradually increase the calcium concentration during the course of a crystallisation experiment in a similar way to other crystal growth strategies, such as the Kitano method used to produce calcite.[43] The timescale of evaporation was that a negligible amount of organic solvent remained after 35 min (less than 0.5 wt. % - see Figure 3.2).

Crystal growth of the entire aqueous droplet interface was initially analysed (see Figure 3.6a and 'video_hexane_overall.avi' attached with this thesis). For the first 30 min, and in contrast to the dodecane case, the aqueous droplet appeared highly unstable, which was most likely a consequence of the evaporation of the hexane solvent, causing convection. Crystal growth became apparent after approximately 30 min, when most of the hexane had evaporated, resulting in a very high concentration of the calcium source.

To obtain a more in depth understanding of the processes taking place, images were collected using a $20\times$ objective lens (see Figure 3.6b and 'video_hexane_interface.avi' attached with this thesis). As for the experiments performed in dodecane, although at shorter times, needle growth initially occurred at the aqueous-organic interface, spreading both into and away from the droplet. These needles are likely to form via a similar mechanism as discussed above for dodecane, but in contrast, a higher density of needles formed in hexane, and these were about 10 times shorter than in the dodecane case. This can be rationalised: larger needles are likely to grow in dodecane, due to the presence of an inert solvent surrounding the aqueous droplet, which prevents evaporation and minimises nucleation, in a similar way to the microbatch technique used to grow high quality protein crystals.[31]

A higher objective lens ($100\times$) was used to determine the fate of the needles in the area of the glass surface highlighted in Figure 3.6b, which was previously covered

with the bulk hexane phase, prior to evaporation. Figure 3.6c shows snapshots of transitions apparent within this sample area (for further detail, see 'video_hexane_plates.avi' attached with this thesis). After approximately two and a half hours, the needles produced began to reduce in length. Although the hexane solvent appeared to have fully evaporated by this stage of the experiment, the observation of needle dissolution suggests the presence of a thin interfacial fluid, an aspect that is discussed in more detail below.

After four hours, there was evidence of needles aligning parallel to each other (indicated by the arrows in the first image of Figure 3.6c and the red cross on the resulting crystal assembly). Examining the time shots in Figure 3.6c, precipitation of a new phase occurs, bridging the two parallel needles, which initially accumulates in the centre (see crosses), and expands out along the length of the needles in both directions. This ultimately results in the formation of plate-shaped crystals, displaying a 'V' shape at each end (see second and third image of Figure 3.6c). Concurrently, small needles that did not transform into plates decrease in length and fully dissolve. Again, this dissolution would most reasonably be mediated by a thin interfacial fluid. At this time, very few needles surrounded the plate-like crystals. Over a period of 17 hr, the plate shaped crystals continue to grow, resulting in the 'V' shaped ends of some of these crystals transforming into 'rectangular' morphologies. This is evident in the final image of Figure 3.6c, taken after 21 hr. These transformations are rationalised later.
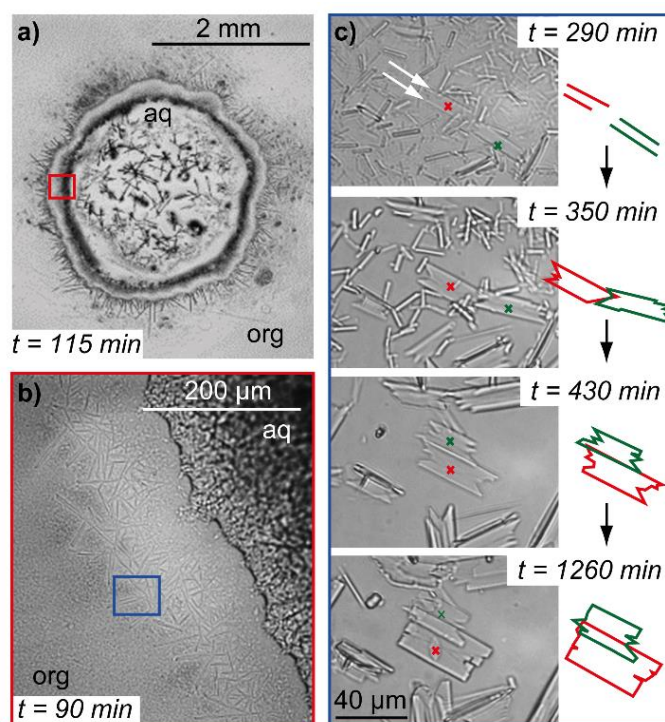
Figure 3.6. Optical images for a configuration comprising 0.35 M $CaCO_3$ in 2 mL hexane and an aqueous droplet containing 0.5 M H_2SO_4. (a) Optical image of a 1 μL droplet in the hexane (organic) phase, showing crystal growth. (b) Optical image of crystal growth near the interface of a 20 μL aqueous droplet. (c) Optical images showing the transformation of needles to plates at various times.

Both interferometry and Raman spectroscopy were used to analyse the crystals in more detail, and to determine whether the different morphologies detected corresponded to different $CaSO_4$ hydrates. Figure 3.7 shows the three main crystal shapes selected, that are representative of the whole sample after all crystal growth had ceased and the hexane had fully evaporated (around 8 hr). These include needles similar to those found in dodecane (crystal 1- Figure 3.7a), plates (crystal 3- Figure 3.7c) and crystals which appear to correspond to a stage between the two (crystal 2- Figure 3.7b). These were obtained from a range of sample areas, as shown in Figure 3.8a (for further examples, see Figure 3.8b). Needles were generally detected near the position of the original aqueous droplet, whereas plates were detected further away from the droplet, in areas of the bulk organic phase, prior to evaporation. Crystals representing an intermediate stage were generally found between these two regions. Although plates were also detected in the centre of the aqueous droplet (e.g. Figure 3.8), these formed over much longer periods (i.e. days rather than hours).

Interferometry measurements showed that the needles formed were relatively smooth, with very few surface features, as for crystallisation in dodecane. In contrast, plates exhibited rougher surfaces. For crystals which represented an intermediate stage, there is evidence that these are comprised of individual needles that have come together, based on the overall crystal morphology (see Figure 3.7bi and bii). In addition, the 'V' shape previously seen in Figure 3.6c is also apparent in some of these intermediate states. The roughness profile for Crystal 2 in Figure 3.8ci shows a clear decrease in crystal height at the centre of the 'V', with higher crystal edges, further confirming that growth is realised through the alignment of two parallel needles, which form the plate edges, with a progressive build-up of material between the two (for further roughness parameters, see Figure 3.8cii).
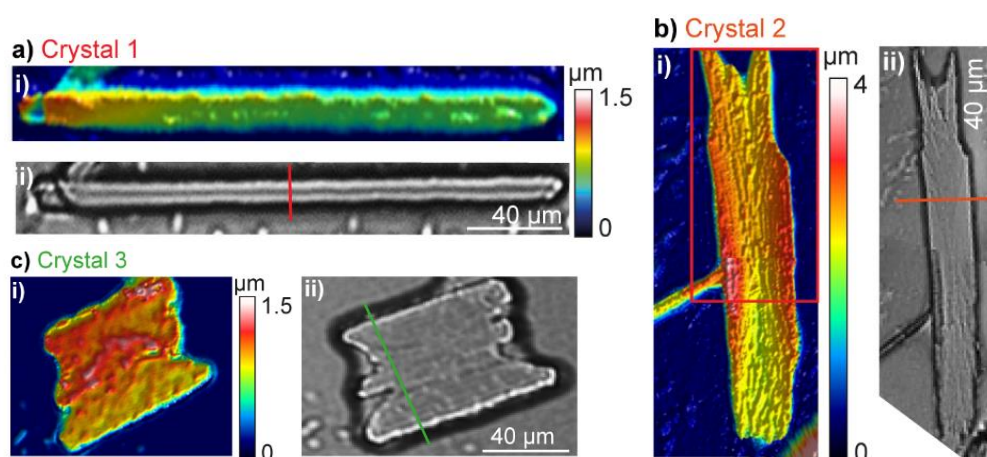
Figure 3.7. Micrographs of crystals from an experiment comprising 0.35 M $CaCO_3$ in 2 mL hexane and a 20 μL aqueous droplet containing 0.5 M H_2SO_4. (ai) Interferometry and (aii) optical images of crystal 1. (bi) Interferometry and (bii) optical images of crystal 2. (ci) Interferometry and (cii) optical images of crystal 3. Coloured lines on optical images correspond to roughness profiles provided in Figure 3.8ci.
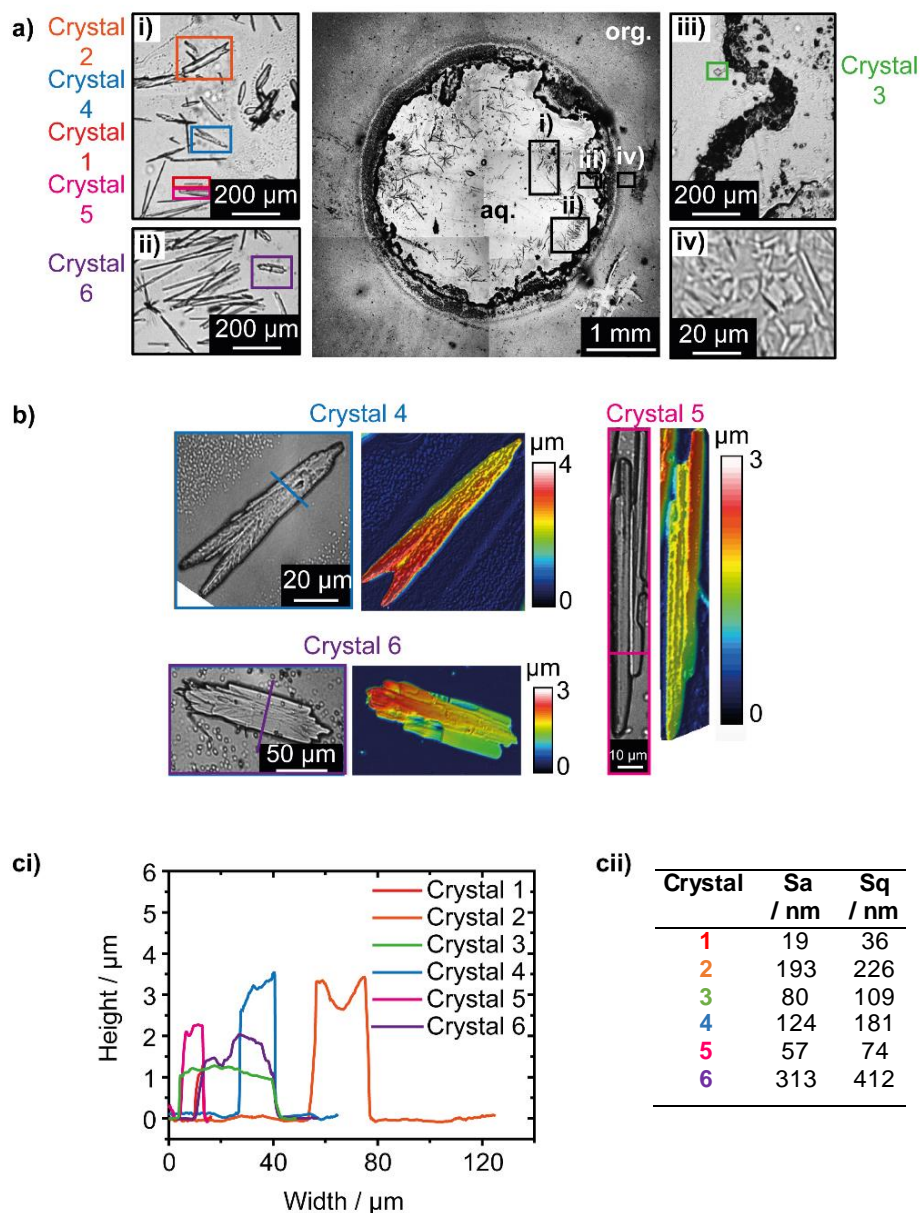
Figure 3.8. (a) Optical images showing a range of crystal morphologies formed from a configuration comprising 0.35 M overbased detergent in 2 mL hexane and 20 µL of aqueous 0.5 M H_2SO_4. (b) Optical and interferometry micrographs of crystals 4-6 in (a) (see Figure 3.7 for optical and interferometry micrographs of crystals 1-3). (ci) Height and (cii) roughness data for each crystal, where Sa is the roughness average and Sq is the root mean square roughness over the whole crystal surface. Profile lines selected for height data are marked on the optical images in (b) and Figure 3.7.

The Raman spectra in Figures 3.9a and b show that the needle-shaped crystal (crystal 1) gives rise to ν_1 SO_4 and ν_1 H_2O shifts corresponding to gypsum. However, both the 'intermediate state' and plate crystals (crystals 2 and 3, respectively) give

spectra that correspond to the fully dehydrated phase, anhydrite, displaying ν_1 SO$_4$ shifts centered around 1017 cm^{-1}, and no peaks within the ν_1 H$_2$O region. Therefore, the needle-to-plate transition previously described corresponds to a gypsum-anhydrite transformation.
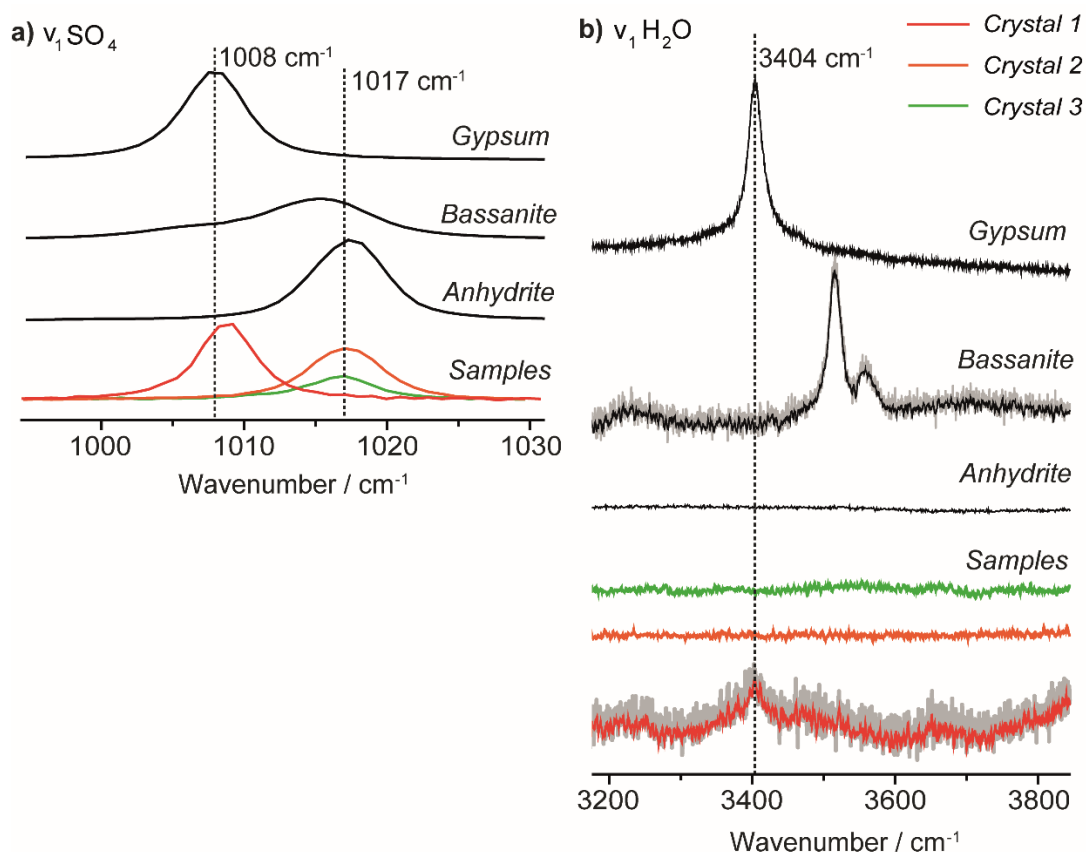
Figure 3.9. Raman reference spectra for gypsum, bassanite and anhydrite, together with spectra for crystals 1, 2 and 3 (samples) grown in hexane.

3.3.4. X-Ray Diffraction Analysis

To support the above analysis, powder X-ray diffraction (XRD) was performed, a technique used to determine the hydrated phase of all the crystalline material present in the whole sample. The results obtained are shown in Figure 3.10, and confirm all the crystals grown in dodecane correspond to gypsum, whereas both gypsum and anhydrite are present in the hexane sample. Furthermore, by comparing the crystallographic parameters for the anhydrite to reference data, it is clear that this corresponds to insoluble anhydrite (see Table 3.2).[44] For full crystallographic characterisation of the gypsum and anhydrite polymorphs grown by the methodology, see Table 3.3.
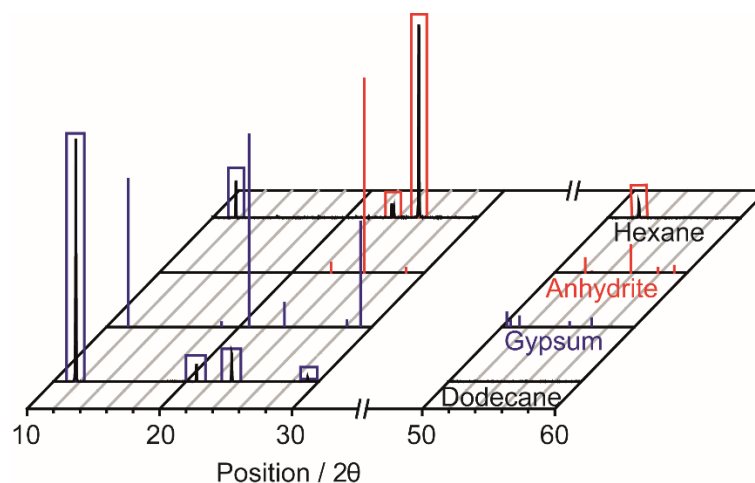
Figure 3.10. Powder XRD patterns for crystal samples produced in a system containing 0.35 M $CaCO_3$ in 2 mL hexane and dodecane and a 20 μL aqueous droplet containing 0.5 M H_2SO_4. Gypsum and anhydrite reference patterns are shown for comparison.

Table 3.2. Crystallographic parameters for the reference pattern identified for the grown anhydrite, compared to reference data for soluble and insoluble anhydrite.

	Anhydrite data[45]	Soluble anhydrite[44]	Insoluble anhydrite[44]
Crystal system	Orthorhombic	Orthorhombic	Orthorhombic
Space group	Cmcm	C222	Amma
Schönflies notation	D_{2h}^{17}	D_2^6	D_{2h}^{17}
a / Å	6.993	6.972	6.998
b / Å	6.241	6.304	6.245
c / Å	7.002	12.078	7.006

Table 3.3. Crystallographic parameters for the reference patterns identified for the gypsum and anhydrite structures formed in the open hexane crystal growth experiment.

Mineral name	Gypsum[46]	Anhydrite[45]
Compound name	Calcium sulfate hydrate	Calcium sulfate
Chemical formula	$CaSO_4 \cdot 2H_2O$	$CaSO_4$
Crystal system	Monoclinic	Orthorhombic
Space group	I2/a	Cmcm
Space group number	15	63
a / Å	5.680	6.993
b / Å	15.100	6.241
c / Å	6.520	7.002
Alpha / °	90.000	90.000
Beta / °	118.383	90.000
Gamma / °	90.000	90.000
Calculated density / g cm^{-3}	2.31	2.96
Volume of cell / 10^6 pm^3	494.59	305.60
Molar volume / cm^3 mol^{-1}	74.4	46.1
Z	4.00	4.00
RIR	1.70	1.76

3.3.5. Mechanism of the Gypsum-Anhydrite Transition

Anhydrite plate growth was only achieved for experiments conducted in hexane, once the bulk organic phase had fully evaporated. In contrast, when non-volatile solvents such as dodecane were used, gypsum needles were the only crystalline phase grown. Indeed, when analogous experiments were conducted in hexane, but with the Petri dish sealed to prevent evaporation, only gypsum needles grew (see Figures 3.11 and 3.12 and 'video_hexane_covered.avi' attached with this thesis), confirming that organic solvent evaporation with a concomitant increase in the concentration of the calcium detergent and enhanced mass transport drives this process.
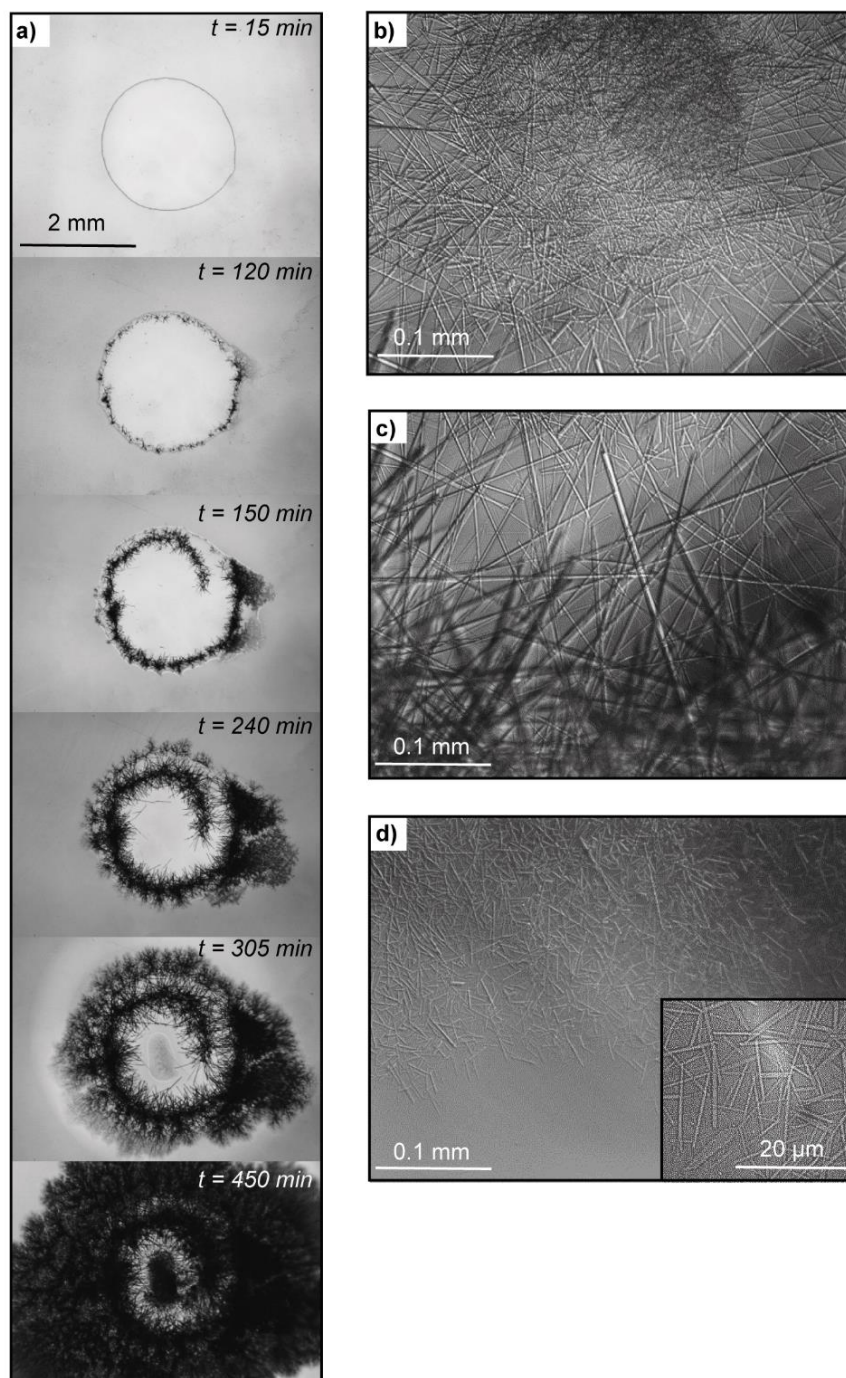
Figure 3.11. Optical images of crystal growth stages for a system comprising 0.35 M overbased detergent in 2 mL hexane and a 1 μL droplet of 0.5 M H_2SO_4. Hexane evaporation was prevented by covering the petri dish with a glass slide and sealing. (a) Images show overall crystal growth as a function of time. (b) Optical image of crystal growth after 24 hr within the centre of the droplet, (c) at the aqueous−organic interface and (d) at the edge of crystal growth within the hexane phase, with the insert, (di) showing an area of (d) at a higher magnification.
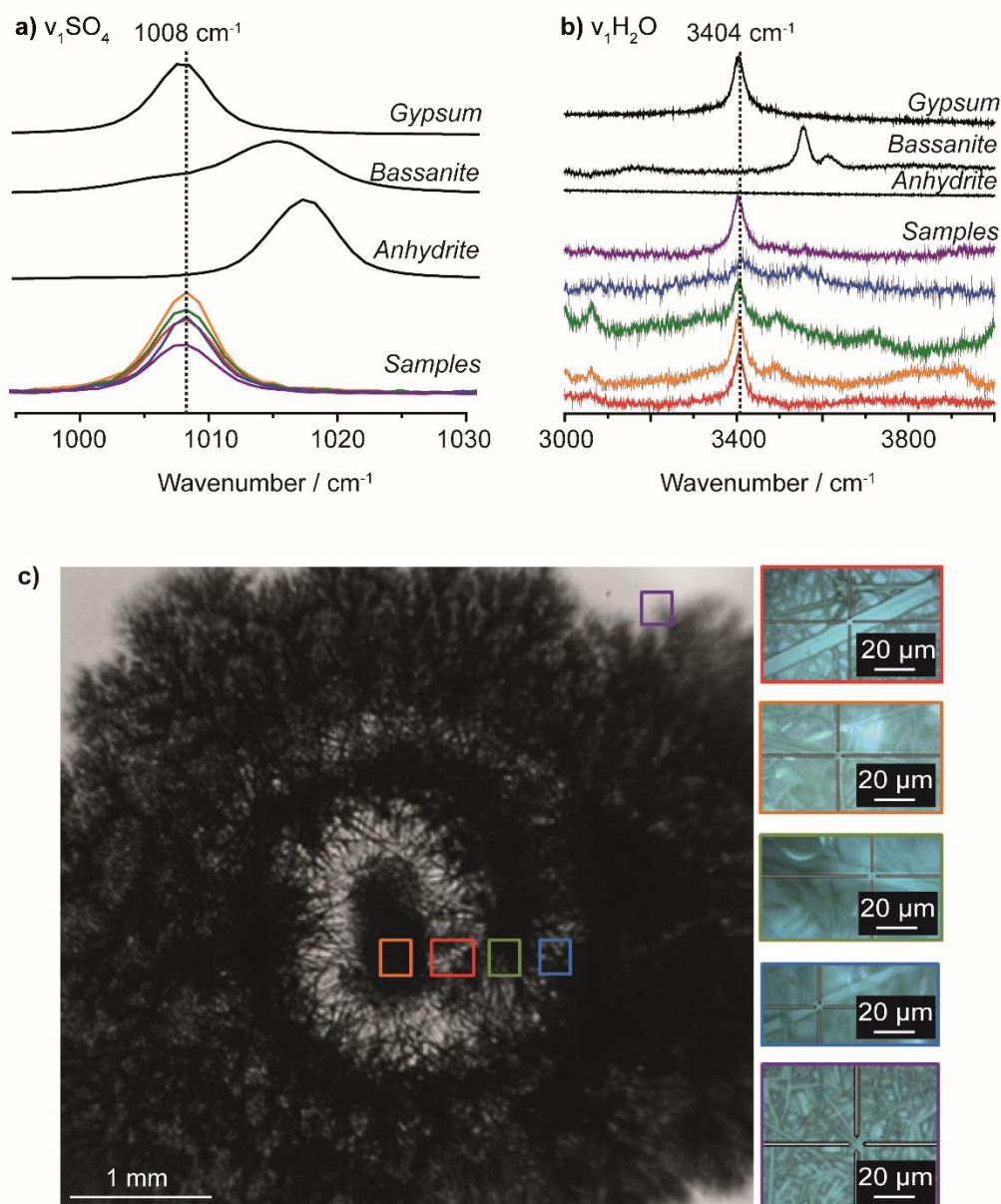
Figure 3.12. Raman spectra obtained for crystals grown in covered hexane experiments. (a) ν_1 SO$_4$ shifts and (b) ν_1 H$_2$O shifts. Crystals corresponding to each Raman spectrum are shown in (c).

There is the possibility of either a solid-state transition in the absence of solvent, or a dissolution-precipitation mechanism within a thin interfacial fluid layer. We consider the latter to be more reasonable. As extremely small volumes of fluid are sufficient for dissolution-precipitation processes, solid-state transformations are not often realised.[47] It has been shown that part-per-million amounts of condensation water,[48] or even seven monolayers of water[49] can induce this process. Both optical and interferometry images, as well as crystal growth videos, provide significant evidence for the dissolution of

gypsum needles, shown through a decrease in their length, as the dissolution flux is higher at the ends of each needle (see Figure 3.13a). This strongly indicates the presence of a thin interfacial layer, which must have some aqueous character, to allow the dissolution of this hydrated phase. This suggestion is reasonable given the existence of thin water films on surfaces subjected to atmospheric conditions, with thicknesses of approximately five monolayers of water.[50] Thus, the conditions in this thin interfacial film, which are largely different to those of bulk aqueous solutions, appear to aid gypsum dissolution and anhydrite precipitation. However, this thin interfacial layer is also likely to contain small residues of hexane solvent, and base oil from the detergent formulation, and thus would have a rather complex structure with a thickness greater than a few monolayers.
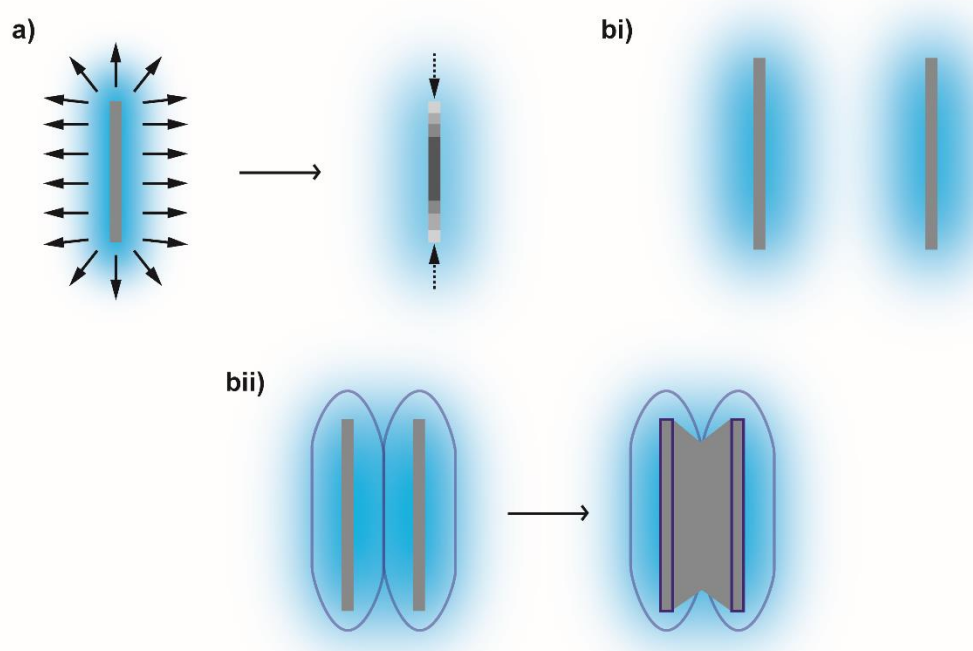
Figure 3.13. (a) Schematic showing the directional fluxes of Ca^{2+} and SO_4^{2-} during the dissolution of the gypsum needles (left), and the consequent direction of dissolution (right). (bi) Schematic showing that when two needles are separated, the diffusional fluxes do not interact significantly, but when in close proximity to each other as in (bii), the diffusional overlap results in the growth of plates with 'V' shaped ends.

As the gypsum needles dissolve, Ca^{2+} and SO_4^{2-} ions are released into the thin aqueous film. $CaSO_4$ micelles are also likely to be within this film, formed from the neutralisation of the overbased $CaCO_3$ detergent particles by H_2SO_4,[51,52] and this

component plays an important role. This was explored by studying the effects of adding hexane and/or detergent particles to a Petri dish containing gypsum seeds. The seeds were grown in the same way as for the dodecane crystal growth experiments, and each sample was rinsed with hexane to remove any excess detergent particles or surfactant. When only hexane was added to the gypsum seeds, no conversion to anhydrite was found at times as long as 48 hr. Similarly, when both hexane and detergent particles were added, no conversion was realised. The gypsum-anhydrite transition was only seen when the H_2SO_4 droplet was also present, suggesting the $CaCO_3$ cores of the overbased detergent must be converted to $CaSO_4$, providing a higher concentration of $CaSO_4$ material in the thin interfacial film.

Recent work demonstrates that by limiting the water content of a solution to 0.2 wt. %, (resulting in a $CaSO_4:H_2O$ ratio of 1:0.5), it is possible for phase-pure anhydrite to precipitate at room temperature. This was achieved by dissolving equimolar amounts of $CaCl_2$ and H_2SO_4 in dry methanol.[8,11] Similarly, we suggest that in our system the high concentration of $CaSO_4$ within a very small volume of solvent would result in a thin interfacial fluid layer with a $CaSO_4:H_2O$ ratio sufficiently high to achieve the critical value for anhydrite precipitation. This idea is also supported by noting that the equilibrium constant for the conversion of gypsum to anhydrite is highly dependent on the temperature and solvent water activity.[15,16,26] Theoretically, if the water activity is lowered to values around 0.77, conversion can take place at temperatures as low as 23 °C.[26]

It is also important to point out that the structure of water in thin interfacial films exhibits very different properties to bulk water. It has been demonstrated that fully hydrogen-bonded, ice-like networks of water molecules form at the surface of amorphous SiO_2,[53] comparable to the glass surfaces used for crystal growth. The structural ordering in these thin interfacial films at the glass surface reduces the hydrogen-bonding ability of these water molecules in comparison to bulk water. This would inhibit the precipitation of the dihydrate $CaSO_4$ phase, gypsum, and favor the formation of the fully dehydrated phase, anhydrite.

Thus, the following are key features of the gypsum-anhydrite transition. When the gypsum needles are far away from each other, they dissolve until they completely disappear (see Figure 3.13bi). However, if these needles align parallel to each other,

there is diffusional overlap of the Ca^{2+} and SO_4^{2-} gradients from the dissolving crystals, leading to a supersaturated region, with respect to anhydrite between the two needles, which is higher in the centre (where the overlap is strongest), leading to anhydrite nucleation and growth (see Figure 3.13bii). With time, the solid anhydrite material grows out towards the needle edges, forming the 'V' shapes seen (e.g. Figure 3.6), with further anhydrite growth causing the 'V' shaped ends to fill in, as shown in the optical images in Figure 3.6c. This transition is not realised in dodecane or covered hexane experiments, as the presence of highly hydrophobic solvents severely hinders gypsum dissolution. This has been confirmed in previous studies, where the use of non-polar solvents hinders the release of; (i) surface water from proteins;[31] and (ii) structural water molecules from gypsum, preventing transformation to the hemihydrate and fully dehydrated phases, bassanite and anhydrite, respectively.[11]

We thus postulate that anhydrite crystal growth is achieved through the conversion of initial gypsum needles. It is well known that primary anhydrite crystal growth is extremely difficult to achieve at moderate temperatures, due to the high kinetic barrier for its formation.[15,17,19,21-23] Therefore, anhydrite nucleation via the formation of gypsum and/or anhydrite seeds is often realised,[16,26,27] and anhydrite crystallisation has been witnessed to occur simultaneously with crystalline gypsum needle dissolution.[27] It is important to point out that, in our system, gypsum needles fully convert to anhydrite. For example, Raman maps for crystal 2 in Figure 3.7b, which exhibits the plate morphology with evidence of 'gypsum needle-like' side walls, confirmed that the whole crystal consisted of anhydrite only. This is evident from Figure 3.14a which shows a map of the intensity of the ν_1 SO_4 shift for anhydrite (at 1017 cm^{-1}), which has high intensity over the whole of the crystal shape. The stronger intensity of the anhydrite peaks at the crystal edges compared to the centre is due to the crystal being higher in these regions. This results in different anhydrite peak intensities across the crystal surface, correlating to the crystal height. A similar map was obtained at 1008 cm^{-1} (the ν_1 SO_4 shift for gypsum), showing no peaks, suggesting that all of the original gypsum needles have been fully converted to anhydrite. To support this, Raman spectra acquired at both the crystal edges and the centre are shown in Figure 3.14b.
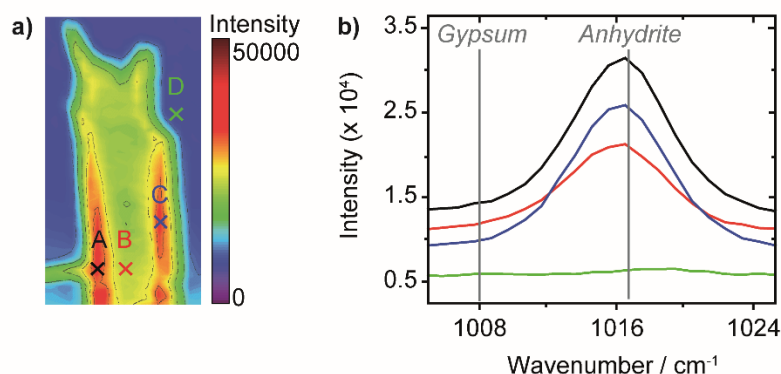
Figure 3.14. (a) Raman map obtained at 1017 cm^{-1} for crystal 2 in Figure 3.7b. (b) Raman spectra obtained at positions A (black), B (red), and C (blue), all showing peaks with varying intensities for the anhydrite v_1 SO$_4$ shift (at 1017 cm^{-1}), and no clear peaks for the gypsum v_1 SO$_4$ shift (at 1008 cm^{-1}). Position D (green) shows a background spectrum.

It has also been suggested that the excess free surfactant in overbased CaCO$_3$ detergent formulations is able to stabilise H$_2$SO$_4$ as microemulsion droplets when used as an acid neutralisation additive in internal combustion engines.[54] To examine whether the presence of free surfactant was important, experiments were also conducted using an overbased calcium carbonate detergent with a much higher free surfactant concentration. This detergent is stabilised by alkyl-phenate groups rather than sulfonate groups. Phenate detergents are also used as additives in engine oil formulations in a similar way to sulfonate detergents. For comparative analysis, a concentration was used that contained the same total base number as for the sulfonate detergent used in experiments throughout this chapter. The crystal growth characteristics were analogous to those seen for the sulfonate detergent, with growth of both gypsum and anhydrite occurring in hexane (see Figure 3.15 and 'video_phenate_overall.avi' attached with this thesis). This suggests that the higher amount of free surfactant in the phenate detergent does not have a significant effect on the crystal growth process, and thus the free surfactant molecules do not play a significant role in controlling the gypsum-anhydrite transition.
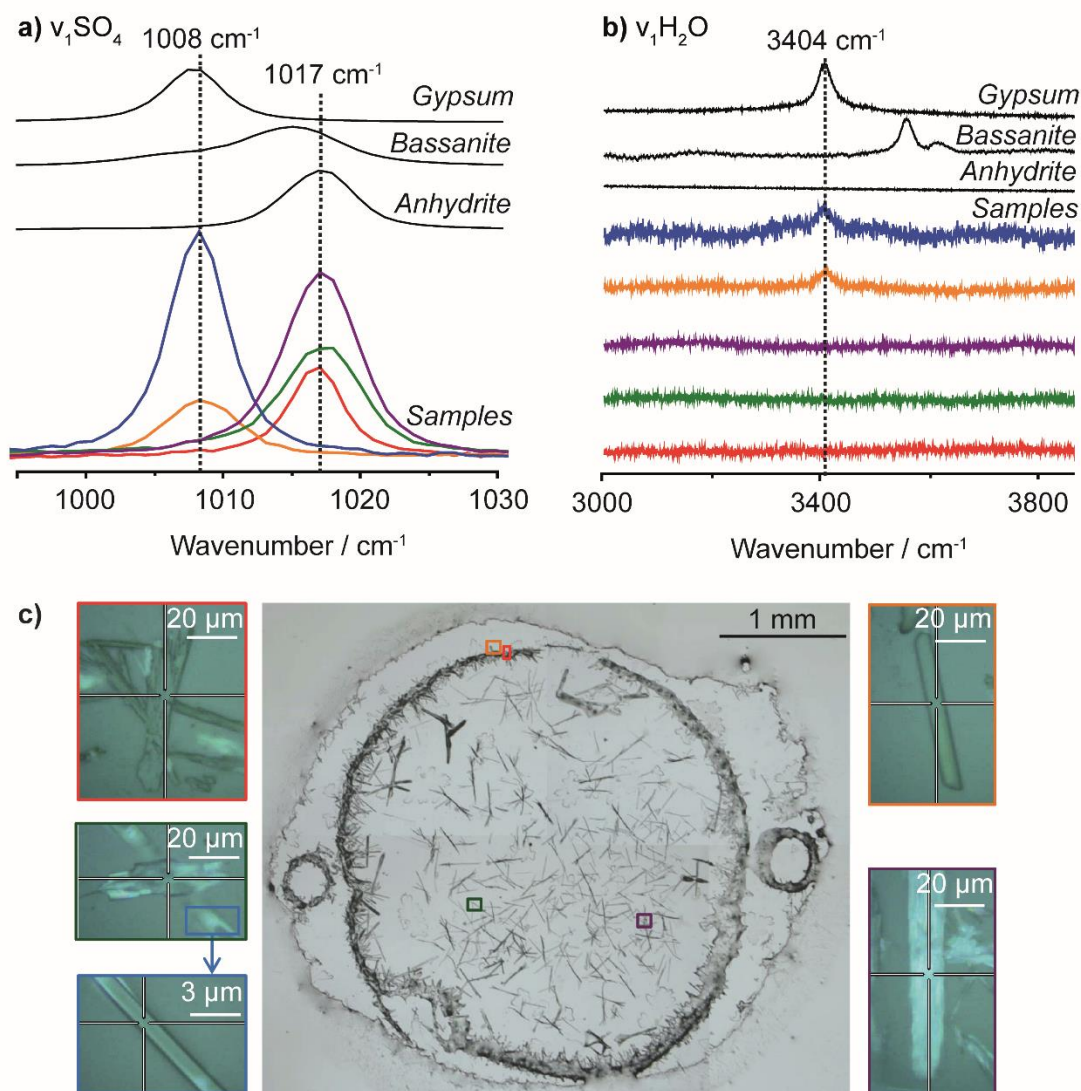
Figure 3.15. Raman spectra obtained for crystals grown in experiments using a detergent with a higher free surfactant concentration. (a) v_1 SO_4 shifts and (b) v_1 H_2O shifts. Crystals corresponding to each Raman spectrum are shown in (c).

Finally, it is worth considering whether gypsum directly converts to anhydrite, as suggested by the lack of bassanite detected from both Raman and XRD data, or whether bassanite is formed as a metastable phase, which may have been overlooked, as phase determinations were not carried out in situ. For aqueous systems, direct dehydration from gypsum to anhydrite is most often realised,[16,21,26] whereas for solid-state transitions occurring above 100 °C, stepwise dehydration is favored.[55-57] For solid-state transitions, the direct removal of all the water molecules from gypsum to form insoluble anhydrite would be unlikely, due to large differences in the two crystal structures. Likewise, the solid-state transformation of gypsum to the hemihydrate, bassanite, and

then insoluble anhydrite, would also be difficult. This is because bassanite has a 'tunneled' crystal structure consisting of water channels, and further water removal to form insoluble anhydrite, with its close packed array structure with no channels would require a high amount of structural rearrangement.[55] This requires temperatures greater than 360 °C.[57] It is therefore extremely unlikely that this structure formed through solid-state transformations at room temperature, further reinforcing the dissolution-precipitation mechanism observed in our system.

Although these experiments were conducted at room temperature, due to the high temperatures found within the piston ring belt zone (up to 350 °C)[58.59] volatilisation of organic compounds may result in the formation of dehydrated calcium sulfate polymorphs in an analogous way to the experiments performed in hexane. We suggest that within the engine, a combination of direct dehydration due to the high temperatures present here, as well as the above mechanism occur to form a combination of the hemihydrate, bassanite and the fully dehydrated polymorph, anhydrite, respectively. The former is likely to result in bassanite formation, as the direct dehydration of bassanite to insoluble anhydrite requires temperatures greater than those found in the engine. The latter explains how stable (insoluble) anhydrite is able to form in this environment, despite engine oil and piston surface temperatures (250-300 and 250-350 °C, respectively)[58,59] being slightly lower than the insoluble anhydrite transition temperature (360 °C).[57] This addresses the questions raised at the end of Chapter 2.

3.4. Conclusions

The transformation of gypsum to anhydrite has been successfully achieved at room temperature, using a two-phase aqueous-organic system. Using in situ optical microscopy and a range of structure-sensitive characterisation techniques, we have been able to identify some of the key steps in the process. The new findings should be useful in constructing design rules to control crystallisation and transformation in other crystal systems, for example, for calcium phosphates, which exhibit a variety of polymorphs that have various degrees of hydration.[15] These studies also provide insight into the formation of inorganic piston deposits, deducing for the first time the mechanisms through which a combination of the calcium sulfate polymorphs anhydrite and bassanite are formed.

Our work has highlighted how simple, time-lapse light microscopy techniques can be used to identify important features of dissolution-precipitation mechanisms that lead to the transformation of gypsum to anhydrite, and that these features can then be confirmed through the application of a range of high-resolution microscopy and spectroscopic methods. The close alignment of gypsum microcrystals is an essential part of the process, with dissolution leading to favourable conditions to promote anhydrite crystallisation in the region between the crystals. This highlights the significance of directional fluxes in crystallisation and transformations that could be of importance in other systems.

3.5. Bibliography

(1)   Mitchell, C. A.; Yu, L.; Ward, M. D. *J. Am. Chem. Soc.* **2001**, *123*, 10830-10839.

(2)   Lang, M.; Grzesiak, A. L.; Matzger, A. J. *J. Am. Chem. Soc.* **2002**, *124*, 14834-14835.

(3)   Hiremath, R.; Basile, J. A.; Varney, S. W.; Swift, J. A. *J. Am. Chem. Soc.* **2005**, *127*, 18321-18327.

(4)   Belcher, A. M.; Wu, X. H.; Christensen, R. J.; Hansma, P. K.; Stucky, G. D.; Morse, D. E. *Nature* **1996**, *381*, 56-58.

(5)   Naka, K.; Keum, D.-K.; Tanaka, Y.; Chujo, Y. *Chem. Commun.* **2000**, 1537-1538.

(6)   Kotachi, A.; Miura, T.; Imai, H. *Cryst. Growth Des.* **2006**, *6*, 1636-1641.

(7)   Xu, A.-W.; Dong, W.-F.; Antonietti, M.; Cölfen, H. *Adv. Funct. Mater.* **2008**, *18*, 1307-1313.

(8)   Tritschler, U.; Van Driessche, A. E. S.; Kempter, A.; Kellermeier, M.; Cölfen, H. *Angew. Chem. Int. Ed.* **2015**, *54*, 4083-4086.

(9)   Nielsen, M. H.; Li, D.; Zhang, H.; Aloni, S.; Han, T. Y.; Frandsen, C.; Seto, J.; Banfield, J. F.; Cölfen, H.; De Yoreo, J. J. *Microsc. Microanal.* **2014**, *20*, 425-436.

(10)   Chen, C.-L.; Qi, J.; Tao, J.; Zuckermann, R. N.; De Yoreo, J. J. *Sci. Rep* **2014**, *4*, 6222.

(11)   Tritschler, U.; Kellermeier, M.; Debus, C.; Kempter, A.; Cölfen, H. *CrystEngComm* **2015**, *17*, 3772-3776.

(12)   Herbstein, F. H. *Cryst. Growth. Des.* **2004**, *4*, 1419-1429.

(13)   Bernstein, J. *Cryst. Growth. Des.* **2011**, *11*, 632-650.

(14)   Seddon, K. R. *Cryst. Growth Des.* **2004**, *4*, 1087.

(15)   Freyer, D.; Voigt, W. *Monatsh. Chem.* **2003**, *134*, 693-719.

(16)   Azimi, G.; Papangelakis, V. G. *Hydrometallurgy* **2011**, *108*, 122-129.

(17)   Ruiz-Agudo, E.; Putnis, C. V.; Hövelmann, J.; Álvarez-Lloret, P.; Ibáñez-Velasco, A.; Putnis, A. *Geochim. Cosmochim. Acta* **2015**, *156*, 75-93.

(18)   Furby, E.; Glueckauf, E.; McDonald, L. A. *Desalination* **1968**, *4*, 264-276.

(19)   Otálora, F.; Garcia-Ruiz, J. M. *Chem. Soc. Rev.* **2014**, *43*, 2013-2026.

(20)   Serafeimidis, K.; Anagnostou, G. *Rock. Mech. Rock. Eng.* **2015**, *48*, 15-31.

(21) Fu, H.; Guan, B.; Jiang, G.; Yates, M. Z.; Wu, Z. *Cryst. Growth Des.* **2012**, *12*, 1388-1394.

(22) Ossorio, M.; Van Driessche, A. E. S.; Pérez, P.; García-Ruiz, J. M. *Chem. Geol.* **2014**, *386*, 16-21.

(23) Ostroff, A. G. *Geochim. Cosmochim. Acta* **1964**, *28*, 1363-1372.

(24) Kashchiev, D., *Nucleation: Basic Theory with Applications*; Eds.; Butterworth-Heinemann: Oxford, 1999.

(25) De Yoreo, J.J.; Velikov, P. G., *Principles of crystal nucleation and growth*. In *Reviews in Minerology and Geochemistry* in *Biomineralisation*; Dove, P. M., De Yoreo, J. J., Weiner, S., Eds.; Mineralogical Society of America: Virginia, 2003; Vol. 54, pp 57-93.

(26) Hardie, L. A. *Am. Mineral.* **1967**, *52*, 171-200.

(27) Cody, R. D. F.; Hull, A. B., *Method of growth of primary anhydrite crystals under moderate conditions*. U.S. Patent 4,337,238, June 29, 1982.

(28) Camacho D. M.; Roberts, K. J.; Lewtas, K.; More, I. *J. Cryst. Growth* **2015**, *416*, 47-56.

(29) Camacho Corzo, D. M.; Borissova, A.; Hammond, R. B.; Kashchiev, D.; Roberts, K. J.; Lewtas, K.; More, I. *CrystEngComm* **2014**, *16*, 974-991.

(30) Smith, G. C.; Hopwood, A. B.; Titchener, K. J. *Surf. Interface Anal.* **2002**, *33*, 259-268.

(31) Silver, B. R.; Fülop, V.; Unwin, P. R. *New J. Chem.* **2011**, *35*, 602-606.

(32) Reddy, S.; Rautaray, D.; Sainkar, S. R.; Sastry, M. *Bull. Mater. Sci.* **2003**, *26*, 283-288.

(33) Rautaray, D.; Banpurkar, A.; Sainkar, R.; Limaye, A. V.; Ogale, S. B.; Sastry, M. *Cryst. Growth. Des.* **2003**, *3*, 449-452.

(34) Allen, K.; Davey, R. J.; Ferrari, E.; Towler, C.; Tiddy, G. J. *Cryst. Growth. Des.* **2002**, *2*, 523-527.

(35) Renishaw, *inVia Raman microscope objective lens options*, Product note from the Spectroscopy Products Division, December 2006.

(36) Buzgar, N.; Buzatu, A.; Sanislav, I. V. *An. Stiint. U. Al. I-Mat* **2009**, *55*, 5-23.

(37) Liu, Y.; Wang. A.; Freeman, J. J., *Raman, MIR, and NIR spectroscopic study of calcium sulfates: gypsum, bassanite, and anhydrite,* 40th Lunar and Planetary Science Conference, Houston, Texas, 2009.

(38) White, S. N. *Chem. Geol.* **2009**, *259*, 240-252.

(39)   Tavacoli, J. W.; Dowding, P. J.; Steytler, D. C.; Barnes, D. J.; Routh A. F. *Langmuir* **2008**, *24*, 3807-3813.

(40)   Benjamin, I. *J. Chem. Phys.* **1992**, *97*, 1432-1445.

(41)   Strutwolf, J.; Barker, A. L.; Gonsalves, M.; Caruana, D. J.; Unwin, P. R.; Williams, D. E.; Webster, J. R. P. *J. Electroanal. Chem* **2000**, *483*, 163-173.

(42)   Mitrinović, D. M.; Tikhonov, A. M.; Li, M.; Huang, Z.; Schlossman, M. L. *Phys. Rev. Lett.* **2000**, *85*, 582-585.

(43)   Dobson, P. S.; Bindley, L. A.; Macpherson, J. V.; Unwin, P. R. *Langmuir* **2005**, *21*, 1255-1260.

(44)   Christensen, A. N.; Olesen, M.; Cerenius, Y.; Jensen, T. R. *Chem. Mater.* **2008**, *20*, 2124-2132.

(45)   McMurdie, H. F.; Morris, M. C.; Evans, E. H.; Paretzkin, B.; Wong, N. W.; Hubbard, C. R. *Powder Diffr.* **1986**, *1*, 265-275.

(46)   Atoji, M.; Rundle, R. *J. Chem. Phys.* **1958**, *29*, 1306-1311.

(47)   Ruiz-Agudo, E.; Putnis, C. V.; Putnis, A. *Chem. Geol.* **2014**, *383*, 132-146.

(48)   Milke, R.; Neusser, G.; Kolzer, K.; Wunder, B. *Geology* **2013**, *41*, 247-250.

(49)   Ruiz-Agudo, E.; Kudlacz, E.; Putnis, C. V.; Putnis, A.; Rodriguez-Navarro, C. *Environ. Sci. Technol.* **2013**, *47*, 11342-11349.

(50)   Verdaguer, A.; Sacha, G. M.; Bluhm, H.; Salmeron, M. *Chem. Rev.* **2006**, *106*, 1478-1510.

(51)   Wu, R. C.; Papadopoulos, K. D.; Campbell, C. B. *AIChE J.* **2000**, *46*, 1471-1477.

(52)   Wu, R. C.; Papadopoulos, K. D.; Campbell, C. B. *AIChE J.* **1999**, *45*, 2011-2017.

(53)   Asay, D. B.; Kim, S. H. *J. Phys. Chem. B.* **2005**, *109*, 16760-16763.

(54)   Galsworthy, J.R.; Robinson, B. H.; Glyde, R. W.; Hone, D. C., *Colloidal Chemistry of Lubricating Oils*. In *Reactions and Synthesis in Surfactant Systems;* Texter, J., Eds.; CRC Press: New York, 2001; Vol. 100, pp 387-388.

(55)   Abriel, W.; Reisdorf, K. *J. Solid State Chem.* **1990**, *85*, 23-30.

(56)   Hudson-Lamb, D. L.; Strydom, C. A.; Potgieter, J. H. *Thermochim. Acta* **1996**, *282-283*, 483-492.

(57)   Prassad, P. S. R.; Pradhan, A.; Gowd, T. N. *Curr. Sci.* **2001**, *80*, 1203-1207.

(58)   Chen, C. I.; Hsu, S. M. *Tribol. Lett.* **2003**, *14*, 83-90.

(59)   Papke, B. L.; Dahlstrom, P. L.; Kreuz, K. L. *Lub. Eng.* **1989**, *45*, 575-585.

Chapter 4: The use of Chemical Force Microscopy for Understanding Dispersant-Deposit Interactions

Parts of this chapter have been published or submitted for publication as detailed below:

Ravenhill, E. R.; Kirkman, P. M.; Unwin, P. R., The use of Atomic Force Microscopy for Investigating Surface Forces at Calcium Sulfate Anhydrite Crystals in Organic Solvents, *article finalised and under review with Lubrizol.*

Chen, C.-H.; Ravenhill, E. R.; Momotenko, D.; Kim, Y.-R.; Lai, S. C. S.; Unwin, P. R., Impact of Surface Chemistry on Nanoparticle-Electrode Interactions in the Electrochemical Detection of Nanoparticle Collisions, *Langmuir* **2015**, *31*, 11932.

Abstract

To prevent inorganic deposit formation on piston surfaces, dispersants are added to lubricating oils to suspend deposits. As calcium sulfate is the main inorganic deposit component, interaction forces between an anhydrite single crystal surface and a range of dispersant-functionalised colloidal atomic force microscopy (AFM) probes are investigated. The gold-coated probes are modified with both polar (hydrophilic) and aromatic (hydrophobic) self-assembled monolayers (SAMs) using thiol molecules, to determine which dispersant head groups are best suited to this application. Measurements are conducted in an organic solvent (hexane) to deduce the relative strengths of these interactions in an environment similar to that in the engine. As demonstrated by the results obtained, the solvent plays a crucial role in the interaction force. Short range repulsive interactions are detected between polar probes and the anhydrite crystal surface, attributed to electrostatic repulsion between the negatively-charged anhydrite crystal face and adsorbed anions at the polar probe surface. In contrast, weak adhesive forces occur between aromatic colloidal probes and the anhydrite crystal surface. The lack of repulsion in the latter case is a consequence of the lack of ion adsorption at these hydrophobic probe surfaces. These results not only provide an insight into the mechanisms of deposit prevention within an internal combustion engine, but also further develop our understanding of the structure of charge in organic solvents, a topic still widely under debate.

4.1. Introduction

As demonstrated in Chapter 2, anhydrite, the fully dehydrated form of calcium sulfate, is one of the main components of inorganic piston deposits. To prevent this material from forming on the piston surface where it can cause the piston rings to stick, wear and break, resulting in reduced engine power and high piston wear,[1,2] dispersants are added to the lubricating oil to keep deposits suspended within it.[3] Although the structures of the organic components present within these deposits are well-known,[1,4-6] very little is known on the structure of the inorganic content, and therefore the dispersant chemistries which bind most strongly to this. Thus, to determine which dispersant chemistries will be most effective at preventing inorganic piston deposit formation, the interaction forces between these head groups and a model calcium sulfate inorganic deposit surface must be studied within an oil-based environment.

Additionally, calcium sulfate is the most common sulfate mineral found in nature, predominantly present in two forms; gypsum ($CaSO_4 \cdot 2H_2O$) and anhydrite ($CaSO_4$).[7] However, despite the abundance of calcium sulfate in evaporitic deposits[7] and low temperature hydrothermal settings,[8,9] and its vital role in industrial processes, including oil recovery from carbonate reservoirs[10-12] and CO_2 sequestration,[9,13] relatively few studies have considered the physiochemical properties of anhydrite. Anhydrite also has several other applications, for example, as a binder in cements and adhesives.[7] On the other hand, in certain industrial settings, anhydrite growth is unwanted, being implicated in scale formation in pipes and reaction vessels.[14,15] It is therefore essential to understand the mechanisms governing the physiochemical behaviour of anhydrite. Although some studies have investigated anhydrite properties for aqueous environments,[7-12,14,15] very little is currently known about the behaviour of this mineral in organic environments, which, given its role in oil recovery,[10-12] is of considerable importance. More specifically, surface forces which are of importance in understanding the stability of and interactions of the solids with their environments are studied much less in non-polar solvents than polar ones.

Atomic force microscopy (AFM) has been previously employed to study interaction forces between various inorganic mineral surfaces and chemical functionalities of both fundamental and industrial interest.[16-20] This technique is highly

sensitive to a wide range of adhesive and repulsive tip-sample forces,[21-25] with force sensitivity on the piconewton scale.[26] Measuring the amount of force felt by the AFM cantilever as the tip approaches and retracts from the sample surface (or vice versa) yields force-distance plots, from which quantitative adhesion force values can be calculated with a high amount of accuracy. Within the scope of the studies herein, single gypsum crystals with specific orientations have been mounted onto AFM cantilevers to determine the interaction forces which influence the mechanisms of plaster hardening in air and solution.[16,17] Additionally, the recovery of fertiliser and cement raw materials by flotation collectors have been investigated by measuring interaction forces between calcium dioleate colloidal probes and calcite and fluorite mineral surface substrates.[18,19] Finally, the nature of the forces between superplasticisers and cleaved calcite and mica surfaces (minerals both commonly found in building materials) have been studied using AFM force measurements, to further understand the role of these dispersing polyelectrolytes in producing high performance concrete.[20]

Little work has been done to investigate interaction forces for anhydrite surfaces, particularly within an oil-based environment, despite the significant practical applications highlighted above. Therefore, in this chapter, we implement the anhydrite single crystals prepared in Chapter 3 as model inorganic deposit substrates for AFM force measurements, to determine interaction forces between these and a wide range of chemically functionalised colloidal AFM probes, which represent different dispersant head group chemistries. Although anhydrite is abundant in nature, its growth is relatively thermodynamically unstable and kinetically unfavourable under ambient conditions, often requiring temperatures greater than 70 °C.[15,27,28] This either results in the growth of thin anhydrite needles,[15] which are impractical for use as surfaces for AFM force measurements, or plates containing a mixture of gypsum and anhydrite.[28] Thus, the preparation of a pure, single anhydrite crystal surface suitable for use as a substrate in AFM force measurements is non-trivial. However, as demonstrated in Chapter 3, we were able to utilise aqueous-organic interfaces, mimicking conditions present in the engine to successfully grow anhydrite single crystals of a plate morphology, with dimensions large enough to use for AFM force experiments.[29] Using these model inorganic deposit surfaces, we successfully investigate interaction forces between anhydrite and a range of chemically

functionalised AFM probes, applying the colloidal probe technique introduced by Butt and Ducker et al.[21,24] By coating these probes with a layer of gold, self-assembled monolayer (SAM) chemistries are used to expose both hydrophilic and hydrophobic dispersant head groups at the tip surface, as previously described by Lieber et al.[30,31] As well as providing a wealth of information on the interactions between inorganic deposits and different dispersant chemistries within an oil-based environment, our studies provide further insights into the nature of charged surfaces in organic solvents, an area which is still under considerable debate. Additionally, these studies highlight the huge impact the solvent environment has on adhesive and repulsive tip-sample interactions in AFM force measurements.

4.2. Experimental

4.2.1. Chemicals

Potassium ferricyanide (Sigma-Aldrich, $\geq$ 99%), potassium chloride (Sigma-Aldrich, $\geq$ 99%), 11-mercapto-1-undecanol (Sigma-Aldrich, $\geq$ 97%), ethanol (VWR, $\geq$ 99.9%), n-hexane (VWR, $\geq$ 98%), 1,2-dichloroethane (Sigma-Aldrich, $\geq$ 99%), tetrabutylammonium hexafluorophosphate (Sigma-Aldrich, $\geq$ 99%) and H_2SO_4 (Fischer Scientific, $\geq$ 95%) were all used as received. All aqueous solutions were prepared using ultrapure water (Milli-Q Reagent, Millipore) with a typical resistivity of 18.2 MΩ cm at 25 °C. The four thiol compounds used for SAM formation and the oil-soluble overbased detergent used for anhydrite crystal growth were donated by Lubrizol.

4.2.2. Dispersant-Functionalised Colloidal Probe Fabrication

The basic experimental setup is summarised in Figure 4.1. AFM tips (Bruker, SNL-10) with triangular, Si_3N_4 cantilevers (length: 205 μm, width: 40 μm, spring constant: 0.12 Nm^{-1}) were modified to produce colloidal probes in the following way. Borosilicate microspheres (Duke Scientific Corporation, Cat. No. 9015) of ca. 14.0 $\pm$ 1.0 μm diameter were placed on a small offcut of a clean Si/SiO_2 wafer (IDB Technologies Ltd., n-type Si, thickness: 525 μm). Using two micropositioners (NewFocus, 9064-XYZ-M) and an optical microscope (Olympus BH2-UMA), these were transferred and glued to the free tip end of the cantilever using a 2.8:1 ratio of epoxy resin (Robnor Resins, RX771C/NC) to aradur hardener (Robnor Resins, HY1300B) and left to dry for at least 48 hr.

A 2.5 nm Cr adhesion layer, followed by a 40 nm Au layer were then deposited on the colloidal probes using a thermal electron-beam evaporator (Moorfield MiniLab 060 Platform) under high vacuum (< 1 x 10^{-6} mbar), at rates of 0.04 and 1 Ås^{-1} for Cr and Au, respectively. The Au-coated probes were then cleaned using a plasma asher (Quorum Technologies, K1050X) in oxygen plasma for 30 seconds (100 W RF power), and immediately immersed in an ethanol solution containing 1 mM of the SAM of interest for at least 24 hr at room temperature. A schematic of the resulting configuration is shown in Figure 4.1c. A range of polar and aromatic thiol molecules terminated with four different dispersant head groups were used to form the SAMs, denoted as C_4H_8OH, $CHCH_2(COOH)_2$, $PhNO_2$, and CH_2Ph (see Figure 4.2a for full structures). These were supplied by Lubrizol. For comparison, 11-mercapto-1-undecanol was also used as a model SAM-forming compound. Finally, the probes were thoroughly rinsed with ethanol to remove any excess thiol, blown dry using nitrogen gas (BOC) and used immediately for force measurements to avoid contamination.

Scanning electron microscopy (SEM) images of the probes (see Figure 4.1a) were obtained using a Zeiss Supra 55-VP field emission gun SEM in secondary electron (SE2) mode, at an acceleration voltage of 10 kV.

4.2.3. Cyclic Voltammetry Measurements for Self-Assembled Monolayer Electrodes

To test the quality of the SAMs formed, cyclic voltammetry (CV) experiments were conducted on bare Au and Au/SAM electrode surfaces. These were prepared by depositing a 2.5 nm Cr adhesion layer, followed by a 40 nm Au layer on Si/SiO_2 wafers (IDB Technologies Ltd., n-type Si, thickness: 525 μm), using a thermal electronic-beam evaporator, as described above. The Au-coated Si/SiO_2 wafers were then cut into ca. 1 cm^2 pieces, and immersed in an ethanol solution containing 1 mM of the SAM of interest for at least 24 hr. These samples were thoroughly rinsed with ethanol to remove any excess thiol, blown dry using nitrogen gas (BOC) and used immediately for force measurements to avoid contamination.

CVs were recorded in a conventional three electrode setup, using a CH Instruments potentiostat (CHI-730a). A small droplet (ca. 5 μL) containing 1 mM K_3FeCN_6 and 0.1 M KCl was placed on the Au/SAM working electrode surface. An

AgCl-coated Ag wire and Pt wire were used as the quasi-reference and counter electrodes, respectively.

4.2.4. Model Inorganic Deposit Substrate Preparation

Anhydrite crystals were grown as described previously.[29] Briefly, a 20 μL droplet of 0.5 M H_2SO_4 was pipetted underneath 2 mL of a hexane solution containing 2 wt. % oil-soluble overbased detergent with a 10 nm 400 total base number (TBN) amorphous calcium carbonate core (0.35 M), surrounded by long-chain alkyl-sulfonate groups. A PANalytical X'Pert Pro X-Ray MPD powder diffractometer was used to determine the calcium sulfate polymorphs grown, equipped with a curved Ge Johnasson monochromator giving focussed Cu $K_{\alpha 1}$ radiation (1.540598 Å), with a Pixcel detector. Scans were obtained ranging from 5-60° in 2θ. Crystalline structures were identified using reference patterns from the HighScore Plus software (PANalytical B. V.) and the latest ICDD powder diffraction database. This confirmed the presence of both gypsum needles and anhydrite plates.

Raman spectra were obtained using a Renishaw micro-Raman inVia spectrometer, to confirm the crystals selected for use as AFM force experiment substrates correspond to the fully dehydrated anhydrite polymorph. A HeNe laser (633 nm) was used at 100 % power, with spectra for individual crystals attainable using an optical microscope with a 50× objective lens to locate these, and due to the small laser spot size (515 nm radius). Spectra were calibrated using the 520.7 nm peak of a silicon standard. Reference spectra for natural gypsum (St. Gobain Gyproc), bassanite (formed by heating natural gypsum, cleaved along the [010] plane, dehydrated at 200 °C using a Mettler Toledo DSC1-Star instrument under an inert N_2 atmosphere) and natural anhydrite (UKGE Limited) were used to determine the calcium sulfate polymorph of each crystal. Acquisition times of 30 s were used in all cases.

Interferometry measurements (Contour GT-I 3D Optical Microscope) provided information on the roughness of the anhydrite crystals selected. A 50× lens was used and images were processed using SPIP software (6.0.14, Image Metrology). The area of the Petri dish containing the selected crystals was cut out, rinsed with hexane to remove any excess detergent or free surfactant from the crystal surfaces and attached to a magnetic disk, ready for use in the AFM.

4.2.5. AFM Force Measurements in an Organic Solvent

Force measurements between the functionalised AFM colloidal probes and the anhydrite crystal surface were performed as previously described,[21] using a Veeco Multimode V AFM with NanoScope V controller electronics. The probes were carefully positioned directly above the crystal of interest, as shown in Figure 4.1b. All measurements were conducted in hexane at room temperature, which was slowly injected into a small flow cell (Bruker, MTFML), using a glass syringe. This setup comprised a Viton O-ring, creating a seal between the flow cell and sample surface, thus preventing solvent evaporation. This was left to equilibrate for ca. 20 min prior to force measurements. The anhydrite sample surface attached to the magnetic disk was placed on the scanner piezo tube (PicoForce scanner, Bruker) to which a voltage was applied, causing the sample to approach towards and retract away from the tip (at a frequency of 1 Hz). For all measurements, a trigger threshold of 15 nN and a ramp size of 1 μm were used. Simultaneously, the deflection of the tip cantilever due to tip-sample interactions was measured by shining a laser onto the back of the cantilever, which was reflected on a photodiode. The tip deflection was recorded as a function of piezo displacement, with a resolution of 512 data points per curve.

Force vs. piezo displacement curves were plotted by converting the cantilever deflection to force, using the measured spring constants for each probe, (obtained from the thermal tune method in the NanoScope 7.30 software (Veeco)) and deflection sensitivity (obtained from the slope of the linear compliance region (contact part) of the force curve on a hard, non-deformable surface).[25] Butt et al[25] have suggested that the start of the linear compliance region corresponds to the initial tip-surface contact. However, in the presence of repulsion, this is difficult to determine, so they assigned this by extrapolating the two linear regimes of the force curves. These methods have been used throughout to assign the initial tip-surface contact. Due to some inhomogeneity associated with crystal surfaces, 200 force curves were obtained at each point in five different sample areas, for each probe. Adhesion values extracted from these measurements were plotted in histograms and normalised to the colloidal probe radius. The mean and standard deviations of the adhesion force for each tip were calculated.

4.2.6. Cyclic Voltammetry Measurements in an Organic Solvent

To investigate the presence of charge in organic solvents, CVs were obtained at the opening of quartz nanopipettes in 1,2-dichloroethane (DCE), using a scanning ion conductance microscopy (SICM)-based setup.[32] Pipettes with diameters of ca. 50 nm were pulled from quartz capillaries (1.0 mm o.d., 0.5 mm i.d., Friedrich and Dimmock, Millville, NJ) using a laser puller (P-2000, Sutter Instruments, USA). The following pulling settings were used: Line 1- Heat: 750, Fil: 4, Vel: 30, Del: 150, Pul: 80, Line 2- Heat: 650, Fil: 3, Vel: 40, Del: 135, Pul: 150. Pipettes were filled with an electrolyte solution containing 1 mM $TBAPF_6$ in DCE, and placed in a Petri dish containing the same solution. Ag wire quasi-reference counter electrodes (QRCEs) were placed in both the pipette and the bulk solution. A bias was applied to the bulk QRCE and the current at the pipette opening was measured.

4.2.7. AFM Force Measurements in an Aqueous Environment

Force measurements were performed using a Veeco Multimode V AFM with NanoScope V controller electronics. All measurements were conducted in an aqueous solution containing 1 mM $K_4Fe(CN)_6$ and 0.4 mM sodium citrate at room temperature, which was slowly injected into a small flow cell (Bruker, MTFML), using a glass syringe. This was left to equilibrate for ca. 20 min prior to force measurements. AFM tips (Bruker, SNL-10) with triangular, Si_3N_4 cantilevers (length: 205 μm, width: 40 μm, spring constant: 0.12 Nm^{-1}) were modified by depositing a 2.5 nm Cr adhesion layer, followed by a 60 nm Au layer on the tips using a thermal electron-beam evaporator (Moorfield MiniLab 060 Platform) under high vacuum (< 1 x 10^{-6} mbar), at rates of 0.04 and 1 $Ås^{-1}$ for Cr and Au, respectively. This resulted in tips with a 60 nm radius of curvature. The Au-coated probes were then immersed in 1 mM sodium citrate solution for at least 12 hr to adsorb citrate ions onto the gold surface, following a literature method.[33]

Au/SAM electrodes were prepared by depositing a 2 nm Cr adhesion layer, followed by a 40 nm Au layer on Si/SiO_2 wafers (IDB Technologies Ltd., n-type Si, thickness: 525 μm), using a thermal electronic-beam evaporator, as described above. The Au-coated Si/SiO_2 wafers were then cut into ca. 1 cm^2 pieces, and immersed in an ethanol solution containing 2 mM of the SAM of interest for at least 24 hr. Three different alkanethiol molecules were used to form SAMs; 11-mercapto-1-undecanol (MUD), 11-mercaptoundecanoic acid (MUA) and dodecanethiol (DDT). These

surfaces were thoroughly rinsed with ethanol to remove any excess thiol, blown dry using nitrogen gas (BOC) and used immediately for force measurements to avoid contamination. To determine the quality of these monolayers, CVs were recorded as outlined in section 4.2.3.

These Au/SAM electrode surfaces were attached to magnetic disks and placed on the scanner piezo tube (PicoForce scanner, Bruker) to which a voltage was applied, causing the sample to approach towards and retract away from the tip (at a frequency of 1 Hz). Simultaneously, the deflection of the tip cantilever due to tip-sample interactions was measured by shining a laser onto the back of the cantilever, which was reflected on a photodiode, recorded as a function of piezo displacement. From this, force vs. piezo displacement curves were plotted by converting the cantilever deflection to force, using the measured spring constants for each probe, (obtained from the thermal tune method in the NanoScope 7.30 software (Veeco)), and deflection sensitivity (obtained from the slope of the linear compliance region (contact part) of the force curve on a hard, non-deformable surface).[25] The start of the linear compliance region, corresponding to the initial tip-surface contact was assigned using the methods proposed by Butt et al.[25] Over 200 force curves were obtained at each point at multiple sample areas for each Au/SAM surface, to account for any inhomogeneity in the surface functionalisation. Adhesion values extracted from these measurements were calculated and plotted in histograms.

Force measurements were conducted under potential-control utilising a two-electrode system using a CH Instruments potentiostat (due to the negligible background currents at the potentials used). The working electrode was the Au/SAM electrode, and an Ag/AgCl wire (50 μm in diameter) was placed in the inlet channel of the cell to serve as a QRCE. A constant potential of 400 mV was applied to the working electrode.

4.3. Results and Discussion

4.3.1. Fabrication and Characterisation of the Dispersant-Functionalised Colloidal Probes

The experimental setup used for determining interaction forces between the model deposit anhydrite crystal surface and a range of functionalised colloidal probes representing different dispersant head group chemistries is shown in Figure 4.1. The effect of an organic solvent environment on the interaction force was investigated by utilising a small flow cell filled with hexane for all experiments, to mimic the solvent environment present within the engine. As outlined in the experimental section, colloidal AFM probes were fabricated by attaching micron-sized borosilicate spheres to the end of commercial AFM tips (see Figure 4.1a). This method is commonly employed to increase the tip surface area exposed to the substrate surface, and thus the sensitivity of the force measurement.[21,24] This allows highly organised, closely packed monolayers to form at the colloidal probe surface with a high degree of structural order, due to the strong Au-S bond formed between the gold surface and thiol, and the stabilising van der Waals interactions between neighbouring CH_2 groups in the hydrophobic chain of the thiol molecule.[34-36]
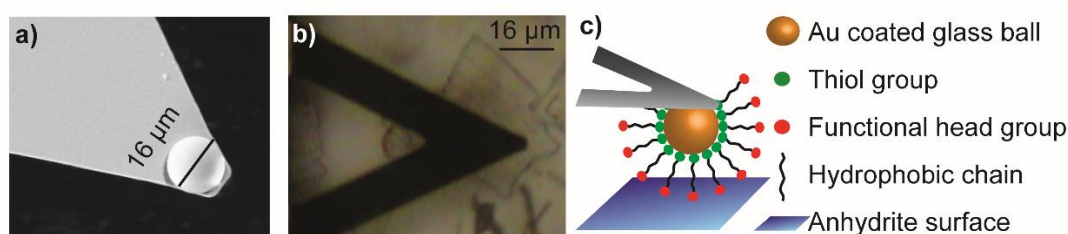
Figure 4.1. Experimental setup. (a) SEM image of an AFM tip functionalised with a glass microsphere. (b) Optical image showing an example of how the AFM tip was positioned over crystal surface. (c) Schematic of experimental setup showing the grown anhydrite single crystal surface and AFM tip, functionalised with a gold-coated glass microsphere, modified with SAMs. Force-displacement curves were obtained as the colloidal probe came towards and into contact with the crystal surface.

As mentioned in the experimental section, each Au-coated colloidal probe was immersed in 1 mM of thiol solution for at least 24 hr to ensure the best quality film, due to the slow reorganisation process of the thiol molecules.[34] As shown in Figure 4.2a, four different common dispersant head group chemistries were considered, two

polar, hydrophilic groups (denoted as C_4H_8OH and $CHCH_2(COOH)_2$) and two aromatic, hydrophobic groups (denoted as $PhNO_2$ and CH_2Ph). In addition, 11-mercapto-1-undecanol ($HSCH_2(CH_2)_9CH_2OH$- denoted as MUD) was used as a reference, as high quality, well-characterised SAMs have been previously formed from this model thiol compound.[37] The SAMs formed from these thiol molecules are accurate models of dispersant compounds, which contain long hydrocarbon chains to keep the dispersant (and deposit) suspended within the lubricating oil (similar to the hydrocarbon chains of the thiol molecules), a polar head group to bind to the deposit surface (similar to the terminal head groups present in the thiol molecules), and a linker group to attach these two together (analogous to the bulky linker group incorporated into the synthesised thiol structures, as shown in Figure 4.2a).
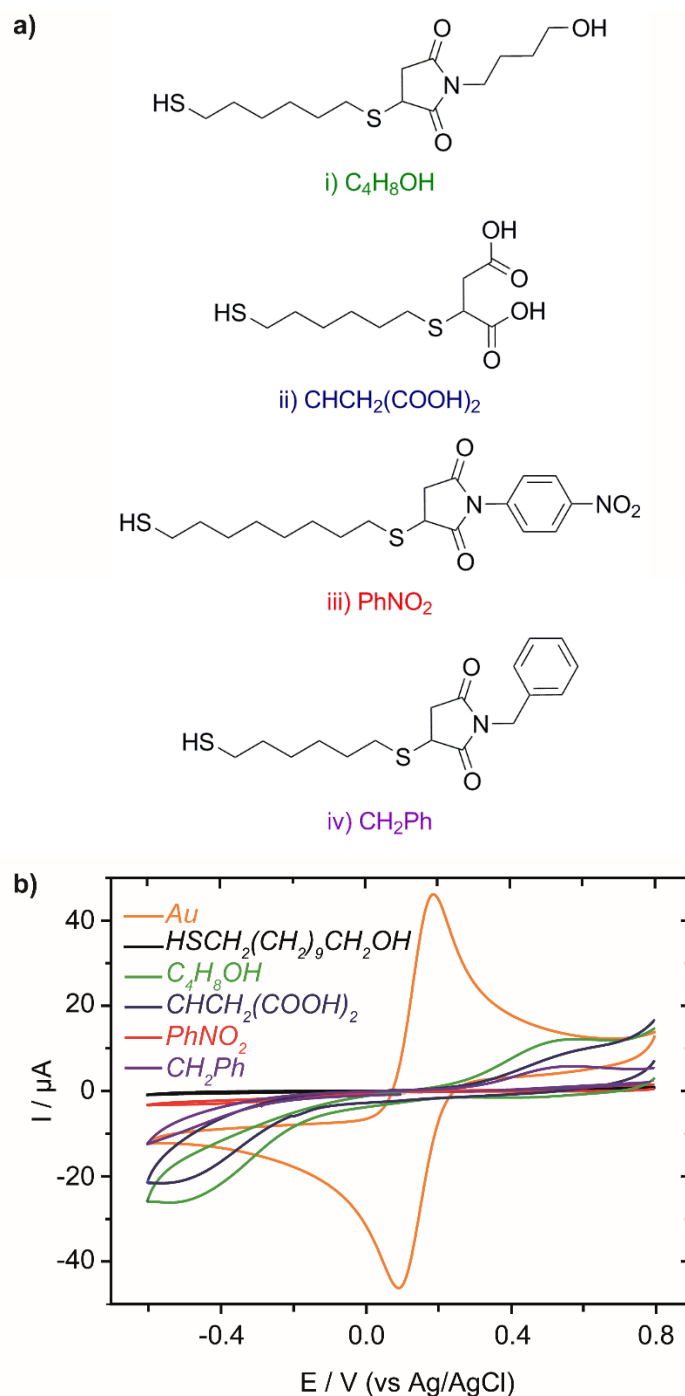
Figure 4.2. (a) Thiol molecules from which the SAMs used for tip functionalisation were formed. These are referred to throughout by the assignments given below for each chemical structure. (b) CVs obtained on a bare Au electrode (orange line), a model 11-mercapto-1-undecanol Au/SAM electrode (black line) and Au/SAM electrodes formed from the thiol molecules in (a) (other coloured lines). Electrolyte solution: 5 μL droplet containing 1 mM $K_3Fe(CN)_6$ and 0.1 M KCl, scan rate: 0.1 V s^{-1}, initial and final E: 0 V, high E: + 0.8 V, low E: – 0.5 V, scan direction: negative.

Alongside tip modification, the quality of the SAMs formed from these thiol molecules (synthesised by Lubrizol) was determined, as these have not been used to form SAMs before. Planar Au/SAM electrode surfaces (ca. 1 cm^2) were prepared as outlined in the experimental section. The redox behaviour of a small droplet of 1 mM K$_3$Fe(CN)$_6$ in 0.1 M KCl was investigated at each surface and compared to that at a bare Au electrode. CVs for the reduction of Fe(CN)$_6^{3-}$ (forward sweep) and reoxidation (reverse sweep) were recorded in a 3-electrode mode, with the (modified) gold as the working electrode at a scan rate of 0.1 V s^{-1}. At the bare Au electrode (see Figure 4.2b), a reversible redox response was obtained (orange curve, peak-to-peak separation of 60 mV). However, for the Au/SAM surfaces, the presence of the SAM blocked the redox response to variable extents, with the extent of blocking manifested as an increased peak-to-peak separation, reflecting slower (more inhibited) electron transfer kinetics.[38] The electrochemical activity decreased in the order Au/C$_4$H$_8$OH > Au/CHCH$_2$(COOH)$_2$ > Au/CH$_2$Ph > Au/PhNO$_2$ > Au/MUD. This trend is unlikely to be a consequence of electrostatic forces between the terminal group and the redox species, because if that were the case, the Au/MUD and Au/C$_4$H$_8$OH electrodes (both terminated with OH groups) would be expected to give similar responses. This is therefore more likely to be due to the lower quality of the SAMs formed from the synthesised thiol molecules, due to the presence of the additional bulky 'linker group' between the terminal group and hydrocarbon chain, added to represent the linker groups present in dispersant compounds resulting from the synthetic step of attaching the polar head group to the long hydrocarbon tail. In addition, the shorter alkyl chain length between this linker group and the thiol group may also contribute to the lower SAM quality. It is well-known that the electron transfer rate for SAM electrode surfaces decreases as the number of CH$_2$ groups increases.[38] The model MUD compound contains an 11-carbon atom chain, whereas the PhNO$_2$ thiol has 8 carbon atoms between the linker and the thiol group, and the CH$_2$Ph, CHCH$_2$(COOH)$_2$ and C$_4$H$_8$OH thiol molecules have 6. Therefore, as the Au/PhNO$_2$ and Au/MUD electrodes block the current to greater extents than the other SAM electrodes, the trends observed in blocking are as expected. However, there is a dramatic decrease in current for all the Au/SAM electrodes compared to the bare Au surface, suggesting that overall, each SAM is well-formed, with few defects,[37,39,40] and thus of high enough quality for use in AFM force measurements.

4.3.2. Fabrication and Characterisation of the Model Deposit Anhydrite Crystal Surfaces used for AFM Force Measurements

The fully dehydrated, model deposit anhydrite ($CaSO_4$) single crystal surfaces used for force measurements were successfully synthesised at room temperature, using a non-miscible aqueous-organic interface,[29] as described in Chapter 3. Figure 4.3 provides interferometry roughness data for a typical anhydrite crystal used as the substrate for experiments. Crystals were grown of a sufficient size to ensure the colloidal AFM probes interacted only with the crystal surface (see Figure 4.1b). An example of the roughness profile along the crystal in Figure 4.3a is plotted in Figure 4.3b. The inset shows a zoomed-in part of this profile over 2 μm, which is approximately 10 times larger than the actual contact area diameter of the AFM probe (calculated to be ca. 200 nm for the $CHCH_2(COOH)_2$ probe on the anhydrite surface using the Johnson-Kendall-Roberts (JKR) contact theory,[41] as previously used for similar systems).[42]
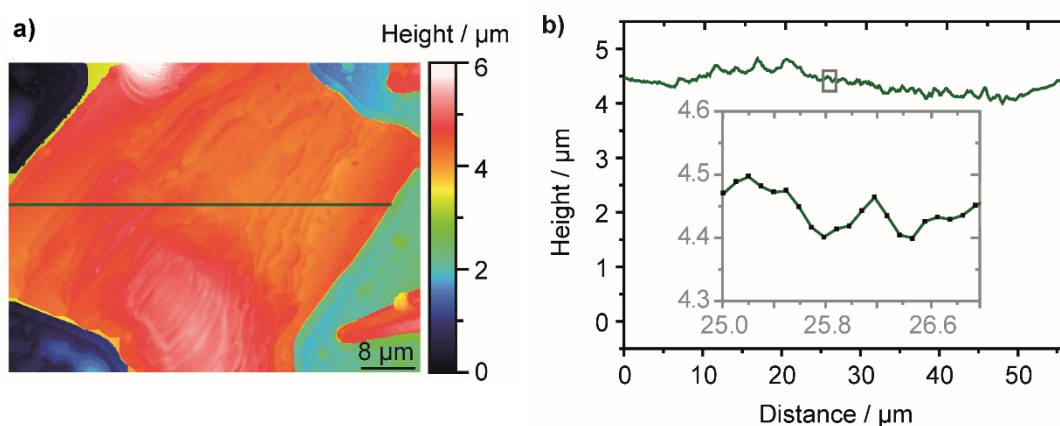
Figure 4.3. (a) Interferometry image of the crystal used for AFM force measurements with the colloidal probes. (b) Roughness profile along the green line in (a). Insert shows a zoom-in of the roughness over 2 μm.

To confirm the crystals selected for force measurements correspond to the fully dehydrated $CaSO_4$ polymorph found in the deposit, powder X-ray diffraction (XRD) was used. This also provided information on the structure of the anhydrite crystal face exposed for force measurements. Figure 4.4a shows the powder XRD pattern obtained for the whole crystal growth sample from which the anhydrite crystals used for force measurements were selected. The purple peaks correspond to fully hydrated gypsum needles (not found in the deposit) and the green peaks correspond to fully dehydrated anhydrite plates (a key inorganic deposit component).
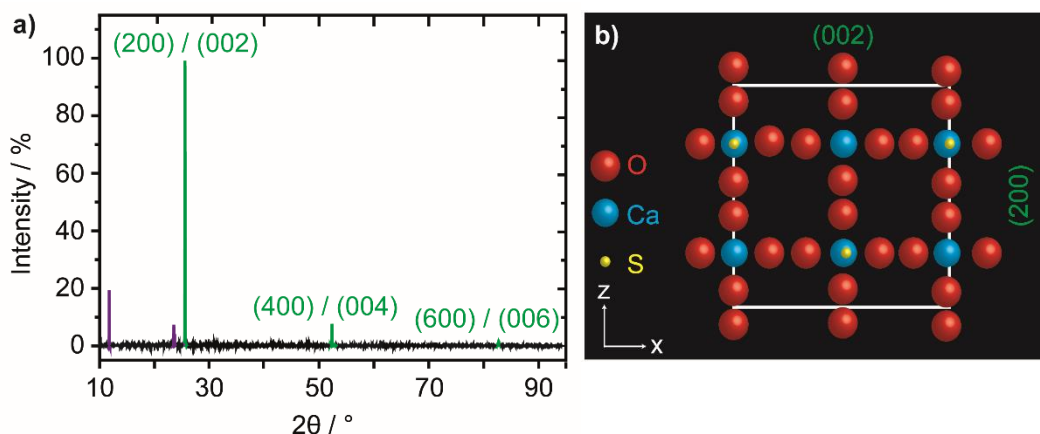
Figure 4.4. (a) Powder XRD pattern for the crystal growth sample from which the anhydrite crystal surfaces were obtained. Purple peaks correspond to gypsum and green peaks correspond to anhydrite. Each anhydrite peak is labelled with an assigned anhydrite crystal face (see Table 4.1). (b) Schematic of the anhydrite crystal structure, highlighting the possible crystal faces exposed during force curve measurements.

To ensure that the crystals selected for force measurements correspond to the anhydrite polymorph found in the deposit and not gypsum, Raman spectroscopy was used. Due to the small laser spot size (515 nm radius) it was possible to obtain spectra corresponding only to the single crystal of interest, confirming the crystals selected correspond to anhydrite, as shown in Figure 4.5.
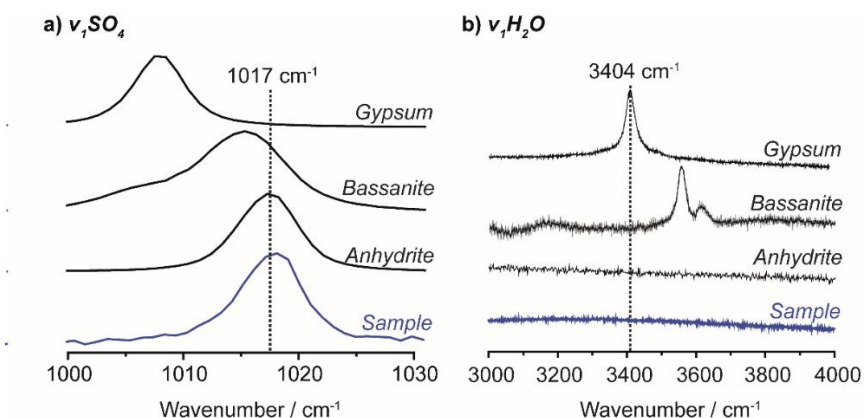
Figure 4.5. Raman reference spectra for gypsum, bassanite and anhydrite and sample spectra (blue), confirming the crystal used as a substrate for AFM force measurements corresponds to anhydrite.

As single crystal XRD measurements were unattainable due to the size of the crystals formed, it is difficult to specifically assign the anhydrite crystal face exposed

during force measurements. However, the peaks obtained in the powder XRD pattern were found to correspond to either the (*h00*) reflections (*h* = 2, 4, 6) or the (*00l*) reflections (*l* = 2, 4, 6), suggesting that either the (200) or (002) face was the surface used for force measurements (see Table 4.1). Nevertheless, both of these faces have O⁻ termination, suggesting the crystal face exposed is negatively charged (see Figure 4.4b).

Table 4.1. Powder XRD anhydrite peaks and possible assignments for the crystal face exposed. *Identified using reference patterns from the HighScore Plus Software (PANalytical B. V.) and the latest ICDD powder diffraction database.*

Experimental data*		Assignment 1*			Assignment 2*		
Peak position / 2θ	Intensity / %	Peak position / 2θ	Intensity / %	(hkl)	Peak position / 2θ	Intensity / %	(hkl)
25.555	100.0	25.422	100.0	(200)	25.422	100.0	(002)
52.348	7.7	52.284	6.8	(400)	52.216	6.7	(004)
82.742	1.6	82.735	2.0	(600)	82.614	1.9	(006)

4.3.3. Background AFM Force Measurements

Initial force measurements were performed on two different anhydrite crystals in hexane to determine whether adhesion values depended on the crystal surface used. The same unmodified Si_3N_4 AFM tip was used, and for each crystal surface, 200 force curve measurements were obtained in the same sample area. Data are summarised in Figure 4.6. Representative force vs. piezo displacement curves for each surface are shown in Figure 4.6b. These were plotted as outlined in the experimental section, using the measured spring constants and deflection sensitivities to convert the raw data obtained.

Initially, when the tip is far away from the sample surface, the cantilever deflection does not change over these large distances of the tip from the surface, resulting in a flat force-distance response, with zero force. Decreasing the tip-sample displacement causes the tip and sample to interact, giving rise to either adhesive or repulsive forces. As this distance is further decreased, the tip and sample come into contact, and if the sample surface is hard and non-deformable, further displacement results in a second linear regime, known as the linear compliance region.[25] Both of

these linear regions are clearly visible in the force curves shown in Figure 4.6b, suggesting there was either negligible or no deformation of the anhydrite surfaces or colloidal probes during these force measurements.[25]

The origin of these force curves corresponds to a tip-sample distance of zero. However, this can be difficult to assign, particularly when repulsive forces occur, leading to premature force responses.[25,43] In these cases, the contact point has been estimated by extrapolating the two linear regimes, as previously suggested.[25] For the unmodified Si_3N_4 AFM tip, weak, short-range repulsive forces (over distances of ca. 20 nm) were experienced on approaching both crystal surfaces, with similar responses in the approach and retract curves. The reasons for this behaviour are discussed in more detail in the next section. Adhesion forces were calculated from the pull-off region of the force curves for both surfaces. Zero adhesion was seen for approximately 75 % of the measurements performed on crystal 1, and 95 % of the experiments performed on crystal 2 (see Figure 4.6a for summary histograms of these data). Negligible force values were obtained for the other measurements (0.25 ± 0.14 nN and 0.13 ± 0.032 nN for crystals 1 and 2, respectively). The high standard deviation obtained for crystal 1 is characteristic of AFM force experiments, with standard deviations of ca. 50 % of the force value often obtained.[30,42] As there was a slight difference in the force response for the same tip on the two crystal surfaces used, force curves were measured on the same anhydrite crystal (see Figure 4.3) for all functionalised colloidal probe studies. To minimise any effects from sample inhomogeneity and differences in crystal structure on the nanoscale, 200 force curves were obtained at each point over five different crystal areas, for each functionalised probe.
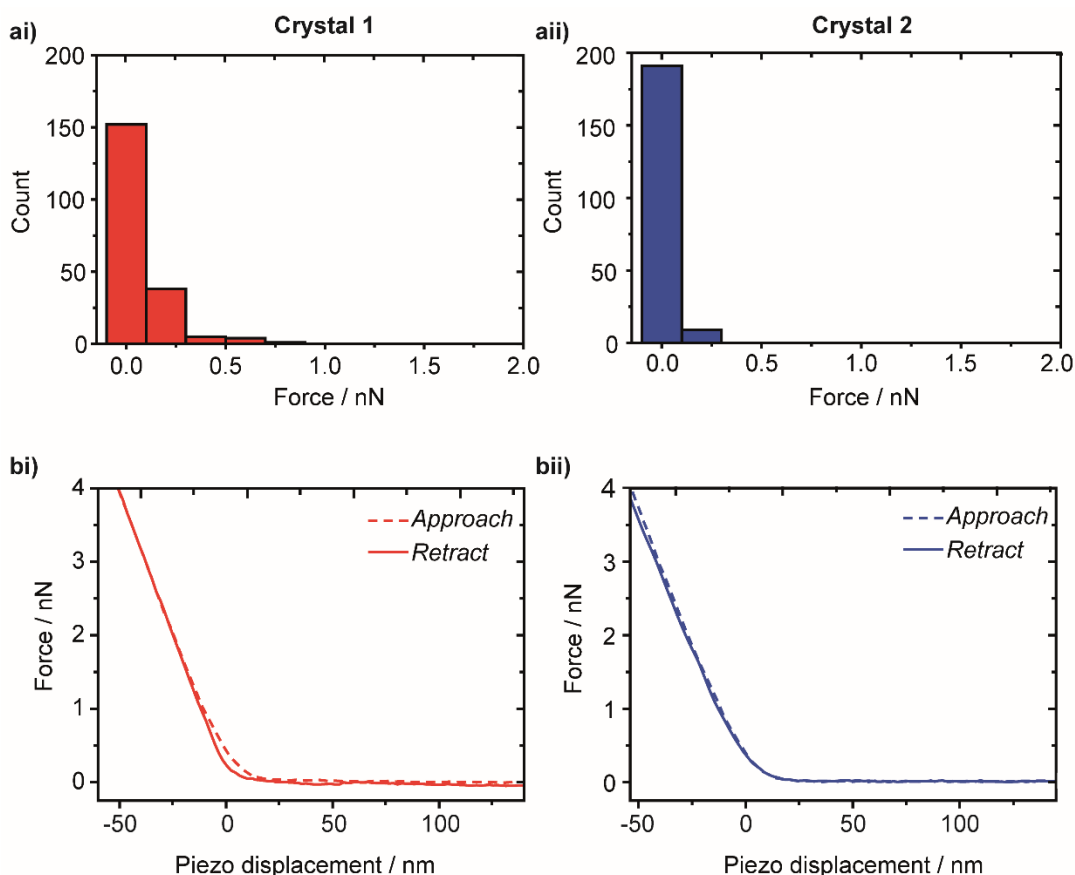
Figure 4.6. Force curve data for the same unmodified AFM tip on two different grown anhydrite crystals in hexane. For each crystal, 200 force curve measurements were obtained in the same sample area in hexane. (a) Histograms of the adhesion force values obtained for (ai) crystal 1 and (aii) crystal 2. (b) Representative force-piezo displacement curves on (bi) crystal 1 and (bii) crystal 2. The point of contact (origin) has been assigned by extrapolating the two linear regimes.

To determine whether the Au layer deposited on the colloidal probes for SAM formation contributes to the overall force response, force curve experiments were performed using an Au-coated colloidal AFM probe prior to SAM-modification. Similar results (with the force normalised to the colloidal probe radius) were obtained to those for the unmodified AFM tip, with no detectable adhesion for approximately 65 % of the experiments, and negligible adhesion values (0.027 ± 0.017 mN/m) for the remainder (see Figure 4.7a). This suggests that the Au layer will contribute very little to any adhesive forces obtained for the functionalised probes, and is therefore a suitable background upon which to add SAMs. Similar negligible adhesion values were obtained in each of the five areas probed, suggesting the sample is relatively

homogeneous (see Figure 4.7a). A representative force/radius vs. piezo displacement curve for the Au-coated probe is shown in Figure 4.7b. As for the unmodified tip (see above), weak, short-range repulsive forces were observed in the approach curves over approximately 20 nm, with either negligible or zero adhesion seen in the retract curves. The reasons for this repulsive behaviour are discussed in the following section. The forces obtained for these colloidal probes are much smaller than expected. The microsphere should have a much larger contact area compared to unmodified AFM tips, but the force values obtained do not scale with this increased probe area. This is likely a consequence of the crystal roughness, as demonstrated in Figure 4.3. As a result, the specific contact area of the colloidal probe is likely to be much smaller than calculated. However, it should be noted that for the smaller, sharper unmodified tips, which are able to penetrate into the cavities produced by the rough surface, the contact area is likely to be much larger than for a planar surface. For the results that follow, with the modified colloidal probe, the main point is that the contact areas should be similar, enabling comparison of the different systems.
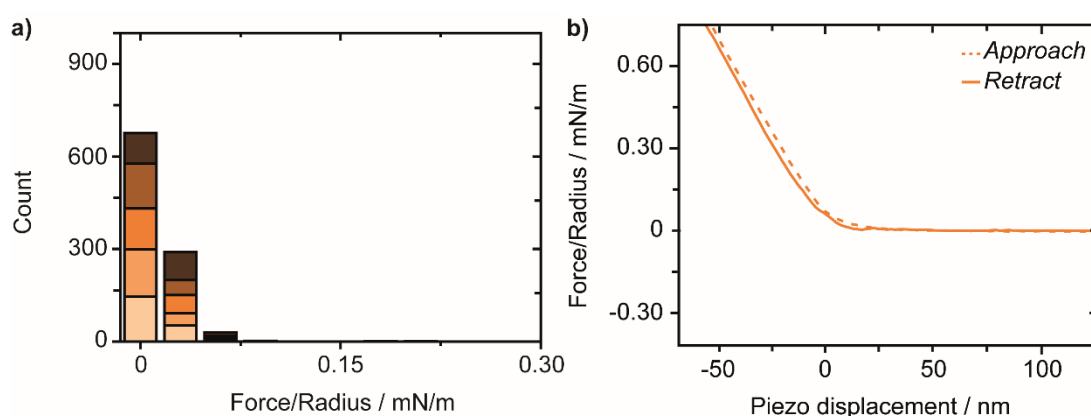
Figure 4.7. Force curve data for a gold-coated AFM tip on the grown anhydrite crystal surface shown in Figure 4.3 in hexane. (a) Histogram of adhesion forces, showing data for the five different sample areas (different shades), with 200 force curve measurements collected in each area. (b) Representative force/radius-piezo displacement curve. The point of contact (origin) has been assigned by extrapolating the two linear regimes.

4.3.4. Surface Charge in Organic Solvents

The nature of surface charge in organic solvents is still under much debate. However, there is sufficient evidence to support the idea of surface charge in solvents with dielectric constants as low as 2.[44,45] For example, as small diameter nanopipettes and nanopores with an applied electric field provide an opportunity to assess surface charge effects in organic solvents,[45] we investigated CVs at the opening of 50 nm quartz capillaries immersed in 1 mM TBAPF$_6$ in 1,2-dichloroethane (DCE, ε = 10.36). These exhibited a phenomenon known as ion current rectification, where the currents obtained at positive and negative potentials of the same magnitude do not result in currents of the same magnitude.[46] In our case, the current at – 0.5 V was approximately four times lower than that at + 0.5 V (see Figure 4.8). This discrepancy is often observed at nanopipettes with small openings in dilute aqueous solutions, particularly when the double layer thickness of the capillary walls becomes similar in size to the diameter of the capillary.[46,47] This causes the double layers of the negatively charged glass or quartz pipette walls to interact with each other, forming a cation-selective region at the pipette opening. Thus, when a positive bias is applied, cations are pushed out of the pipette, and as mass transport outside the pipette is much faster than inside, (due to the conical geometry), this leads to a depleted region in this area, creating a low conductance state and thus decreased ion current at these positive potentials.[47] Although the double layer thickness is expected to be much lower in organic solvents, our studies, as well as others,[45] demonstrate that ion current rectification is still detectable in a wide range of organic solvents with low dielectric constants. However, in all cases, the direction of the rectification for organic solvents is reversed in comparison to aqueous solvents. It is thought that this is caused by the large organic salt cations adsorbing to the glass or quartz pipette walls, creating a positive surface charge, rather than the negative charge of the glass and quartz surfaces in aqueous solutions, therefore reversing the rectification.[45]
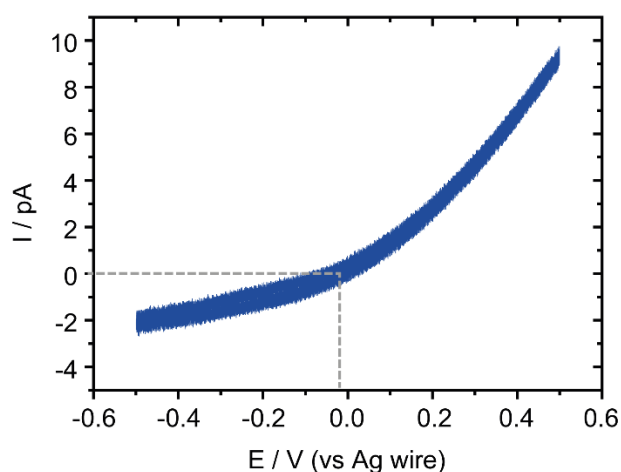
Figure 4.8. (a) CVs obtained at the opening of a 50 nm diameter quartz nanopipette in the SICM setup,[32] showing the resulting tip current, with voltages corresponding to those at the tip vs. the QRCE Ag wire electrode in the bulk solution. Electrolyte solution: 1 mM TBAPF$_6$ in DCE, scan rate: 0.1 V s^{-1}.

It is therefore plausible that effects caused by the presence of surface charge are also detectable in the organic hexane environment used for all our AFM force experiments, and thus the repulsive forces observed between the unmodified Si$_3$N$_4$ AFM tip and Au-coated colloidal probes and the anhydrite crystal surfaces in hexane are a result of electrostatic repulsion. The charge on surfaces in organic solvents is thought to originate from either (i) adsorption of dissociated molecules and/or (ii) proton exchange between the organic solvent and substrate.[44] As no attempt was made to dry the hexane solvent used in our experiments, small amounts of water would be present, behaving as a weak electrolyte and supplying H$^+$ and OH$^-$ ions. These ions are likely to adsorb to the hydrophilic surfaces of the Si$_3$N$_4$ and Au-coated probes. Therefore, the repulsion observed may be a consequence of electrostatic interactions between adsorbed ions on hydrophilic tips and the negatively charged anhydrite crystal surface (due to the O$^-$ termination of the crystal face exposed - see Figure 4.4b). Similar repulsive forces have been detected between two hydrophilic silica surfaces in an organic environment (decane), over distances of 7.5 nm during approach and 15 nm on retraction. However, no repulsion was seen for hydrophobic surfaces under the same conditions, suggesting the repulsive behaviour results from the hydrophilic character of the surfaces,[44] thus supporting this hypothesis.

4.3.5. AFM Force Measurements for Hydrophilic, Polar Colloidal Probes

The adhesion force values obtained for all the experiments performed using the dispersant-functionalised colloidal probes are compared in Figure 4.9a. Again, these results were normalised to the colloidal probe radius, and were obtained over five different sample areas. For the C_4H_8OH terminated probe, approximately 98 % of the experiments gave zero adhesion force, with negligible forces obtained for the remaining experiments (0.034 ± 0.020 mN/m) (see Figure 4.9ai). Similarly, for the $CHCH_2(COOH)_2$ probe, approximately 92 % of the experiments gave negligible force, with weak adhesive forces obtained for the remaining experiments (0.063 ± 0.068 mN/m), although slightly higher in value than for the C_4H_8OH probe (see Figure 4.9aii). Nonetheless, both polar probes showed negligible adhesion. Typical force/radius vs. piezo displacement plots are shown in Figure 4.9b. For the C_4H_8OH terminated probe, very slight repulsion (over < 5 nm) was seen in both the approach and retract curves (Figure 4.9bi), and for the $CHCH_2(COOH)_2$ probe, a more apparent, slightly longer range (ca. 10 nm) repulsive response was seen (Figure 4.9bii).

As mentioned above, we suggest this characteristic is due to the presence of water in the hexane solvent. In addition, the presence of OH groups in these functionalities may result in proton transfer between the probe molecules and hexane solution, as similarly proposed between silica surfaces and decane.[44] It was suggested that as silica is much more acidic than decane, protons from the silica surface were donated to the solvent, resulting in a negative surface charge produced on the silica surface. In our system, we envisage a similar effect between the $CHCH_2(COOH)_2$ terminated probe and the hexane solvent, rendering these probes negatively charged, thus resulting in repulsion when approaching the O^- termination of the anhydrite crystal surface. As the COOH groups are much stronger proton donors than the OH group, and because there are two COOH groups present at the colloidal probe surface compared to one OH group, this is a reasonable explanation as to why the repulsive forces obtained for the COOH-terminated probe are stronger than those obtained for the OH-terminated probe. These results suggest that if there is any water present within the engine, which is highly likely as this is a by-product of the combustion process, dispersants with COOH head groups may not be as effective at dispersing inorganic deposits as expected, particularly if these deposit surfaces are terminated with negatively charged groups.
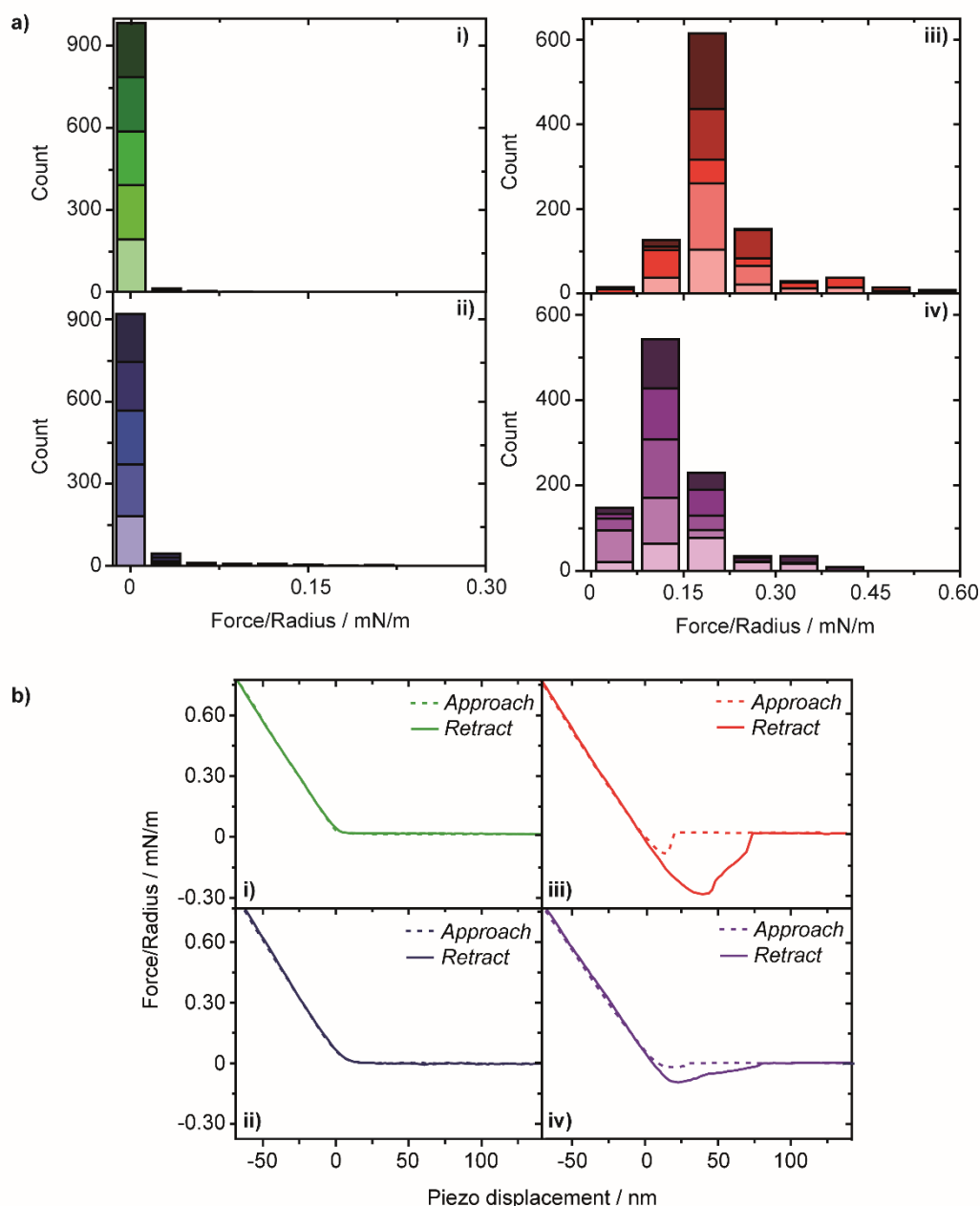
Figure 4.9. Force curve data for all the SAM-functionalised AFM tips on the same grown anhydrite crystal surface in hexane. (a) Histograms of adhesion forces for each functionalised tip: (bi) C_4H_8OH; (bii) $CHCH_2(COOH)_2$; (biii) $PhNO_2$ and (biv) CH_2Ph, showing data for the five different sample areas (different shades), with 200 force curve measurements collected in each area. (b) Representative force/radius-piezo displacement curves for each functionalised tip: (bi) C_4H_8OH; (bii) $CHCH_2(COOH)_2$; (biii) $PhNO_2$ and (biv) CH_2Ph. The point of contact (origin) has been assigned by extrapolating the two linear regimes for (i) and (ii), and as the start of the linear compliance regime for (iii) and (iv).

4.3.6. AFM Force Measurements for Hydrophobic, Aromatic Colloidal Probes

In strong contrast to the behaviour seen for the polar AFM probes, probe molecules terminated with aromatic functional groups ($PhNO_2$ and CH_2Ph) gave rise to significant adhesion force values for the majority of experiments performed. Adhesion values of 0.20 ± 0.081 mN/m and 0.12 ± 0.064 mN/m were obtained for the $PhNO_2$ (see Figure 4.9aiii) and CH_2Ph probes (see Figure 4.9aiv), respectively. These larger adhesion values are unlikely to be a consequence of a higher number of functional groups exposed at the aromatic probe surfaces compared to the polar probe surfaces, as the presence of the rigid, aromatic benzene head groups is likely to disrupt the monolayer packing of these molecules for steric reasons.[48] In fact, a higher number of functionalised groups are expected to be exposed at the polar-functionalised AFM probes. Rather, the behaviour seen with the aromatic probes is chemical in origin. Typical force/radius vs. piezo displacement curves for both aromatic functionalities show a clear jump to contact on approach, and adhesion on retraction (see Figures 4.9biii and iv). We suggest this is a consequence of the hydrophobic character of the benzene functional group, which prevents the adsorption of water and thus ions on the colloidal probes (in contrast to the polar probes), thus preventing repulsive tip-sample interactions. The weak adhesive behaviour seen in hexane is similar to that previously reported between aromatic asphaltene-functionalised surfaces and polar mica surfaces in heptane, giving rise to weak adhesive forces on separation.[49]

In both cases, the adhesion force is broad (over approximately 75 nm). This is most likely a consequence of the roughness of the crystal surface used. The broad adhesive forces are unlikely to be due to solvation forces between the surfaces, as it has been demonstrated that these are only seen for sufficiently rigid non-polar solvent molecules such as cyclohexane,[50,51] and in the case of flexible molecules (such as hexane), these forces only extend as far as a few molecular layers (less than a few nanometres).[52]

Box charts of the adhesion values obtained for the two aromatic probes were plotted to determine whether the forces obtained for these functionalities can be classed as statistically different. Figure 4.10 shows data from three different sample areas for each probe. The first point to note is that for the same probe, the median values for the three different sample areas do not always overlap with the upper and lower quartiles of the other two plots, suggesting the results obtained for the same

probe at different sample areas are not statistically similar. This is most likely due to the small size of the calculated contact area diameter (ca. 200 nm, as described above), which is likely to be even smaller due to the substrate surface roughness. On this scale, the colloidal probe may access different crystal faces and/or step edges when moved to different sample areas. However, as the median values obtained for the $PhNO_2$ probe do not overlap with the upper and lower quartiles of the CH_2Ph plots, the $PhNO_2$ adhesion values are statistically larger than the CH_2Ph adhesion values. Thus, the presence of the NO_2 functional group is detectable in these measurements, as the two different aromatic functionalities give rise to statistically different adhesion forces. The larger adhesion forces obtained for the $PhNO_2$ probe can be attributed to the polar NO_2 group binding to the polar anhydrite surface, resulting in a larger adhesive force on retraction. As mentioned above, adhesive forces have been observed in heptane between the polar functional groups of asphaltene films and polar mica surfaces in toluene.[49] Additionally, the larger forces obtained for the $PhNO_2$ probe compared to the CH_2Ph probe are unlikely to be a consequence of a larger number of these groups being exposed at the probe surface, as it has been previously shown that SAMs terminated with benzene and 4-(methoxy)benzene groups result in similar packing densities.[48]

We suggest that in contrast to the Au, Si_3N_4, C_4H_8OH and $CHCH_2(COOH)_2$ probe experiments, repulsion is not seen, as the aromatic nature of the benzene groups of these probes disfavour water adsorption, and hence ion adsorption, which would introduce electrostatic repulsion. Although these results suggest that dispersants with aromatic head groups may bind more strongly to inorganic deposit surfaces than polar, OH or COOH dispersant head groups, the adhesion values obtained are still very small, suggesting there is very little adhesion between the aromatic groups and polar deposit surface. Thus, determining the best dispersant head groups for binding this inorganic deposit is a complex process, affected by the degree of hydration of the organic environment, as well as the presence of charge within the engine.
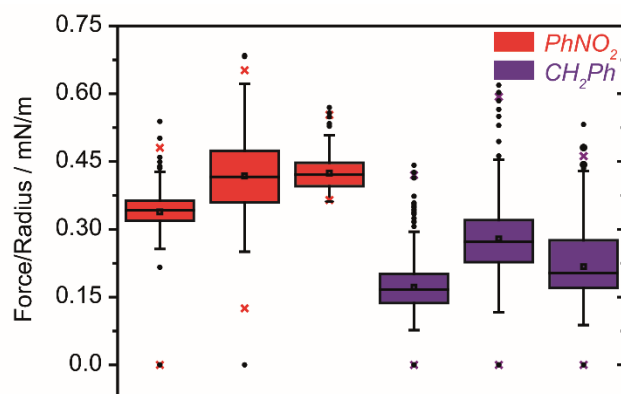
Figure 4.10. Box and whisker plots showing a statistical analysis of the 200 adhesion force values obtained in three different sample areas for the PhNO$_2$ (red) and CH$_2$Ph (purple) tips on the grown anhydrite crystal surface in hexane. The upper and lower edges of the boxes represent the upper and lower quartiles, respectively, and the centre lines represent the median values. The ends of the higher and lower whiskers represent the highest and lowest data points within 1.5 times the interquartile range of the upper and lower quartiles, respectively. Any points outside of this range are shown as outliers (black dots), and the upper and lower coloured crosses represent the 99th and 1st percentiles, respectively.

4.3.7. AFM Force Measurements in an Aqueous Environment

As well as in organic solvents, the impact of the solvent environment on the resulting adhesive and repulsive tip-sample interaction forces in AFM force experiments is also crucial in aqueous solvents. This is demonstrated by force measurements conducted in aqueous (1 mM K$_4$Fe(CN)$_6$ and 0.4 mM sodium citrate) solutions between citrate-capped gold nanoparticles and different Au/SAM modified electrode surfaces.[53] This was achieved by modifying AFM tips to represent the nanoparticles, by coating unmodified AFM tips with Au, followed by the adsorption of citrate ions (see section 4.2.7 in the experimental section), and measuring their interaction forces with three different Au/SAM electrode surfaces. Both hydrophilic and hydrophobic SAMs were investigated, namely 11-mercapto-1-undecanol (MUD), 11-mercaptoundecanoic acid (MUA) and dodecanethiol (DDT).

For the OH-terminated MUD SAM surfaces, no attractive interactions were seen during approach, and no adhesion was seen during the retraction, (see Figure 4.11a) giving a similar force response to that seen between the OH-terminated colloidal probe

and the anhydrite crystal surface in hexane (see Figure 4.9bi). However, for the COOH-terminated MUA SAM surfaces, weak repulsive forces were seen over distances of approximately 10 nm, (see Figure 4.11b), again, very similar to those seen in hexane between the COOH-terminated colloidal probe and anhydrite surface (see Figure 4.9bii). This is again a consequence of electrostatic repulsion between the partially negatively charged carboxylate groups at the SAM surface (pKa ~ 5.5-10.3)[54-56] and the citrate ions at the tip, due to the pH of the solution (~ 7.3).

In contrast, for the CH_3-terminated DDT SAM surface, small repulsive forces (~ 20 nm) occurred on approach, similarly to the COOH-terminated SAM, but a jump to contact was seen after this (see Figure 4.11c). Upon retraction, adhesive forces were seen over approximately 20 nm, with an average value of 1.5 ± 0.22 nN. This adhesive response is typically seen for hydrophobic surfaces in aqueous solutions, and is due to a hydrophobic interaction,[25] caused by either a change in the water structure at the hydrophobic surface,[57] electrostatic interactions within the aqueous solvent or on the surface,[58] or the presence of nanobubbles at the hydrophobic surface,[25,59] particularly for non-degassed solutions,[60,61] such as those used in this work. Due to capillary effects, these nanobubbles result in long-range adhesion in AFM force measurements.[62] Therefore, in these studies, the adhesive values obtained at the CH_3-terminated surfaces are a result of probing the tip-nanobubble interaction, rather than the tip-sample interaction.
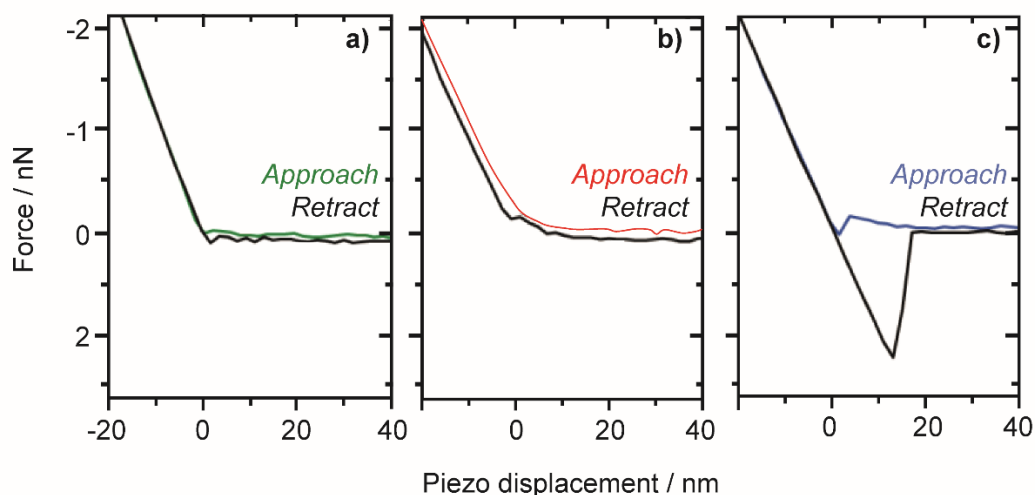
Figure 4.11. Representative force-piezo displacement curves for citrate-modified AFM tips in 1 mM $K_4Fe(CN)_6$ and 0.4 mM sodium citrate, with the following Au/SAM electrode surfaces: (a) MUD (OH-terminated); (b) MUA (COOH-terminated) and (c) DDT (CH_3-terminated). The point of contact (origin) has been assigned as the start of the linear compliance regime. Measurements were conducted under potential control, with each Au/SAM electrode biased at 400 mV vs. an Ag/AgCl quasi-reference counter electrode.

Thus, the above studies further highlight the unusual interaction forces often obtained from AFM force experiments as a consequence of the solvent environment. Interestingly, repulsive forces are seen for COOH-terminated tips in both organic and aqueous solvents, suggesting the presence of electrostatic charge in both systems, which dominates the interaction force. The adhesion forces seen between hydrophobic and hydrophilic surfaces in both solvents are unexpected, however, in aqueous solvents, this is purely a result of the tip-sample interaction being screened by the high interfacial energy present at the hydrophobic surface-aqueous solvent interface, and in organic solvents, these forces were negligible. These findings demonstrate the huge dependence of AFM interaction forces on the surrounding solvent environment.

4.4. Conclusions

Interaction forces between a range of hydrophilic, polar and hydrophobic, aromatic dispersant-functionalised colloidal probes and a model deposit single crystal anhydrite surface were directly measured in hexane using AFM. SAM chemistry was used to expose either hydrophilic, polar groups or hydrophobic, aromatic groups at the surface of the colloidal probes. The measurements reported demonstrate the crucial role of the solvent in governing adhesive and repulsive behaviours studied between functionalised surfaces using AFM force measurements. Polar-polar tip-substrate interactions in hexane were repulsive in nature, a consequence of electrostatic repulsion, attributed to the adsorption of OH⁻ ions on these hydrophilic AFM probes. This supports ion current rectification phenomena observed in organic solvents in SICM studies, which indicate the presence of surface charge in very low polarity organic environments.[45] In contrast, weak adhesion was observed between colloidal probes terminated with aromatic functional groups and the polar anhydrite surface due to the lack of ion adsorption at these hydrophobic probe surfaces. These studies further provide insight into the interactions occurring between different dispersant chemistries and inorganic piston deposits formed in the oil-based environment present in the engine. Effects such as the degree of hydration of the organic solvent and the presence of charge on the relative binding strengths between the two are highlighted, and therefore the consequences this may have on preventing deposit formation.

Additionally, AFM force measurements conducted in aqueous solutions further demonstrate the perturbing effects solvents have on these interaction forces, again resulting in repulsive forces for polar-polar interactions, and adhesive forces for polar-non-polar interactions, a consequence of electrostatic repulsion and high hydrophobic surface-water interfacial energies, respectively. These studies provide a further understanding of adhesive and repulsive interactions, as well as the structure of charge in both aqueous and organic solvents, areas which are all still under considerable debate.

4.5. Bibliography

(1)   Covitch, M. J.; Richardson, J. P.; Graf, R. T. *Lub. Sci.* **1990**, *2*, 231-251.

(2)   Shu, G.; Dong, L.; Liang, X. *Int. J. Engine Res.* **2011**, *13*, 357-369.

(3)   Papke, B. L. *Lub. Eng.* **1991**, *48*, 209-218.

(4)   Smith, G. C.; Hopwood, A. B.; Titchener, K. J. *Surf. Interface Anal.* **2002**, *33*, 259-268.

(5)   Diaby, M.; Sablier, M.; Le Négrate, A.; El Fassi, M.; Bocquet, J. *Carbon* **2009**, *47*, 355-366.

(6)   Guan, N.; Ng, G. K. L.; Zheng, H. Y.; Hong, M. H.; Hong, X.; Zhang, Z. *Appl. Surf. Sci.* **2013**, *270*, 526-530.

(7)   Freyer, D.; Voigt, W. *Monatsh. Chem.* **2003**, *134*, 693-719.

(8)   Blount, C. W.; Dickson, F. W. *Geochim. Cosmochim. Acta* **1969**, *33*, 227-245.

(9)   Ruiz-Agudo, E.; Putnis, C. V.; Hövelmann, J.; Álvarez-Lloret, P.; Ibáñez-Velasco, A.; Putnis, A. *Geochim. Cosmochim. Acta* **2015**, *156*, 75-93.

(10)   Austad, T.; Shariatpanahi, S. F.; Strand, S.; Aksulu, H.; Puntervold, T. *Energy Fuels* **2015**, *29*, 6903-6911.

(11)   Sharma, H.; Dufour, S.; Pinnawala Arachchilage, G. W. P.; Weerasooriya, U.; Pope, G. A.; Mohanty, K. *Fuel* **2015**, *140,* 407-420.

(12)   ShamsiJazeyi, H.; Verduzco, R.; Hirasaki, G. J. *Colloids Surf., A* **2014**, *453*, 168-175.

(13)   Hangx, S. J. T.; Spiers, C. J.; Peach, C. J. *Energy Procedia* **2011**, *4*, 5358-5363.

(14)   Dutrizac, J. E.; Kuiper, A. *Hydrometallurgy* **2006**, *82*, 13-31.

(15)   Azimi, G.; Papangelakis, V. G. *Hydrometallurgy* **2011**, *108*, 122-129.

(16)   Finot, E.; Lesniewska, E.; Mutin, J.-C.; Goudonnet, J.-P. *J. Chem. Phys.* **1999**, *111,* 6590-6598.

(17)   Finot, E.; Lesniewska, E.; Mutin, J.-C.; Goudonnet, J.-P. *Langmuir* **2000**, *16*, 4237-4244.

(18)   Fa, K.; Jiang, T.; Nalaskowski, J.; Miller, J. D. *Langmuir* **2003**, *19*, 10523-10530.

(19)   Fa, K.; Nguyen, A. V.; Miller, J. D. *Int. J. Miner. Process.* **2006**, *81*, 166-177.

(20)   Ferrari, L.; Kaufmann, J.; Winnefeld, F.; Plank, J. *J.Colloid Interface Sci.* **2010**, *347*, 15-24.

(21)   Ducker, W. A.; Senden, T. J.; Pashley, R. M. *Nature* **1991**, *353*, 239-241.

(22)   Hoh, J. H.; Revelt J.-P.; Hansma P. K. *Nanotechnology* **1991**, *2*, 119-122.

(23) Binnig, G.; Quate, C. F. *Phys. Rev. Lett.* **1986**, *56*, 930-934.

(24) Butt, H.-J. *Biophys. J.* **1991**, *60,* 1438-1444.

(25) Butt, H.-J.; Cappella B.; Kappl, M. *Surf. Sci. Rep.* **2005**, *59,* 1-152.

(26) Prater, C. B.; Maivald, P. G.; Kjoller, K. J.; Heaton, M. G., *Probing Nano-Scale Forces with the Atomic Force Microscope.* Veeco Instruments Inc., Santa Barbara, California, 1995.

(27) Ossorio, M.; Van Driessche, A. E. S.; Pérez, P.; García-Ruiz, J. M. *Chem. Geol.* **2014**, *386,* 16-21.

(28) Hardie, L. A. *Am. Mineral.* **1967**, *52,* 171-200.

(29) Ravenhill, E. R.; Kirkman, P. M.; Unwin, P. R. *Cryst. Growth Des.* **2016**, *16,* 5887-5895.

(30) Frisbie, D.; Rozsnyai, L. F.; Noy, A.; Wrighton, M. S.; Lieber, C. M. *Science* **1994**, *265*, 2071-2074.

(31) Noy, A.; Frisbie, C. D.; Rozsnyai, L. F.; Wrighton, M. S.; Lieber, C. M. *J. Am. Chem. Soc.* **1995**, *117,* 7943-7951.

(32) Hansma, P. K.; Drake, B.; Marti, O.; Gould, S. A.; Prater, C. B. *Science* **1989**, *243,* 641-643.

(33) Zhang, H.; He, H.-X.; Wang, J.; Liu, Z.-F. *Langmuir* **2000**, *16*, 4554-4557.

(34) Love, J. C.; Estroff, L. A.; Kriebel, J. K.; Nuzzo, R. G.; Whitesides, G. M. *Chem. Rev.* **2005**, *105,* 1103-1170.

(35) Bain, C. D.; Whitesides, G. M. *Science* **1988**, *240,* 62-63.

(36) Vericat, C.; Vela, M. E.; Benitez, G.; Carro, P.; Salvarezza, R. C. *Chem. Soc. Rev.* **2010**, *39,* 1805-1834.

(37) Chidsey, C. E. D.; Loiacono, D. N. *Langmuir* **1990**, *6,* 682-691.

(38) Adams, D. M.; Brus, L.; Chidsey, C. E. D.; Creager, S.; Creutz, C.; Kagan, C. R.; Kamat, P. V.; Lieberman, M.; Lindsay, S.; Marcus, R. A.; Metzger, R. M.; Michel-Beyerle, M. E.; Miller, J. R.; Newton, M. D.; Rolison, D. R.; Sankey, O.; Schanze, K. S.; Yardley, J.; Zhu, X. *J. Phys. Chem. B* **2003**, *107,* 6668-6697.

(39) Finklea, H. O.; Snider, D. A.; Fedyk, J.; Sabatani, E.; Gafni, Y.; Rubinstein, I. *Langmuir* **1993**, *9*, 3660-3667.

(40) Porter, M. D.; Bright, T. B.; Allara, D. L.; Chidsey, C. E. D. *J. Am. Chem. Soc.* **1987**, *109,* 3559-3568.

(41) Johnson, K. L.; Kendall, K.; Roberts, A. D. *Proc. R. Soc. London, Ser. A* **1971**, *324*, 301-313.

(42) Gourianova, S.; Willenbacher, N.; Kutschera, M. *Langmuir* **2005**, *21,* 5429-5438.

(43) Huang, Q.; Yoon, I.; Villanueva, J.; Kim, K.; Sirbuly, D. J. *Soft Matter* **2014**, *10,* 8001-8010.

(44) McNamee, C. E.; Tsujii, Y.; Matsumoto, M. *Langmuir* **2004**, *20*, 1791-1798.

(45) Yin, X.; Zhang, S.; Dong, Y.; Liu, S.; Gu, J.; Chen, Y.; Zhang, X.; Zhang, X.; Shao, Y. *Anal. Chem.* **2015**, *87*, 9070-9077.

(46) Wei, C.; Bard, A. J.; Feldberg, S. W. *Anal. Chem.* **1997**, *69,* 4627-4633.

(47) McKelvey, K.; Kinnear, S. L.; Perry, D.; Momotenko, D.; Unwin, P. R. *J. Am. Chem. Soc.* **2014**, *136*, 13735-13744.

(48) Tao, Y.-T.; Wu, C.-C.; Eu, J.-Y.; Lin, W.-L. *Langmuir* **1997**, *13*, 4018-4023.

(49) Natarajan, A.; Xie, J.; Wang, S.; Liu, Q.; Masliyah, J.; Zeng, H.; Xu, Z. *J. Phys. Chem. C* **2011**, *115*, 16043-16051.

(50) Christenson, H. K. *J. Chem. Phys.* **1983**, *78*, 6906-6913.

(51) Horn, R. G.; Israelachvili, J. N. *J. Chem. Phys.* **1981**, *75*, 1400-1411.

(52) Christenson, H. K.; Horn, R. G.; Israelachvili, J. N. *J. Colloid Interface Sci.* **1982**, *88*, 79-88.

(53) Chen, C.-H.; Ravenhill, E. R.; Momotenko, D.; Kim, Y.-R.; Lai, S. C. S.; Unwin, P. R. *Langmuir* **2015**, *31*, 11932-11942.

(54) Schweiss, R.; Welzel, P. B.; Werner, C.; Knoll, W. *Langmuir* **2001**, *17*, 4304-4311.

(55) Hu, K.; Bard, A. J. *Langmuir* **1997**, *13*, 5114-5119.

(56) Chen, S.; Liu, Y.; Chen, J. *Chem. Soc. Rev.* **2014**, *43*, 5372-5386.

(57) Eriksson, J. C.; Ljunggren, S.; Claesson, P. M. *J. Chem. Soc. Faraday Trans. 2* **1989**, *85*, 163-176.

(58) Wood, J.; Sharma, R. *Langmuir* **1995**, *11*, 4797-4802.

(59) Ederth, T.; Liedberg, B. *Langmuir* **2000**, *16*, 2177-2184.

(60) Ishida, N.; Inoue, T.; Miyahara, M.; Higashitani, K. *Langmuir* **2000**, *16*, 6377-6380.

(61) Tyrrell, J. W. G.; Attard, P. *Phys. Rev. Lett.* **2001**, *87*, 176104.

(62) Attard, P. *Langmuir* **2000**, *16*, 4455-4466.

Chapter 5: Calcium Carbonate Crystallisation at Charged Graphite Surfaces

Parts of this chapter have been submitted for publication:

Abstract

The previous chapters have focussed on inorganic calcium sulfate deposit formation. However, calcium carbonate deposition is also of extreme importance in several industrial settings, such as the costly formation of scale at commonly employed metal surfaces. Additionally, this material comprises the core of the overbased calcium carbonate detergents from which the engine deposits analysed in the previous chapters are formed. Thus, understanding the nucleation and growth of this crystal system is also of high importance. Due to its rich polymorphism and importance in biomineralisation, several studies have focussed on $CaCO_3$ crystallisation at a range of functionalised interfaces. However, few have analysed the effects of surface charge on this process, which are thus still poorly understood. Therefore, in this chapter, the effects of surface charge on $CaCO_3$ crystallisation are studied at biased Highly Oriented Pyrolytic Graphite (HOPG) surfaces via in situ optical microscopy, providing details of the dynamic processes occurring at the charged surface. High resolution scanning electron microscopy and Raman spectroscopy are employed for a detailed analysis of the morphologies and polymorphs formed in each case. At negatively charged surfaces, a range of high energy, positively charged vaterite, aragonite and calcite crystal planes are nucleated, whereas at positively charged surfaces, nucleation of the neutral (104) calcite face is solely achieved. These studies demonstrate the huge impact of surface charge on the resulting orientation and polymorph of calcium carbonate obtained, providing new insights into the role of charge on crystallisation processes.

5.1. Introduction

In addition to the calcium sulfate deposits studied in the previous chapters of this thesis, the calcium carbonate crystal system also plays a huge role in the undesirable formation of inorganic deposits in a wide range of domestic, commercial and industrial settings.[1] This can again occur in both aqueous and organic environments. For example, calcium carbonate is one of the main components of scale formation on the walls of pipelines,[2] where its presence results in equipment damage due to corrosion, restricted pipeline flow, and in the case of oilfield pipelines, decreased oil and gas production.[3] Several different methods have been investigated for preventing this process. The use of chemical scale inhibitors containing negatively charged functional groups, such as orthophosphates[4] and carboxylic acids[5] have been found to reduce scale formation due to adsorption of these additives via their PO_3^{2-} and CO_3^{2-} groups onto the $CaCO_3$ crystal, preventing its growth. Positively charged ions such as Zn^{2+} also reduce scale formation, but it is not known whether this occurs via promoting $CaCO_3$ nucleation and thus hindering growth, or due to preferential formation of $ZnCO_3$.[6] Physical methods have been investigated, including the effect of magnetic[7] and electric fields[8] on scale formation, as well as the structure of the fouling surface itself, with common metal surfaces such as steel, copper and aluminum studied. The severity of scale formation via transportation of the deposit formed in the bulk solvent to the surface was found to depend on the surface free energy and roughness, with diamond-like carbon surfaces offering significant reduction in scale formation, a consequence of their much lower surface roughness.[1] All of the above strategies largely depend on electrostatic interactions occurring at the $CaCO_3$ crystal-inhibitor interface, for which little is currently known.

The nucleation and growth of $CaCO_3$ has also received significant attention due to its role in biomineralisation, whereby nature employs a range of different functionalised interfaces which exert high levels of control over the orientation, morphology and polymorph of $CaCO_3$ obtained, often resulting in much more desirable structural properties than their synthetic equivalents.[9-11] Thus, several biomimetic methods have been used to try to replicate these nucleation and growth mechanisms, many of which are analogous to the methods discussed above for controlling scale formation. One of the most widely employed strategies is the use of self-assembled monolayers (SAMs), exposing functionalised head group chemistries of interest to the

growth solution. For example, at Au/SAM surfaces terminated with COO^- and SO_3^- groups, the most thermodynamically stable $CaCO_3$ polymorph, calcite, was found to preferentially and selectively nucleate from its (015) and (1 0 12) planes, respectively.[12,13] In contrast, at the bare Au metal surface, controlled orientation during nucleation was not observed, with a combination of calcite, and the metastable vaterite polymorph nucleating.[12,14] The negatively charged SAM head groups are thought to act as 'surrogate oxyanions' for the CO_3^{2-} ions of specific nucleating calcite planes, thus promoting their growth,[15] which may explain why calcite crystallisation is promoted at lower concentrations of negatively charged additives in comparison to positively charged additives, as explained in section 1.2.1.3., thus suggesting that charge and electrostatics play a key role in these templating processes. However, it has been noted that a strict match of the crystallographic structures of the nuclei and underlying substrate is not necessarily required, with some lattice mismatch between the two often seen.[10,16] This has been highlighted by modelling the oriented nucleation of calcite at rigid and flexible COO^--terminated SAMs.[17,18] Although the (001) calcite plane has the best epitaxial match with the SAM, (012) nucleation occurs at the flexible monolayers via a kinetic effect, due to a closer match between the random orientation of the carbonate groups in the disordered $CaCO_3$ state and the carbonate distribution in the (012) plane. This poor epitaxial match is accommodated for by point defects in the first calcite layer, modifying the charge density to quench the net dipole of the high energy (012) plane. Therefore, these growth mechanisms are not purely controlled by epitaxial relationships, but through a combination of geometric, stereochemical and electrostatic effects,[10,16,19,20] the latter of which are poorly understood.

Therefore, in this chapter, calcium carbonate crystallisation is explored at charged HOPG surfaces, to shed some light onto the role electrostatic effects play in these nucleation and growth processes. Unlike the Au/SAM surfaces extensively used for studying these phenomena, which naturally contain defects due to imperfections in the self-assembly process, and an increased surface roughness post self-assembly caused by imperfections in the substrate[21] the cleaved HOPG surfaces employed in our studies are free from these problems, providing terraces of atomically flat, homogeneous planes for studying crystallisation, with well-defined step edge densities.[22,23] Additionally, this allows the effects of charge to be studied in the absence of different chemical functionalities. Similar studies have been conducted on negatively biased, bare Au

(111) and Ag (111) surfaces on mica without the formation of SAMs, demonstrating that epitaxial relationships are still achievable in the absence of these head group chemistries.[14] However, in these studies, $CaCO_3$ growth occurs at the surface due to an increase in the local pH and thus supersaturation via electrochemical methods. Our setup permits the application of extreme potentials to the HOPG surface without significant electrolysis, due to the wide double layer region of HOPG electrodes and the strong dependence of charge on the applied potential,[22,23] thus allowing the effects of surface charge to be studied in the absence of products formed from solvent electrolysis. To the best of our knowledge, this is the first time that both negative and positive surface charges have been investigated in this way. The use of in situ optical microscopy revealed the preferential nucleation of high energy, positively charged crystal faces of calcite, vaterite and aragonite at negatively biased surfaces, in contrast to the neutral, low energy faces nucleated at positively biased surfaces. These contrasting behaviours emphasise the crucial role charge and electrostatics play in determining the $CaCO_3$ orientations and polymorphs achievable. Furthermore, this work expands on studies which demonstrate that a strict lattice match between the nucleating crystal face and underlying surface is not an essential requirement for the nucleation of unusual, high energy crystal planes.

5.2. Experimental

5.2.1. Crystal Growth Experiments

All aqueous solutions were prepared using ultrapure water (Milli-Q Reagent, Millipore) with a typical resistivity of 18.2 MΩ cm at 25 °C. This was used immediately, without equilibrating with the atmosphere. In each experiment, 2 mL of 5 mM $CaCl_2$ (Sigma Aldrich, ≥ 97 %) and 2 mL of 20 mM $NaHCO_3$ (Sigma Aldrich, ≥ 99.7 %) were pipetted directly onto the surface of interest, to create a supersaturated solution. Both solutions were prepared fresh, immediately before starting the experiment, and were filtered using Minisart syringe filters with a 0.20 μm pore (Sartorius). For all experiments, the measured pH of these solutions combined was 8.07, in agreement with that calculated by MINEQL+ (version 4.6, Environmental Research Software). This was calculated assuming the system was closed to the atmosphere, as is the case at the start of the growth experiments. A temperature of 22 ºC was used for the simulation, with the ionic strength calculated by the MINEQL+ software and the pH calculated based on

electroneutrality conditions. This calculated a saturation ratio with respect to calcite at the start of these experiments of 16.4.

Calcium carbonate crystallisation was investigated at a range of different surfaces, including plastic petri dishes (Polystyrene, 35 mm diameter, Greiner Bio-One) and circular borosilicate D-263 M glass slides (30 mm diameter, Thermo Scientific) fitted into Petri dishes (Willco Wells) equipped with a perspex rim and lid. The latter exposed a glass diameter of 12 mm to the growth solution. Both of these surfaces were cleaned thoroughly with ultrapure water, ethanol (VWR, $\geq$ 99.9 %), and blown dry using nitrogen gas (BOC).

To determine the effect of surface charge on the resulting calcium carbonate orientations, morphologies and polymorphs, HOPG surfaces were used (grade: SPI-2, ca. 1 cm^2). These were cleaved immediately before use to avoid contamination of the surface using the micromechanical cleaving method.[24,25] This was attached to the base of Petri dishes (Willco Wells) equipped with a perspex rim and lid, with a 12 mm hole in the centre, exposing the cleaved HOPG side of the Scotch tape to the growth solution. To prevent the adhesive side of the Scotch tape also being exposed, Kapton tape was attached around the outer edges of the cleaved HOPG, as shown in Figure 5.1.
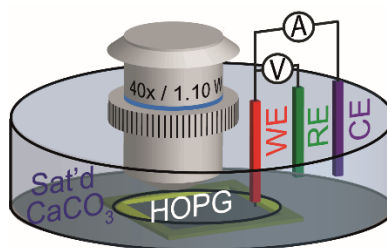
Figure 5.1. Schematic of experimental setup, showing the immersion lens used to follow calcium carbonate crystal growth at charged HOPG surfaces. A three-electrode setup was used, where the working electrode (WE) was HOPG, connected from above by an insulated Pt wire. A saturated calomel reference electrode (RE) and a Pt mesh counter electrode (CE) were used.

A potential was applied to this HOPG surface by implementing a conventional three electrode setup using a potentiostat (CH Instruments-1140b). A Pt wire (0.75 mm diameter) was used to connect the HOPG surface from above, serving as the working electrode (WE). The majority of this wire was insulated by covering it with a fast setting

two-component epoxy (Araldite Rapid), leaving only the very end of the wire exposed to the growth solution (~ 0.65 mm^2) to allow for contact with the HOPG surface and connection as the WE. A commercial saturated calomel electrode (SCE) (CH Instruments-150) and a Pt mesh electrode were implemented as the reference (RE) and counter electrodes (CE), respectively. Potentials of – 1.00, + 0.50 and + 1.00 V vs. SCE were applied to the HOPG surface over the five hr period for which crystal growth was monitored. These potentials correspond to potentials of – 0.76, + 0.74 and + 1.24 V vs. SCE, with respect to the PZC, respectively, which has been measured as ~ – 0.24 V vs. SCE.[26] The open circuit potential was measured as + 0.05 V.

5.2.2. Analysis of Crystal Morphologies

Crystal growth was monitored in situ for five hr for each experiment using a Leica DM4000 M optical microscope. This was imaged using a 40× objective water immersion lens, and a series of time-lapse images were taken throughout the crystal growth process to provide information on the dynamic processes occurring at each surface. After five hr, the growth solution was removed and the samples were rinsed with ultrapure water (Milli-Q Reagent, Millipore) and blown dry using nitrogen gas (BOC). To resolve the morphologies of the crystals obtained at the HOPG surfaces at higher magnifications, a Zeiss Supra 55-VP field emission scanning electron microscope (SEM) was used in secondary electron (SE2) mode at an acceleration voltage of 5 kV.

5.2.3. Analysis of Crystal Polymorphs

Crystals with the same morphologies as those shown in the SEM images were analyzed using Raman spectroscopy to determine the calcium carbonate polymorphs formed at each surface. Spectra were obtained using a Renishaw micro-Raman inVia spectrometer, and the crystals of interest were selected using an optical microscope with a 50× objective lens. The 633 nm line of a HeNe laser was used at 100 % power, with an acquisition time of 10 s for each spectrum. Due to the small laser spot size (515 nm radius), it was possible to resolve and obtain spectra for individual crystals. Spectral calibration was performed using the 520.7 nm peak of a silicon standard.

5.3. Results and Discussion

5.3.1. Background Crystal Growth Experiments

The experimental setup used for investigating calcium carbonate crystallisation is shown in Figure 5.1. A saturated solution with respect to calcite (S = 16.4, as calculated using MINEQL+ (see section 5.2.1) was obtained by combining equal volumes of 5 mM $CaCl_2$ and 20 mM $NaHCO_3$ at an initial pH of 8.07. Images were acquired from above the growth surface throughout the five hr experiment using a 40× objective water immersion lens. This was placed as far away from the electrodes as possible (~ 1 cm), to observe crystallisation in the absence of interference from any reactions occurring at these electrode surfaces. A three electrode setup was used to apply both positive and negative potentials to HOPG surfaces to determine the effect of surface charge on the resulting orientation, morphology and polymorph of $CaCO_3$ grown at the surface. This was connected from above via a Pt wire immediately before adding the growth solution, allowing the HOPG surfaces investigated to be freshly cleaved (less than 5 min before starting the experiment) to avoid contamination.[27] A saturated calomel electrode (SCE) was employed as the RE, and a Pt mesh as the CE.

Before investigating the effects of surface charge, background experiments were performed with no applied potential on a HOPG surface, glass surface and plastic surface. A similar experimental setup was used to that shown in Figure 5.1, whereby the glass or HOPG surface was attached to the base of the petri dish, exposing it to the growth solution at the 12 mm diameter hole in the centre. Plastic surfaces were investigated using 30 mm diameter polystyrene petri dishes. The growth solution used was the same as that for all experiments under potential control (5 mM $CaCl_2$, 20 mM $NaHCO_3$, initial pH = 8.07). After five hr, this was removed and the surfaces were rinsed with ultrapure water and dried. The results are shown in Figure 5.2.
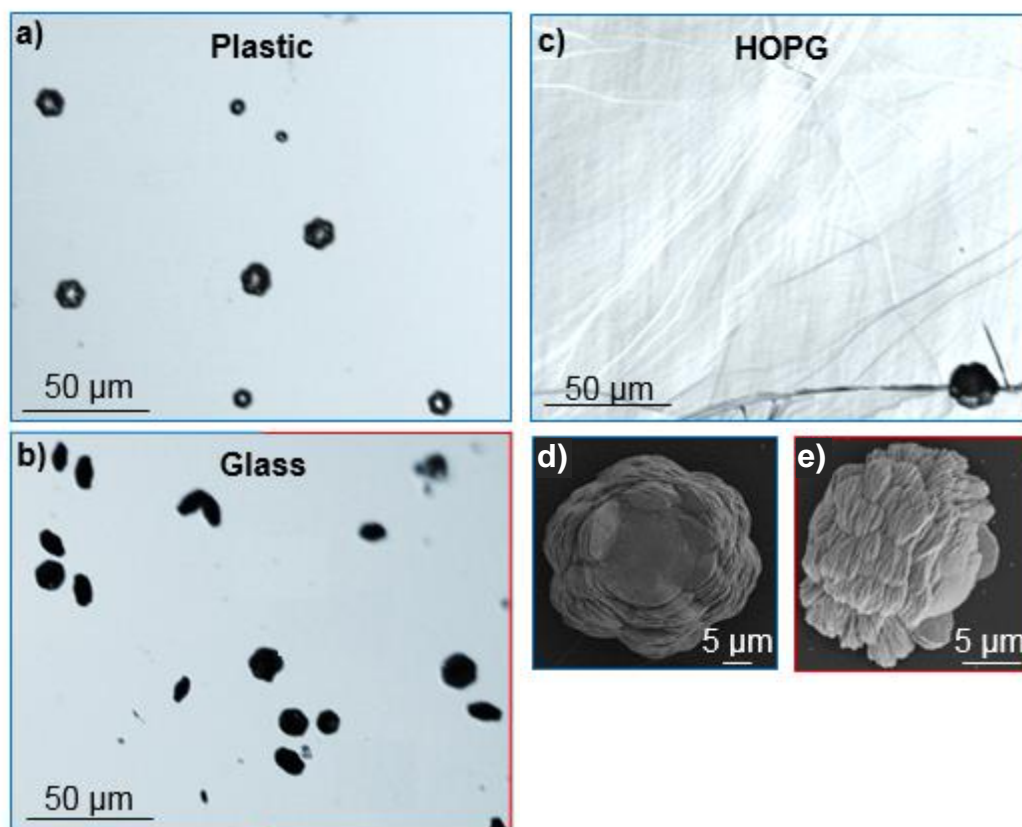
Figure 5.2. Optical images of $CaCO_3$ growth after 5 hr on (a) plastic, (b) glass and (c) HOPG surfaces with no applied potential (PZC of HOPG ~ − 0.24 V)[26] for 5 mM $CaCl_2$ and 20 mM $NaHCO_3$ at an initial pH of 8.07 (OCP = + 0.05 V). The different crystal orientations obtained on glass are shown at higher magnifications in the SEM images, (d) and (e).

A higher number of crystals formed on the plastic and glass surfaces than on the HOPG surface. In fact, on HOPG, very few crystals were found, only at step edges. This is partially a function of surface roughness, as the cleaved HOPG surface consists of atomically flat terraces (basal planes), at which the energy barrier for nucleation will be much higher in comparison to the rougher plastic surface. This is consistent with studies that show diamond-like carbon has excellent antifouling properties with respect to calcium carbonate, in comparison to common metal surfaces, which is attributed to the low diamond-like carbon surface roughness.[1] Therefore, under the conditions employed, nucleation and subsequent growth only occurred very infrequently at step edges, where the energy barrier for nucleation is reduced, due to a decrease in the unfavourable surface energy term.[28] $CaCO_3$ nucleation and growth is also likely to be favoured at step edges over the basal plane due to the presence of carbonyl and carboxyl functional groups at these edges,[29,30] the latter of which will be deprotonated and thus

negatively charged at the pH value employed in these experiments. For example, graphene nanoflakes synthesised with a high density of carboxylic acid edge groups have been found to complex Ca^{2+},[31] which would promote $CaCO_3$ crystallisation.

Although the borosilicate glass surface has a much lower roughness than the polystyrene surface, denser crystal growth was obtained at the former, especially in comparison to the HOPG surface. This is likely to be a consequence of charge effects, as under the pH conditions employed, the non-functionalised borosilicate glass surface will display a slightly negative charge due to dissociation of silanol groups,[32] in contrast to the neutral polystyrene surface and the slightly positively charged HOPG surface (as the open circuit potential (OCP - measured as 0.05 V vs. SCE) is + 0.29 V of the potential of zero charge (PZC ~ – 0.24 V vs. SCE for a variety of aqueous electrolytes).[26] This is explained in more detail below.

At all three surfaces, vaterite was the main calcium carbonate polymorph obtained. This was confirmed via Raman spectroscopy, which is ideal for determining the $CaCO_3$ polymorph formed, as each gives rise to different Raman peaks.[33] Additionally, due to the small laser spot size used (~ 1 μm diameter), spectra were obtained corresponding to the micron-sized crystal of interest only. This was performed on the crystals shown in Figures 5.2 d and e, representative of the main structures found within the background experiments. Both crystals gave very similar Raman spectra, with all peaks in agreement with literature values for vaterite,[33] (see Figure 5.3). The high abundance of vaterite at all three surfaces is likely to be a consequence of the high initial saturation ratio employed (S = 16.4) at which, according to Ostwald's rule of stages, multiple nucleation pathways may occur, with the most soluble and least stable, high energy form crystallising first,[34] which, for the $CaCO_3$ system, corresponds to vaterite. Thus, the formation of vaterite under conditions highly supersaturated with respect to $CaCO_3$ has been extensively reported.[35-37] Due to the short timescales of growth used in these experiments (5 hr) this metastable phase remains throughout, and does not recrystallise to the thermodynamically stable calcite phase. Similar results have been recently reported, where crystal growth at short lifetimes in highly supersaturated solutions resulted in crystallisation of metastable phases, which remained stable at the short timescales employed.[38,39]
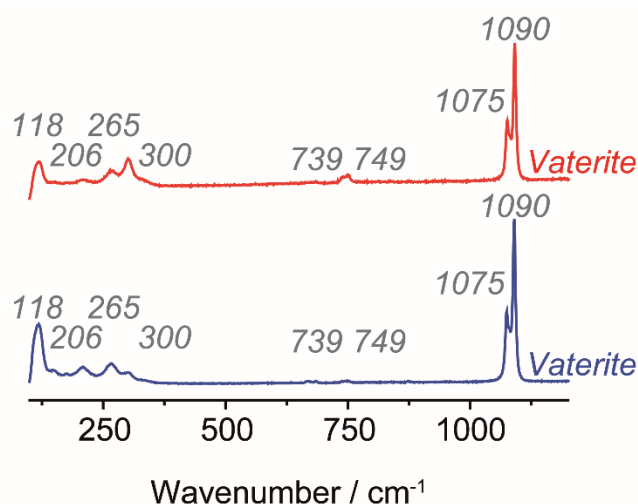
Figure 5.3. Raman spectra obtained for the crystals shown in Figures 5.2d (blue) and 5.2e (red), both of which correspond to vaterite.

It has been found that depending on the growth conditions, vaterite is able to crystallise with several different morphologies.[40] In these background experiments, the flower-like morphology was obtained. The mechanism of growth of this vaterite morphology has been extensively studied,[40] revealing that these initially precipitate as spherical structures, consisting of randomly oriented vaterite nanoparticles, which gives rise to a polycrystalline texture. Over time, hexagonal plates start to grow from the periphery of these spheres, tilting towards the centre of the sphere, creating a 3D structure with a pit in the centre. These hexagonal plates actually comprise hexagonal single vaterite crystals, (see Figure 5.4a) each ~ 1 µm in diameter. Initially, these have blunt, rounded edges, but with time, (after ~ 4 hr) they become sharper and well defined. Eventually, (after ~ 16 hr) the hexagonal plates align with an almost vertical orientation. In our studies, there is clear evidence of these parallel-aligned hexagonal plates forming around the periphery of the vaterite crystals (see Figures 5.2d and e), which, at the timescales employed (5 hr), have slightly curved edges and are aligned in a more horizontal than vertical arrangement. Thus, the final vaterite morphology obtained in these background experiments exhibits a flower-like structure, with sixfold symmetry created by the hexagonal plates and a pit at the centre, very similar to the structure obtained after four hr in the previous study.[40]

Figure 5.4. (a) Schematic of a single crystal hexagonal vaterite plate, formed at the periphery of the vaterite crystals, highlighting the corresponding crystal faces. (b) Projection of the vaterite lattice viewed do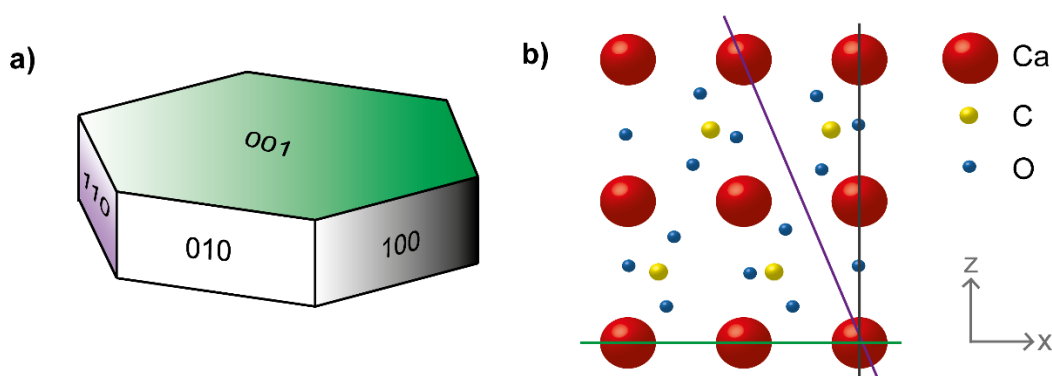wn the (010) crystal plane, with the black line highlighting the (100) plane, the green line, the (001) plane and the purple line, the (110) plane. Note that this is just one of the three possible arrangements of the CO_3^{2-} groups.[41]

The different orientations of these vaterite flowers at the surfaces used in the background experiments provides an initial insight into the effects of surface charge on $CaCO_3$ growth. At both plastic and HOPG surfaces, these crystals oriented face-up in all cases, as shown in Figure 5.2d. However, at the glass surface, two different orientations occurred, including the face-up orientation as well as a side-on orientation (see Figure 5.2e). This is thought to be a consequence of the negative surface charge present at the glass surface, as discussed above. To investigate whether this is the case, the structures of these vaterite flowers were further analysed. Previous studies of this morphology show that for the face-up orientation, the crystal surface which attaches to the petri dish is the pit in the centre of the vaterite flower, which consists of an aggregation of randomly oriented vaterite nanoparticles. This was found to remain in a disordered array throughout the growth process, with dissolution and recrystallisation to a crystalline structure not seen after their initial nucleation.[40] Thus, the face-up oriented crystals found on all three surfaces appear to nucleate from a crystal surface lacking a well-defined arrangement of atoms. Conversely, the side-on vaterite crystals found only on the negatively charged glass surface nucleate with the edges of the hexagonal petals of the flower attaching to the petri dish (see Figure 5.2e). The structure of these plates, which consist of single crystal hexagonal vaterite plates, have been previously resolved, with their basal planes corresponding to the (001) vaterite crystal

face,[40,42,43] and the edges to the (110), (010) and (100) crystal planes[42,43] (see Figure 5.4a). The hexagonal plate edges attaching to the negatively charged glass surface (i.e. the (110), (010) and/or (100) faces) all have a high positive surface charge density, due to the presence of ordered arrangements of Ca^{2+} atoms, as shown in Figure 5.4b. This explains why nucleation from these crystal planes was only observed at the negatively charged glass surface, and not at the neutral polystyrene and slightly positively charged HOPG surface. The above explanation seems viable, as similar, preferential nucleation of the positively charged (001) vaterite basal plane has been previously reported at negatively charged surfaces.[44] To investigate these suspected charge-induced orientation effects further, both positive and negative potentials were applied to the HOPG surface, as described in the following section.

5.3.2. Crystal Growth at Biased Surfaces

HOPG is an ideal surface for investigating the effects of charge on the crystallisation of calcium carbonate, as it has a very well-defined PZC with the minimum density of states (DOS) approximately 2 orders of magnitude lower than that at Au surfaces,[45,46] typically used for investigating the effects of different SAMs on $CaCO_3$ crystallisation. It is also an excellent conductor, displaying high surface charges at low potentials as a result of the DOS rapidly increasing away from the minimum value with potential.[22,23,45] Additionally, through the use of the simple micromechanical cleaving technique,[24,25] thin layers of HOPG can be obtained with atomically flat basal planes, providing an extremely homogeneous, flat surface for investigating crystal growth, without interferences due to surface roughness. Potentials both positive and negative of the PZC were applied to HOPG surfaces using the setup shown in Figure 5.1 to determine the effect of surface charge on the orientation, morphology and polymorph of calcium carbonate grown at the surface. As shown in Figure 5.1, a potential was applied to the HOPG WE by contacting the sample from above using a Pt wire. This arrangement allowed experiments to be started within five min of cleaving the HOPG surface, to minimise exposure of the HOPG surfaces to atmospheric contamination.[27] To demonstrate the importance of this, the resulting crystal growth obtained at a cleaved HOPG surface left exposed to air overnight before performing the experiment (at $-$ 1.00 V vs. SCE) is shown in Figure 5.5, at which crystals with ill-defined morphologies grew.
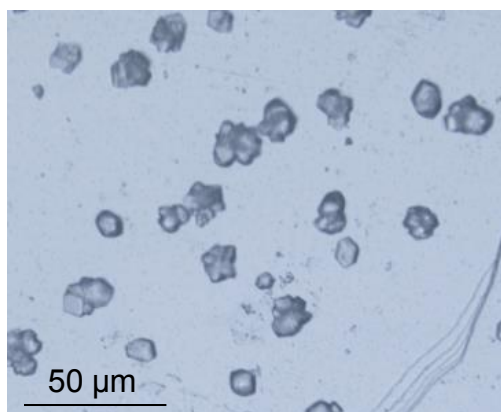
Figure 5.5. Optical image of CaCO$_3$ growth after 5 hr on a HOPG surface, cleaved 24 hr prior to adding the growth solution (5 mM CaCl$_2$, 20 mM NaHCO$_3$, initial pH = 8.07, applied potential = – 1.00 V vs. SCE).

However, avoiding the use of materials to seal the WE meant that a small amount of Pt from the contact was exposed to the solution. As Pt is an efficient catalyst for the hydrogen evolution reaction (HER)[47] (see Equation 5.1), the majority of this wire was insulated using fast set epoxy (see section 5.2.1 for details), to reduce the current generated at this surface at cathodic potentials, which may result in the formation of interfering species due to solvent electrolysis.

$$O_2 + 2H_2O + 2e^- \rightarrow H_2O_2 + 2OH^-$$
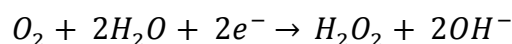
Equation 5.1. Hydrogen evolution reaction (HER) occurring at cathodic potentials at the Pt wire surface.

Only a very small surface area of the Pt wire (~ 0.65 mm^2) was left exposed to the growth solution, to allow contact to the HOPG surface. The resulting currents generated at this exposed Pt wire, and at the Pt wire + HOPG surface when connected are shown in Figure 5.6 for the extreme applied potentials of – 1.00 and + 1.00 V vs. SCE (– 0.76 and + 1.24 V with respect to the PZC, respectively). At the most extreme anodic potential investigated, negligible currents (~ + 0.1 µA) were generated at the Pt wire surface, thus the effects of surface reactions at this potential (such as that shown in Equation 5.2) will also be negligible.

$$2H_2O \rightarrow O_2 + 4H^+ + 4e^-$$
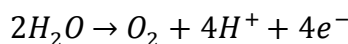
Equation 5.2. Oxygen evolution reaction (OER) occurring at anodic potentials at the Pt wire surface.

As a precaution, in situ optical microscopy images were acquired from above the HOPG surface, for a period of 5 hr, using a 40× objective water immersion lens, which was placed as far away from the CE and WE contact as possible (~ 1 cm), to observe the effects of HOPG surface charge, and not secondary effects from water electrolysis. Note, however, that as currents at the WE and CE were very small (Figure 5.6), any species generated via these processes that might affect the supersaturation (such as OH⁻ or H⁺ ions at cathodic potentials - see Equation 5.1) would be negligible (μM concentrations), and the diffusion length from the CE and WE contact small over the timescale at which crystallisation was initially observed. Additionally, the relatively high concentrations of NaHCO₃ employed (20 mM) acted as a very effective buffer, given the fluxes of OH⁻ or H⁺ produced at the electrode surface. Overall, the presence of this small Pt surface area is a worthwhile compromise in order to be able to conduct experiments immediately on non-contaminated, freshly cleaved HOPG surfaces. As shown by the dotted lines in Figure 5.6, contacting the Pt wire to the HOPG surface resulted in a small increase in the current magnitude at both potentials (~ 0.5 μA), demonstrating that solvent electrolysis at the HOPG surface is also negligible.
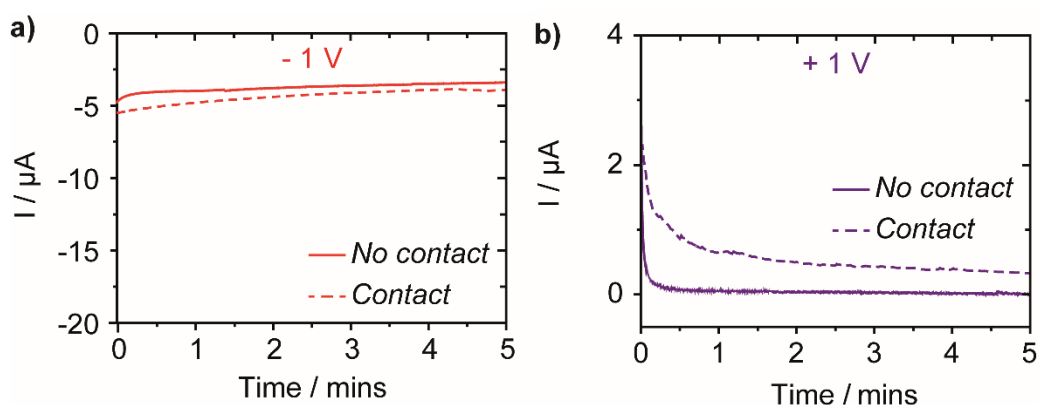
Figure 5.6. Currents obtained at the partially insulated Pt wire WE when not in contact with the HOPG surface (solid lines) and when in contact with the HOPG surface (dashed) for applied potentials of (a) − 1.00 V and (b) + 1.00 V vs. SCE (electrolyte: 5 mM CaCl₂ and 20 mM NaHCO₃, initial pH = 8.07).

The crystals obtained at the HOPG surface for applied potentials of -1.00, $+0.50$ V and $+1.00$ V (-0.76, $+0.74$ and $+1.24$ V vs. SCE with respect to the PZC) are shown in Figure 5.7, demonstrating dramatic differences. The first thing to note is the significantly higher greater coverage of crystals observed at -1.00 V (Figure 5.7a) and $+1.00$ V (Figure 5.7c), compared to at $+0.50$ V (Figure 5.7b) and the HOPG background experiment with no applied potential, (Figure 5.2c) which is only slightly positively charged ($+0.29$ V with respect to the PZC). This is in agreement with previous studies, which demonstrate that polar surfaces induce nucleation to a larger extent than their non-polar counterparts.[48]
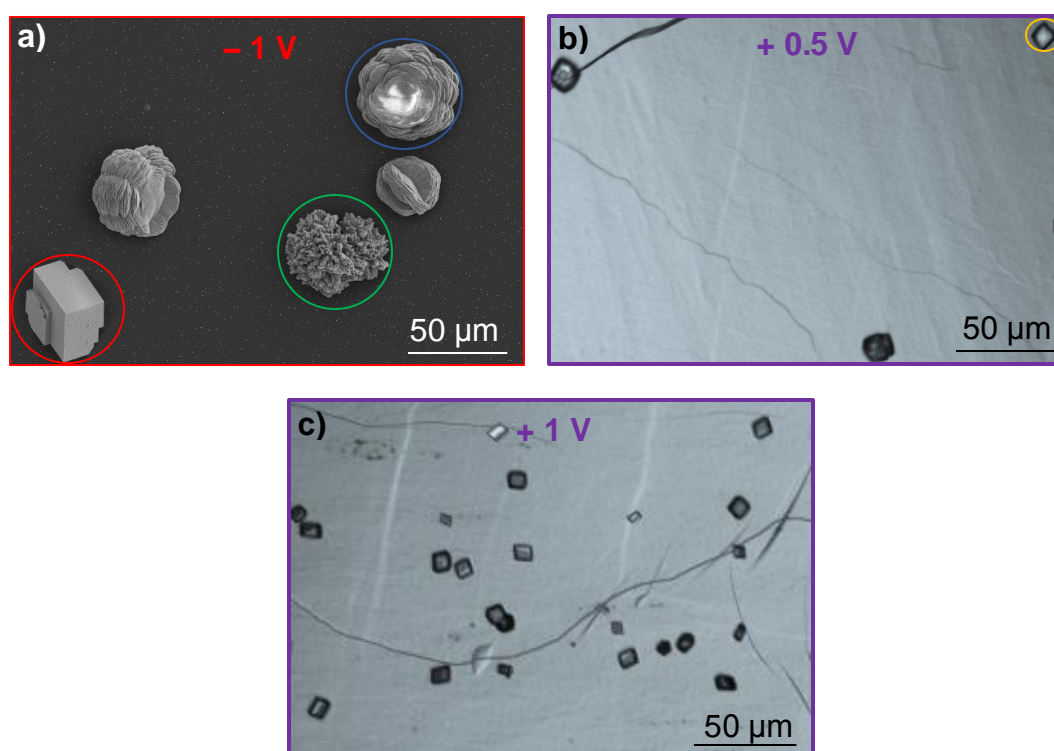
Figure 5.7. Images of $CaCO_3$ growth at biased HOPG surfaces after 5 hr in 5 mM $CaCl_2$ and 20 mM $NaHCO_3$ (initial pH= 8.07). (a) SEM image of resulting growth for an applied potential of -1.00 V vs. SCE at the HOPG WE, with calcite (red), aragonite (green) and vaterite (blue) highlighted. (b) Optical image of calcite crystal growth (yellow highlight) at an applied potential of $+0.50$ V vs. SCE at the HOPG WE. (c) Optical image of calcite crystal growth for an applied potential of $+1.00$ V vs. SCE at the HOPG WE.

Far fewer studies have investigated the role of positively charged surfaces on calcium carbonate nucleation, so very little is currently known on this topic. This is a consequence of the high abundance of polyanionic proteins present during biomineralisation, which several studies have focussed on mimicking due to the full control offered by these over the precipitating calcium carbonate polymorph.[49] As a result, the majority of studies in the literature focus on the growth of calcium carbonate at negatively charged SAM or Langmuir monolayer terminal head groups, or in the presence of soluble and insoluble growth additives with similar amino acid structures to those found in biomineralisation, containing repeating negative charges.[50]

5.3.2.1. Crystal Growth at Negatively Biased Surfaces

Crystal growth occurred at the negatively charged surface after approximately 5 min, as shown in 'video_–1V.mp4' attached with this thesis. At these short timescales, very little diffusion of the negligible concentrations of species generated at the electrode surface occurred, as discussed above. Therefore the nucleation and growth of these crystals will not be affected by the small currents generated at the HOPG surface, as the surrounding solvent environment will not be perturbed to a significant extent by interfering electrode surface reactions. A range of different calcium carbonate polymorphs grew at this surface, as demonstrated in Figure 5.7a, and the corresponding Raman analysis (see Figure 5.8). Crystals that give rise to spectra matching those in the literature for calcite, vaterite and aragonite[33] were all found at this sample surface. These results agree with studies of $CaCO_3$ crystallisation at polycrystalline Au surfaces biased at – 1.00 V vs. SCE, at which a range of calcium carbonate polymorphs were also obtained.[14] However, in our studies, the majority of crystals formed are the metastable vaterite polymorph, as found in the background experiments (see Figure 5.2), due to the high supersaturation conditions employed as discussed above.
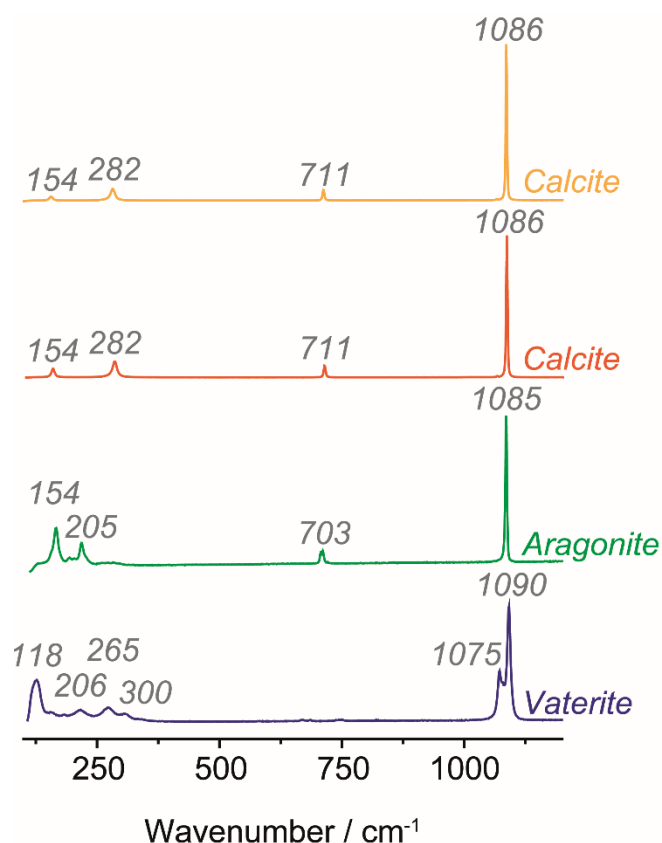
Figure 5.8. Raman spectra obtained for the crystals highlighted in Figures 5.7a and b. Colours of spectra correspond to crystals circled in the same colour.

Interestingly, similar side-on vaterite orientations were observed as those found at the negatively charged glass background experiments shown in Figure 5.2b. Additionally, vaterite crystals oriented face-up moved around on the HOPG surface for approximately 10-30 min. In some cases, it is clear that these crystals continue to move until they find an energetically favourable step edge site (see 'video_-1V.mp4' attached with this thesis). In contrast, vaterite crystals oriented side-on did not exhibit this behaviour (see 'video_–1V.mp4' attached with this thesis). Thus, the side-on orientation, which has only been observed at negatively charged surfaces in our studies, appears to be more stable and have a higher affinity for the negatively charged surface than the face-up orientation. This is rationalised by considering the structures of these two different nucleating planes, as discussed above in section 5.3.1. As the side-on orientation displays a crystal face with a high positive charge density, this will have a strong affinity for the negatively charged surface, and thus does not move around on the surface. However, as the surface of the face-up orientation consists of an amorphous, disordered array of vaterite particles at the centre of the vaterite flowers, it

is likely to have a much weaker (or neutral) charge compared to the side-on orientation, and thus a weaker affinity for the negatively charged surface, resulting in its instability and movement across the surface.

Aragonite and calcite crystals grown at this surface remained in the positions where they originally nucleated. In the case of aragonite, the resulting 'sheaf-of-wheat' morphology[51] (see 'video_–1V.mp4' attached with this thesis) initially nucleated with an elongated structure, which spread out along its length, resulting in spherulitic growth at one end. The elongated planes of aragonite correspond to the (110) and (010) crystal faces,[52] which contain layers of Ca^{2+} ions (as shown in Figure 5.9), which will preferentially interact with the negatively charged surface, explaining why they do not move around on the negatively charged HOPG surface. Furthermore, these aragonite crystal planes have been found to promote the adsorption of negatively charged complexing agents, supporting this conclusion.[53]

Figure 5.9. Projection of the aragonite lattice viewed down the (001) plane, with the black line highlighting the (110) crystal plane, and the green line, the (010) crystal plane.

In the case of calcite, nucleation often occurred from the unusual (001) plane (see Figure 5.7a). Again, this nucleation plane displays a strong positive charge density, of 4.5 Ca^{2+} ions per nm^2,[44] as shown in Figure 5.10a. The nucleation of calcite from a range of different nucleation planes has been previously observed at negatively charged SAM interfaces.[12,13] For example, Aizenberg et al. found that at CO_2H-terminated Au/SAM surfaces, calcite preferentially nucleated on the (015) plane, and on the (104) and (1 0 12) planes at OH- and SO_3^-- terminated Au/SAM surfaces, respectively.[12] Interestingly, the (012) face nucleated at the negatively charged COO^--terminated SAM

groups displays the highest positive charge density of the calcite faces, at 6.7 Ca^{2+} per nm^2.[44] Similar (001) nucleation planes to those found in our studies have also been observed at SO_3^--terminated Pd/SAM surfaces.[13] In all of these cases, these results were attributed to epitaxial relationships between the negatively charged functional groups of the SAM and the positions of the CO_3^{2-} ions in the nucleating $CaCO_3$ crystal faces, with the SAM head groups acting as 'surrogate oxyanions' for specific calcite nucleation planes, thus promoting their growth.[12,13] However, it has been noted that a strict match of the crystallographic structures of the nuclei and underlying substrate is not necessarily required for these processes to occur, with some lattice mismatch between the two often seen.[10,16] In fact, for the epitaxial growth of NaCl on mica, a lattice mismatch as high as 23.2 % was found.[54] This suggests lattice matching is not the only requirement for the nucleation of these unusual, high energy calcite planes.
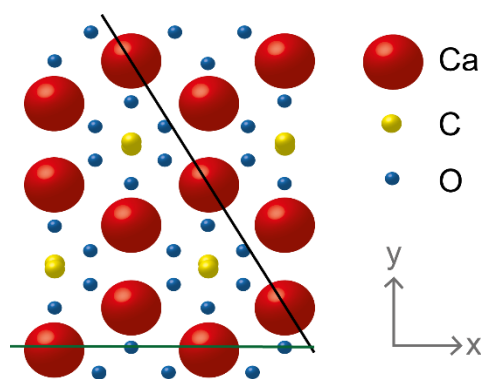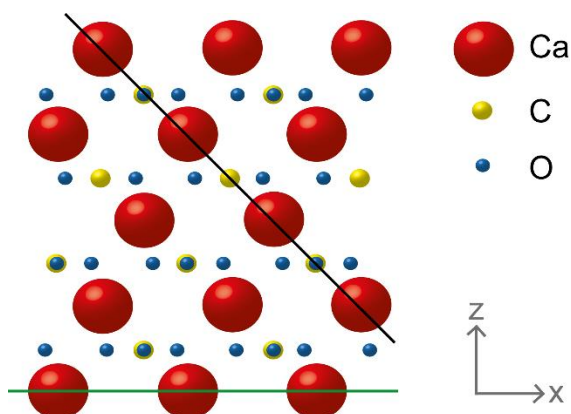

Figure 5.10. Projection of the calcite lattice viewed down the (010) plane, with the black line highlighting the neutral (104) crystal plane, and the green line, the high energy (001) crystal plane.

Epitaxial relationships have also been established between the (001) calcite face and underlying bare surface in the absence of templating SAM functional head groups. For example, preferential calcite (001) nucleation occurred at negatively charged mica surfaces due to a lattice match between the nucleation plane and the (001) mica cleavage plane, and a strong affinity of the negative surface for the Ca^{2+} ions of this crystal face.[55] However, at low Ca^{2+} concentrations, this was not possible unless the mica surface was weathered, as this resulted in the presence of K_2CO_3 crystals, which increased the local concentrations of both HCO_3^- and Ca^{2+} ions to a high enough value to promote epitaxy.[56] Selective nucleation of the (001) calcite plane has also been

observed at bare Au and Ag (111) surfaces on mica biased at -1.00 V vs SCE,[14] using a similar approach to our studies. Again, an epitaxial relationship was found between the Ca^{2+} atoms of the (001) calcite plane and the underlying Au and Ag surfaces, with a lattice mismatch below 0.5 %. However, this also highlighted the importance of the negative charge in controlling this phenomenon, as at Ag surfaces (which have a PZC more negative than Au surfaces) a more negative potential was required than at Au surfaces to see this epitaxial relationship. Thus, in all of the above cases, it is likely that a combination of lattice matching and the presence of a negative charge at the surface is responsible for the preferential nucleation of the high energy, positively charged (001) calcite nucleation plane.

Furthermore, these findings are consistent with $CaCO_3$ growth at the monolayer-solution interface for a range of Langmuir monolayers of macrocyclic, amphiphillic calixarenes and resorcarenes, displaying carboxylic acid functionalities at the air-water interface.[57-60] Differences in the surface areas occupied by these molecules results in the formation of monolayers with different average surface charge densities of carboxylate residues (COO^- nm^{-2}). At low surface pressures, uniformly oriented single calcite crystals nucleated via their (012) crystal faces at the interface for monolayers of tetracarboxy-calix[4]arenes,[57,58] octacarboxy-calix[8]arenes,[59] and tetracarboxy-resorc[4]arenes,[60] which all have an average charge density of 1.90-2.44 COO^- nm^{-2}. In contrast, monolayers of octacarboxy-resorc[4]arenes, which display a higher average charge density of 4.71-4.75 COO^- nm^{-2} resulted in the crystallisation of acicular aragonite crystals,[59] similar to the growth of aragonite at 5-hexadecyloxyisophthalic acid monolayers, with a surface charge density of 4.65 COO^- nm^{-2}.[61] This demonstrates that monolayers with high charge densities are able to nucleate high energy, metastable crystal polymorphs via kinetic control, as seen for in this thesis. Thus, despite structural differences, monolayers with similar surface charges result in similar controlled oriented nucleation and polymorph selection, further supporting our hypothesis that templated $CaCO_3$ nucleation depends strongly on non-specific interfacial electrostatics, with geometric and stereochemical aspects having lower importance. In addition, at these low surface pressures, the monolayers portray a liquid-expanded state, with the molecules present in a mobile template, and therefore oriented nucleation is not a consequence of an epitaxial relationship between the monolayer lattice and the Ca^{2+} ions of the (012) calcite crystal face.

These studies support our findings, which further demonstrate that a chemically functionalised SAM or Langmuir monolayer is not necessary to nucleate the (001) calcite face. A reasonable epitaxial relationship is present in our system between the Ca^{2+} ions of the (001) calcite nucleating plane and the underlying HOPG surface, as demonstrated by Figure 5.11. The Ca-Ca distances in this calcite plane are 0.499 nm,[62] closely matching 2 x the centre-centre distances of the HOPG basal plane (0.492 nm).[63] This results in a lattice mismatch of 1.4 %, much lower than that required for epitaxial growth to be realised.
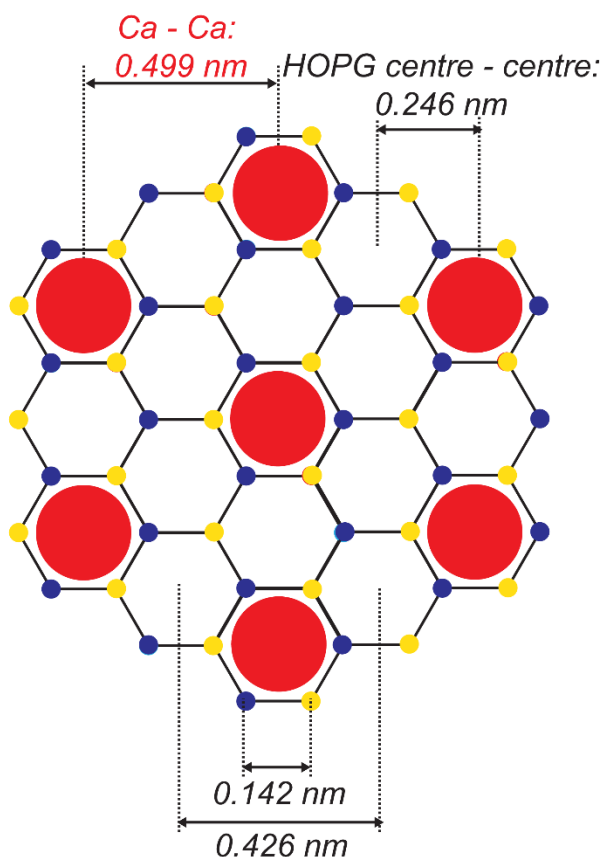
Figure 5.11. Epitaxial relationship between the calcium atoms of the calcite (001) crystal plane (represented by the red circles) and the centre-centre distances of the underlying HOPG basal plane.

However, the fact that all three calcium carbonate polymorphs nucleated at this surface suggests this epitaxial relationship is not particularly strong. Additionally, lattice matches between the vaterite and aragonite crystals formed at the negatively charged surface and the underlying HOPG structure were not found. Nonetheless, for all polymorphs crystallised, nucleation appeared to preferentially occur from a crystal

plane with a high positive charge density, which demonstrates the crucial role of the negative surface charge in controlling the nucleation and growth of $CaCO_3$. This suggests that a lattice match between the crystal and substrate is not essential for the nucleation of unusual, high energy crystal planes. The lack of epitaxy at Au (111) and Ag (111) surfaces unless potentials significantly negative of the PZC were applied,[14] at mica surfaces unless high local concentrations of Ca^{2+} and CO_3^{2-} were present,[56] and for our background experiments on HOPG without applying a negative surface charge further highlight that these nucleating mechanisms are not purely controlled by a lattice match between the nucleating plane and substrate. Therefore, as previously suggested, oriented nucleation is controlled via a combination of electrostatic, geometric and stereochemical effects,[10,16,19,20] with our studies specifically demonstrating the importance of ion concentration profiles normal to the growth surface, and thus electrostatics. To further investigate the role of charge, analogous experiments were performed at positively charged HOPG surfaces, as described below.

5.3.2.2. Crystal Growth at Positively Biased Surfaces

At the positively charged surfaces employed, crystal growth was again observed after approximately five min, (see 'video_+1V.mp4' attached with this thesis) at which, as explained above, species produced at the electrode surface will not interfere with the nucleation and growth. In this case, only calcite crystals were observed, solely nucleating from the stable, neutral (104) face (see Figure 5.10), as shown for the experiments performed at + 0.50 V and + 1.00 V, in Figures 5.7b and c, respectively. These results are similar to those obtained at OH-terminated SAMs[12,13] and hydrogen-bonded monolayers,[64] where nucleation of calcite only occurred via the stable (104) crystal face. This was suggested to be a consequence of the OH functionality not having a significant effect on the template-induced oriented nucleation of calcite. As our results suggest that the surface charge has a huge impact on the nucleation process, this may be a consequence of the higher pKa values associated with OH groups compared with, for example, COOH groups, meaning under the neutral conditions applied in the previous studies, OH-terminated monolayers will have a very weak negative charge in comparison to the COOH-terminated monolayers. This may explain why oriented growth of high energy calcite faces is achievable at COOH-terminated SAMs, but not at OH-terminated SAMs.

Thus, our studies show that positively charged surfaces only promote growth of the thermodynamically stable calcite polymorph, from a stable, neutral nucleating plane. This is in contrast to the range of different polymorphs nucleated at the negatively charged surface, from high energy, positively charged nucleation planes. Although the carbonate ions of the calcite (001) plane occupy analogous positions to the calcium ions (shown in Figure 5.10), and thus a highly negatively charged (001) plane exists, epitaxial growth of this on the positively charged surface is not seen. This may be a consequence of the larger volume of the carbonate ions compared to the Ca^{2+} ions, meaning an analogous epitaxial relationship to that shown in Figure 5.11 is not favoured for the CO_3^{2-} ions at the positively charged surface. These contrasting results at the two extreme potentials further demonstrate the huge impact surface charge plays in determining the orientation of the crystals grown at these surfaces.

5.4. Conclusions

In this chapter, the effect of surface charge on the crystallisation of calcium carbonate has been successfully studied at cleaved HOPG surfaces. These permitted the application of extreme negative and positive potentials without generating significant currents, and thus the study of surface charge effects without interference from products formed as a result of solvent electrolysis. In the absence of an applied potential, very little crystal growth occurred at the HOPG surface, in contrast to the dense growth obtained at both positively and negatively biased surfaces. Furthermore, substantial differences were seen at these two potentials, with negatively charged surfaces favouring the nucleation of high energy, positively charged nucleation planes of vaterite, aragonite and calcite, and positively charged surfaces favouring the nucleation of the neutral (104) calcite plane only.

These results suggest that, although necessary for selective nucleation of a single nucleation plane, lattice matching between the crystal and underlying substrate is not essential for the nucleation of high energy crystal planes, with only a potentially weak epitaxial relationship found in the case of (001) calcite nucleation on the negatively charged HOPG surface. Thus, as previously suggested, a combination of electrostatic, geometric and stereochemical effects control nucleation processes,[10, 16, 19, 20] with our studies specifically highlighting the importance of the former. These findings are not only important for understanding biomineralisation mechanisms, but also have applications in the prevention of costly scale formation processes which occur in several industrial environments.

5.5. Bibliography

(1)   MacAdam, J. P.; Parsons, S. A. *Rev. Environ. Sci. Bio.* **2004**, *3*, 159-169.

(2)   Karabelas, A. J. *Int. J. Therm. Sci.* **2002**, *41*, 682-692.

(3)   Olajire, A. A. *J. Pet. Sci. Eng.* **2015**, *135*, 723-737.

(4)   Roques, H., *Conditioning using scale inhibitors*. In *Chemical Water Treatment Principles + Practise*; Eds.; VCH Pub Inc: New York, 1996; pp 229-270.

(5)   Müller-Steinhagen, H. M.; Institution of Chemical Engineers, *Heat Exchanger Fouling: Mitigation and Cleaning Technologies*; Eds.; Publico Publications: Germany, 2000.

(6)   Pernot, B.; Euvrard, H.; Remy, F.; Simon, P. *J. Water SRT-Aqua* **1999**, *48*, 16-23.

(7)   Baker, J. S.; Judd, S. J. *Water Res.* **1996**, *30*, 247-260.

(8)   Cho, Y. I.; Fan, C. F.; Choi, B.-G. *Int. J. Heat Mass Tran.* **1998**, *41*, 2961-2966.

(9)   Meldrum, F. C.; Cölfen, H. *Chem. Rev.* **2008**, *108*, 4332-4432.

(10)   Sommerdijk, N. A. J. M.; de With, G. *Chem. Rev.* **2008**, *108*, 4499-4550.

(11)   Nudelman, F.; Sommerdijk, N. A. J. M. *Angew. Chem. Int. Ed.* **2012**, *51*, 6582-6596.

(12)   Aizenberg, J. B.; Black, A. J.; Whitesides, G. M. *J. Am. Chem. Soc.* **1999**, *121*, 4500-4509.

(13)   Aizenberg, J. B.; Black, A. J.; Whitesides, G. M. *Nature* **1999**, *398*, 495-498.

(14)   Teghidet, H.; Bernard, M. C.; Borensztajn, S.; Chaal, L.; Joiret, S.; Saidani, B. *J. Cryst. Growth* **2011**, *331*, 72-77.

(15)   Han, Y.-J.; Aizenberg, J. *J. Am. Chem. Soc.* **2003**, *125*, 4032-4033.

(16)   Heywood, B. R.; Mann, S. *Adv. Mater.* **1994**, *6*, 9-20.

(17)   Harding, J. H.; Freeman, C. L.; Duffy, D. M. *CrystEngComm* **2014**, *16*, 1430-1438.

(18)   Côte, A. S.; Darkins, R.; Duffy, D. M. *J. Phys. Chem. C* **2014**, *118*, 19188-19193.

(19)   Heywood, B. R.; Rajam, S.; Mann, S. *J. Chem. Soc. Faraday Trans.* **1991**, *87*, 735-743.

(20)   Rajam, S. H.; Heywood, B. R.; Walker, J. B. A.; Mann, S.; Davey, R. J.; Birchall, J. D. *J. Chem. Soc. Faraday Trans.* **1991**, *87*, 727-734.

(21)   Sprenger, K. G.; He, Y.; Pfaendtner, J., *Probing How Defects in Self-assembled Monolayers Affect Peptide Adsorption with Molecular Simulation.* In *Foundations of Molecular Modelling and Simulation: Select Papers from FOMMS 2015*; Snurr, R. Q.; Adjiman, C. S.; Kofke, D. A., Eds.; Springer Singapore: Singapore, 2016; pp. 21-35.

(22)   Patel, A. N.; Guille Collignon, M.; O'Connell, M. A.; Hung, W. O. Y.; McKelvey, K.; Macpherson, J. V.; Unwin, P. R. *J. Am. Chem. Soc.* **2012**, *134*, 20117-20130.

(23)   Unwin, P. R.; Güell, A. G.; Zhang, G. *Acc. Chem. Res.* **2016**, *49*, 2041-2048.

(24)   Novoselov, K. S.; Geim, A. K.; Morozov, S. V.; Jiang, D.; Zhang, Y.; Dubonos, S. V.; Grigorieva, I. V.; Firsov, A. A. *Science* **2004**, *306*, 666-669.

(25)   Novoselov, K. S.; Jiang, D.; Schedin, F.; Booth, T. J.; Khotkevich, V. V.; Morozov, S. V.; Geim, A. K. *Proc. Natl. Acad. Sci. U.S.A.* **2005**, *102*, 10451-10453.

(26)   Kneten, K. R.; McCreery, R. L. *Anal. Chem.* **1992**, *64*, 2518-2524.

(27)   Nioradze, N.; Chen, R.; Kurapati, N.; Khvataeva-Domanov, A.; Mabic, S.; Amemiya, S. *Anal. Chem.* **2015**, *87*, 4836-4843.

(28)   Hamilton, B. D.; Ha, J.-M.; Hillmyer, M. A.; Ward, M. D. *Acc. Chem. Res.* **2012**, *45*, 414-423.

(29)   Lounasvuori, M. M.; Rosillo-Lopez, M.; Salzmann, C. G.; Caruana, D. J.; Holt, K. B. *Faraday Discuss.* **2014**, *172*, 293-310.

(30)   Evans, J. F.; Kuwana, T. *Anal. Chem.* **1979**, *51*, 358-365.

(31)   Lounasvuori, M. M.; Holt, K. B. *Chem. Commun.* **2017**, *53*, 2351-2354.

(32)   Sa, N.; Lan, W.-J.; Shi, W.; Baker, L. A. *ACS Nano* **2013**, *7*, 11272-11282.

(33)   Kontoyannis, C. G.; Vagenas, N. V. *Analyst* **2000**, *125*, 251-255.

(34)   Ostwald, W. *Z. Phys. Chem.* **1897**, *22*, 289-330.

(35)   Colfen, H.; Antonietti, M. *Langmuir* **1998**, *14*, 582-589.

(36)   Kralj, D.; Brecevic, L.; Kontrec, J. *J. Cryst. Growth* **1997**, *177*, 248-257.

(37)   Ogino, T.; Suzuki, T.; Sawada, K. *Geochim. et Cosmochim. Acta* **1987**, *51*, 2757-2767.

(38)   Lee, S.; Wi, H. S.; Jo, W.; Cho, Y. C.; Lee, H. H.; Jeong, S.-Y.; Kim, Y.-K.; Lee, G. W. *Proc. Natl. Acad. Sci. U.S.A.* **2016**, *113*, 13618-13623.

(39)   Shahidzadeh, N.; Schut, M. F.; Desarnaud, J.; Prat, M.; Bonn, D. *Sci. Rep.* **2015**, *5*, 10335.

(40) Hu, Q.; Zhang, J.; Teng, H.; Becker, U. *Am. Mineral.* **2012**, *97*, 1437-1445.

(41) Meyer, H. J. *Z. Kristallogr.* **1969**, *128*, 183.

(42) Pouget, E. M.; Bomans, P. H. H.; Dey, A.; Frederik, P. M.; de With, G.; Sommerdijk, N. A. J. M. *J. Am. Chem. Soc.* **2010**, *132*, 11560-11565.

(43) Xu, A.-W.; Antonietti, M.; Cölfen, H.; Fang, Y.-P. *Adv. Funct. Mater.* **2006**, *16*, 903-908.

(44) Falini, G.; Fermani, S.; Gazzano, M.; Ripamonti, A. *J. Chem. Soc., Dalton Trans.* **2000**, 3983-3987.

(45) Gerischer, H. M.; McIntyre, R.; Scherson, D.; Storck, W. J. *J. Phys. Chem.* **1987**, *91*, 1930-1935.

(46) Kokko, K.; Ojala, E.; Mansikka, K. *Phys. Status Solidi B* **1989**, *153*, 235-241.

(47) Sheng, W.; Myint, M.; Chen, J. G.; Yan, Y. *Energy Environ. Sci.* **2013**, *6*, 1509-1512.

(48) Küther, J.; Seshadri, R.; Knoll, W.; Tremel, W. *J. Mater. Chem.* **1998**, *8*, 641-650.

(49) Belcher, A. M.; Wu, X. H.; Christensen, R. J.; Hansma, P. K.; Stucky, G. D.; Morse, D. E. *Nature* **1996**, *381*, 56-58.

(50) Weiner, S.; Addadi, L. *J. Mater. Chem.* **1997**, *7*, 689-702.

(51) Nielsen, M. H.; Aloni, S.; De Yoreo, J. J. *Science* **2014**, *345,* 1158-1162.

(52) Aquilano, D.; Rubbo, M.; Catti, M.; Pavese, A. *J. Cryst. Growth* **1997**, *182*, 168-184.

(53) Westin, K.-J.; Rasmuson, A. C. *J. Colloid Int. Sci.* **2005**, *282*, 359-369.

(54) Lisgarten, N. D. *Trans. Faraday Soc.* **1954**, *50*, 684-690.

(55) Xu, X.-R.; Pan, H.-H.; Tang, R.-K.; Cho, K. *CrystEngComm* **2011**, *13*, 6311-6314.

(56) Stephens, C. J.; Mouhamad, Y.; Meldrum, F. C.; Christenson, H. K. *Cryst. Growth Des.* **2010**, *10*, 734-738.

(57) Volkmer, D.; Fricke, M.; Vollhardt, D.; Siegel, S. *J. Chem. Soc., Dalton Trans.* **2002**, *0*, 4547-4554.

(58) Volkmer, D.; Fricke, M. *Z. Anorg. Allg. Chem.* **2003**, *629*, 2381-2390.

(59) Volkmer, D.; Fricke, M.; Agenab, C.; Mattay, J. *J. Mater. Chem.* **2004**, *14*, 2249-2259.

(60) Volkmer, D.; Fricke, M.; Agena, C.; Mattay, J. *CrystEngComm.* **2002**, *4*, 288-295.

(61)   Litvin, A. L.; Valiyaveettil, S.; Kaplan, D. L.; Mann, S. *Adv. Mater.* **1997**, *9*, 124-127.

(62)   Dove, M. T.; Winkler, B.; Leslie, M.; Harris, M. J.; Salje, E. K. H. *Am. Mineral.* **1992**, *77*, 244-250.

(63)   Henriksen, K.; Stipp, S. L. S. *Am. Mineral.* **2002**, *87*, 5-16.

(64)   Champ, S. D.; Dickinson, J. A.; Fallon, P. S.; Heywood, B. R.; Mascal, M. *Angew. Chem. Int. Ed.* **2000**, *39*, 2716-2719.

Chapter 6: Conclusions

The work presented in this thesis uses a combination of in situ OM analysis with various spectroscopic techniques, to provide a holistic overview of the impact of several experimental factors on inorganic crystallisation processes occurring within both biological and industrial environments. This approach allowed crystallisation phenomena to be investigated at different novel functionalised interfaces relatively unexplored in comparison to more classical crystal growth approaches in bulk aqueous solvents, or at commonly employed SAM and Langmuir monolayer interfaces. In situ studies elucidated morphological and polymorphic changes during the crystal growth process, with the wide range of structural analytical techniques used post-experiment unambiguously identifying the unusual crystal structures obtained at these applied growth interfaces. The methods employed throughout highlighted the key mechanistic factors which control crystallisation in two contrasting scenarios: during calcium sulfate deposit formation at aqueous-organic interfaces in internal combustion engines and during the growth of calcium carbonate on charged graphite surfaces.

To set the scene for studying the formation of inorganic deposits within an internal combustion engine, Chapter 2 presented the results of an in depth analytical and structural characterisation of the main components present within deposits obtained at the surface of pistons from diesel engines. The approach involved the use of TGA, demonstrating the significant abundance (~ 40 wt. %) of inorganic components in deposits near the top of the piston surface, and thus the importance of understanding how to prevent their deposition. Implementing SEM-EDX revealed the amorphous structure of the deposit, and showed calcium to be the most abundant inorganic element present. Further analysis via Raman spectroscopy and XRD confirmed calcium to be present in the form of the crystalline polymorphs, bassanite ($CaSO_4 \cdot 0.5H_2O$) and anhydrite ($CaSO_4$). The formation of these highly dehydrated polymorphs was speculated to be a consequence of the high temperature conditions and organic solvent environment present within the engine during the crystallisation process.

The mechanism of formation of these dehydrated calcium sulfate polymorphs was investigated to a much higher level of detail in Chapter 3, to further understand and thus prevent the deposition process. To replicate crystallisation occurring within the engine, aqueous-organic interfaces were applied. These growth interfaces model the

environment thought to be responsible for calcium sulfate deposition. At the end of Chapter 2, we proposed this occurs due to the neutralisation of emulsified aqueous sulfuric and sulfurous acids in the oil and fuel by overbased calcium carbonate detergent additives, forming calcium sulfate as a neutralisation product. Thus, real commercial detergent particles comprising calcium carbonate cores and long alkyl-chain surfactant tails were dispersed in either hexane or dodecane oil phases, to which a microlitre-sized aqueous sulfuric acid droplet was added. The resulting crystal growth at the aqueous-organic interface formed was followed via in situ OM, and it was found via ex situ Raman spectroscopy and XRD analysis that when hexane was used as the bulk organic solvent environment, a combination of the fully hydrated gypsum ($CaSO_4 \cdot 2H_2O$) and anhydrite ($CaSO_4$) polymorphs were obtained, with needle and plate morphologies, respectively. However, employing dodecane as the organic phase resulted in the formation of gypsum needles only. This was attributed to the high volatility and thus fast evaporation of the hexane solvent, which acts to increase the local $CaSO_4$ concentration. This results in a solution supersaturated with respect to anhydrite, a consequence of the low water content environment. In contrast, dodecane is inert and thus did not evaporate to an appreciable extent over the course of the crystal growth studies and the formation of anhydrite was not realised. A gypsum needle dissolution-anhydrite plate precipitation mechanism was proposed for the hexane environment. These findings not only provided a wealth of knowledge on the deposit formation mechanism, but also highlighted the applicability of non-aqueous solvent environments for obtaining crystal structures considered thermodynamically unstable in aqueous environments, under ambient conditions.

Following on from the results obtained in Chapters 2 and 3, a method was developed to investigate the binding efficiencies of a range of dispersant additives to the calcium sulfate deposit surface. This allows dispersant chemistries to be developed to effectively suspend the deposit within the lubricating oil, thus preventing deposit formation on the piston surface. In doing so, additive chemistries can be tuned to their maximum efficiency, reducing additive concentrations, which has a beneficial impact on fuel efficiency and CO_2 emissions. This was conducted using CFM, by employing the anhydrite surfaces grown in Chapter 3, as this material was found to be one of the main inorganic deposit components in Chapter 2. AFM probes were functionalised with different dispersant model structures using SAM chemistry, which exposed a range of

different functional groups at the end of the AFM probe. By approaching and retracting the functionalised probes towards and away from the model inorganic deposit surface in an organic solvent, quantitative values were determined for the adhesion between the two, showing that aromatic dispersant head groups have a low adhesion for the polar deposit surface, as expected, whereas polar dispersant functional groups unexpectedly showed no adhesion to the polar crystal surface. This was attributed to electrostatic repulsion between the two, due to the presence of water within the non-dried organic solvent environment and thus ion adsorption. These studies not only elucidated fundamental considerations necessary for the development of fuel additive chemistries, but also have key implications on understanding adhesive and repulsive behaviours, as well as the structure of charge in organic solvent environments, areas which are all still under considerable debate.

All of the results obtained in Chapters 2-4 related to a key industrial problem caused by crystallisation at an industrially-relevant applied functionalised interface. In Chapter 5, a similar methodology was used to focus on a different crystallisation process, namely the role of surface charge in the biomimetic growth of calcium carbonate. In moving from studying an industrially important crystallisation process to a more fundamental system, more freedom is obtained to investigate the impact of a specific experimental parameter on crystal polymorphism, rather than using the techniques described above to determine the parameters responsible for the resulting crystallisation. Again, in situ OM was used to follow crystal growth, this time at charged graphite surfaces, which provided a flat surface for studying the effects of surface charge on the orientation and polymorphism of calcium carbonate, in the absence of head group chemistries and defects inherent of previously employed methods. At negatively charged surfaces, all three calcium carbonate polymorphs, calcite, vaterite and aragonite nucleated from high energy, positively charged crystal planes, in contrast to the low energy, neutral (104) planes of the thermodynamically stable polymorph calcite nucleated at positively charged surfaces. These results provided for the first time details on the role of charge in the templated nucleation of calcium carbonate, without interference from solvent electrolysis or head group chemistries, highlighting that lattice matching between the nucleating crystal face and the underlying substrate is not an essential requirement for the nucleation of high energy

crystal planes. This is of fundamental importance for understanding the role of charge in biomineralisation processes occurring in nature.

To summarise, this thesis provides crucial advances in understanding and implementing unusual crystal growth interfaces for the formation of unique crystalline materials with highly desirable structural properties, which are often unattainable under low energy, ambient conditions. This work contributes further to the increasingly popular field of studying crystallisation at aqueous-organic and specifically designed biomimetic interfaces, with a particular focus on the key factors which promote undesirable crystallisation in oil-based industrial environments, and in the desirable nucleation of high energy calcium carbonate planes, using similar, powerful approaches to those inherent in biomineralisation to specifically direct the crystallisation process. Thus, these findings are of significant fundamental and industrial importance, particularly aiding the development of more effective additive chemistries within the oil industry.